**Universidade do Minho**
Escola de Engenharia

Liliana Sofia da Silva Ferreira Pinto de Melro

# Development of antimicrobial coated bacterial nanocellulose-based hernia mesh devices for postoperative infection prevention

Setembro de 2026

Development of antimicrobial coated bacterial nanocellulose-based hernia mesh devices for postoperative infection preventionitul

Liliana Melro

UMinho | 2026

**Universidade do Minho**
Escola de Engenharia

Liliana Sofia da Silva Ferreira Pinto de Melro

# Development of antimicrobial coated bacterial nanocellulose-based hernia mesh devices for postoperative infection prevention

Tese de Doutoramento
Doutoramento em Engenharia Têxtil

Trabalho efetuado sob a orientação de
**Professor Doutor Andrea Zille**
**Doutor Jorge Manuel Padrão Ribeiro**

September 2026

**DIREITOS DE AUTOR E CONDIÇÕES DE UTILIZAÇÃO DO TRABALHO POR TERCEIROS**

Este é um trabalho académico que pode ser utilizado por terceiros desde que respeitadas as regras e boas práticas internacionalmente aceites, no que concerne aos direitos de autor e direitos conexos.

Assim, o presente trabalho pode ser utilizado nos termos previstos na licença abaixo indicada.

Caso o utilizador necessite de permissão para poder fazer um uso do trabalho em condições não previstas no licenciamento indicado, deverá contactar o autor, através do RepositóriUM da Universidade do Minho.

***Licença concedida aos utilizadores deste trabalho***



**Atribuição-NãoComercial-SemDerivações**
**CC BY-NC-ND**

https://creativecommons.org/licenses/by-nc-nd/4.0/

## ACKNOWLEDGEMENTS

I would like to acknowledge the Portuguese Foundation for Science and Technology (FCT) for the research grant 10.54499/2020.04919.BD, co-funded by the Ministry of Science, Technology and Higher Education (MCTES), the European Social Fund (FSE), and the European Union (EU).

I would like to express my deepest gratitude to my supervisors Professor Andrea Zille and Dr. Jorge Padrão for their invaluable scientific guidance and mentorship. My thanks also go to the Centre for Textile Science and Technology (2C2T) for providing the facilities essential to this PhD. I am grateful to our technicians for their constant availability and technical support throughout these years. To my laboratory colleagues, thank you for your camaraderie, patience, and collaboration. I also extend my thanks to Dr. Helena Felgueiras for her generosity and insightful comments.

I am indebted to MD Fernando Ferreira for his valuable clinical insights and the provision of samples, and to Miguel Portela at the MIPMED - Smart Medical Solutions for supplying the commercial meshes. I extend my sincere gratitude to Professor Diego Moldes from the Department of Chemical Engineering at the University of Vigo for providing the Kraft lignin and to Valpaços Oleiculture Cooperative winery for supplying the olive pomace. At the National Institute for Lasers, Plasma and Radiation Physics in Romania, I would like to thank Dr. Bogdana Mitu and Dr. Veronica Satulu for the XPS analysis and their valuable insights. From the Centre of Biological Engineering (CEB), I would like to thank Professor Francisco Miguel Gama and Professor Fernando Dourado for providing the bacterial strain, and to Dr. Ana Cristina Rodrigues for her expert assistance with the freeze-drying sample preparation and very helpful insights to this work. Within the Mechanical Engineering Department (DEM), the Center for Microelectromechanical Systems (CMEMS), and the University of Trás-os-Montes and Alto Douro (UTAD) I extend special thanks to Professor Nuno Dourado and to Professor Fábio Pereira for granting access to the mechanical testing equipment. In particular I am deeply grateful to Teresa Campos for her significant assistance with the mechanical analyses and discussions. At the Toxicology Laboratory Group of the Faculty of Farmacy at the University of Porto (FFUP), my thanks to Professor Félix Carvalho for providing the laboratory facilities. I am particularly grateful to Dr. João Pedro Silva for his assistance with laboratory materials, methodology, and productive discussions. At CMEMS, special thanks are due to Dr. Vanessa F. Cardoso, Eduarda Oliveira, Cláudia Silva, and Dr. Margarida Fernandes, for providing the facilities and materials for the cellular assays. I also thank Dr. Carlos Silva, Professor Óscar Carvalho, and Nuno Fernandes (DEM/CMEMS) for their technical assistance with the LASER

cutting of the bacterial nanocellulose (BNC). And to Dr. Raul Machado at the Centre of Molecular and Environmental Biology for providing and assisting with the electrophoresis.
Finally, at last but definitely not least, my heartfelt thanks go to my family and closest friends for their unwavering support.

## STATEMENT OF INTEGRITY

I hereby declare having conducted this academic work with integrity. I confirm that I have not used plagiarism or any form of undue use of information or falsification of results along the process leading to its elaboration.

I further declare that I have fully acknowledged the Code of Ethical Conduct of the University of Minho.

University of Minho, September 2026

Full name: Liliana Sofia da Silva Ferreira Pinto de Melro

Signature:

## PUBLICATIONS AND COMMUNICATIONS

### Publications related to the PhD

Manuscripts in preparation for submission

1 **Melro, L.**; Fernandes, M.; Mehravani, B.; Ribeiro, A. I.; Mitu, B.; Satulu, V.; Rodrigues, A. C.; Gama, M.; Padrão, J.; Zille, A.; "BNC-based hernia mesh with prospective decrease of post-operative infections – Part I (*ex situ* and *in situ* production and characterization)". Prospective Journal for submission:

2 **Melro, L.**; Fernandes, M.; Campos, T.; Mehravani, B.; Ribeiro, A. I.; Mitu, B.; Satulu, V.; Fernandes, N.; Carvalho, O.; Faria, C.; Ferreira, F.; Pereira, F.; Dourado, N.; Silva, J. P.; Carvalho, F.; Padrão, J.; Zille, A.; "BNC-based hernia mesh with prospective decrease of post-operative infections – Part II (biological activity and mechanical properties)". Prospective Journal for submission

Indexed journal papers

1 **Melro, L.**; Alves, C.; Fernandes, M.; Fernandes, R. D. V.; Pereira, A.; Moldes, D.; Rodrigues, A. C.; Sencadas, V.; Mitu, B.; Satulu, V.; Lourenço, J.; Pace, G.; Martins, L.A.; Gómez Ribelles, J. L.; Salgado, A. J.; Padrão, J.; and Zille, A. "Phenolic-modified bacterial nanocellulose composites with antimicrobial and antioxidant activity for implantable biomaterials". Composites Part A: Applied Science and Manufacturing (2026): https://doi.org/10.1016/j.compositesa.2026.109970..

2 **Melro, L.**; Alves, C.; Fernandes, M.; Rocha, S.; Mehravani, B.; Ribeiro, A. I.; Azevedo, S.; Cardoso, V. F.; Carvalho, O.; Dourado, N.; Salgado, A. J.; Zille, A.; Padrão, J.; "Bacterial nanocellulose as a versatile scaffold for biomedical applications: Synthesis, functionalization, and future prospects". Applied Materials Today (2025): https://doi.org/10.1016/j.apmt.2025.102858.

3 Fernandes, M.; Padrão, J.; Ribeiro, A. I.; Fernandes, R. D. V.; **Melro, L.**; Nicolau, T.; Mehravani, B.; Alves, C.; Rodrigues, R.; Zille, A.; "Polysaccharides and Metal Nanoparticles for Functional Textiles: A Review". Nanomaterials (2022): https://doi.org/10.3390/nano12061006.

Book chapters

1 Fernandes, M.; Alves, C.; **Melro, L.**; Fernandes, R. D. V.; Padrão, J.; Salgado, A. J.; Zille, A.; "Modification of Nanocellulose". In Handbook of Biomass, 1-39. Springer Nature Singapore, 2023. https://doi.org/10.1007/978-981-19-6772-6_35-1.

2 Song, X.; Padrão, J.; Fernandes, M.; Ribeiro, A. I.; **Melro, L.**; Alves, C.; Yu, L.; Zille, A.; "Antibacterial hydrogel dressings and their applications in wound treatment". In Antimicrobial Dressings The Wound Care Applications, 153-185. Chennai, India: Stacy Masucci, 2023. https://doi.org/10.1016/B978-0-323-95074-9.00010-5.

3 Song, X.; **Melro, L.**; Padrão, J.; Ribeiro, A. I.; Yu, L.; Zille, A.; "Nonwoven materials and technologies for medical applications". In Medical Textiles from Natural Resources, edited by Md. Ibrahim H. Mondal, 605-662. Woodhead Publishing, 2022. https://doi.org/10.1016/B978-0-323-90479-7.00008-7.

4 Padrão, J.; **Melro, L.**; Fernandes, M.; Fernandes, R. D. V.; Ribeiro, A. I.; Song, X.; Yu, L.; Zille, A.; "Biocompatibility of Nanocellulose". In Handbook of Biopolymers, 1-32. Springer Nature Singapore, 2022. https://doi.org/10.1007/978-981-19-0710-4_36.

Conference abstracts

1 **Melro, L.**; Fernandes, M.; Ribeiro, A. I.; Mehravani, B.; Campos, T.; Silva, J. P.; Dourado, N., Ferreira, F.; Padrão, J.; Zille, A.; “Mechanical and cellular adhesion assessment of metal nanoparticles functionalised bacterial nanocellulose (BNC) mesh”. Microbiotec, 4—6 th December, Ponta Delgada (São Miguel, Azores) 2025.

2 Alves, C.; **Melro, L.**; Mehravani, B.; Ribeiro, A. I.; Selvi, B.; Bozaci, E.; Dourado, F.; Gama, M.; Padrão, J.; Zille, A. "The assessment of bacterial nanocellulose functionalized with metal nanoparticles". Seventh International Symposium Frontiers in Polymer Science, 29 May—1 June, Gothenburg (Sweden), 2023.

3 Padrão, J.; **Melro, L.**; Moldes, D.; Dourado, F.; Gama, M.; Zille, A.; "Antimicrobial Performance of Lignin Embedded in Bacterial Nanocellulose Membranes". 5th International Conference on Natural Fibers (ICNF), 17—19 May, Guimarães (Portugal), 2021.

4 Padrão, J.; **Melro, L.**; Ribeiro, A. I.; Dourado, F.; Gama, M.; Ferreira, F.; Zille, A.; "Bio-Synthesised Fibrous-Based Meshes for Abdominal Hernia with Enhanced Mechanical and Antimicrobial Properties". 1° Workshop Online Latinoamericano em Nanobiotecnología - Aplicaciones en Agricultura, Medicina e Indústria Textil, 2—3 December, Temuco (Chile), 2020.

Oral presentations

1 **Melro, L.**; Fernandes, M.; Ribeiro, A. I.; Mehravani, B.; Campos, T.; Silva, J. P.; Dourado, N., Ferreira, F.; Padrão, J.; Zille, A.; "Mechanical and cellular adhesion assessment of metal nanoparticles functionalised bacterial nanocellulose (BNC) mesh". MICROBIOTEC Congress of Microbiology and Biotechnology, 4–6 December, Ponta Delgada (São Miguel, Azores) 2025.

2 Padrão, J.; **Melro, L.**; Moldes, D.; Dourado, F.; Gama, M.; Zille, A.; "Antimicrobial Performance of Lignin Embedded in Bacterial Nanocellulose Membranes". 5th International Conference on Natural Fibers (ICNF), 17–19 May, Guimarães (Portugal), 2021.

Poster presentations

1 Alves, C.; **Melro, L.**; Mehravani, B.; Selvi, B.; Bozaci, E.; Padrão, J.; Zille, A.; "The assessment of bacterial nanocellulose functionalized with metal nanoparticles". Seventh International Symposium Frontiers in Polymer Science, 29 May–1 June, Gothenburg (Sweden), 2023.

2 **Melro, L.**; Mehravani, B.; Silva, G.; Nicolau, T.; Dourado, F.; Gama, M.; Padrão, J.; Zille, A.; "Antibacterial properties of bacterial nanocellulose functionalized with metal nanoparticles via *in situ* synthesis". Seventh International Symposium Frontiers in Polymer Science, 29 May–1 June, Gothenburg (Sweden), 2023.

Other output

1 **Melro, L.**; Fernandes, M.; Nicolau, T.; Tavares, T. D.; Fernandes, R. D. V.; Felgueiras, H. P.; Dourado, F.; Gama, M.; Zille, A.; e-book "Produção de nanocelulose bacteriana" in Comunicação de Ciência em Microbiologia, Lisboa; Sociedade Portuguesa de Microbiologia, 2022. Published. https://spmicrobiologia.files.wordpress.com/2022/09/ebook_spm.pdf.

Event participation/Exhibition

1 **2023/09/30** Noite Europeia dos Investigadores (NEI) - European Researchers' Night – iniciativa financiada pela Comissão Europeia no âmbito do programa Horizonte 2020, Ações Marie Sklodowska-Curie (MSCA), que tem como objetivo aproximar investigadores e cidadãos. Sensibilização dos mais jovens para a relevância da investigação e inovação na Europa com vista a um futuro mais sustentável e inclusivo, mas também para o facto das carreiras científicas poderem ser determinantes para encontrar soluções que minimizem problemas da sociedade. Ciência para todos (SCIEVER) – Inclusão e Sustentabilidade. Universidade do Minho Escola de Ciências, Portugal.

2 **2022/09/30** Noite Europeia dos Investigadores (NEI) - European Researchers' Night – iniciativa financiada pela Comissão Europeia no âmbito do programa Horizonte 2020, Ações Marie Sklodowska-Curie (MSCA), que tem como objetivo aproximar investigadores e cidadãos. Ciência para todos (SCIEVER) – Inclusão e Sustentabilidade. Universidade do Minho Escola de Ciências, Portugal.

3 **2021/09/24** Noite Europeia dos Investigadores (NEI) - European Researchers' Night – iniciativa financiada pela Comissão Europeia no âmbito do programa Horizonte 2020, Ações Marie Sklodowska-Curie (MSCA), que tem como objetivo aproximar investigadores e cidadãos. Ciência para todos (SCIEVER) – Inclusão e Sustentabilidade. Universidade do Minho Escola de Ciências, Portugal.

Distinctions

1 **2021** Honourable Mention at Conference: Fibrenamics: ICNF 2021 - 5th International Conference on Natural Fibers, Portugal.

2 **2020** PhD FCT grant 2020.04919.BD - "Development of antimicrobial coated bacterial nanocellulose-based hernia mesh devices for postoperative infection prevention". Associação para a Inovação e Desenvolvimento da FCT, Portugal.

## Other publications not directly related to the PhD

### Indexed journal papers

1 Alves, C.; Fernandes, R. D. V.; **Melro, L**.; Fernandes, M.; Padrão, J.; Moldes, D.; Salgado, A. J.; Puga, H.; and Zille, A.; "Kraft Lignin Tunable-Sized Nanoparticles Production Via Ultrasonication And Surfactant-Assisted Methods". Submitted to Small.

2 Caseiro, B.; Alves, C.; Fernandes, R. D. V.; **Melro, L.**; Mehravani, B.; Peixoto, J.; Monteiro, F.; Zille, A.; Antunes, J. C.; Padrão, J. "Reusable multifunctional textile-based smart packaging for fruit preservation and spoilage monitoring". Reactive and Functional Polymers (2026): https://doi.org/10.1016/j.reactfunctpolym.2026.106772.

3 Alves, C.; **Melro. L.**; Fernandes, M.; Padrão, J.; Moldes, D.; Serra, S. C.; Salgado, A. J.; and Zille, A.; "Plasma-Treated Bacterial Nanocellulose-Lignin Composites for Biomedical Applications". International Journal of Biological Macromolecules (2025): https://doi.org/10.1016/j.ijbiomac.2025.149544.

4 Alves, C.; **Melro, L.**; Fernandes, M.; Padrão, J.; Moldes, D.; Serra, S. C.; Salgado, A. J.; and Zille, A.; "Plasma-Treated Bacterial Nanocellulose-Lignin Composites for Neuralgia Implants". AUTEX Conference 2025 Worl Conference, 11–13 June, Dresden (Germany), 2025.

5 Rodrigues, P. V.; Castro, M. C. R.; Soares, A. M. S.; **Melro, L.**; Machado, A. V.; "Development of a Polyethylene Breathable Packaging Film with Modified Microcrystalline Cellulose for Fresh Products". Macromol (2024): https://doi.org/10.3390/macromol4020015.

6 Fernandes, R. D. V.; **Melro, L.**; Padrão, J.; Ribeiro, A. I.; Mehravani, B.; Monteiro, F.; Pereira, E.; Martins, M. S.; Dourado, N.; Zille, A.; "Active Neutralizing Mats for Corrosive Chemical Storage". Gels (2022): https://doi.org/10.3390/gels8080489.

### Book chapter

1 Fernandes, M.; Fernandes, R. D. V.; Padrão, J.; **Melro, L.**; Alves, C.; Rodrigues, R.; Ribeiro, A. I.; Zille, A.; "Plasma in Textile Wastewater Treatment". In Advances in Plasma Treatment on Textile Surfaces, edited by Sahid Ul Islam; Aminoddin Haji, 267-322. Elsevier, 2024. https://doi.org/10.1016/B978-0-443-19079-7.00008-7.

Conference papers

1 **Melro, L.**; Tavares, T. D.; Padrão, J.; Dourado, F.; Gama, M.; Silva, C.; Antunes, J. C.; Felgueiras, H. P.; Zille, A.; "Antimicrobial Activity of a Bacterial Nanocellulose Film Functionalized with Nisin Z for Prospective Burn Wounds Treatment". Paper presented in ECA: The 2nd International Electronic Conference on Antibiotics—Drugs for Superbugs: Antibiotic Discovery, Modes of Action And Mechanisms of Resistance, 15—30 June, 2022 (Online). https://doi.org/10.3390/eca2022-12708.

2 **Melro, L.**; Fernandes, R. D. V.; Peixoto, J.; Pinheiro, I.; Ribeiro, A.; Bouça, V.; Dourado, F.; Gama, M.; Padrão, J.; Zille, A.; "Antiviral properties of flame retardant bacterial nanocellulose modified with mordenite". Paper presented in N: 21th World Textile Conference, 7—10 June 2022 (Online). https://doi.org/10.34658/9788366741751.129.

3 Padrão, J.; Pinheiro, I.; Silva, C.; Ribeiro, A.; Bouça, V.; **Melro, L.**; Fernandes, R. D. V.; Ribeiro, A. I.; Felgueiras, H. P.; Zille, A.; "Distinct antimicrobial analysis to evaluate multi-component wound dressing performance". Paper presented in 20th AUTEX World Textile Conference, 5—9 September, Guimaraes (Portugal), 2021. https://doi.org/10.4028/p-kdad2h.

4 Ribeiro, A. I.; Mehravani, B.; Magalhães, C.; Nicolau, T.; **Melro, L.**; Fernandes, R. D. V.; Shvalya, V.; Cvelbar, U.; Padrão, J.; Zille, A.; "Enhancing the antimicrobial efficacy of polyester fabric impregnated with silver nanoparticles using DBD plasma treatment". Paper presented in 20th AUTEX World Textile Conference, 5—9 September, Guimaraes (Portugal), 2021. https://doi.org/10.4028/p-256i32.

Conference abstracts

1 Santiago, Silva, M.; Alves, C.; Fernandes, R. D. V.; **Melro, L.**; Zille, A.; Padrão, J.; Violacein as a sustainable biopigment for textile dyeing and printing applications. AUTEX World Conference 2025, 3—5 June, Marrakesh (Morocco), 2026: Accepted.

2 Caseiro, B.; Alves, C.; Fernandes, R. D. V.; **Melro, L.**; Mehravani, B.; Peixoto, J.; Monteiro, F.; Zille, A.; Antunes, J.; Padrão, J.; Multifunctional textile-based active and smart packaging for fruit preservation and freshness monitoring. AUTEX World Conference 2025, 3—5 June, Marrakesh (Morocco), 2026: Accepted.

3 Alves, C.; **Melro, L.**; Fernandes, M.; Padrão, J.; Moldes, D.; Serra, S. C.; Salgado, A. J.; Zille, Andrea; Corresponding author: Zille, Andrea. "Plasma-Treated Bacterial Nanocellulose-Lignin Composites for Neuralgia Implants". AUTEX 2025 World Conference, 11—13 June, Dresden (Germany), 2025.

4 Mehravani, B.; Fernandes, M.; Alves, C.; **Melro, L.**; Fernandes, R. D. V.; Moldes, D.; Padrão, J.; Zille, A.; "Active wound dressing of electrospun lignin/cellulose acetate on cotton gauze". AUTEX 2025 World Conference, 11—13 June, Dresden (Germany), 2025.

5 Rocha, S.; **Melro, L.**; Alves, C.; Santos, A. Z.; Oliveira, S.; Cardoso, V. F.; Carvalho, O.; Padrão, J.; "Study of the effect of the physical characteristics of bacterial nanocellulose on

the proliferation of triple negative breast cancer cells". 2nd. International Workshop on Additive Manufacturing and Sustainability (IWAM), 30 September, Bragança (Portugal), 2025.

6 Zille, A.; Fernandes, M.; Alves, C.; **Melro, L.**; Carvalho, O.; Padrão, J.; Serra, S.; Salgado, A. J.; Moldes, D.; Ferreira, F.; "Bacterial nanocellulose nanocomposites for medical applications". 2nd International Conference on Laser, Plasma and Radiation Science and Technology, 16–21 June, Crisan (Romania), 2024.

7 Fernandes, M.; **Melro, L.**; Fernandes, R. D. V.; Ribeiro, A. I.; Felgueiras, H. P.; Silva, C.; Pinheiro, I.; Bouça, V.; Ribeiro, A.; Padrão, J.; Zille, A.; "Physical properties of an antibacterial and antiviral woven cotton functionalized with a multi-nanocomposite". Seventh International Symposium Frontiers in Polymer Science, 29 May–1 June, Gothenburg (Sweden), 2023.

8 Tavares, T. D.; **Melro, L.**; Antunes, J. C.; Silva, C.; Dourado, F.; Gama, M.; Padrão, J.; Zille, A.; Felgueiras, H. P.; "Bacterial nanocellulose films loaded with nisin Z -antibacterial efficacy against *Staphylococcus aureus* strains". IECBM: The 2nd International Electronic Conference on Biomolecules: Biomacromolecules and the Modern World Challenges, 1–15 November 2022 (Online, 11 November).

9 **Melro, L.**; Fernandes, M.; Dourado, F.; Gama, M.; Felgueiras, H. P.; Padrão, J.; Zille, A; "Antimicrobial activity of bacterial nanocellulose modified with chestnut extract". 5th International Symposium on Bacterial Cellulose, 22–23 September, Jena (Germany), 2022.

10 Padrão, J.; Pinheiro, I.; Silva, C. J. S. M.; Ribeiro, A.; Bouça, V.; **Melro, L.**; Fernandes, R. D. V.; Ribeiro, A. I.; Felgueiras, H. P.; Zille, A.; "Multicomponent Wound Dressing". 5th International Conference on Natural Fibers (ICNF), 17–19 May, Guimarães (Portugal), 2021.

11 Ribeiro, A. I.; Padrão, J.; **Melro, L.**; Souto, A. P.; Zille, A.. "Deposition of Silver Nanocomposite on Textiles for Controllable Antibacterial Activity Using Atmospheric Pressure Dielectric Barrier Discharge (DBD) Plasma". 1° Workshop Online Latinoamericano em Nanobiotecnología - Aplicaciones en Agricultura, Medicina e Indústria Textil, 2–3 December, Temuco (Chile), 2020.

Oral presentations

1 Tavares, T. D.; **Melro, L.**; Antunes, J. C.; Silva, C.; Dourado, F.; Gama, M.; Padrão, J.; Zille, A.; Felgueiras, H P; “Bacterial nanocellulose films loaded with nisin Z -antibacterial efficacy against *Staphylococcus aureus* strains”. IECBM: The 2nd International Electronic Conference on Biomolecules: Biomacromolecules and the Modern World Challenges, 1–15 November 2022 (Online).

Poster presentations

1 Fernandes, M.; **Melro, L.**; Fernandes, R. D. V.; Ribeiro, A. I.; Felgueiras, H. P.; Silva, C.; Pinheiro, I.; Bouça, V.; Ribeiro, A.; Padrão, J.; Zille, A.; "Physical properties of antibacterial and antiviral woven cotton functionalized with a multi-nanocomposite". Seventh International Symposium Frontiers in Polymer Science, 29 May—1 June, Gothenburg (Sweden), 2023.

2 Nicolau, T.; Alves, C.; **Melro, L.**; Fernandes, R. D. V.; Mehravani, B.; Forte, J.; Ribeiro, V.; Ribeiro, M.; Dourado, F.; Gama, M.; Padrão, J.; and Zille, A.; "A functionalized nanobiopolymer as an alternative for burn wound dressing". Seventh International Symposium Frontiers in Polymer Science, 29 May—1 June, Gothenburg (Sweden), 2023.

3 **Melro, L.**; Fernandes, M.; Dourado, F.; Gama, M.; Felgueiras, H. P.; Padrão, J.; Zille, A.; "Antimicrobial activity of bacterial nanocellulose modified with chestnut extract". 5th International Symposium on Bacterial Cellulose, 22—23 September, Jena (Germany), 2022.

4 **Melro, L.**; Tavares, T. D.; Padrão, J.; Dourado, F.; Gama, M.; Silva, C.; Antunes, J.; Felgueiras, H. P.; Zille, A. "Antimicrobial activity of a bacterial nanocellulose film functionalized with Nisin Z for prospective burn wounds treatment". ECA: The 2nd International Electronic Conference on Antibiotics—Drugs for Superbugs: Antibiotic Discovery, Modes of Action And Mechanisms of Resistance, 15—30 June, 2022 (Online).

5 Padrão, J.; Pinheiro, I.; Silva, C. J. S. M.; Ribeiro, A.; Bouça, V.; **Melro, L.**; Fernandes, R. D. V.; Ribeiro, A. I.; Felgueiras, H. P.; Zille, A.; "Multicomponent Wound Dressing". 5th International Conference on Natural Fibers (ICNF), 17—19 May, Guimarães (Portugal), 2021.

**Desenvolvimento de rede de suporte para hérnias à base de nanocelulose bacteriana com revestimento antimicrobiano para prevenção de infeções pós-operatórias**

## RESUMO

As redes de suporte a hérnias são amplamente utilizadas como suporte para músculos enfraquecidos ou danificados. As redes sintéticas comerciais apresentam complicações a curto e longo prazo, devendo-se maioritariamente a defeitos no material resultantes da reação ao corpo estranho, levando a infeções que, na maioria dos casos, exigem a remoção completa da rede. Este projeto teve como objetivo a produção de redes de suporte a hérnias com propriedades e arquitetura controladas, utilizando um biomaterial puro e estável, a nanocelulose bacteriana (BNC) funcionalizada com agentes orgânicos ou inorgânicos com propriedades antimicrobianas que previnam ativamente infeções pós-operatórias a longo prazo. Agentes orgânicos como a lignina Kraft (KL) e o bagaço de azeitona (OP), foram testados utilizando diferentes abordagens de funcionalização: filtração e esgotamento. Apesar de se ter obtido uma melhor homogeneização da amostra no processo por esgotamento, estes compósitos demonstraram atividade antimicrobiana negligenciável. A etapa seguinte consistiu na funcionalização da BNC com partículas metálicas de ouro (Au), prata (Ag), cobre (Cu) e óxido de cobre ($Cu_2O$). Neste caso, foram testadas três abordagens diferentes: filtração, esgotamento, e *in situ*. Considerando a semelhança entre os resultados do esgotamento e *in situ*, este último foi o escolhido, uma vez que apenas é necessária uma etapa para a funcionalização. As análises de química de superfície, morfologia e propriedades térmicas não mostraram alterações no substrato original, sugerindo a ausência de ligações químicas. A avaliação das propriedades antibacterianas revelou uma excelente atividade (redução logarítmica: contact killing < 5 e shake flask < 8), em particular para os compósitos à base de Cu. Nos ensaios celulares, à exceção das redes de BNC/Ag, não foi observada influência na morfologia e proliferação celular dos restantes compósitos. A introdução de arquitetura porosa e de partículas metálicas foi favorável, tendo-se observado um aumento da rigidez de 0.5 MPa para 12 MPa, para a membrana e rede de BNC, respetivamente. A reidratação também foi crucial, aumentando o módulo de elasticidade *(E)* para 16 MPa. O valor de *E* mais elevado foi obtido para a rede de BNC/$Cu_2O$ com 20.5 MPa. Estes valores são, no entanto, mais baixos que a rede comercial Optilene, embora suficientes para hérnias inguinais de menores dimensões.

**Palavras-chave:** lignina/lenhina, partículas metálicas, antibacteriano, nanocelulose bacteriana, adesão celular, redes para hérnia.

**Development of antimicrobial coated bacterial nanocellulose-based hernia mesh devices for postoperative infection prevention**


## ABSTRACT

Hernia support meshes are widely used in surgical procedures where support for weakened or damaged muscles is required. Commercial synthetic meshes exhibit short- and long-term complications, mostly due to material defects resulting from the foreign body reaction, which leads to infections that, in most cases, require complete mesh removal. This project envisaged the production of hernia support meshes with precise specifications based on a pure and stable biomaterial, bacterial nanocellulose (BNC), functionalised with organic or inorganic active agents with antimicrobial properties to actively prevent long-term post-operative infections. Organic active agents, Kraft lignin (KL) and olive pomace (OP), were tested in different solubilisation media, in particular due to the poor KL solubility at neutral and acidic pH. Multiple functionalisation methodologies were evaluated, such as filtration and exhaustion. Exhaustion displayed the best homogenisation, with the composites demonstrating negligible antimicrobial activity (< Log 2). Metallic particles of gold (Au), silver (Ag), copper (Cu) and copper oxide ($Cu_2O$) were used to functionalize BNC through filtration, exhaustion, and *in situ*. Considering the similar results between exhaustion and the *in situ* methodologies, the latter was chosen, since only one step is required for functionalisation. Surface chemistry, morphology, and thermal property analyses showed no changes in the original substrate, suggesting the absence of chemical bonding. Evaluation of antibacterial properties revealed excellent antimicrobial activity (log reduction: contact killing: < 5 and shake flask < 8), particularly for the Cu-based composites. Unlike BNC/Ag meshes, which proved to be highly cytotoxic, no influence on cell morphology and proliferation was observed from the remaining composites. The introduction of a porous architecture and metal particles was beneficial since an increase in stiffness was observed. From 0.5 MPa for the BNC membrane to 12 MPa for the BNC mesh. The rehydration was also crucial, increasing the elastic modulus to 16 MPa for the rehydrated BNC mesh. The higher $E$ was obtained for the BNC/$Cu_2O$ mesh with 20.5 MPa. These values are however low compared to commercial Optilene mesh, but sufficient for smaller inguinal hernia defects.



**Keywords:** Lignin, metallic particles, antibacterial, bacterial nanocellulose, cell adhesion, hernia meshes.

## TABLE OF CONTENT

DIREITOS DE AUTOR E CONDIÇÕES DE UTILIZAÇÃO DO TRABALHO POR TERCEIROS ..... i
ACKNOWLEDGEMENTS ..... ii
STATEMENT OF INTEGRITY ..... iv
PUBLICATIONS AND COMMUNICATIONS ..... v
RESUMO ..... xiii
ABSTRACT ..... xiv
TABLE OF CONTENT ..... xv
ACRONYMS AND ABBREVIATIONS ..... xviii
FIGURE INDEX ..... xxii
TABLE INDEX ..... xxvii
1. Introduction ..... 2
1.1. Framework ..... 2
1.2. Research questions ..... 3
1.3. Objectives ..... 3
1.4. Outline ..... 4
2. Literature review ..... 8
2.1. Abdominal hernias ..... 8
2.2. Hernia meshes ..... 9
2.2.1. Commercial meshes ..... 11
2.2.2. New approaches for mesh implants ..... 25
2.3. Bacterial nanocellulose ..... 25
2.3.1. Production ..... 29
2.3.2. Modification ..... 36
2.3.3. BNC functionalised with organic and inorganic agents ..... 38
2.3.4. BNC composites as implants ..... 46
2.3.5. BNC mesh composites ..... 54
3. Functionalisation with organic agents ..... 58
3.1. Introduction ..... 58
3.2. Materials ..... 58
3.3. Methods ..... 59
3.3.1. BNC processing ..... 59
3.3.2. Organic active agents ..... 60
3.3.3. Functionalisation methodologies ..... 61
3.4. Characterisation ..... 62
3.4.1. Size and morphology of KL and BNC composites ..... 62
3.4.2. Crystalline structure ..... 63
3.4.3. Pore size ..... 63

3.4.4. Surface area and adsorption isotherms..... 64
3.4.5. Chemical structure..... 64
3.4.6. Surface chemistry..... 64
3.4.7. Thermal properties..... 65
3.4.8. Swelling profile..... 66
3.4.9. Release profile..... 67
3.4.10. Antimicrobial activity..... 67
3.4.11. Antioxidant properties..... 68
3.5. Results and discussion..... 69
3.5.1. Media and functionalisation methodology selection..... 69
3.5.2. Size and morphology of KL and OP and BNC composites..... 71
3.5.3. Crystalline structure..... 75
3.5.4. Pore size..... 75
3.5.5. Surface area and adsorption isotherms..... 76
3.5.6. Chemical structure..... 77
3.5.7. Surface chemistry (XPS) ..... 78
3.5.8. Thermal properties..... 84
3.5.9. Swelling profile..... 86
3.5.10. Release profile..... 88
3.5.11. Antimicrobial activity..... 90
3.5.12. Antioxidant properties..... 93
3.6. Conclusions..... 95
4. Functionalisation with inorganic agents..... 97
4.1. Introduction..... 97
4.2. Materials..... 97
4.3. Methods..... 98
4.3.1. Cultivation of *Komagataeibacter hansenii*..... 98
4.3.2. Synthesis of Au nanoparticles..... 98
4.3.3. Synthesis of Ag nanoparticles..... 99
4.3.4. Synthesis Cu and $CuO_2$ particles..... 99
4.3.5. Functionalisation methodologies..... 100
4.4. Characterisation..... 103
4.4.1. Charge and size of the particles..... 103
4.4.2. Morphology and elemental composition..... 103
4.4.3. Chemical characterization..... 104
4.4.4. Thermal analysis..... 105
4.4.5. Swelling profile..... 105
4.4.6. One-month release..... 106
4.4.7. Antimicrobial activity..... 106

4.5. Results and discussion ..... 107
4.5.1. Size and charge and of the particles ..... 107
4.5.2. Morphology and elemental composition ..... 111
4.5.3. Chemical composition ..... 114
4.5.4. Surface chemistry ..... 116
4.5.5. Thermal analysis ..... 118
4.5.6. Swelling profile ..... 120
4.5.7. One-month release ..... 122
4.5.8. Antimicrobial activity ..... 123
4.6. Conclusions ..... 124
5. BNC mesh composites ..... 126
5.1. Introduction ..... 126
5.2. Materials ..... 126
5.3. Methods ..... 127
5.3.1. BNC mesh production ..... 127
5.3.2. Functionalisation in situ ..... 130
5.4. Characterisation ..... 131
5.4.1. Morphology ..... 131
5.4.2. Swelling profile ..... 131
5.4.3. Release profile ..... 131
5.4.4. Antibacterial activity ..... 132
5.4.5. Cell adhesion and viability ..... 132
5.4.6. Mechanical properties ..... 135
5.5. Results and discussion ..... 139
5.5.1. Morphology ..... 139
5.5.2. Swelling profile ..... 142
5.5.3. Release profile ..... 143
5.5.4. Antibacterial activity ..... 144
5.5.5. Cellular adhesion ..... 146
5.5.6. Mechanical properties ..... 154
5.6. Conclusions ..... 163
6. General conclusions and future perspectives ..... 165
6.1. General conclusions ..... 165
6.2. Future perspectives ..... 166
References ..... 167

## ACRONYMS AND ABBREVIATIONS

**#**

| | |
|---|---|
| 3D | Three-dimensional |

**A**

| | |
|---|---|
| AA | Ascorbic acid |
| AAS | Atomic absorbance spectroscopy |
| ASTM | American Society for Testing and Materials |
| ATCC | American type culture collection |
| ATP | Adenosine trisphosphate |
| ATR-FTIR | Attenuated total reflectance-Fourier transform infrared spectroscopy |

**B**

| | |
|---|---|
| BBB | Blood brain barrier |
| Bcs | BNC synthase operon |
| BET | Brunauer, Emmett, Teller |
| BNC | Bacterial nanocellulose |
| BR | Britton-Robinson |

**C**

| | |
|---|---|
| C3D10 | Quadratic tetrahedral elements |
| CFU | Colony-forming units |
| CI | Crystallinity index |
| Cryo-FESEM | Cryo-field emission scanning electron microscopy |

**D**

| | |
|---|---|
| di-GMP | di-guanosine monophosphate |
| DLS | Dynamic light scattering |
| DMEM | Dulbecco's modified Eagle's medium |
| DNA | Deoxyribonucleic acid |
| DPPH | 2,2-diphenyl-1-picrylhydrazyl radical |
| DSC | Differential scanning calorimetry |
| DMSO | Dimethyl sulphoxide |

**E**

| | |
|---|---|
| EDS | Energy dispersive spectrometer |
| ePTFE | Expanded polytetrafluoroethylene |
| ECM | Extra cellular matrix |
| EPS | Extracellular polymeric substances |

**F**

| | |
|---|---|
| FBS | Fetal bovine serum |
| FDA | Food and Drug Administration |
| FEM | Finite element modelling |
| FEG-SEM | Field emission gun – scanning electron microscope |

**H**

| | |
|---|---|
| HBSS | Hanks balanced salt solution |
| HEX | N-acetyl-β-d-hexosaminidase |

**I**

| | |
|---|---|
| ISO | International Organisation for Standardisation |

**K**

| | |
|---|---|
| KL | Kraft lignin |

**L**

| | |
|---|---|
| LASER | Light amplification by stimulated emission of radiation |
| LED | Light-emitting diodes |

**M**

| | |
|---|---|
| MEW | Electrowritting |
| mPCL | Medical grade polycaprolactone |
| MHB | Mueller-Hinton broth |
| MTT | Thiazolyl blue tetrazolium bromide |
| MTS | 3-(4,5-dimethylthiazol-2-yl)-5-(3-carboxymethoxyphenyl)-2-(4-sulfophenyl)-2H-tetrazolium |

**N**

| | |
|---|---|
| NA | Nutrient agar |
| NB | Nutrient broth |
| NIR | Near-infrared |
| NR | Neutral red |

**O**

| | |
|---|---|
| OP | Olive pomace |

**P**

| | |
|---|---|
| P4HB | Poly-4-hydroxybutyrate |
| PBS | Phosphate-buffered saline |
| PCL | Polycaprolactone |
| PCUU | Polycarbonate polyurethane urea |
| PDA | Polydopamine |

| | |
|---|---|
| PdI | Particle dispersion index |
| PDO | Polydioxanone |
| PE | Polyethylene |
| PEDOT | Poly(3,4-ethylenedioxythiophene) |
| PET | Poly(ethylene terephthalate) |
| PFU | Plaque-forming units |
| PGA | Polyglycolide |
| P(GA-TMC) | Poly (glycolide-co-trimethylene carbonate) |
| PGC-25 | Poliglecaprone |
| PGLA | Polyglactin |
| PLA | Polylactide |
| P(LA-TMC) | Poly(lactide-co-trimethylene carbonate) |
| PLGA | Poly(lactide-co-glycolide) |
| PP | Propylene |
| PP At.% | Peak percentage atomic percent |
| PTFE | Polytetrafluoroethylene |
| PU | Polyurethane |
| PVA | Poly(vinyl alcohol) |
| PVDF | Polyvinylidene fluoride |

**R**

| | |
|---|---|
| RBL-2H3 | Rat basophilic leukaemia mast cells |
| RNA | Ribonucleic acid |
| ROS | Reactive oxygen species |
| RSC96 | Rat Schwann cell line |

**S**

| | |
|---|---|
| SBF | Simulated body fluid |
| SDS | Sodium dodecyl sulfate |
| SEM | Scanning transmission electron microscopy |
| SERS | Surface-enhanced Raman scattering spectroscopy |
| SF | Silk fibroin |
| SIS | Porcine intestinal submucosa |
| SPIONs | Superparamagnetic iron oxide nanoparticles |
| STA | Scanning thermogravimetric analysis |
| STEM | Scanning transmission electron microscopy |

**T**

| | |
|---|---|
| TEM | Transmission electron microscopy |
| TEMPO | 2,2,6,6-Tetramethylpiperidine-1-oxyl |
| TGA | Thermogravimetric analysis |
| TMC | Trimethylene carbonate |

| | |
|---|---|
| TSA | Trypticase soy agar |
| TSB | Trypticase soy broth |

**U**

| | |
|---|---|
| UDP-Glc | Uridine diphosphate glucose |
| UV | Ultraviolet |
| UV-vis | Ultraviolet-visible spectroscopy |

**V**

| | |
|---|---|
| VC | Viable counts |

**X**

| | |
|---|---|
| XPS | X-ray photoelectron spectroscopy |
| XRD | X-ray diffraction |

## FIGURE INDEX

**Figure 1.1.** Schematic representation of the experimental strategy: Chapter 3 explores two methodologies for organic agent incorporation onto BNC; Chapter 4 explores three approaches for inorganic agent incorporation; and Chapter 5 details the production and functionalisation of BNC meshes.. ..... 6

**Figure 2.1.** Example of an abdominal hernia defect showing a protrusion resultant from the force exerted by the intestine through the path of least resistance [16]. Locations of abdominal hernias. Adapted from [17]..... 8

**Figure 2.2.** Commercial meshes: (a) PET ProGrip™ from Medtronic, (b) expanded polytetrafluoroethylene (ePTFE) Soft Tissue Patch from GORE-TEX®, (c) composite ProHeal™ from BioHealth, and (d) completely bioabsorbable Phasix™ ST from Sepra®. ..... 10

**Figure 2.3.** Photos of commercial meshes (A) Bard Mesh, (B) C-QUR Lite Large, (C) C-QUR Lite Small, (D) INFINIT Mesh, (E) Parietex Flat Sheet TEC, (F) PROLENE, (G) ProLite Ultra, (H) ProLite, (I) ULTRAPRO. Reproduced from Ref. [38] with permission, Copyright 2011, Journal of the American College of Surgeons..... 13

**Figure 2.4.** Scanning Transmission Electron Microscopy (STEM) images of BNC from *Komagataeibacter hansenii* American Type Culture Collection (ATCC) 53582..... 26

**Figure 2.5.** BNC in three different physical states: (a) dried, (b) freeze-dried, and (c) never-dried BNC. ..... 27

**Figure 2.6.** BNC produced by *K. hansenii* ATCC 53582 in Hestrin-Schramm medium. ..... 29

**Figure 2.7.** Schematic representation of the biosynthetic pathway for BNC and organization of the various subunits in the bacterial cellulose synthase complex. Adapted from Ref. [111], under the Licence CC BY 4.0, 2021, Nanjing Medical University..... 32

**Figure 2.8.** Optical images of BNC produced by five strains of *K. xylinus*, (a–e) in static condition, and (f–j) in agitated condition. Reproduced from Ref. [122] with permission, Copyright 2018, Springer Nature. ..... 34

**Figure 2.9.** Steps of antimicrobial action of particles. Based on [160]. ..... 39

**Figure 2.10.** (a) Schematic representation of metal nanoparticles, (b) KL and the chemical structure of its phenolic compounds – primary lignin alcohol monomers: p-coumaryl, coniferyl, and sinapyl, and (c) OP (p-coumaric acid, tyrosol, and hydroxytyrosol) [204, 205]. ..... 42

**Figure 3.1.** Cultivation of *K. hansenii* in Hestrin-Schramm culture medium..... 60

**Figure 3.2.** Schematic representation of BNC functionalisation through vacuum filtration..... 61

**Figure 3.3.** Schematic representation of BNC functionalisation through exhaustion using an Ibelus machine. ..... 62

**Figure 3.4.** Demonstration of a BNC membrane (a) perforated with a polyamide filament, and (b) suspended vertically for excess medium drainage..... 66

**Figure 3.5.** BNC/KL composites functionalised trough (a) filtration and (b) exhaustion approaches. ..... 69

**Figure 3.6.** Microscopic images of the KL, OP, and KL/OP suspensions in $dH_2O$ (1 wt%), PBS, 0.1 M NaOH, and BR..... 70

**Figure 3.7.** (a) pristine BNC, (b) KL, (c) OP, and (d) KL/OP functionalised BNC prepared using PBS as dispersion media of the biopolymers. ..... 70

**Figure 3.8.** STEM image of (a) KL 2 wt%, (c) OP 1 wt%, and (e) KL/OP in PBS and particle area analysis of (b) KL, (d) OP, and (f) KL/OP. ..... 71

**Figure 3.9.** Cryo-FESEM image of the untreated never-dried samples: (a, b) cross-section, (c, d) surface; and (e) the histogram describing the estimated fibre diameter. ..... 73

**Figure 3.10.** SEM images of the freeze-dried samples: cross-section of (a) BNC, (c) BNC/KL; (e) BNC/OP, and (g) BNC/KL/OP, and surface of (b) BNC, (d) BNC/KL, (f) BNC/OP, and (h) BNC/KL/OP. ..... 74

**Figure 3.11.** XRD diffractogram of untreated freeze-dried BNC. ..... 75

**Figure 3.12.** (a) BET surface area and (b) $N_2$ absorption/desorption isotherms of pristine and functionalised BNC. ..... 76

**Figure 3.13.** ATR-FTIR of the extracts, BNC and composites. ..... 78

**Figure 3.14.** XPS survey spectra and high resolution. ..... 78

**Figure 3.15.** (a) C1s and (b) O1s spectra of BNC and their composites; and the peak deconvolution at the C1s region obtained for (c) BNC, and composites (d) BNC/KL, (e) BNC/OP, and (f) BNC/KL/OP. ..... 81

**Figure 3.16.** (a) Carbon bonds contribution for BNC and its KL/OP composites, and (b) the O1s binding energy region spectra obtained for BNC and its composites: BNC/KL, BNC/OP, and BNC/KL/OP. ..... 83

**Figure 3.17.** (a) DSC thermogram, (b) TGA curves, and (c) DTG curves of BNC composites. . 85

**Figure 3.18.** Swelling profile of (a) BNC and composites (b) BNC/KL, (c) BNC/OP, and (d) BNC/KL/OP in SBF. ..... 87

**Figure 3.19.** Swelling equilibrium in SBF. ..... 88

**Figure 3.20.** Cumulative drug release profiles of KL, OP, and KL/OP throughout 1008 h in SBF. ..... 88

**Figure 3.21.** Fitting of the experimental drug release data of (a) KL, (b) OP, and (c) KL/OP from the BNC composites in SBF with Korsmeyer-Peppas, Makoid-Banakar, Weibull, Logistic, Gompertz, and Probit models. ..... 90

**Figure 3.22.** Antimicrobial activity: (a) shake flask and (b) contact killing of BNC and composites against *S. aureus*, *P. aeruginosa*, *C. albicans*, *C. krusei*, and MS2. VC stands for viable counts.92

**Figure 3.23.** Antioxidant activity of BNC composites. AA was used solely as positive control....94

**Figure 4.1.** Syntheses of (a) Au, (b) Ag, (c) Cu, and ($Cu_2O$) particles.....100

**Figure 4.2.** Schematic representation of BNC functionalisation through vacuum filtration..... 101

**Figure 4.3.** Schematic representation of BNC functionalisation through exhaustion using an Ibelus machine..... 102

**Figure 4.4.** Schematic representation of BNC functionalisation through in situ synthesis of metal particles..... 102

**Figure 4.5.** UV-vis spectra of (a) Au, (b), Ag, (c) Cu, and (d) $Cu_2O$ particles. The maximum absorbance is highlighted..... .....107

**Figure 4.6.** DLS measurements of (a) particle size and PdI and (b) zeta potential of the metal particles..... 109

**Figure 4.7.** STEM images of metal particles (a) Au, (b) Ag, (c) Cu, and (d) $Cu_2O$..... 110

**Figure 4.8.** Area of the metal particles calculated through the STEM images..... 110

**Figure 4.9.** Functionalised BNC by ex situ methods: filtration and exhaustion, and in situ.....111

**Figure 4.10.** Mapping of BNC/Au nanocomposites and elemental mass % composition..... 112

**Figure 4.11.** Mapping of BNC/Ag nanocomposites and elemental mass % composition..... 112

**Figure 4.12.** Mapping of BNC/Cu composites and elemental mass % composition..... 113

**Figure 4.13.** Mapping of BNC/$Cu_2O$ composites and elemental mass % composition... 113

**Figure 4.14.** ATR-FTIR spectra of BNC/metal particle composites obtained through ex situ (a) filtration and (b) exhaustion, and (c) in situ methodologies.....115

**Figure 4.15.** Survey spectra of (a) BNC/Au, (b) BNC/Ag, (c) BNC/Cu, and (c) BNC/$Cu_2O$ composites..... 117

**Figure 4.16.** Thermal analysis spectra relating to the weight loss of (a) BNC/Au, (b) BNC/Ag, (c) BNC/Cu, and (d) BNC/$Cu_2O$ composites obtained through ex situ – filtration, ex situ – exhaustion, and in situ syntheses. The derivative weight loss is presented for (e) BNC/Au, (f) BNC/Ag, (g) BNC/Cu, and (h) BNC/$Cu_2O$ composites..... 119

**Figure 4.17.** Weight loss percentage for each composite at different temperature stages. ..... 120

**Figure 4.18.** Swelling behaviour of BNC composites obtained through (a) ex situ – filtration, (b) ex situ – exhaustion, and (c) in situ syntheses..... 121

**Figure 4.19.** Release profile of Ag, Cu and $Cu_2O$ particles from the respective composites obtained from ex situ and in situ methods after 1 month.....122

**Figure 4.20.** Antibacterial activity (a) contact killing and (b) shake flask of BNC and BNC composites obtained through ex situ (F) filtration and (E) exhaustion, and (IS) in situ methodologies..... 124

**Figure 5.1.** LASER patterned BNC membranes obtained from (a) $CO_2$ LASER with hole diameters of (a.1) ⌀ 1.0 mm, (a.2) ⌀ 1.5 mm, (a.3) ⌀ 2.0 mm, (a.4) ⌀ 2.5 mm, and ⌀ 3.0 mm, and (a.6) interspace between holes of 3.0 mm; and obtained from (b, c) Bende LASER showing the heterogeneous cutting of BNC..... 127

**Figure 5.2.** (a) Metal-based template used during BNC production and (b) resulting washed membrane..... 128

**Figure 5.3.** (a) Template used to create BNC meshes, (b) cultivation of *K. hansenii* in the presence of the template and (c) resulting BNC mesh.....129

**Figure 5.4.** Commercial polypropylene meshes: (a) Optilene B. Braun-Portugal (60 $g \cdot m^{-2}$), (b) Ethicon Ultrapro Advanced (28 $g \cdot m^{-2}$), and (c) Optilene Mesh Elastic B. Braun-Portugal (48 $g \cdot m^{-2}$). ..... 129

**Figure 5.5.** Images of never-dried BNC meshes: (a) BNC, (b) BNC/Au, (c) BNC/Ag, (d) BNC/Cu, (e) BNC/$Cu_2O$, and rehydrated BNC meshes: (f) BNC, (g) BNC/Au, (h) BNC/Ag, (i) BNC/Cu, and (j) BNC/$Cu_2O$.....130

**Figure 5.6.** Schematic representation of the (a) cell seeding with samples and medium, and (b) the meshes transference to a new plate. Columns refer to 1. Optilene, 2. BNC H, 3. BNC R, 4. BNC/Ag H, 5. BNC/Ag R, 6. BNC/Cu H, 7. BNC/Cu R, 8. BNC/$Cu_2O$ H, 9. BNC/$Cu_2O$ R.....133

**Figure 5.7.** Tensile testing setup of the BNC sample. ..... 136

**Figure 5.8.** Images of the BNC meshes used as reference for building the numerical model.137

**Figure 5.9**. Finite Element model showing the used boundary conditions a) BNC membrane; b) BNC structure..... 138

**Figure 5.10.** SEM images of the surface of the BNC composites (a) BNC/Au, (b) BNC/Ag, (c) BNC/Cu, and (d) BNC/$Cu_2O$, displaying the particles. ..... 140

**Figure 5.11.** SEM images of the cross-section of the BNC composites (a) BNC/Au, (b) BNC/Ag, (c) BNC/Cu, and (d) BNC/$Cu_2O$, displaying the particles.....141

**Figure 5.12.** Swelling behaviour of BNC composites in the (a) hydrated and (b) rehydrated states. ..... 142

**Figure 5.13.** Cumulative release profiles of the metal particles after 1, 3, and 6 months. .... 143

**Figure 5.14.** Contact killing results of BNC and its composites in the hydrated and rehydrated states, and commercial Optilene 60 $g \cdot m^{-2}$ mesh.....145

**Figure 5. 15.** Shake Flask results at (a) 5h and (b) 24h for BNC and its composites in the hydrated and rehydrated states, and commercial Optilene 60 $g \cdot m^{-2}$ mesh. ..... 146

**Figure 5.16.** Lionheart images of the 96-well plates of the 24 h seeding of L929 cells: (a) control cells, (b) Optilene commercial mesh; (c) hydrated BNC, (e) hydrated BNC/Ag, (g) hydrated BNC/Cu, (i) hydrated BNC/$Cu_2O$, (d) rehydrated BNC, (f) rehydrated BNC/Ag, (h) rehydrated BNC/Cu, and (j) rehydrated BNC/$Cu_2O$..... 148

**Figure 5.17.** Microscopy images of cell proliferation from an inverted microscope (Kern®, Albstadt, Germany) after 168 h incubation of L929 cells in DMEM: (a) Control L929, hydrated meshes: (b) BNC, (c) BNC/Ag, (d) BNC/Cu, and (e) BNC/$Cu_2O$; (f) Optilene commercial mesh; and rehydrated meshes: (g) BNC, (h) BNC/Ag, (i) BNC/Cu, and (j) BNC/$Cu_2O$. ..... 149

**Figure 5.18.** NR assay of adhered cells metabolism per contact area of mesh. ..... 150

**Figure 5.19.** Cell metabolism per contact area of mesh through the MTT assay. ..... 151

**Figure 5.20.** MTT assay of L929 (a) cell metabolism (%) of adhered cells per area of mesh contact ($mm^2$) and (b) influence of meshes on cell metabolism. ..... 152

**Figure 5.21.** SEM images of L929 cells adhesion to the meshes after 168 h: (a) Optilene, (b) hydrated BNC, (c) rehydrated BNC, (d) hydrated BNC/Ag, (e) rehydrated BNC/Ag, (f) hydrated BNC/Cu, (g) rehydrated BNC/Cu, (h) hydrated BNC/$Cu_2O$, and (i) rehydrated BNC/$Cu_2O$..... 153

**Figure 5.22.** Example of the traction applied to a commercial and a BNC functionalised mesh. ..... 154

**Figure 5.23.** Example of the deformation of the specimens after traction was applied. ..... 155

**Figure 5.24.** Numerical fitting of the 1 mm thick BNC membrane performed for 7 measurements using *E* of 0.5 MPa and Poisson's ratio of 0.01. ..... 156

**Figure 5.25.** Deformed model of the BNC membrane with boundary conditions. ..... 157

**Figure 5. 26.** Deformed model of the (a) BNC mesh and (b) a magnified image of the deformation of the holes. ..... 157

**Figure 5.27.** Graphics of the load vs displacement curves and the corresponding fitting of the commercial meshes: (a) Optilene B. Braun-Portugal, (b) Ethicon Ultrapro Advanced, and (c) Optilene Mesh Elastic B. Braun-Portugal. ..... 160

**Figure 5.28.** Graphics of the load vs displacement curves and the corresponding numerical fitting of the meshes: hydrated (a) BNC, (c) BNC/Ag, (e) BNC/Cu, (g) BNC/$Cu_2O$ hydrated, and rehydrated (b) BNC, (d) BNC/Ag, (f) BNC/Cu, (h) BNC/$Cu_2O$. ..... 161

## TABLE INDEX

**Table 2.1.** Commercial meshes approved for inguinal hernia repair. ..... 12

**Table 2.2.** Types of hernia mesh materials [39]. ..... 14

**Table 2.3.** Physical characteristics of commercial meshes [14]. ..... 17

**Table 2.4.** Mechanical properties of commercially available meshes [14]. ..... 19

**Table 2.5.** Comparison of the physical and mechanical properties of commercial meshes used for inguinal hernia repair [38]. M – Medium, L – Large, XL – Very large, S- Small, XS – Very small, T – Thin, XT – Very thin, Hw – Heavy-weight, Mw – Medium-weight, Lw – Light-weight. ..... 22

**Table 2.6.** Mesh material removed in patients that underwent mesh removal due to mesh implant illness (MII) or other reasons (non-MII) show no significant difference ($p < 0.05$) [26]. ..... 23

**Table 2.7.** Mechanical properties of BNC produced under static mode, according to the physical state of the sample. ..... 28

**Table 2.8.** Purification methods applied to different bacteria and the carbon source used throughout their fermentation. ..... 35

**Table 2.9.** BNC based meshes ..... 56

**Table 3.1.** Elemental atomic percentages on the surface of the samples from the XPS survey spectra ..... 79

**Table 3.2.** Deconvolution analysis of the C1s peaks of the sample. ..... 82

**Table 3.3.** Mathematical modelling results of experimental drug release data of BNC release models in SBF. ..... 89

**Table 3.4.** Minimal inhibitory concentration of KL in $dH_2O$ and 0.1 M NaOH. ..... 91

**Table 3.5.** Minimal bactericidal/virucidal concentration of KL in $dH_2O$ and 0.1 M NaOH. ..... 91

**Table 4.1.** Atomic percentages (%) of C1s, O1, Auf4, Ag3d, and Cu2p3 in the functionalised BNC composites ..... 118

**Table 5.1.** Dimensions of pore and interspace between pores of BNC and commercial PP-based meshes ..... 130

**Table 5.2.** Size of the particles on the BNC composites surfaces and interior. ..... 141

**Table 5.3.** Interference of NR and MTT on the metal particles functionalised meshes in the hydrated and rehydrated states. ..... 150

**Table 5.4.** Absorbance values obtained after a 24 h incubation of the meshes in DMEM/MTS. ..... 151

**Table 5.5.** Comparison of the elastic modulus ($E$) of the commercial meshes. ..... 162

**Table 5.6.** Comparison of the elastic modulus ($E$) and Poisson's ratio of BNC membrane and hydrated and rehydrated functionalised BNC meshes. ..... 162

# Chapter 1

## Introduction

# 1. Introduction

## 1.1. Framework

Hernia mesh devices are a successful solution for hernia defects, displaying a mostly successful outcome with less postoperative pain and recurrence than suture repair [1-3]. However, long term complications occur in considerable percentages for plastic-based meshes, usually due to a lack of inhibition of microbial growth or material defects [4]. Mesh infection is extremely hard to treat, being in its vast majority resilient to severe treatments, such as intravenous antibiotic therapy. The most common mesh material defects occur in polypropylene (PP) and polyester (PET) meshes. PP is usually oxidized as a result of the foreign body reaction, and PET becomes brittle due to hydrolysis. Therefore, most of these cases require complete mesh removal [2, 5, 6]. To overcome such problems bio-based meshes have been developed and tested [7]. Nevertheless, these meshes are expensive and generally considered inappropriate due to lower mechanical properties [8]. Thus, synthetic plastics are still the most successful mesh core material [9, 10]. A highly promising alternative to petrochemical based medical devices is bacterial nanocellulose (BNC), a pure biopolymer excreted by bacteria. BNC displays notable mechanical properties and is composed of a porous nanofibrous three-dimensional (3D) matrix with pores between 20 to 100 nm, similar to that of collagen [11-13]. Nonetheless the porosity of BNC may be insufficient for leukocytes and fibroblasts permeability, and the setup of blood vessels and collagen, essential for an adequate healing and fixation of the mesh. To circumvent this issue, a template was used during the production of BNC in the static mode, resulting in a porous mesh membrane. Considering the lack of antimicrobial properties of BNC, and of the high postoperative infections that result from bacterial adherence and proliferation within the mesh [2], long term antimicrobial activity was attempted with the functionalisation with organic and inorganic agents such as Kraft lignin (KL), olive pomace (OP), gold (Au), silver (Ag), and copper-based particles (Cu and $Cu_2O$). The mechanical properties of the meshes are a key factor, hence the choice of mesh being critical and dependent on the type of defect. Despite the problems associated with commercial meshes, they are still popular due to the underreaching mechanical properties [14]. Thus, the BNC-based mesh was tested mechanically and compared to commercial PP-based meshes.

## 1.2. Research questions

This research aims to explore the following fundamental questions:

1. Are the mechanical properties of the BNC mesh adequate?
2. Does the functionalisation of the BNC meshes affect the mechanical properties?
3. Does the release of organic or inorganic agents from the BNC mesh lead to cytotoxicity?
4. Are the organic or inorganic agents able to mitigate microbial viability and activity for a long period of time?
5. Is the never-dried BNC mesh preferred to re-hydrated BNC in terms of mechanical properties and cytocompatibility?
6. Does the BNC mesh display comparable mechanical properties and cytocompatibility to commercial PP meshes?

## 1.3. Objectives

The main objective was the development of a potential replacement of conventional synthetic hernia mesh devices able to provide increased comfort to patients and prevent recurrence. Therefore, a tailored affordable biomaterial, BNC, with improved biocompatibility was evaluated as a replacement for traditional meshes. The novel meshes were functionalised with organic KL and OP particles and inorganic Ag, Au, Cu, and $Cu_2O$ particles. The aim was to minimise the probability of infection during a substantial period of time (up to 6 months), without compromising its cytocompatibility.

The PhD project specific objectives comprise:

- BNC production optimisation: selection of bacteria strain and incubation conditions to be used as hernia mesh material matrix. Characterisation according to its mechanical properties and pore size;
- Synthesis of metal-based particles, namely Ag, Au, Cu, and $Cu_2O$, and characterisation of their antimicrobial activity and cytotoxicity;
- BNC functionalisation with antimicrobial agents by embedding them in the BNC matrix through distinct approaches;

- Design and production of a template to establish a suitable microporous architecture to BNC to allow the establishment of fascia and blood vessels, and passively prevent granulomas and seromas;
- Achieving optimal functionalised BNC mesh as a suitable medical device for abdominal hernia application, encompassing adequate mechanical properties, potent antimicrobial activity and preferably negligible or absent cytotoxicity.

## 1.4. Outline

The content of this thesis is presented across 6 chapters. The experimental chapters 3 – 5 are schematised in Fig. 1.1.

**Chapter 1.** Introduction
This chapter includes the motivation of the research and the thesis outline.

**Chapter 2.** Literature review
This chapter comprises the state of the art of the hernia pathology, including its incidence and clinical and socioeconomic implications. A comprehensive overview of commercially available hernia meshes and their characteristics is provided, highlighting current limitations, and establish target properties for the development of BNC-based meshes. In addition, a thorough description of BNC is presented, together with the state of the art on BNC functionalisation using organic and inorganic agents, as well as the development of BNC-based meshes reported in the literature.

**Chapter 3.** Functionalisation with organic agents
In this chapter, two different methodologies for the functionalisation of BNC with organic macromolecules are presented. These include *ex situ* functionalisation with KL and OP via filtration and exhaustion. The physical, thermal, antimicrobial and antioxidant characterisation of the resulting composites are presented.

**Chapter 4.** Functionalisation with inorganic agents
In this chapter, the functionalisation of BNC via *ex situ* (filtration and exhaustion) and *in situ* methodologies with metal particles are presented. The physical, thermal, and antimicrobial characterisation of the resulting composites supported the selection of the BNC mesh functionalisation methodology, described in the next chapter.

**Chapter 5.** BNC mesh composites

This chapter describes the preparation and characterisation of functionalised BNC composite meshes. Never-dried and rehydrated functionalised meshes were compared in terms of antimicrobial activity, cytotoxicity, cell adhesion, and mechanical properties.

**Chapter 6.** General conclusions and future perspectives

This chapter presents a comprehensive overview of the thesis, discusses the main conclusions, and outlines future perspectives.

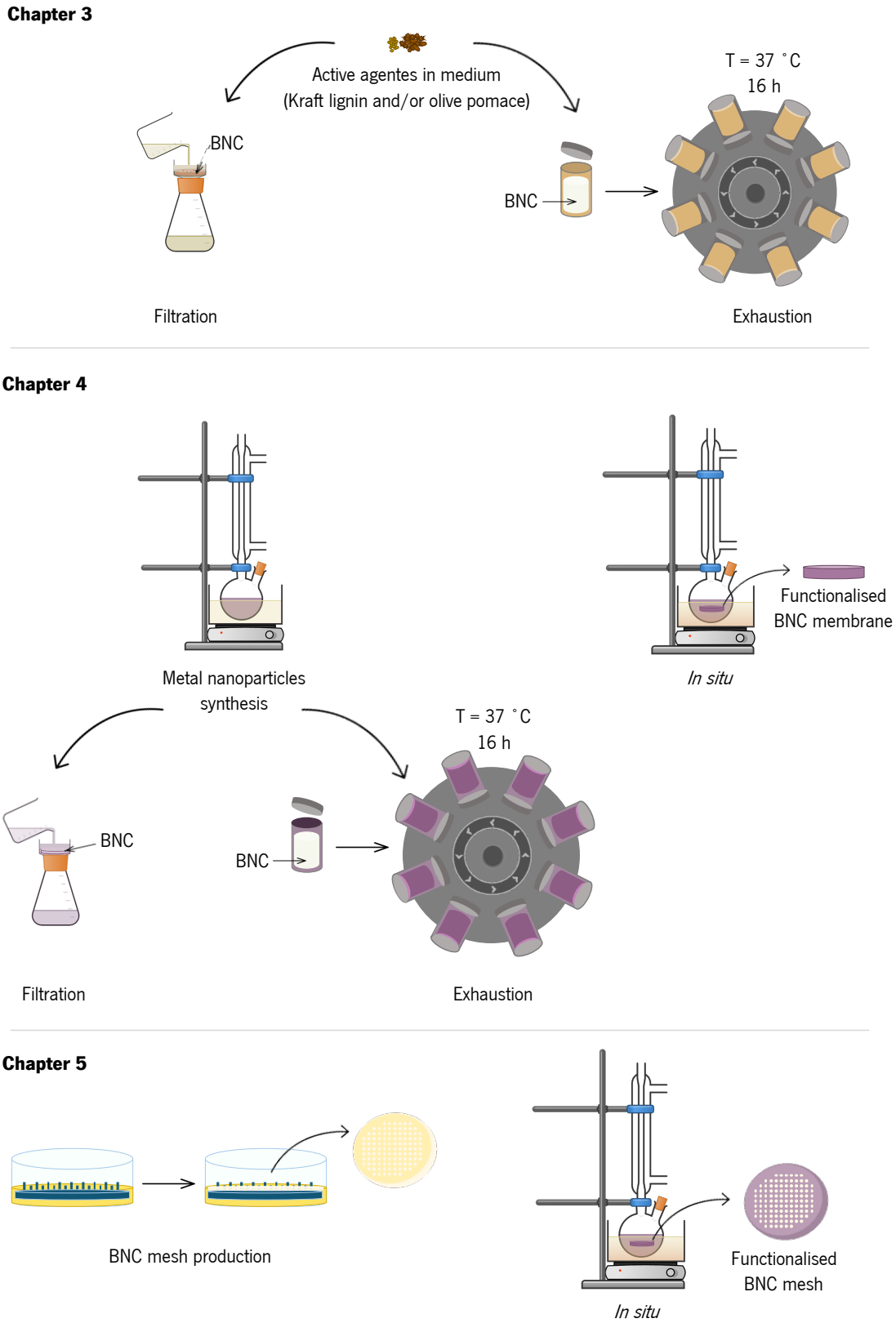



**Figure 1.1.** Schematic representation of the experimental strategy: Chapter 3 explores two methodologies for organic agent incorporation onto BNC; Chapter 4 explores three approaches for inorganic agent incorporation; and Chapter 5 details the production and functionalisation of BNC meshes.

# Chapter 2

## Literature review[1]

[1] This chapter is based on the following publications:

Book chapters:

Song, Xinyu; Melro, Liliana; Padrão, Jorge; Ribeiro, Ana Isabel; Yu, Liangmin; Zille, Andrea. "Nonwoven materials and technologies for medical applications". In Medical Textiles from Natural Resources, edited by Md. Ibrahim H. Mondal, 605-662. Woodhead Publishing, 2022. https://doi.org/10.1016/B978-0-323-90479-7.00008-7.

Fernandes, M.; Alves, C.; Melro, L.; Fernandes, R. D. V.; Padrão, J.; Salgado, A. J.; Zille, A.; "Modification of Nanocellulose". In Handbook of Biomass, 1-39. Springer Nature Singapore, 2023. https://doi.org/10.1007/978-981-19-6772-6_35-1.

Song, X.; Padrão, J.; Fernandes, M.; Ribeiro, A. I.; Melro, L.; Alves, C.; Yu, L.; Zille, A.; "Antibacterial hydrogel dressings and their applications in wound treatment". In Antimicrobial Dressings The Wound Care Applications, 153-185. Chennai, India: Stacy Masucci, 2023. https://doi.org/10.1016/B978-0-323-95074-9.00010-5.

Review articles:

Melro, L.; Alves, C.; Fernandes, M.; Rocha, S.; Mehravani, B.; Ribeiro, A. I.; Azevedo, S.; Cardoso, V. F.; Carvalho, O.; Dourado, N.; Salgado, A. J.; Zille, A.; Padrão, J.; "Bacterial nanocellulose as a versatile scaffold for biomedical applications: Synthesis, functionalization, and future prospects". Applied Materials Today (2025): https://doi.org/10.1016/j.apmt.2025.102858.

Fernandes, M.; Padrão, J.; Ribeiro, A. I.; Fernandes, R. D. V.; Melro, L.; Nicolau, T.; Mehravani, B.; Alves, C.; Rodrigues, R.; Zille, A.; "Polysaccharides and Metal Nanoparticles for Functional Textiles: A Review". Nanomaterials (2022): https://doi.org/10.3390/nano12061006.

Padrão, J.; Melro, L.; Fernandes, M.; Fernandes, R. D. V.; Ribeiro, A. I.; Song, X.; Yu, L.; Zille, A.; "Biocompatibility of Nanocellulose". In Handbook of Biopolymers, 1-32. Springer Nature Singapore, 2022. https://doi.org/10.1007/978-981-19-0710-4_36.

# 2. Literature review

## 2.1. Abdominal hernias

A hernia is defined as the protrusion of an organ or fatty tissue through a defect or perforation in the surrounding muscle or connective tissue (Fig. 2.1a) [15]. These conditions are categorised into several types based on their anatomical location, as illustrated in Fig. 2.1b.

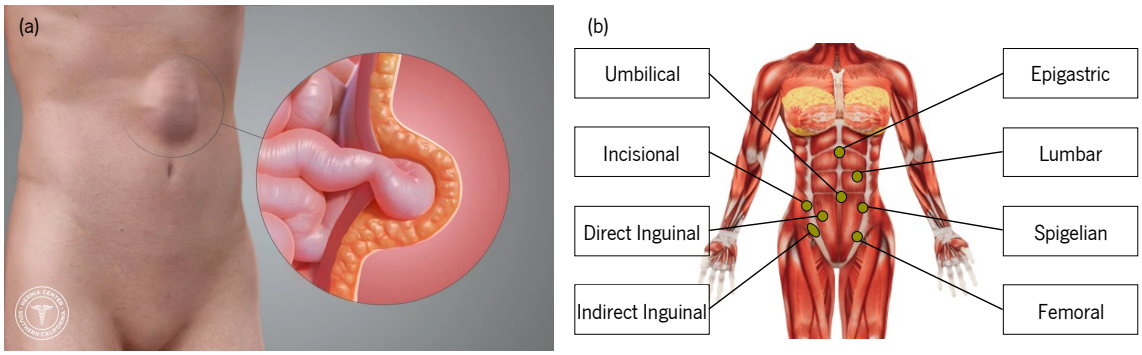



**Figure 2.1.** Example of an abdominal hernia defect showing a protrusion resultant from the force exerted by the intestine through the path of least resistance [16]. Locations of abdominal hernias. Adapted from [17].

This thesis is mainly focused on abdominal wall hernias, which encompass groin and ventral hernias. Groin hernias are the most common, and include: indirect inguinal, direct inguinal, and femoral, whilst ventral hernias encompass umbilical, epigastric, Spigelian, lumbar, and incisional [17]. Hernias can be symptomatic or asymptomatic and have an estimated probability of occurring during a lifetime of 27% in men and only 3% in women [18]. Over time, the hernia defect can increase in size due to the tissues giving way to the pressures exerted even when performing daily tasks. When symptomatic, hernias can lead to discomfort or pain, and in some cases can even become strangulated. Thus, depending on the size and severity of the hernia defect, surgical repair may be necessary [18]. Incarcerated inguinal hernias are the protrusion of the organs in the abdominal cavity (e.g. greater momentum, small and large bowel intestines) that cannot be returned. Thus, emergency surgical intervention is required to prevent intestinal obstruction, perforation and necrosis [19]. Abdominal hernias in total, account as one of the most common surgical interventions worldwide [20], in particular inguinal hernias that account for 70 – 75% of cases, compared to femoral with 6.0 – 17%, umbilical with rates of 3.0 – 8.5%, incisional at 6.2% and the others epigastric or hiatal with a maximum of 8.6% incidence [14]. There are more than

20 million inguinal hernia surgeries performed annually worldwide [21]. In Europe alone, 173.6 inguinal hernia surgeries per 100 000 inhabitants were performed in 2022 [22].

Suture-based techniques were the initial method applied, but the intrinsic high tensions that resulted from this procedure, the increase in complications and recurrence rates, led to the development of the hernia mesh support [14]. The first mesh was idealised in 1890 by Theodor Billroth [23], but it was only in the late 1950s that they have been proven successful, displaying lower recurrence rates [24]. Current studies denote lower recurrence rates in inguinal hernia surgeries for mesh related interventions (3.0%) compared to non-mesh surgeries (12.0%) ($p$=0.013) [25]. However, long term complications occur in considerable percentages for plastic-based meshes, usually due to a lack of inhibition of microbial growth or material defects [26]. Polypropylene (PP) is usually oxidised as a result of the foreign body reaction, and polyester (PET) becomes brittle due to hydrolysis. Therefore, most of these cases require complete mesh removal [5, 27]. Bio-based materials have been developed and used [7] and display a much lower percentage of recurrence [26]. Nevertheless, bio-based meshes are expensive and generally considered inappropriate due to lower mechanical properties [8]. Thus, synthetic plastics are still the most successful mesh core material [9, 10].

## 2.2. Hernia meshes

Key requirements for implant materials include an absence of toxicity, the induction of a desired host response, and an effective integration with surrounding tissues. A porous structure is essential to allow cell permeability (e.g. leukocytes and fibroblasts), which is vital for collagen deposition and neovascularization to support tissue integration or organ growth [28]. A prosthetics must be capable of mimicking the biomechanical nature of the human body. The abdominal wall, in particular the intraabdominal pressure in humans is as high as 171 mmHg, generated during coughing, sneezing, or jumping. Thus, a hernia mesh, according to the Laplace Law should, in theory, be capable of withstanding a tensile strength between 16 – 32 $N \cdot cm^{-1}$ [17]. Initial meshes provided tensile strengths close to 100 $N \cdot cm^{-1}$ [2]. Nowadays, mesh design is shifting towards lighter and more elastic prostheses, capable of simulating the behaviour of human body [29]. Examples of commercial meshes are displayed in Fig. 2.2. Surgical meshes should also demonstrate good handling properties for friendly surgical implantation and be able to endure sterilizing procedures [2].

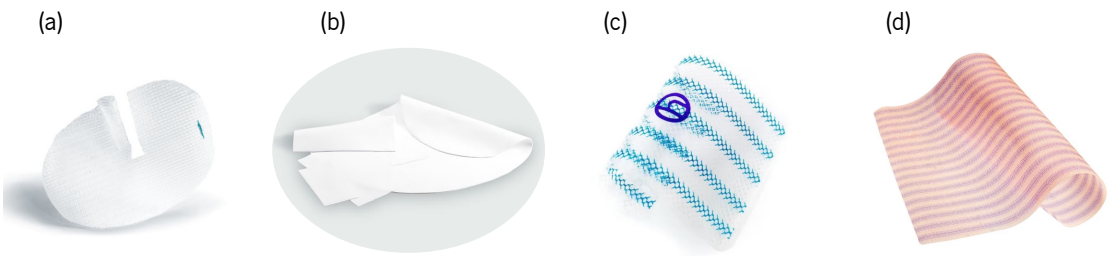



**Figure 2.2.** Commercial meshes: (a) PET ProGrip™ from Medtronic, (b) expanded polytetrafluoroethylene (ePTFE) Soft Tissue Patch from GORE-TEX®, (c) composite ProHeal™ from BioHealth, and (d) completely bioabsorbable Phasix™ ST from Sepra®.

Meshes can be categorised in terms of weight: heavy-weight, medium-weight or light-weight. Heavier meshes imply greater material density and lower flexibility. Heavy-weight meshes traditionally possess small pore size. On the opposite, lighter meshes are more flexible and typically have larger pores and thinner filaments. The decreased amount of material density is favourable since there is a lower risk of foreign body reaction. Moreover, the mechanical properties of light-weight meshes are usually retained, and the repaired abdominal wall is able to maintain its flexibility and functions. Therefore, light-weight meshes are often more advantageous than heavy-weight meshes, even though their use is dependent of the hernia defect [29, 30]. The porosity of a mesh is related to the diameter and interspace between pores. This aspect is of extreme relevance since meshes containing pores larger than 75 μm allow the permeability of leukocytes, fibroblasts, and the setup of blood vessels and collagen essential for an adequate healing and fixation of the mesh, simultaneously preventing the development of seromas and granulomas. Meshes with pore sizes larger than 1 mm can still promote adequate wound healing and reduce the presence of dense scar tissue. However, in the case of meshes with very large pores there is a higher risk of internal viscera adhesion. In addition, the mechanical properties also dimmish considerably [29].

Depending on the hernia mesh material, there are different categories that define them [31]:

- Synthetic hernia meshes can be woven or non-woven layers. They can be absorbable, non-absorbable or a combination of both;
- Non-absorbable mesh is a permanent implant, expected to provide lasting reinforcement;
- Absorbable mesh degrades and loses strength over time, therefore do not provide long-term reinforcement. However, new tissue growth is intended to replace the adsorbed support;
- Coated or composite mesh may prevent adhesions;

- Animal-derived meshes may be made of the intestine or skin, usually from pig or cow. This type of mesh is absorbable.

### 2.2.1. Commercial meshes

Hernia repair prosthetics are in majority made of synthetic plastics through mono or multi-filament extrusion. Monofilament PP meshes are the most commonly used since they accomplish the criteria of molecular permeability, mechanical properties and a good resistance to infection. Multifilament meshes are more often associated with a higher risk of infection due to the interstices in-between braided fibres that allow the infiltration of bacteria but are too small to permit the penetration of macrophages and neutrophils [29, 32, 33]. Knitted meshes are more flexible and possess larger pores, nonetheless they lack the required mechanical properties due to the lower filament density [29]. Hernia meshes made of nonwoven materials have proven to reduce infection associated complications as a result of its microporous structure allowing a good tissue in-growth capacity, thus avoiding cellular attachment and consequent formation of a fibrous capsule around the mesh leading to its contraction [34]. PP surgical meshes are widely accepted as the primary surgical approach to primary suture repair [20]. Alongside PP, other polymers such as PET and e-PTFE are also prominent in mesh material composition (Table 2.1) [2]. The advantage of using PP is the ability of the host tissue to infiltrate and integrate into the mesh. Nonetheless, PP implants have a higher propensity to form adhesions than e-PTFE. Thus, the promotion of parietal host tissue in-growth in the latter is much lower. PET meshes present superior histological properties than PP though they lack long term stability. Despite generally positive, some studies suggest the existence of immune responses upon implantation of these non-absorbable materials that lead to an increase of chronic pain and a general restriction of physical movement [35, 36]. Absorbable protheses provoke inferior foreign body and immune responses since they minimise the amount of foreign material remaining in the body. Nevertheless, they will degrade over time, losing strength in addition to being associated with higher rates of recurrence [37]. Common materials include: polyglycolide (PGA), polyglactin (PGLA), polylactide (PLA), and poly(4-hydrobutyrate) [29]. Biological materials are generally made of extracellular matrices obtained from decellularized scaffolds and have a tendency of becoming highly vascularised, promoting tissue in-growth thus providing strength and integrity to the damaged site. Despite these positive aspects, their mechanical properties are still underreaching [9, 29]. The combination of different materials can

promote positive properties to the implant. Composite meshes made of adsorbable and non-adsorbable materials possess the mechanical characteristics of synthetic polymers (*e.g.* PP and polyethylene (PE)) and low weight as a result of the adsorbable fibres [29].

Mesh material functionalisation is another step to take into account since the coating of the polymers is able to promote tissue integration, minimise biofilm formation and infections due to antimicrobial properties of the coatings [29]. Notwithstanding the development of bio-based materials, hernia repair remains largely dependent on non-adsorbable materials considering the broad application possibilities and appropriate implant responses.

Commercial meshes for inguinal hernia repair approved by the Food and Drug Administration (FDA) are presented in Table 2.1 and in Fig. 2.3.

**Table 2.1.** Commercial meshes approved for inguinal hernia repair.

| Material | Commercial meshes |
|---|---|
| **Uncoated PP** | Bard Mesh (Davol, Inc) |
| | PROLENE (Ethicon, Inc) |
| | ProLite (AtriumMedical Corp) |
| | ProLite Ultra (Atrium Medical Corp) |
| **Uncoated PET** | Parietex Flat SheetTEC (Covidien) |
| **Uncoated PTFE** | INFINIT Mesh (WL Gore & Associates, Inc) |
| **Partially absorbablePP-based** | C-QUR Lite "Small" 6-inch mesh sizes (Atrium Medical Corp) |
| | C-QUR Lite "Large" 6-inch mesh sizes (Atrium Medical Corp) |
| | ProLite with an absorbable omega-3 fatty acid coating (Atrium Medical Corp) |
| | ULTRAPRO (Ethicon, Inc), PP with an absorbable poliglecaprone-25 (PGC-25) filament ("Monocryl") |
| **Absorbable porcine-based** | STRATTICE™ Reconstructive Tissue Matrix (AbbVie company) |
| **Absorbable Poly-4-hydroxybutyrate (P4HB)-based** | Phasix™ Mesh (Becton, Dickinson and Company) |

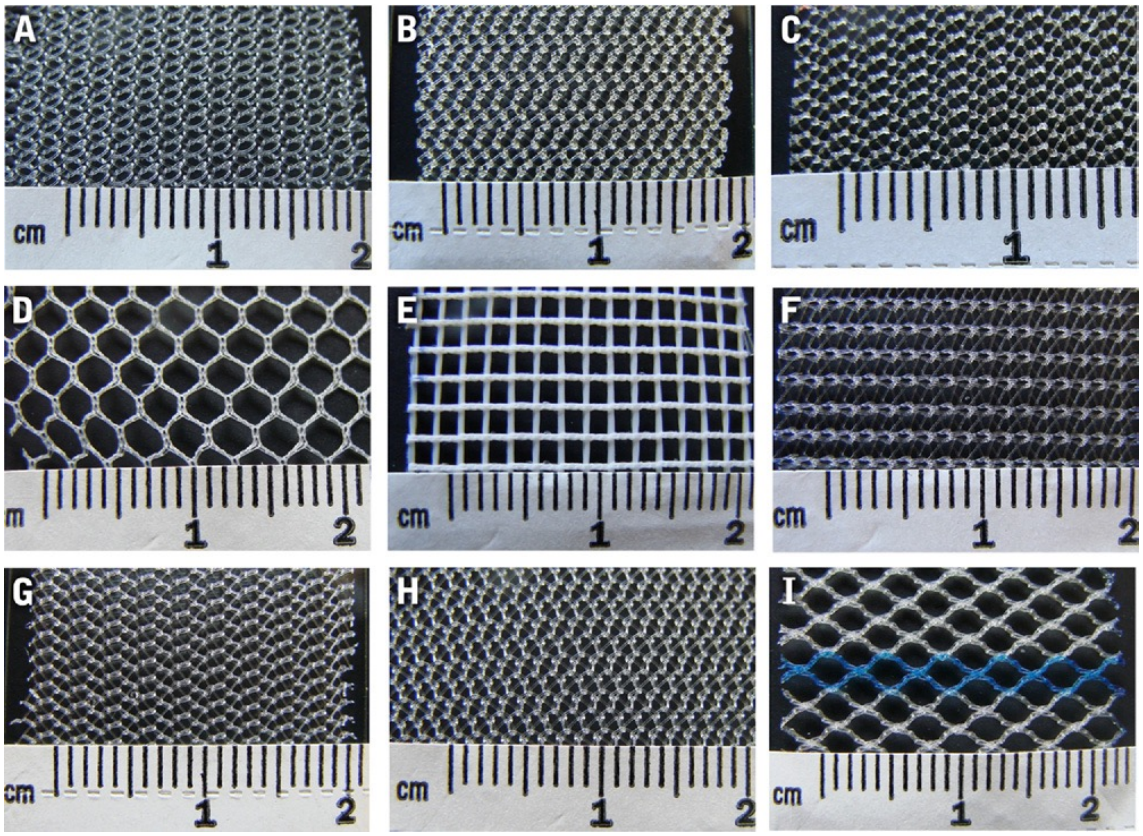



**Figure 2.3.** Photos of commercial meshes (A) Bard Mesh, (B) C-QUR Lite Large, (C) C-QUR Lite Small, (D) INFINIT Mesh, (E) Parietex Flat Sheet TEC, (F) PROLENE, (G) ProLite Ultra, (H) ProLite, (I) ULTRAPRO. Reproduced from Ref. [38] with permission, Copyright 2011, Journal of the American College of Surgeons.

Table 2.2 presents several examples of hernia mesh composition materials, Table 2.3 displays some commercially available meshes and their physical characteristics, and Table 2.4 presents their mechanical properties, namely initial and equilibrium stress ($T_0$ and $T_{eq}$, respectively), and the modulus of initial and equilibrium strain ($E_0$ and $E_{eq}$, respectively).

**Table 2.2.** Types of hernia mesh materials [39].

| Type of material | Designation of material | Reference |
|---|---|---|
| **Non-adsorbable synthetic materials** | PP | [40] |
| | PTFE | [38] |
| | ePTFE | [41] |
| | Polyvinylidene fluoride (PVDF) | [41] |
| | PET | [38] |
| | Polycarbonate polyurethane urea (PCUU) | [42] |
| | Cross-linked acrylic polymer | [43] |
| | Polycaprolactone (PCL) based poly (urethane urea) (PUU) | [44] |
| | ePTFE reinforced with fluorinated ethylene propylene | [45] |
| | Co-knitted using PP and PVDF | [46] |
| | Co-knitted using PP and Polyurethane (PU) | [47] |
| | Co-knitted using PP and PCUU | [48] |
| | PP with titanium (Ti) coating (plasma activated chemical vapor deposition of atomic Ti) | [29] |
| | PP with titanium dioxide coating (Wet-chemical coating procedure) | [29] |
| **Fibre-based adsorbable synthetic materials scaffold** | PGA | [37] |
| | PLA | [49] |
| | Polydioxanone (PDO) | [50] |
| | Poly(lactide-co-glycolide) (PLGA) | [37] |
| | Poly(glycolide-co-trimethylene carbonate) (P(GA-TMC)) | [51] |
| | Co-knitted using P(GA-TMC) and Poly(lactide-co-trimethylene carbonate) copolymer (P(LA-TMC)) | [52, 53] |

| Type of material | Designation of material | Reference |
|---|---|---|
| | Co-knitted using poly(glycolide-co-lactide-co-trimethylene carbonate) copolymer and P(LA-TMC) | [53] |
| | Bioresorbable L-tyrosine succinate polymer | [41] |
| **Fibre-based absorbable natural materials scaffold** | Silk fibroin (SF) protein | [54] |
| | P4HB | [55, 56] |
| **Absorbable or part-absorbable allogenic acellular tissue matrix** | Allogenic acellular dermal matrix | [57] |
| **Absorbable or part-absorbable xenogenic acellular tissue matrix** | Porcine intestinal submucosa (SIS) | [58] |
| | Porcine urinary bladder matrix | [59, 60] |
| | Porcine liver matrix | [61] |
| | Porcine acellular dermal matrix | [62] |
| | Bovine acellular dermal matrix | [63] |
| | Collagen derived from bovine pericardium | [64] |
| | Cross-linked porcine dermal collagen | [65] |
| | Cross-linked fibrous collagen derived from bovine hides | [66] |
| **Non-absorbable or part-absorbable biological tissue** | Porcine pericardium | [67] |
| | Bovine pericardium | [64] |
| | Equine pericardium | [68] |
| **Non-absorbable natural materials** | Bacterial nanocellulose (BNC) | [69] |
| **Composite material** | Co-knitted using PP and PGA | [70] |
| | Co-knitted using PP and PDO | [71] |
| | Co-knitted using PP and poly(glycolide-co-caprolactone) | [72] |
| | Co-knitted using PP and PLGA | [29] |
| | Hybrid mesh: Multi-layer using PTFE and porous PGA/TMC | [55] |

| Type of material | Designation of material | Reference |
|---|---|---|
| | Hybrid mesh: Multi-layer using PP and SIS | [55, 73] |
| | Hybrid mesh: Ovine forestomach or rumen derived extra cellular matrix (ECM) with PP embroidery | [55, 74, 75] |
| | Electrospinning technology: poly (L-lactide-co-caprolactone) and Porcine fibrinogen | [76] |
| | Co-knitted using P4HB and PGA | [77] |
| | Multi-layers using lyophilised porcine collagen and PLA | [78] |
| | Ovine forestomach or rumen derived ECM with PGA embroidery | [55, 74, 75] |

**Table 2.3.** Physical characteristics of commercial meshes [14].

| Mesh name | Material | Filament type | Pore size (mm) | Weight (g·cm$^{-2}$) | Manufacturer |
|---|---|---|---|---|---|
| Marlex | PP | monofilament | 0.600 | 95.0 | Becton, Dickinson and Company (BD), Franklin Lakes, NJ, USA |
| Prolene | PP | dual-filament | 1.00 – 2.00 | 105 | Ethicon, Johnson & Johnson, Somerville, NJ, USA |
| Trelex | PP | monofilament | 0.600 | 95.0 | Meadox Medicals, Boston Scientific, Marlborough, MA, USA |
| Surgipro | PP | multifilament | 0.900 | 87.0 | USSC, Norwalk, CT, USA |
| Lars | PET | multifilament | N/A | N/A | USSC, Norwalk, CT, USA |
| Fluoropassiv | PET | multifilament | N/A | N/A | PFM Medical, Cologne, Germany |
| Bard Teflon | PTFE | multifilament | N/A | N/A | Becton, Dickinson and Company (BD), Franklin Lakes, NJ, USA |
| Goretex | ePTFE | N/A | 0.000 – 0.0300 | 200 – 400 | Gore Medical, Flagstaff, AZ, USA |
| Optilene | PP | monofilament | 1.00 | 36.0 | B-Braun, Melsungen, Germany |
| Bard Mesh | PP | monofilament | 0.0200 – 0.460 | 97.0 | Becton, Dickinson and Company (BD), Franklin Lakes, NJ, USA |
| Parietene LW | PP | monofilament | 1.80 × 1.50 | 38.0 | Medtronic, Minneapolis, MN, USA |
| Prolite | PP | monofilament | 0.800 | 85.0 | Atrium Medical Corporation, Hudson, NH, USA |
| Infinit Mesh | PTFE | monofilament | 1.13 | 70.0 | N/A |
| Mersilene | PET | multifilament | 0.600 – 1.00 | 40.0 | Ethicon, Johnson & Johnson, Somerville, NJ, USA |
| Vypro II | PP/PGLA 910 | multifilament | 3.00 | 50.0 | Ethicon, Johnson & Johnson, Somerville, NJ, USA |
| Dual Mesh | ePTFE | N/A | N/A | N/A | Gore Medical, Flagstaff, AZ, USA |
| Parietex | PET-Collagen | monofilament | 2.40 | 78.0 | Covidien, Mansfield, MA, USA |
| Composix | PP-ePTFE | monofilament | N/A | N/A | Becton, Dickinson and Company (BD), Franklin Lakes, NJ, USA |
| Proceed | PP-Cellulose | monofilament | N/A | N/A | Ethicon, Johnson & Johnson, Somerville, NJ, USA |
| Dynamesh | PP-PVDF | N/A | N/A | N/A | FEG, Aachen, Germany |

| Mesh name | Material | Filament type | Pore size (mm) | Weight (g·cm$^{-2}$) | Manufacturer |
|---|---|---|---|---|---|
| Sepramesh | PP-Sodium | monofilament | N/A | N/A | Becton, Dickinson and Company (BD), Franklin Lakes, NJ, USA |
| Ultrapro | PP-Polyglecaprone | monofilament | 3.50 | 54.0 | Ethicon, Johnson & Johnson, Somerville, NJ, USA |
| Ti-mesh | PP-Ti | monofilament | N/A | N/A | PFM Medical, Cologne, Germany |
| C-Qur | PP-Omega3 | N/A | N/A | N/A | Atrium Medical Corporation, Hudson, NH, USA |

N/A: Not available

**Table 2.4.** Mechanical properties of commercially available meshes [14].

| Mesh name | Type | Direction | $T_0$ (MPa) | $T_{eq}$ (MPa) | $\Delta T$ (%) | $E_0$ (MPa) | $E_{eq}$ (MPa) |
|---|---|---|---|---|---|---|---|
| MicroVal 2D Mesh | PP | L | 0.2380 ± 0.04200 | 0 (t = 1400 s) | 100.0 | 4.760 | 0.0000 |
| MicroVal 2D Mesh | PP | T | 0.1820 ± 0.02800 | 0 (t = 250 s) | 100.0 | 3.640 | 0.0000 |
| Parietex Composite | PET/collagen | L | 0.06400 ± 0.008000 | 0.04100 | 35.93 | 1.280 | 0.8200 |
| Parietex Composite | PET/collagen | T | 0.03900 ± 0.01300 | 0 (t = 151 s) | 100.0 | 0.7800 | 0.0000 |
| Surgimesh | PP | L | 0.1110 ± 0.05000 | 0.05900 | 46.85 | 2.220 | 1.180 |
| Surgimesh | PP | T | 0.1680 ± 0.04000 | 0.08200 | 51.19 | 3.360 | 1.640 |
| Surgipro | PP | L | 0.1440 ± 0.0290 | 0.05800 | 59.72 | 2.880 | 1.160 |
| Surgipro | PP | T | 0.3210 ± 0.1200 | 0.1280 | 60.12 | 6.420 | 2.560 |
| TecnoMesh | PP | L | 0.1870 ± 0.06000 | 0.08000 | 57.22 | 3.740 | 1.600 |
| TecnoMesh | PP | T | 0.5110 ± 0.04000 | 0.2180 | 57.33 | 10.20 | 4.360 |
| Optilene | PP | L | 0.1870 ± 0.1490 | 0 (t = 180 s) | 100.0 | 3.740 | 0.0000 |
| Optilene | PP | T | 1.028 ± 1.270 | 0.5420 | 47.28 | 20.60 | 10.80 |

| Mesh name | Type | Direction | $T_0$ (MPa) | $T_{eq}$ (MPa) | ΔT (%) | $E_0$ (MPa) | $E_{eq}$ (MPa) |
|---|---|---|---|---|---|---|---|
| Parietex LW | PET | L | 0.4290 ± 0.04000 | 0.3060 | 28.67 | 8.580 | 6.120 |
| Parietex LW | PET | T | 0.2450 ± 0.02000 | 0.1840 | 24.90 | 4.900 | 3.680 |
| Ultrapro | PP/PGC-25 | L | 0.1410 ± 0.01600 | 0 (t = 300 s) | 100.0 | 2.820 | 0.0000 |
| Ultrapro | PP/PGC-25 | T | 0.1540 ± 0.003000 | 0.04400 | 71.43 | 3.080 | 0.8800 |
| Vypro II | PP/PGLA 910 | L | 0.5100 ± 0.2400 | 0.4120 | 19.22 | 10.20 | 8.240 |
| Vypro II | PP/PGLA 910 | T | 0.09800 ± 0.03000 | 0.0780 | 20.41 | 1.960 | 1.5600 |

Note: Orthogonal directions: Longitudinal (along the wales; L direction) and transverse (across the courses; T direction). Initial stress ($T_0$), equilibrium stress ($T_{eq}$), modulus at initial strain ($E_0$), modulus at equilibrium state ($E_{eq}$), the level of orthotropy of meshes, and stress reduction parameter ΔT.

Tearing of a suture, measured by suture retention strength, indicates the potential of tear before the abdominal wall tissue, and occurs for values below 20 N. Among the commercial meshes evaluated in a study by Deeken et al. [38] and presented in Table 2.5., only ULTRAPRO failed to comply with these values. Regarding the tensile strength, all evaluated meshes provide the required strength for hernia repair. However, for very large hernia defects or obese patients, where tensile strength of 50 $N \cdot cm^{-1}$ is required, INFINIT Mesh and ULTRAPRO should not be used. Strain measurements are dependent on load direction and are an essential factor for hernia mesh materials. At a stress of 16 $N \cdot cm^{-1}$, the human anterior abdominal wall measures a strain of approximately 10% to 30% [79]. Therefore, meshes with strain values lower than 10% measured at 16 $N \cdot cm^{-1}$ are likely to stretch less than the human abdominal wall tissue increasing the discomfort. On the other hand, if a material has strains above 30% they become too elastic therefore likely to result in bulging or recurrence [38]. Overall, mesh structural features such as pore size, filament diameter, mesh thickness and density play a vital part on the functional characteristics of the implant. A reduction in mesh filament diameter and mesh density can reduce inflammatory reaction, improve tissue integration, thus decreasing long-term pain and discomfort [38].

**Table 2.5.** Comparison of the physical and mechanical properties of commercial meshes used for inguinal hernia repair [38]. M – Medium, L – Large, XL – Very large, S- Small, XS – Very small, T – Thin, XT – Very thin, Hw – Heavy-weight, Mw – Medium-weight, Lw – Light-weight.

| Mesh type | Pore diameter | Filament diameter | Thickness | Density | Suture retention strength (N) | Tear resistance (N) | Ball burst strength ($N \cdot cm^{-1}$) | Strain at 16 $N \cdot cm^{-1}$ (%) |
|---|---|---|---|---|---|---|---|---|
| **Bard Mesh** | M | L | T | Hw | > 20 | > 20 | > 50 | 10 – 30 |
| **PROLENE** | M | S | T | Mw | > 20 | > 20 | > 50 | < 10 |
| **ProLite** | M | M | XT | Mw | > 20 | > 20 | > 50 | 10 – 30 |
| **ProLite Ultra** | M | XS | XT | Lw | > 20 | < 20 | > 50 | 10 – 30 |
| **Parietex Flat Sheet TEC** | L | XL | T | Hw | > 20 | > 20 | > 50 | < 10 |
| **INFINIT Mesh** | XL | XS | XT | Mw | > 20 | < 20 | < 50 | < 10 |
| **C-QUR Lite S** | M | XS | XT | Mw | > 20 | < 20 | > 50 | 10 – 30 |
| **C-QUR Lite L** | M | M | XT | Hw | > 20 | > 20 | > 50 | 10 – 30 |
| **ULTRAPRO** | XL | XS | T | Mw | < 20 | < 20 | < 50 | 10 – 30 |
| **INFINIT Mesh** | XL | XS | XT | Mw | > 20 | < 20 | < 50 | < 10 |

Unfortunately, the number of implant-associated infections is still high. According to the Centers for Disease Control and Prevention, up to 1.4 million healthcare-associated infections are attributed to implanted medical devices [80]. The most recurrent and difficult to treat infections are usually related to biofilm formation, where invading pathogenic bacteria firstly attach to the implant surface, secondly, the bacteria start producing extracellular polymeric substances (EPS), and finally once the biofilm is mature, planktonic cells are released from the biofilm for further host colonization. EPS is a substance or a group of compounds that envelopes the attached bacteria, being responsible for providing structural sturdiness, antibiotic impermeability and protection against host immune defence mechanisms. The removal of the bacterial biofilm that forms on the surface of the implant usually requires an aggressive approach that may include surgery and prolonged systemic antibiotic treatment [81, 82]. Nevertheless, despite the forceful treatments, the infected indwelling devices are often surgically removed [83]. Prevention is, therefore, an important strategy to avoid these infections. Coating of implants has been one of the most common applications to solve this problem. However, local antibiotic therapy through its embedding in a coating has not been particularly effective in orthopaedic surgery as they are normally designed for single antibiotic release. A controlled release of antibiotic over time would be the ideal approach.
Post-surgery complications include infection, fibrosis, adhesions, mesh rejection, that lead to hernia recurrence [17]. Table 2.6 displays the percentages of mesh removal surgeries performed, that do not depend on the type of mesh material (non-MII), and the ones that do (MII). According to Fadaee *et al.*, the most common mesh material defects occur in PP and PET meshes [26].

**Table 2.6.** Mesh material removed in patients that underwent mesh removal due to mesh implant illness (MII) or other reasons (non-MII) show no significant difference ($p < 0.05$) [26].

| Mesh material removed | MII (N=28) | Non-MII (N=137) |
|---|---|---|
| PP | 20.0 (71.0%) | 107 (78.0%) |
| PP + ePTFE | 3.00 (11.0%) | 12.0 (9.00%) |
| PET | 2.00 (7.00%) | 4.00 (3.00%) |
| Hybrid | 2.00 (7.00%) | 3.00 (2.00%) |
| Biologic | 1.00 (4.00%) | 3.00 (2.00%) |
| PP + Hybrid | 0.000 (0.000%) | 1.00 (1.00%) |
| ePTFE | 0.000 (0.000%) | 6.00 (4.00%) |
| Unknown | 0.000 (0.000%) | 1.00 (1.00%) |

Ways to tackle the above-mentioned problems are the different fibre size and porosity of the meshes, manufacturing methods, and surgical and implantation procedures. Another factor is the anatomical location of the hernia that impact on the mechanical loads and consequently lead to specific clinical considerations for implant selection. Despite being the most common, inguinal hernias mechanical stress is low. Thus, typically, light-weigh PP meshes are implanted since their mechanical properties provide sufficient support without being too cumbersome. Oppositely, ventral or incisional hernias require medium-weight mesh implants [14].

Hernia meshes made of nonwoven materials have proven to reduce infection-associated complications as a result of its microporous structure allowing a good tissue in-growth capacity thus avoiding cellular attachment and consequent formation of a fibrous capsule around the mesh leading to its contraction [34]. Nevertheless, infection is still recurrent for PP meshes, the most popular material used for hernia implant, display a 1.0 – 15% infection after surgery [4]. Moreover, the antibacterial loading of PP meshes is limited by the low wettability of its surface. Plasma treatment of the PP surface results in C–H bond cleavage, allowing its oxidation, making it prone to react with other functional groups. As a proof of concept, triclosan – an antibacterial agent used in suture material, was immobilised at the surface of plasma-treated PP mesh with the aid of amphiphilic cyclodextrin molecules [84]. The hydrophilic outer structure of cyclodextrin links to the modified polypropylene, whilst the hydrophobic cavity captures the triclosan [85]. Another successful methodology was accomplished by grafting electrospun PCL fibres on top of a knitted PP mesh, that permitted the adhesion of antimicrobial peptide PEP-1 loaded gellan gum to its surface. The antimicrobial peptide PEP-1 was able to sustain a controlled release for over 10 days and the mechanical properties of the mesh were not compromised [4].

Despite significant progress, there is no ideal mesh for every surgery. The single mesh model design fit for all types of abdominal hernia repair is still unrealistic, despite all the efforts for finding an ideal material, structure, and implantation method [29]. In addition, alongside the most adequate mesh for a successful abdominal hernia defect repair, the selection of mesh fixation technique is of outmost importance. Mesh fixation may provide an equal distribution of tension, favouring biodynamics, and a better integration. There are several methods that include suture, tack, fibrin glue, mesh strip, and self-adhering modes of fixation. Transfascial sutures provide a strong strength repair, moderate to low postoperative pain and are not very costly economically. Tacks provide equally strong strength of repair, higher postoperative pain but is a slightly more expensive technique. Fibrin glue provides less strength, and together with self-adhering meshes,

cause a very reduced postoperative pain and are not costly. Mesh sutures, like transfascial and tacks, provide the higher strength of repair, but is less expensive [86].

### 2.2.2. New approaches for mesh implants

The advance of technologies like 3D-printing, electrospinning and melt electrowritting (MEW), in combination with medical imaging techniques such as magnetic resonance imaging and computer tomography scan, allows the development of not only patient customised anatomical models, but also implants. Electrospinning is particularly interesting due to the ability to produce nanofibres with high surface area [14]. MEW allows the creation of complex patient-specific scaffolds due to the excellent control over fibre deposition [87]. New hernia support scaffolds composed of biopolymers, such as collagen and medical grade PCL (mPCL) were created, providing a good mechanical stability and reconstruction of the abdominal wall [14], with minimal inflammatory response and good tissue regeneration. 3D printing allowed the creation of a hernia mesh that permitted the tissue to anatomose into its pores enabling the proliferation of the connective tissue and neovascularisation [88]. By joining 3D printing and MEW, a mesh based on mPCL was able to mimic the biomechanical behaviour of native soft tissues [89], due to the ability to produce structures with sinusoidal and auxetic geometries [90]. Besides mechanical, antimicrobial properties can be implemented into the mesh, preventing infections, promoting tissue integration, and reducing postoperative adhesions, as reported by Hu and co-workers [91].

## 2.3. Bacterial nanocellulose

Cellulose is a natural polymer of fibrous nature with nanoscale dimensions, thus referred to as nanocellulose [92]. The natural sources of cellulose include plants, bacteria, algae, and marine animals [93]. Nanocellulose can be divided into three types: cellulose nanocrystals, cellulose nanofibrils, and BNC. Contrary to the other nanocelluloses, BNC is obtained directly from bacteria in a pure form. It neither includes byproducts like lignin, pectin, nor hemicelluloses, simply requiring mercerisation treatment with sodium hydroxide to remove bacterial cells, medium culture components, and other debris [94]. Nanocellulose based materials possess very interesting chemical, physical and biological properties. Its inertness and increased surface area, due to its nanosized structure, have an impact on the availability of hydroxyl groups (–OH), thus facilitating the adsorption of different ions, atoms, and molecules. Besides being generally mechanically

strong, the morphological, chemical, and optical properties of nanocellulose can be tailored. Furthermore, it is an abundant and renewable material with a relatively reduced production cost [93, 94].

The nano size of nanocellulose (Fig. 2.4) greatly enhances the availability of the –OH that populate their surface. Fibrinogen, a glycoprotein present in blood, may be cleaved in an array of different peptides that regulate cell adhesion, cell migration, and may work as chemotactic for key angiogenesis cells such as fibroblasts, keratinocytes, macrophages, myocytes and endothelial cells. Fibrinogen bonds tightly to –OH groups [95] thus, the outstanding –OH availability in nanocellulose may result in a favourable promotion of angiogenesis.

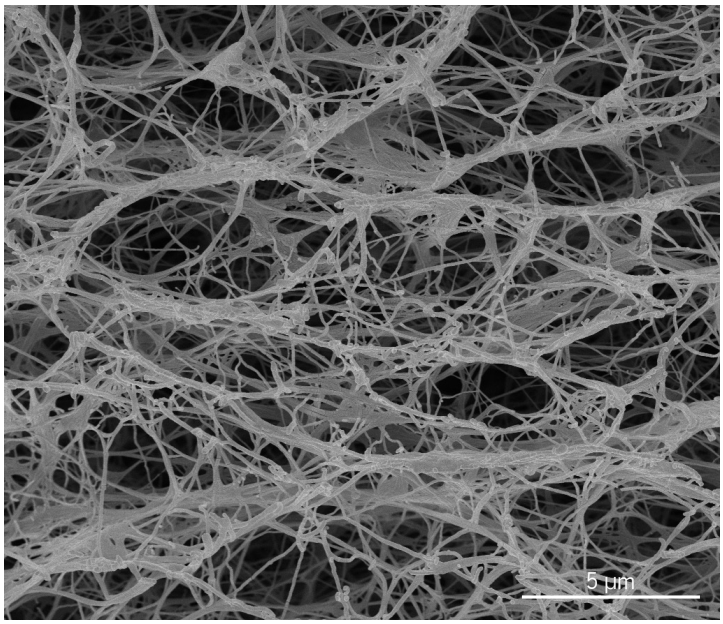



**Figure 2.4.** Scanning Transmission Electron Microscopy (STEM) images of BNC from *Komagataeibacter hansenii* American Type Culture Collection (ATCC) 53582.

The mechanical strength of BNC is equivalent to synthetic polymers, resulting from the complex interlaced nanofibres that develop into a porous matrix. The arrangement of BNC microfilaments within the 3D nanofibrillar network gives rise to a thin, extremely fluid, and hydrophilic structure. In addition, the crucial mechanical strength of BNC is attributable to its linear cellulose chains and high cohesion between macromolecules [96].

BNC exhibits excellent mechanical properties. Although varying from bacteria strains, they have been reported to have a tensile strength in the range of 200 – 300 MPa and a Young's modulus up to 15.0 – 35.0 GPa. Much higher than petrol based polymers such as polypropylene, 30.0 – 45.0 MPa for tensile strength and 1.00–1.50 GPa for Young's modulus [97]. Different values for

tensile strength and Young's modulus found in literature are presented in Table 2.7. Besides its improved mechanical properties, BNC is a biocompatible material and is easily sterilised [98].

The Young's modulus and stiffness are significantly higher in dry samples compared to hydrated BNC [99]. Drying at atmospheric pressure and temperature leads to a higher density of cellulose fibrils due to its smaller volume (thickness), reflected in less porosity, more homogeneous structure, higher quantity and stronger hydrogen bonds and higher crystallinity, ultimately improving strength and Young's modulus. The freeze-drying method maintains the cavities between the layered structure leading to lower crystallinity and less quantity and weaker hydrogen bonds between the cellulose molecules, impacting Young's modulus [100]. If on the one hand, the typical behaviour of brittle materials was evidenced by oven-dried BNC, freeze-dried BNC on the other hand, exhibited low Young's modulus and higher elongation before fracture [101].

If the BNC is dried (independently if it is dried in an oven or at room temperature) due to the evaporation of the water present within BNC nanofibrils, these tend to collapse by forming additional hydrogen bounds, becoming "paper-like" (Fig. 2.5). The freedom of the nanofibrils to rearrange is drastically reduced which considerably reduces stretch ability [102]. Furthermore, this event is irreversible, despite the swelling degrees achieved by dried BNC (approximately 200%) [13]. BNC has been used in biomedical applications for at least two decades. In particular, BNC was particularly effective per se (when never-dried) as a dressing for burn wounds. BNC offered a sterilised, comfortable, protective and adequately moist environment for clean burn wounds, which accelerated wound healing [103]. Furthermore, never-dried BNC is highly mouldable, tightly adapting to the wound site. Never-dried BNC is more stretchable, however it is less resistant to tear than dried BNC [102]. One of the most important BNC limitations is its absence of antimicrobial activity, which greatly limits its application as an active wound dressing and other application prone to infection, such as urinary catheters [104].

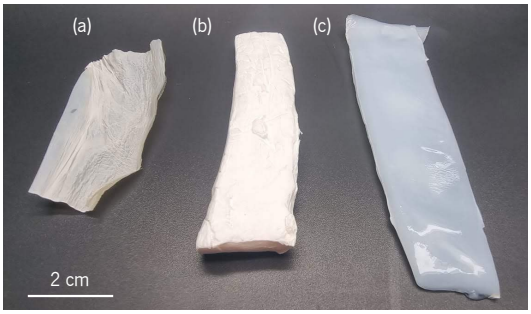



**Figure 2.5.** BNC in three different physical states: (a) dried, (b) freeze-dried, and (c) never-dried BNC.

**Table 2.7.** Mechanical properties of BNC produced under static mode, according to the physical state of the sample.

| Sample | Size (cm) | Thickness (μm) | Load (kN) | Strain rate (mm·min$^{-1}$) | Young's modulus (GPa) | Tensile strength (MPa) | Elongation at break (%) | Ref |
|---|---|---|---|---|---|---|---|---|
| **Vacuum dry** | n.d. | n.d. | n.d. | n.d. | 5.13 | n.d. | n.d. | [100] |
| **Dry** | n.d. | n.d. | n.d. | n.d. | 13.0 | n.d. | n.d. | [100] |
| **Oven dried** | 2.0 × 6.0 | 22.700 | 1.0 | 5.0 | 5.60 ± 0.760 | 37.2 ± 3.30 | 2.20 ± 0.0600 | [101] |
| **Dry (25 °C)** | 1.5 × 10 | 300.0 – 500.0 | n.d. | 10 | n.d. | 17.4 ± 7.23 | 6.63 ± 1.55 | [105] |
| **Dry (25 °C) - rehydrated** | 1.5 × 10 | 300.0 – 500.0 | n.d. | 10 | n.d. | 17.4 ± 3.68 | 11.0 ± 3.68 | [105] |
| **Dry (40 °C)** | 6.5 × 2.0 | 2670 ± 670.0 | 10 | 2.0 – 4.0 | 0.140 ± 0.0200 | 10.3 ± 3.69 | 7.94 ± 3.39 | [99] |
| **Dry (80 °C)** | 1.5 × 10 | 300.0 – 500.0 | n.d. | 10 | n.d. | 12.9 ± 1.80 | 6.40 ± 1.61 | [105] |
| **Dry (80 °C) - rehydrated** | 1.5 × 10 | 300.0 – 500.0 | n.d. | 10 | n.d. | 8.49 ± 5.47 | 11.1 ± 2.75 | [105] |
| **Hydrated** | 0.6 × 3.5 | 800.0 | 0.0050 | 10 | 0.0100 ± 0.000 | n.d. | n.d. | [106] |
| **Hydrated** | 0.6 × 3.5 | 800.0 | 0.0050 | 10 | 0.00100 ± 0.000 | n.d. | n.d. | [106] |
| **Hydrated** | 1.0 × 10 | 300.0 – 500.0 | n.d. | n.d. | 9.14 | 112.4 | 0.600 | [107] |
| **Hydrated** | 1.5 × 10 | 300.0 – 500.0 | n.d. | 10 | n.d. | 1.18 ± 1.01 | 12.8 ± 2.17 | [105] |
| **Moist (1.82%)** | 1.5 × 10 | 280.0 | n.d. | 4.8 | 1.04 | 20.8 | 2.28 | [108] |
| **Moist** | 6.5 × 2.0 | 2670 ± 670.0 | 10 | 2.0 – 4.0 | 0.0260 ± 15.2 | 4.64 ± 0.320 | 21.7 ± 6.25 | [99] |
| **Freeze dried** | 2.0 × 6.0 | 34.90 | 1.0 | 5.0 | 0.180 ± 0.0600 | 7.20 ± 1.10 | 4.92 ± 1.20 | [101] |
| **Freeze dried** | 6.0 × 1.0 | n.d. | n.d. | n.d. | 2.68 ± 0.730 | n.d. | n.d. | [109] |

### 2.3.1. Production

The biosynthesis of BNC is an extremely complex and highly regulated metabolic process. It undergoes several steps and involves a series of genes responsible for the encoding of both enzymes and different catalytic complexes [110, 111]. There are different genera of bacteria able to produce BNC. Among them are *Rhizobium*, *Azotobacter*, *Agrobacterium*, *Aerobacter*, *Salmonella*, and *Escherichia*. However, the most prominent are *Komagataeibacter*, that belong to the *Acetobacteraceae* family [112]. BNC is excreted by the bacteria as fibres that intertwine with each other, retaining bacterial cells between the produced cellulosic ribbons. Because these are non-motile and strictly aerobic bacteria, the 3D network, also designated as membrane (Fig. 2.6), is produced at the interface of the culture medium [112, 113]. BNC production yield and properties, such as mechanical, crystallinity, and thickness, are mainly governed by two factors, the carbon source used (e.g. glucose, fructose, and galactose), and the bacterial strains of different metabolic profiles [113, 114].

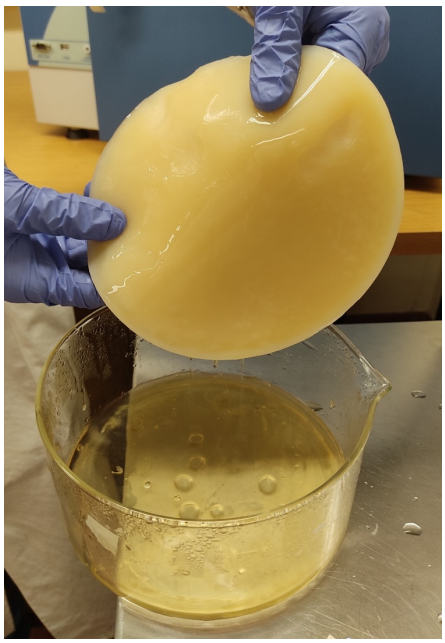


**Figure 2.6.** BNC produced by *K. hansenii* ATCC 53582 in Hestrin-Schramm medium.

The most common and straightforward metabolic pathway for BNC biosynthesis (Fig. 2.7) is using glucose as the main carbon source. Glucose may be broken down into four main enzymatic steps: (i) phosphorylation of glucose into glucose-6-phosphate via glucokinase; which is followed by the (ii) preparation of linear glucan chains, meaning the isomerization of glucose-6-phosphate by

phosphoglucomutase into glucose-1-phosphate; (iii) uridine diphosphate glucose (UDP-Glc), a direct precursor of cellulose, is synthesised by UDPG-pyrophosphorylase, which translates into the assembly and crystallization of glucan chains into hierarchically structured cellulose ribbons; lastly, (iv) UDP-Glc polymerizes into cellulose by a membrane protein complex called cellulose synthase, and it is secreted to the extracellular environment [110, 111, 115-118]. Besides monosaccharides, disaccharides, such as sucrose, lactose, and maltose, may also be used as carbon sources, however, the initial metabolic process is different. The disaccharides must first be converted into their respective monosaccharides through an additional hydrolysis step and only then undergo the cycle described above for glucose [114, 115]. concerning the genes involved in this process, it is important to highlight those belonging to the BNC synthase operon (bcs), namely bcsA, bcsB, bcsC, and bcsD [110, 112, 115]. BcsA has a catalytic role in cellulose production, and its activity can be regulated through the cyclic di-guanosine monophosphate (di-GMP) messenger. It is embedded in the inner membrane as eight transmembrane helices and consists of two cytoplasmatic domains: a catalytic β-1,4-glycosyltransferase domain conserved between transmembrane helices four and five and a C-terminus containing a PilZ domain. The binding of cyclic di-GMP to BcsA occurs in its PilZ domain and induces a conformational change that allows UDP-Glc access to the catalytic site. Once activated, this catalytic domain promotes the polymerization of UDP-Glc monomers into β-1,4-glucan chains [111, 115]. BcsB is a large periplasmic protein anchored to the inner membrane through a single transmembrane helix. This protein interacts with BcsA, being responsible for the BcsA stabilization and enabling its catalytic activity. It is assumed that BcsB also has an important function in the transportation of the synthesised glucan chain through the periplasm into the outer membrane [111, 115].

BcsC is a β-barrel type outer membrane porin protein. It is suggested that BcsC leads to the formation of membrane pores that allow cellulose secretion into the extracellular environment. In periplasmic domain of BcsC there is a tetratricopeptide repetition [110, 111, 115]. BcsD is a periplasmic protein that assists in the association and crystallization processes of the glucan chain. Moreover, the hierarchical cellulose assembly process is also largely controlled by the BcsD-driven arrangement of linear terminal complex arrays and their orientation longitudinal to the axis of the cell. It also prepares the glucan chain for secretion through BcsC protein; however, the mechanism of its function is not fully described yet. Nevertheless, it is evident that this protein is essential for the optimal production of BNC [110, 111, 114, 115]. The up regulation of carboxymethyl cellulase has been suggested as an additional factor for BNC enhanced production. This enzyme catalyses

the hydrolysis of endo-β-1,4-glycosidic bonds of cellulose chains. However, its activity has been correlated with higher production of BNC due to its potential as cellulose error correction enzyme. This enzyme is expressed by the cmcAx gene [111]. Other proteins with a hypothesised relevant role in BNC production are ccpAx protein and ß-glucosidase. CcpAx protein possibly assists BNC production during the crystallisation phase. It interacts with the BcsD subunit and is also able to facilitate protein-protein interactions during the assembly of the cellulose synthase complex [111, 112]. Finally, ß-glucosidase (expressed by bglxAx gene), is envisioned to modify and affect the degree of polymerization of the newly synthesised glucan chains. However, the details of its actual role were not yet unveiled [111, 115]. Initially, sub-fibrils are formed, then they crystallize and organize themselves to form fibrils, which in turn combine to form cellulose nano- or microfibres, consisting of about 1,000 individual glucan chains [110, 111, 118].

In conclusion, the BNC 3D network is developed and stabilised through inter- and intramolecular hydrogen bonds. The high amount of hydrogen bonds endow the material with its remarkable water-holding capacity (about 200 times its dry weight) [111] and also the formation of its hierarchical structure. The nanofibrous structure of BNC is able to mimic the fibrous architecture of the ECM (*e.g.* collagen, elastin and fibrin fibres that are components of connective tissues), and its resistance, flexibility, and porosity are important in the support of tissues that undergo constant stress and deformation like skin, muscle and cartilage, and the porosity and permeability that allows diffusion of gases or nutrients [110, 111, 114-116] [114, 117].

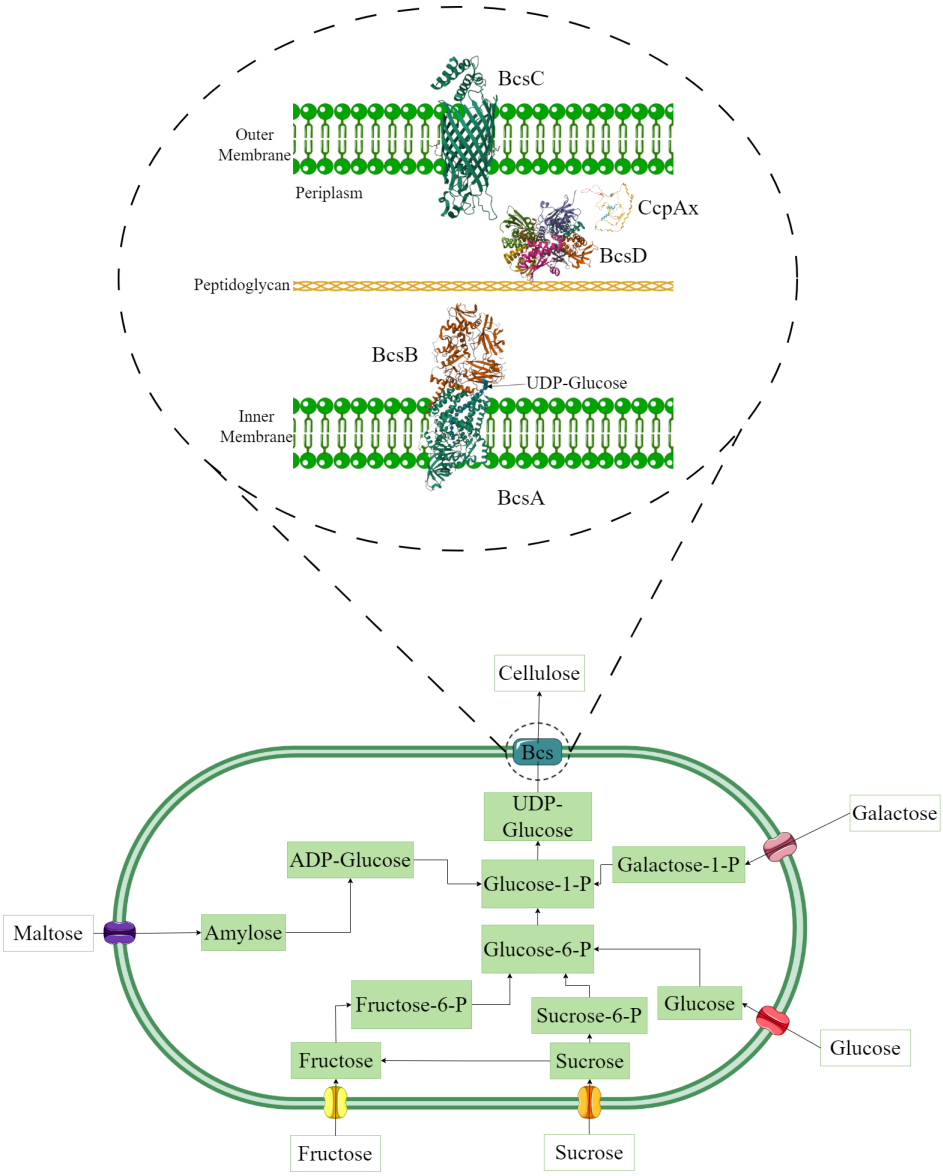



**Figure 2.7.** Schematic representation of the biosynthetic pathway for BNC and organization of the various subunits in the bacterial cellulose synthase complex. Adapted from Ref. [111], under the Licence CC BY 4.0, 2021, Nanjing Medical University.

The morphology of BNC can vary depending on the culture methods used, ranging from uniform membranes to spherical or irregular pellet-shaped hydrogels. There are two main types of bacterial culture used to obtain BNC: static and agitated culture. Fig. 2.8 displays some examples of BNC produced from different strains, obtained from static and agitated cultures. This distinction influences not only the supramolecular structure of the obtained product but also its mechanical characteristics and physical properties [111]. Due to its simplicity, static culture represents the most commonly used technique for the production of BNC as a flat membrane with a homogeneous supramolecular structure [110, 111, 116, 118, 119]. This approach allows the use of containers

of any shape, which in turn, will dictate the shape of the membrane formed [115, 116]. In this technique, BNC producing bacterium are incubated for 2 to 20 days at temperatures between 25 and 30 °C [110, 111]. The most commonly used culture medium is the Hestrin-Schramm medium, which uses glucose as the main carbon source, yeast extract as a source of nitrogen and growth factors, peptone as a nitrogen source, and citrate-phosphate buffer to prevent pH reduction caused by gluconic acid during the bacteria aerobic growth [114, 119]. The Hestrin-Schramm medium is a rich and expensive culture medium that can increase the final production cost of the biopolymer which could be considered unfeasible for commercial production of BNC. However, it depends on the applications intended. The medical area may support especially considering that through this way, it is possible to obtain a pure membrane free of contaminations [120]. It should be noted that the variation of any of these parameters affects the final product, making the incubation time the most critical factor. It is relevant to mention that the membrane is generated at the air-liquid interface, where there is more oxygen available. As the membrane produced on the medium grows downwards and entangles the bacteria, it limits the oxygen supply, resulting in reduced oxygenation and overall lower productivity. Incubation time is the main factor that governs the thickness of the BNC membrane produced [110, 111, 114-116, 118, 121]. However, historically, static culture is characterized as incompatible with industry. The most common arguments are the high costs associated with culture medium and the assurance of aseptic conditions in a large area. An established strategy to reduce costs is the use of alternative culture media based on agricultural and industrial wastes particularly rich in carbon sources, such as sugar cane processing industries and fruit juice production plants [111]. The agitated or dynamic culture comprises agitation or mixing of the culture medium to enhance the dissolved oxygen and improve the availability of nutrients concentration, consequently increasing the rate of BNC biosynthesis [111, 114-116, 119]. The shape and size of BNC is governed by the applied rotational speed. It usually presents itself with a spherical, cocoon-shaped, pellet-shaped, or even irregular clump-shaped morphology, therefore its applications are generally different from the membranes obtained through static culture [110, 115, 116, 121]. Furthermore, BNC from dynamic culture possesses higher water absorptivity and higher suspension viscosity. The dynamic culture increases the amount of dissolved oxygen [119, 121]. Furthermore, in dynamic culture, BNC usually possesses lower crystallinity and inferior mechanical properties such as lower Young's modulus, due to the decreased degree of polymerization and organization of the BNC nanofibres [110, 111, 114, 119].

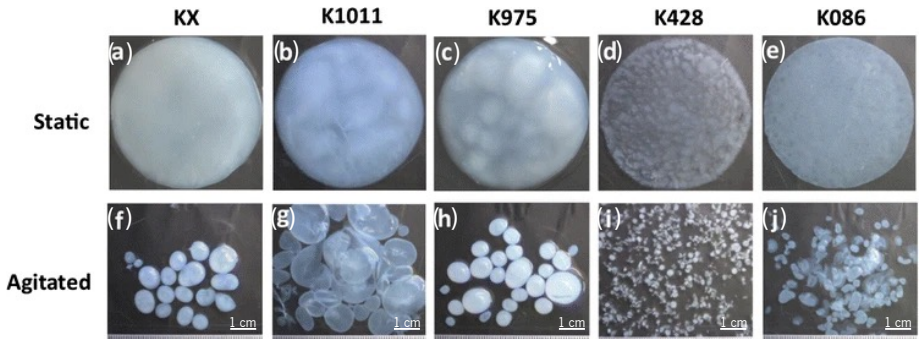



**Figure 2.8.** Optical images of BNC produced by five strains of *K. xylinus*, (a–e) in static condition, and (f–j) in agitated condition. Reproduced from Ref. [122] with permission, Copyright 2018, Springer Nature.

Ubiquitously BNC is embedded with bacterium cells and culture medium containing secondary metabolites [123]. Living bacterium cells and other impurities represent potential safety hazards and will impact the quality and characteristics of the BNC fibres. Thus, BNC must be submitted to different purification steps. Typical purification procedures are described in Table 2.8. [124]. Pure BNC displays improved mechanical strength, biocompatibility, and enhanced functional characteristics, such as water-holding capacity. In addition, if BNC contains a low thickness, it becomes more transparent, becoming more adequate for optics and electronics applications [125]. Furthermore, since BNC is solely composed of cellulose, to obtain a 100% nanocellulose material, the only purification procedure required is to remove bacteria, bacteria debris and culture media constituents from the collected BNC [126]. The most common purification consists in a maceration procedure. This purification procedure reduces the liposaccharide concentration values considerably below the threshold defined by FDA [12]. Therefore, the size of BNC fibres and their concentration (which influences pore size) is highly variable: width between 10 to 100 nm and 50 nm up to 100 μm in length.

The purification protocols displayed in Table 2.8 are sufficient to meet biomedical applications requirements, such as physicochemical, cytotoxicity, hemocompatibility, and biocompatibility [127]. Numerous industries are exploring the potentialities of BNC, and as this field of study develops, so do novel methods for purification and functionalisation. As observable in Table 2.8, all purification methodologies comprise the use of an alkali solution (NaOH or KOH). In the case of purification using high concentrations of alkali solution, mercerization occurs, which will simultaneously degrade amorphous regions of cellulose and will convert cellulose I polymorphs to cellulose II. Cellulose II polymorph contains one additional hydrogen bond per cellulose monomer; thus, it is a more thermodynamically stable polymorph. Therefore, purified BNC exhibits enhanced properties in comparison to unpurified BNC [128].

**Table 2.8.** Purification methods applied to different bacteria and the carbon source used throughout their fermentation.

| Bacterium | Carbon Source | Purification Method | Ref |
|---|---|---|---|
| *Bacillus* sp. strain SEE-3 | Glucose | – Distilled water ($dH_2O$) (wash and boil)<br>– 0.1 M NaOH (3 h, 80 °C)<br>– $dH_2O$ (until neutral pH) | [123] |
| *Komagataeibacter europaeus* SGP37 | Glucose | – Tap water (wash)<br>– 0.5 M NaOH (1 h, boil)<br>– $dH_2O$ (30 min, boil)<br>– $dH_2O$ (until neutral pH) | [129] |
| *Starkeya* sp. strain N1B | Naphthalene | – 0.09 M aqueous KOH solution<br>– Water (until neutral pH) | [130] |
| *Komagataeibacter* sp. | High fructose corn syrup (Hungrasweet F50) | – 1 or 4 M NaOH (depending on the thickness, 10 to 30 times)<br>– $dH_2O$ (until neutral pH) | [131] |
| *Komagataeibacter pasteurianus* ATCC 23760 | Glucose | – Tap water (24 h, wash)<br>– 0.03 M solution of NaOH (15 min, 70 °C)<br>– $dH_2O$ (until neutral pH)<br>– Sterilised by Gamma irradiation (20 kGy) | [132] |
| *Komagataeibacter hansenii* | Glucose, mannitol, fructose, sucrose, and glycerol | – 1 M KOH solution (48 h)<br>– 0.5 M HCl bath (1 h)<br>– $dH_2O$ (until neutral pH) | [133] |
| *Komagataeibacter sucrofermentans* DSM15973 | Glucose, pure glycerol, and crude glycerol (20%) | – 0.1 M NaOH solution (2 h, 80 °C)<br>– $dH_2O$ (until neutral pH) | [134] |
| *Komagataeibacter sucrofermentans* ATCC 700178 | Fructose | – 0.5 M NaOH solution (3 days, solution replaced twice a day)<br>– Deionised water (until neutral pH) | [135] |
| *Komagataeibacter hansenii* ATCC 53582 | Glucose | – 0.07 M sodium dodecyl sulphate (SDS) solution (magnetic stirrer, overnight)<br>– $dH_2O$ (until SDS removal)<br>– 1 M NaOH solution (50 rpm, 90 min, 60 °C)<br>– $dH_2O$ (until neutral pH) | [136] |

### 2.3.2. Modification

BNC properties encompass high specific surface area, high tensile strength, light-weight, biodegradability, and good barrier properties when dry, while maintaining high moisture absorption and hydrophilicity. However, despite the many advantages of BNC, the abundant number of –OH groups on its surface also present disadvantages. These include low dispersibility and incompatibility with hydrophobic polymers, and poor thermal stability, which restrict a wider range of applications [137]. Nevertheless, the reactive –OH groups along the cellulose polymer chain, may undergo surface modification through chemical and physical methodologies to generate novel functional groups or moieties on its surface. Thus, the range of properties and applications can be significantly expanded. BNC modification involves both chemical and physical methodologies [138, 139].

#### Chemical modification

Chemical modification of nanocellulose is a straightforward strategy to introduce desired functionality by introducing additional functional groups in its structure. Common chemical modifications methods of nanocellulose include esterification, oxidation, silanization, and graft copolymerization. Esterification is the most well-known and simplest method to reduce the –OH density of nanocellulose to render it hydrophobic. It consists in the reaction between the –OH groups present in its structure and different acids that result in ester groups [140]. 2,2,6,6-Tetramethylpiperidine-1-oxyl (TEMPO)-mediated oxidation converts the –OH groups into their carboxylic forms. With this oxidation, the breakdown of glycosidic bonds does not occur due to the mildness of the process [141]. Silanization is a process that allows to superficially modify this biopolymer through the incorporation of hydrophobic alkyl moieties (silanes) in its structure. It is distinguished from other chemical modification processes since its coupling agents (silanol) can establish covalent bonds with the –OH groups of the cellulose and the reinforcement, thus serving as anchor points [142]. Graft copolymerization comprises the anchoring or covalent bonding of polymers onto a base or backbone polymer. The grafting polymerization may occur as: grafting-onto, grafting-from, and grafting-through. In grafting-onto, pre-synthesised polymer chains, called graft polymers, are attached or grafted onto the base polymer. This process typically involves functionalizing the base polymer with reactive groups or sites, which can then react with or chemically bond to the graft polymers. Grafting-from involves initiating the growth of polymer chains directly from the base polymer. It starts by anchoring initiators or initiator sites onto the base

polymer. These initiators then initiate the polymerization of monomers, which become grafted onto the base polymer. Grafting-through, also known as macromonomer grafting, involves incorporating polymerised monomers into the base polymer structure. The base polymer monomers containing the grafted polymers are polymerised within the base polymer matrix, resulting in the growth of the base polymer [143-145]. Non-covalent modification consists in surfactant adsorption that bears an opposite charge from nanocellulose, thus interacting through electrostatic attractions, van der Walls forces, or hydrogen bonds [146].

Sulfonation is a chemical process to covalently bond sulphate groups to cellulose, creating the commonly named sulphate half-esters [143]. In the amination process, the nanocellulose –OH groups are oxidized, generally through periodate oxidation, into aldehydes. Afterward, the NH groups (primary, secondary, or tertiary) react with the aldehyde groups [147, 148]. In the case of amidation, nanocellulose –OH groups are also oxidized, commonly via TEMPO-mediated oxidation, which will convert the –OH groups to carboxylic units [143]. Carbamation can be achieved through the usage of isocyanates. Mono-isocyanates with long alkyl chains are commonly used to hydrofobize nanocellulose surface. Di-isocyanates act primarily as crosslinking agents, often used for the synthesis of polyurethanes. Carboxymethylation is generally used as an oxidative pre-treatment of nanocellulose, followed by esterification, amidation, or other processes that require a carboxylic acid group to covalently bond other molecules. Similar to what occurs in sulfonation, the negative charge at nanocellulose surface will create electrostatic repulsions [149]. Through fluorination, nanocellulose can be converted into a hydrophobic material. The incorporation of fluorine groups into the nanocellulose structure leads to a reduction in adhesion and surface tension. Additionally, the high electronegativity of fluorine enables the formation of stronger covalent bonds [150]. These disadvantages include toxicity, limited sustainability, and potential environmental harm [150].

### Physical modification

Several physical techniques can be used for the surface modification and functionalisation of nanocellulose, including heat treatment, Gama irradiation, and plasma treatment. Heat treatment can change the fibre structure and improve hydrophobicity. Gamma irradiation is used for sterilization but can also be applied to induce physical or chemical modifications. During exposure to gamma irradiation (high-energy-ionizing radiation), the surface of this biopolymer becomes ionized through the collision of the atoms present in the nanocellulose and the radiation rays at the atomic and molecular levels. Subsequently, reactive radicals and ions are produced through

water hydrolysis, performing as initiators to facilitate subsequent surface chemical modifications (e.g., oxidation, grafting, and cross-linking) [151]. Plasma treatment is an eco-friendly, cost-effective, and efficient fast-growing technique for the surface modification and functionalisation of cellulose materials. Plasma is generated by applying high-voltage electrical discharges to a gas where its molecules are ionized or excited, resulting in a reactive media, mainly composed of electrons, ions, atoms, free radicals, and excited molecules [141, 152-154]. The interactions of the plasma with the surface of polymeric materials can result in different effects, including (i) surface etching or cleaning; (ii) formation of functional groups; (iii) deposition of a coating layer by plasma polymerization of a precursor; and (iv) formation of nanoparticles from monomers and reactive gases [155].

### 2.3.3. BNC functionalised with organic and inorganic agents

Notwithstanding the high biocompatibility of BNC and the physical barrier against infections that it represents, there is no antimicrobial activity reported [156]. Therefore, the incorporation of antimicrobial active agents onto a BNC based mesh was envisaged to mainly prevent the long-term prosthetic infection. The application of active agents such as metal micro/nanoparticles and organic compounds (e.g. lignin, peptides, proteins, or enzymes) is an alternative to the increasing resistance of bacteria and pathogens to antibiotics. In addition, the envisaged antimicrobial efficacy must be maintained during over several months [157]. Nanoparticles are capable of generating reactive oxygen species (ROS) which induce important damage to the bacteria cell membrane, key metabolic enzymes and in the genome, ultimately compromising their proliferation and viability.
Numerous metal nanoparticles modus operandi have been proposed, such as: i) direct electrostatic interactions with the microorganism cell membrane and/or cell wall components; ii) homeostatic stress generation due to an abnormal imbalance of ions, which impair respiration, interrupt energy transduction, and lead to cell death; iii) interactions with sulphur-containing molecules such as proteins; iv) the production of ROS and the release of metal ions that denature proteins and damage ribonucleic acid (RNA), deoxyribonucleic acid (DNA), and lipids [158, 159]. Fig. 2.9 describes the steps of antimicrobial action of metal particles.

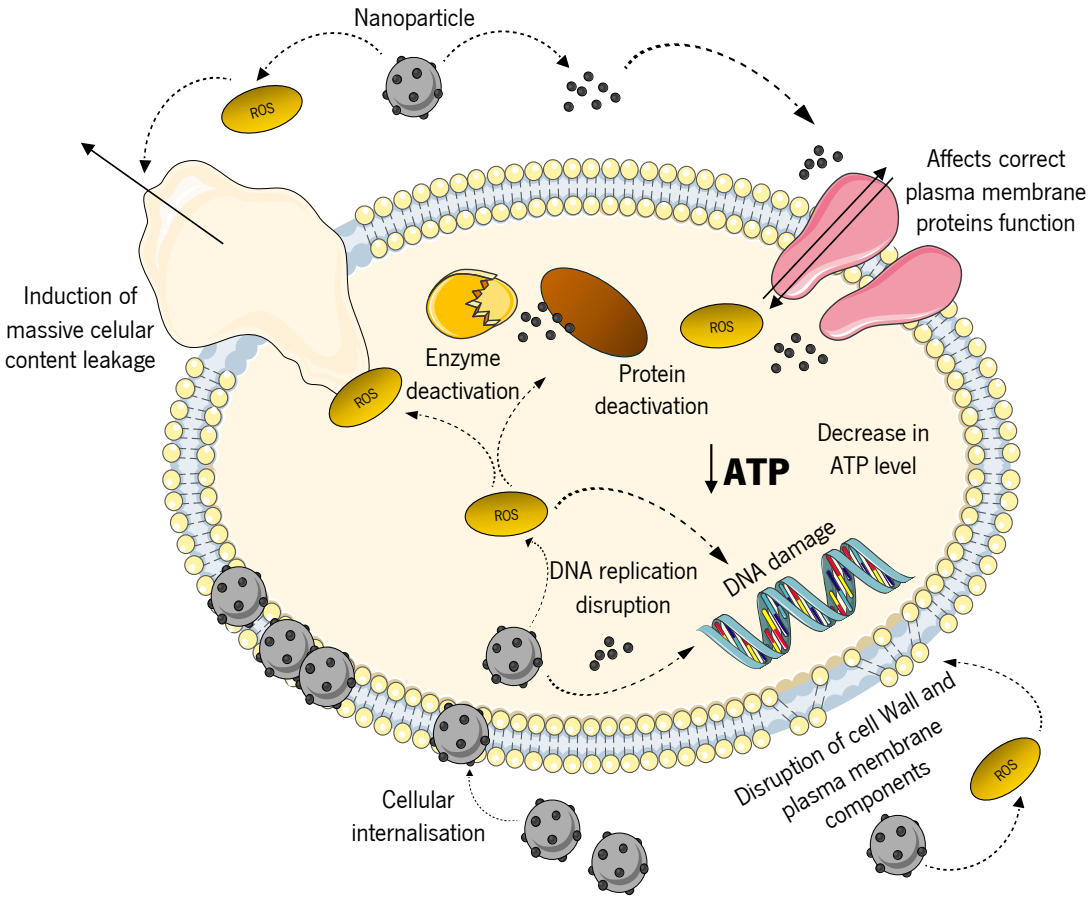



**Figure 2.9.** Steps of antimicrobial action of nanoparticles. Based on [160].

Unlike bacteria, animal cells have a plethora of ROS damage mitigation strategies, thus nanoparticles cytotoxicity is usually considerably lower [161-163]. However, nanoparticles toxicity is still a factor to consider. Metal nanoparticles can penetrate cells and display cytotoxicity and genotoxicity in human body limiting practical applications [164]. Their toxicity is dependent not only on the intrinsic toxicity of the metal but also their dispersity, because when agglomerated, nanoparticles precipitate, causing significant changes in their physico-chemical properties [165]. The dimensions of metal nanoparticles are another factor for potential toxicity. Smaller nanoparticles, below 10 nm, present greater antimicrobial effect but also grievous cytotoxicity owed to better diffusion of smaller nanoparticles into bacterial cells and human cells [166]. Surface charge has proven to be one of the most important properties influencing toxicity. The more negative the charge, the less toxicological effect is observed. In contrast, positively charged metal nanoparticles present higher cytotoxicity [167]. Notwithstanding, the release of nanoparticles into the blood stream of the patients may represent a non-negligible threat of systemic toxicity, in particular if they are able to cross the blood brain barrier (BBB). Therefore, to avoid these relevant

threats, the functionalisation of BNC envisages the immobilization of the organic and inorganic active agents. In addition, the size of the active nanoparticles will always be above 30 nm to prevent any BBB crossing, since at 15 nm gold (Au) nanoparticles have been efficiently delivered into the brain [168].

Silver (Ag) nanoparticles are one of the most popular due to its excellent antimicrobial activity against bacteria, including drug-resistant strains, fungi, and viruses [169]. Ag nanoparticles in the metal form can interact with oxygen originating different species as $Ag_2O$, AgO, $Ag_3O_4$, and $Ag_2O_3$. Furthermore, several studies have showed that films with oxidized silver present a better antimicrobial effect than zero-valent silver [170]. Others mention that Ag nanoparticles are less toxic than some antibiotics and fungicides. However, Ag nanoparticles also can present cytotoxicity that is dependent on the dose and time of the exposure, size, charge, and shape. Therefore, when using Ag nanoparticles as antimicrobials, it is crucial to establish an equilibrium between the maximum antimicrobial effect and minimum cytotoxicity [171-173].

Copper (Cu) and copper oxide (CuO) nanoparticles have been used in several fields such as antimicrobial materials, pharmaceutical industry, and cosmetics. Nevertheless, their use as antimicrobial agent presents more toxicity and lower efficacy compared with other metal nanoparticles such as zinc oxide (ZnO) nanoparticles or Ag nanoparticles [174]. CuO nanoparticles are however still interesting because they are less expensive than other materials. The mechanism of action is not clear, but several works cited the electrostatic attraction between Cu ions and plasma membrane, increasing the permeability into bacteria cells [175-177]. Cu nanoparticles lead to the generation of free radicals in pathogenic bacteria as a result of the oxidative stress caused by an intracellular signalling cascade produced by the Cu nanoparticles [178].

Au nanoparticles, despite being the least active metal, have shown a broad antibacterial spectrum, with antibacterial activity against both Gram-positive and Gram-negative bacteria. Besides, gold is multivalent, capable of binding many types of ligands. Their very large specific area provides abundant sites for binding with target bacteria. Because they target a variety of molecules in bacteria, it is hard for bacteria to produce resistance by establishing a system that can defend against damage. Besides, Au nanoparticles are chemically stable, non-toxic, and possess good biocompatibility [179].

Metal nanoparticles (Fig. 2.10a) in particular, encompass several safety concerns regarding living organisms and the environment, which hinder their applicability. Their properties and corresponding potential toxicity profile is complex and may undergo numerous mechanisms. The

main mechanisms for nanoparticles toxicity comprise i) direct nanoparticles association with an organism's cell surface, ii) release of toxic ions that damage enzymes and genetic material, and iii) generation of ROS and subsequent oxidative stress [180, 181]. For living organisms, the metal nanoparticles' toxicity is commonly correlated to the size, shape, stability, agglomeration, surface charge and chemistry [182, 183]. Metal nanoparticles synthesis method, stability, life cycle, and the related disposal procedure are particularly important to determine their environmental impact [184]. For these reasons, the safe-by-design concept is gaining exponential importance once it foresees the risk assessment in the early stages of the development of metal nanoparticles. Thus, prematurely preventing negative impacts on living organisms and the environment [181, 185, 186].

Several toxicological aspects of the nanoparticles are defined by their physicochemical properties. The size of the nanoparticles below 10 nm is related to superior multifunctional properties (*e.g.*, antimicrobial and Ultraviolet (UV) protection and grievous cytotoxicity owed to facile permeation of smaller nanoparticles into cells [166]. The most common shapes of nanoparticles are spheres, ellipsoids, cylinders, sheets, cubes, and rods, but other shapes can be obtained depending on the synthesis method. Spherical nanoparticles showed a low cytotoxicity profile when compared with other nanoparticles shapes [187]. The agglomeration state also plays a vital role in their toxicity, since it can contribute to the sedimentation process and reduce the diffusion of nanoparticles, resulting in higher effective doses and organ deposition. When applied in materials, the agglomeration can promote the non-uniform distribution of nanoparticles, resulting in materials with poor reproducibility and compromised properties [188, 189]. The charge of nanoparticles presents an essential function in regulating the protein bindings to nanoparticles, cellular uptake, oxidative stress, autophagy, inflammation, and apoptosis. Charged nanoparticles showed to be more cytotoxic than neutral forms. Moreover, positively charged nanoparticles depict higher cytotoxic than negative alternatives of similar size [190-192].

Chemical reduction is the most common approach for the synthesis of nanoparticles. The most commonly used chemical reducing and stabilizing agents are extremely hazardous and depict carcinogenic and teratogenic effects. The chemical synthesis can also restrict the application possibilities and biocompatibility of the nanoparticles [193, 194]. Green synthesis, through precursors of biological origin such as polysaccharides, prevents pollution and mitigates cytotoxicity during the early stages of chemical processes [195]. The successful synthesis and the stabilization of nanoparticles using these biological macromolecules was achieved in several works by the

coordination bonds between the metal salts and functional groups of polysaccharides [196-202]. Moreover, the controlled release from polysaccharide can be designed according to the porosity or degree of swelling, pH, temperature, ionic strength and electric fields [203].

The action of metal nanoparticles against microbes consists in three different mechanisms: the release of metal ions, the production of ROS, and physical membrane interactions. The release of ions from the metal nanoparticles occurs due to the electrochemical potential in solution. The bacteriostatic effect of nanoparticles that come in contact and disrupt bacterial cell walls is dependent on ion concentration, shape, size, and element. The higher the concentration, the smaller the size and the rougher the surface, the more efficient are the nanoparticles. In addition, $Ag^{+}$ are able to produce a much higher antimicrobial activity than, for example, $Cu^{2+}$, even if the latter release more ions. ROS are highly active molecules consisting of hydrogen peroxide nonradicals ($H_2O_2$), hydroxyl radicals (•OH), and superoxide anions ($O_2^{\cdot-}$). When ROS generation exceeds the normal antioxidant capacity of microbial cells, essential macromolecules (e.g. proteins, lipids, RNA and DNA) undergo rapid oxidative degradation. Metal ions can trigger oxidative stress, leading to lipid peroxidation, thus permeating the cell envelope. Physical membrane interactions are based on nanoparticle adsorption and penetration into cell membranes. These are negatively charged and prone to permeation with positively charged nanoparticles through electrostatic interactions. This process can induce membrane depolarisation, leading to structural damage. Furthermore, the disruption of the cell envelope often generates ROS, compounding the oxidative stress. If the nanoparticle is small enough, cellular uptake may occur, causing internal organelle damage and total membrane disruption [160].

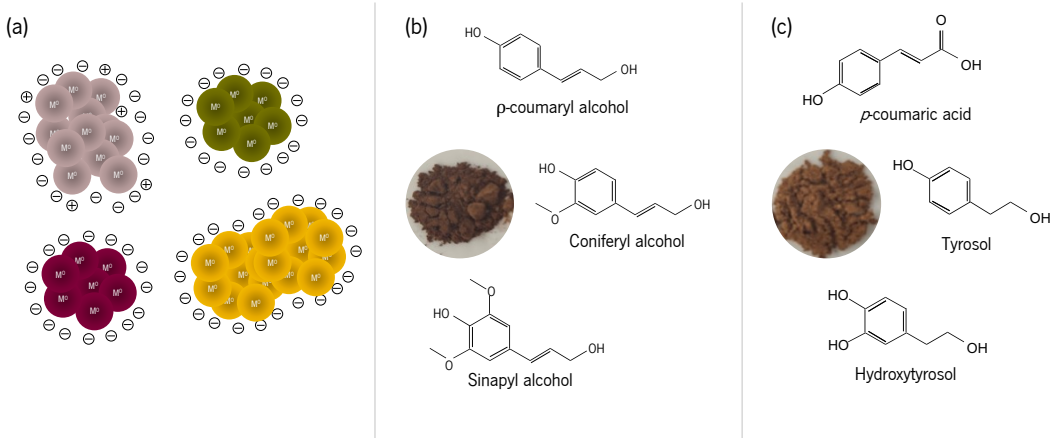



**Figure 2.10.** (a) Schematic representation of metal particles, (b) KL and the chemical structure of its phenolic compounds – primary lignin alcohol monomers: *p*-coumaryl, coniferyl, and sinapyl, and (c) OP (*p*-coumaric acid, tyrosol, and hydroxytyrosol) [204, 205].

Metal nanoparticles, including Au, Ag, Cu, Ti and ZnO, are less susceptible to drug resistance. Their effectiveness as antimicrobial agents rely on their physiochemical properties, particularly size, morphology, and functionalisation, either by a biomolecule or metal [206]. Au nanoparticles are biocompatible, with a propensity for functionalisation, and considered to be one of the most efficient antimicrobial agents. The actuation mechanism of Au nanoparticles is attributed to both metabolic and physical pathways: depolarization of the bacteria cell membrane and a decrease in adenosine trisphosphate (ATP) levels, and the physical crossing of bacterial wall releasing small amounts of ROS. The smaller the size of the Au nanoparticles, the higher the antimicrobial activity [160]. However, too small sizes are often discarded for biomedical applications due to the increased risk of crossing the BBB. In fact, Au nanoparticle sizes of 20 nm permeated the BBB and accumulated in the brain, according to in vivo studies performed in male Balb/C mice. 50 nm nanoparticles reached the brain, peaking the concentration after 30 minutes, gradually decreasing over time [207]. The antimicrobial activity is also influenced by the surface area, hence aggregation could lead to a decrease, resulting in lower activity. Capping agents such as citrate, may overcome this problem. The applications of BNC/Au nanocomposites are varied and include wound dressings [208], actuators [209], bone regeneration [210], and cancer therapy [211]. Functionalised BNC membranes with Au nanoclusters improved the tensile strength of the membranes, compared to pristine BNC, and showed good antibacterial activity against Gram negative bacteria. The healing ratios of the composite were also higher, with cell viability of more than 80% [208]. The incorporation of Au nanoparticles in BNC for rabbit model of femoral defect enabled new bone formation. The values of bone mineral density treated with neat BNC and BNC/Au indicated that the implantation of neat BNC in defect sites could provide the matrix for osteogenic cells to adhere and further mineralize. The bone volume fraction, and bone trabecular parameters, including number and thickness, were also impressively elevated after treatment. Moreover, mechanism studies suggested that Au nanoparticles increased autophagy response, confirming BNC/Au as a proper pathway for osteogenic differentiation of human mesenchymal stem cells [210]. As a photothermal agent, near-infrared (NIR)–activated BNC/Au nanorods presented antifouling properties against proteins, bacteria and mammalian fibroblasts. Moreover, with 5 min of NIR irradiation light, both Gram positive and Gram negative bacterium could be fully eliminated due to the heat generated from the Au nanorods. In vitro biocompatibility showed negligible cytotoxicity and in vivo tests showed good histocompatibility with almost complete wound closure on day 12 post-treatment [212]. Au nanocages with anti-programmed death 1 antibody, together with

thrombin, were incorporated into oxidized BNC, as a potential multifunctional therapeutic system to be used as a versatile implant for avoiding the recurrence of head and neck squamous cell carcinoma after resection. The immunotherapeutic system was further evaluated in vivo where the tumour was resected after reaching 100 $mm^3$, leaving a small amount of tumour behind. Likewise, the NIR laser irradiation treatment inhibited the tumour growth and suppressed the residual tumour recurrence, with no apparent toxicity. This effect is a consequence of the increased intracellular ROS levels that triggered tumour pyroptosis, a type of programmed cell death, induced by the inflammatory Caspase-1 cleavage of gasdermin D protein, the increase in T-cell infiltration, and the decrease in the number of immunosuppressive cells [211].

Ag nanoparticles have strong antimicrobial activity mainly due to their sulphur and phosphorous affinities, but also due to their surface, charge and size. Like Au nanoparticles, the smaller the size of Ag nanoparticles, the better the activity. The shape is also important because of the surface area due to increased $Ag^+$ ions availability. Furthermore, because Ag nanoparticles release ions under physiological conditions, positively charged Ag nanoparticles present better antimicrobial activity, compared to negatively charged. This is due to the electrostatic attraction to negatively charged cell membranes, since the Ag ions accumulate on the functional groups of enzymes and proteins, sulfhydryl- and phosphoryl-, that are important for the metabolism of bacteria cells [160, 213]. Ag actuation mode is based on physical interactions, with $Ag^+$ ions generating ROS, targeting bacteria cell envelope and causing DNA damage [214]. In terms of biocompatibility, Ag nanoparticles are less biocompatible than Au, however, like any other compound, it is dependent on the concentration. The main issue is their cellular uptake [160]. Applications of Ag nanoparticles in its varied shapes are immense and varied, from wound dressings [215-221], to tissue engineering [222, 223], and cancer therapy [224, 225]. Despite some negative views and facts over the use of Ag nanoparticles, films of BNC/Ag nanowires provided biophysical cues that facilitated cell proliferation and progressed the wound-repairing process. The inherent toxicity to mammalian cells of Ag nanoprisms, was reduced using a light-induced transformation reaction with light-emitting diodes (LED), and the BNC/Ag films with prospective applications as wound dressings, were considered non-toxic [216]. Other methods, such as the use of polydopamine (PDA), or the complex curcumin:hydroxypropyl-β-cyclodextrin, as reducing agents to produce Ag nanoparticles, can be used to reduce their toxicity and enhance the biological compatibility [217, 218]. The enhancement of the mechanical properties of BNC with Ag nanoparticles was possible with the inclusion of chitosan and/or PDA, with increased tensile strength, stress at break, and elongation

at break. In addition, both antimicrobial activity and cytocompatibility were verified [219, 220]. The combination of hydroxyapatite with BNC/Ag has shown great potential for bone regeneration, revealing optimal guided bone regeneration effects, providing long-term mechanical supports, and preventing potential infections [222, 223]. The potential of BNC/Ag composites in the biomedical field include cancer diagnosis. A low-cost hybrid substrate based on BNC/Ag was developed for direct surface-enhanced Raman scattering (SERS) analysis of exosomes, diagnosing tumoral and nontumoral exosomes discrimination with a 95% confidence [225]. Another application of BNC/Ag composites using SERS is the monitoring of glutathione, used in cancer detection, as the levels of this tripeptide small molecule are higher in the serum of cancer patients [224].

Cu-based nanoparticles, including copper oxide, are of the most extensively explored metals due to its higher biocompatibility, excellent antibacterial properties, low production cost, and electrochemical properties. Similar to Ag nanoparticles, Cu exhibits antimicrobial properties against both Gram-positive and Gram-negative bacteria [158, 214]. Antimicrobial mechanism of action is based on ion release upon solution oxidation. The produced free radicals oxidize and lead to the collapse of the lipids constituent of the microbials membranes [160]. In fact, Cu-based nanoparticles have a high affinity to amine and carboxyl groups, which is believed to contribute to their strong antimicrobial activity, since such functional groups can be found in bacteria cell walls [214]. Main applications include wound dressings [226, 227] and drug carrier [228]. Several works showed the enhancement of the antibacterial properties of BNC membranes in the presence of Cu or CuO nanoparticles [226, 229]. A scaffold of a composite film containing BNC/chitosan/poly(vinyl alcohol) (PVA)/CuO nanoparticles presented antibacterial and larval activity, and were able to induce the disruption of cancer cell membranes and the formation of vacuoles, altering the metabolism and leading to apoptosis, which, consequently, resulted in cancer cell death [228]. CuO nanoparticles as nanosheets, together with BNC and graphene oxide, presented good antibacterial activity, and good cell viability due to the slow release of $Cu^{2+}$ [227].

Presently, organic nanoparticles such as lipids, proteins, or polymers are used mostly as carriers. However, others such as proteins, enzymes, bacteriocins, and lignin are able to promote inhibition of the microbial growth [230]. Lignin is the second most abundant biopolymer in lignocellulosic material, after cellulose, and accounts for 18 – 35% of the wood dry matter [231]. It assures a structural role to plant cell walls providing rigidity and resilience. Lignin is amorphous and rich in aromatic alcohols, composed mainly of basic phenylpropanolic monomers, commonly named monolignols: *p*-coumaryl, coniferyl, and sinapyl (Fig. 2.10b). There are three main types of lignin,

depending on the isolation method: Kraft lignin (KL), sulfonated lignin, and organosolv lignin. KL contains small amounts of sulphur groups in its structure, making it soluble at higher pH values [232]. In the present work, lignin was obtained by Kraft process, the most common method, responsible for 85% of lignin recovery [233, 234]. One of the main disadvantages of this compound is its reduced solubility in water, due to the extremely alkaline conditions applied during the isolation process [234]. Some of lignin's interesting properties are its satisfactory stiffness, good thermal stability, and resistance to moisture and fungi [235, 236]. UV protection, antioxidant, antimicrobial, and flame-retardant properties may be ascribed due to functional groups such as methoxy (–$OCH_3$), phenolic hydroxyl (Ar–OH), aliphatic hydroxyl (Alk–OH), and side-chain carbonyl (C=O) on the benzene ring present in lignin molecules [237]. Such properties present lignin with potential use in drug delivery, tissue engineering, wound dressing, pharmaceutics, and medical devices [238]. The inclusion of lignin within a BNC matrix generates a fully bio-based composite encompassing the excellent properties of both components, improved water and gas barrier properties [239], biocide activities [240], and UV-absorbing characteristics [241]. Olive pomace (OP) is a semi-solid to semi-liquid by-product obtained from the olive's skin (10 – 11%, w/w), core (42 – 54%, w/w), and pulp (21 – 33%, w/w) [242] and constitutes over 35% of the total weight of processed olives [243]. The general composition of OP is similar, depending on the olive cultivar, culture conditions or production process [205]. It is primarily composed of cellulose, hemicellulose, lignin, proteins, phenolic compounds (*p*-coumaric acid, tyrosol, hydroxytyrosol) (Fig. 2.10c), sugars, lipids, and mineral salts (potassium, calcium, and sodium), and has an acidic pH. As a result of the large number of phenolic compounds in its composition, OP has antioxidant activity and antimicrobial properties. The phenol content is typically higher when OP is obtained by a two-phase centrifugation process [205].

### 2.3.4. BNC composites as implants

Biocompatibility may be briefly summarized as the impact of a medical application on the host. If it triggers an adequate or beneficial response by the host, it is considered as biocompatible. However, if it cascades into an ominous reaction, such as necrotic foreign body granulomas, the application or material is classified as non-biocompatible [244]. Therefore, relevant biocompatibility properties include the assessment of the cytotoxicity of the novel applications developed *in vitro*, prior to experiment *in vivo*. Cytotoxicity may simplistically be regarded as how the materials will

impact the living cells in terms of viability, proliferation, metabolism, adhesion, morphology, expression of key metabolites or signals, among others. If the material has a clear negative impact on one or several of these parameters, it will be classified as cytotoxic [245]. The established threshold for acceptable loss of viability is 30% [246]. If a material is considered cytotoxic, then it will most likely fail to exert an adequate or beneficial host response, thus failing to be biocompatible. If the material is considered as non-cytotoxic it will possess a higher probability to trigger a suitable response by the host. However, a non-cytotoxic material may still fail to be biocompatible. In addition, hemocompatibility is a key parameter for medical applications. Hemocompatibility of a material is defined by its propensity to lyse erythrocytes, as well as by its level of adsorption of coagulating agents and other signalling molecules that interact with the complement activation pathway [247].

Non-toxicity, biocompatibility, mechanical, and physical requirements are mandatory when classifying a biomaterial as ideal. It is hypothesized that the similarity of BNC with ECM prevents immunological reactions and inhibits chronic inflammatory response. Their degradation within the human body may or may not be desirable, depending on the proposed application [248, 249]. BNC is highly biocompatible and has been tested in animals and humans as long-term implants for up to one year. Furthermore, the literature supports this statement through tests performed with BNC-based implants that showed no severe signs of inflammation, no formation of fibrotic capsule, nor did it present toxicity according to genetic and cellular assays [250]. This proves that BNC can be an excellent material for wound dressing, hard and soft tissue engineering (*e.g.* skin regeneration, artificial dura mater membrane, facial nerve regeneration, prosthetic hernioplasty, cancer diagnosis, drug delivery, tissue-engineered cornea stroma, and neuroendovascular applications) [249].

Relating to its *in vivo* degradation, that is, degradation under physiological conditions, BNC is known to be principally degraded by cellulase, an enzyme that is not produced by the human body. So, in principle, this is beneficial for long-term implants. But it also limits its applications, for instance, to achieve a drug delivery system, BNC should be degraded within a short period [249, 250]. Factors affecting biodegradation are the mechanical stress of bodily movements or inflammatory cellular response, that contribute to changes in crystallinity and molecular weight. In addition, several other mechanisms that contribute to BNC degradation have been identified: hydrolysis, enzymatic degradation, oxidation, and physical degradation. The chemical structure of BNC is composed of linear glucose units, each with one primary –OH group and two secondary –OH groups. These

acting sites form glycosides that can be chemically attacked by body fluids constituents forming oligomers, and consequently monomers. During hydrolysis, the biomaterial absorbs the body fluids, leading to swelling and degradation. Enzymatic degradation occurs due to the presence of endogenous hydrolase enzymes present in plasma and interstitium that accelerate the hydrolysis of the glycosidic linkages. Oxidative degradation occurs as a result of hydrogen removal from the polymer chains by oxidants produced by tissues. Physical and chemical scission of bonds in the polymer chain can be due to swelling and wearing, which accelerate the damaging of the amorphous region by environmental stress [249].

If desired, a biomaterial can be tailored to become biodegradable through modification with bioactive molecules [249]. Considering the fibrous nanosized 3D network, high –OH content, and water retention capacity, it is expected that BNC can retain considerable concentrations of drugs, either small (*e.g.*, diclofenac, octenidine, and lidocaine) or large molecules (polymeric drugs, peptides, or proteins) relevant for drug delivery [250].

Bioactive agents promote tissue growth by interacting with and integrating into damaged tissue, thus exhibiting biological activity. Their incorporation within BNC, such as natural polymers (*e.g.*, proteins: collagen, silk, gelatine, and fibrin; polysaccharides: starch, chitosan, cellulose, and alginate; polynucleotides: DNA, RNA) and inorganic compounds (*e.g.*, metal nanoparticles: Cu, Ag, Ti, and Au; minerals: hydroxyapatite, calcium phosphate, and silica (Si)) instil very desirable properties to the polymeric scaffold. These may include structural, regenerative, and/or antimicrobial properties [251, 252]. Biopolymers, for example PLA or PGA, are found in implant and suture [248]. A more thorough description and examples of the applicability of such bioactive molecules within the BNC matrix are described below. BNC can be applied in the replacement of synthetic soft implants, namely, cardiovascular systems (*e.g.*, artificial blood vessels and heart valve replacement), nervous system (*e.g.*, nerve scaffold and dura mater replacement), ophthalmic applications (*e.g.*, artificial cornea and contact lenses), urinary conduits, and skeletal system (*e.g.*, cartilage regeneration, meniscus implant, artificial ligament/tendon, tympanic membranes, and vocal cords) [253-255].

A magnetic field gradient can potentially target magnetic nanoparticles-loaded cells locally to the BNC surface and be a retention platform to increase cell homing at damaged vasculature. The incorporation of magnetite ($Fe_3O_4$) within BNC was possible through *in situ* precipitation of $Fe^{3+}$ and $Fe^{2+}$. To avoid oxidation, dextran was used to protect the iron oxide nanoparticles and improve cytocompatibility. BNC membranes were modified using PEG-coated iron oxide nanoparticles with

grafted Arginil-Glycyl-Aspartic peptide used as cell anchors. Seeded murine endothelial cells were subjected to a magnetic field and adhesion and growth of endothelial cells showed to be significantly oscillation frequency dependent, with cell growth promotion under lower frequency, leading to successful endothelialization on the modified BNC membranes. Superparamagnetic iron oxide nanoparticles (SPIONs) are a good example since their applicability in biomedicine includes: drug delivery, making use of their targeting through an external magnetic field [256], contrast agents for magnetic resonance imaging to enhance the visibility of specific tissues [257], and hyperthermia therapy due to the ability of SPIONs to generate heat when exposed to an alternating magnetic field [258]. The incorporation of these nanoparticles within BNC to be potentially used as actuators was reported by Roig-Sanchez and co-workers (2021), who tested a static and agitated culture of BNC in the presence of SPIONs. Magnetic actuation is conferred by SPIONs. The combination of platinum (Pt) nanoparticles or Au nanoparticles with SPIONs allows the controlled motion of the hydrogels by a magnetic field and an $H_2O_2$ oxidation reaction. These Janus Pt/SPIONs structures increased by five times the directionality and movement [209].

Loss of function of articulation and muscles due to cartilage damage constitutes a problem. Such injuries are frequent in the aging population and athletes. The human body's capacity for self-regeneration faces limitations due to the restricted proliferation of chondrocytes, the absence of blood vessels and nerves, and the relatively low metabolic rate [255, 259]. The predominant treatment method involves autografting chondrocytes, specialized cells that stimulate the generation of new cartilage tissue. Nonetheless, the demand for dual surgeries and an extended recovery period has prompted exploring a biomaterial-based approach to cartilage transplantation [255]. Implants require high porosity to support chondrocyte migration and ECM production. However, BNC presents different sizes and interconnectivity that may inhibit chondrocyte proliferation [260]. Numerous approaches have been developed to adjust pore size, similar to the ECM dimensions (ranging from 100 to 500 µm) [261]. These methodologies include laser drilling, photoreticulation, freeze-drying, and incorporating nanoparticles/microparticles during synthesis [262-264]. Photoreticulation of a BNC/methacrylate gelatine hydrogel decreased the pore size from 200 to 10 µm, attributed to hydrogen bonding. Notwithstanding the reduced pore size, chondrocyte growth and proliferation were successful [265]. To increase the number of pores in BNC, freeze-drying becomes a practical and cost-effective method to achieve this attribute. Li *et al.* (2017) developed a BNC-chitosan composite (1 wt%). The combination of the freeze-drying process and the viscosity enhancement, resulting from the presence of chitosan, contributed to a

substantial 50% increase in pore size [266]. Healthy cartilage has a high-water content of about 80%, so the replacement implant must maintain this property [267]. BNC exhibits a notable inert water retention capacity, rendering it suitable for cartilage replacement applications. Incorporating BNC into cartilage implants must facilitate the progression of new tissue development, a phenomenon referred to as chondrogenesis [268]. Furthermore, BNC hydrogels were modified with alginate and/or hyaluronic acid to achieve this property. The composite BNC/chitosan/alginate/gelatine (80:20%, w/w) was evaluated, promoting cell adhesion, proliferation, and cell differentiation of chondrocytes [269]. The production of 3D-printable BNC and gelatine methacryloyl hydrogels, enhanced mechanical properties. After 24 weeks of *in vivo* implantation, the ear cartilage implant exhibited Young's modulus (1.33 ± 0.13 MPa) similar to the modulus of elasticity of human ear cartilage (1.41 ± 0.67 MPa). Cell viability displayed promising results, with values exceeding 97% following a 7-day testing [270]. The *in situ* polymerization modification with an additional organic compound, PGA, resulted in a biomaterial that exhibited improved mechanical properties. This modification enhanced bond interactions, amplifying elastic recovery after compression, fracture strength, and tenacity. The composite shows promising properties in cartilage application, including excellent cell viability [271]. Moreover, the application of natural proteins was also analysed for mechanical improvement. The integration of SF into BNC, followed by the freeze-drying procedure, revealed an enhancement in compressive strength and deformation. This improvement can be attributed to the crosslinking interaction between BNC and SF [272]. All the exemplified examples indicate that utilizing these organic materials did not compromise the non-cytotoxicity of the final composites. The high viability can be attributed to the similarity of BNC to the ECM of hyaline cartilage [261].

Severe cardiovascular conditions require a vascular transplant to replace obstructed pathways. These replacements may involve applying alternative body tissues (from oneself or a donor) or using artificial vascular grafts (*e.g.*, blood vessels or cardiac valves) [273]. Surgically, synthetic materials are employed to replace large-diameter blood vessels (ranging from 6 to 10 mm in diameter), commonly utilizing PTFE and e-PTFE. Nevertheless, these materials are inadequate for replacing small-diameter vessels (with diameters less than 6 mm) due to their susceptibility to clotting and restenosis. This inherent limitation constitutes the main obstacle preventing commercially accessible prostheses designed for this type of vessel [274]. BNC hemocompatibility makes it a promising choice for adequately replacing both types of implants [275]. BASYC® (BActerial SYnthesized Cellulose) is a commercially available BNC-based product that replaces

artificial blood vessels. It features a tubular configuration and mechanical properties resembling natural blood vessels [276]. Applying this biomaterial as a cardiovascular tube necessitates the preservation of blood vessel characteristics, including internal roughness and pressure resistance [110]. Furthermore, issues related to limited elasticity and anti-thrombogenic properties must be addressed to establish BNC as a viable product. For this purpose, a crucial modification is required [273]. PVA-modified BNC were developed for application in artificial blood vessels. The D-BNC tube possesses a bigger external diameter and more homogeneous character along the diametric direction and the S-BNC tube possesses denser nano-cellulose close to the inner wall. The hydrogen bonds are notably reduced within the BNC matrix increasing the elasticity/stretch at break. Higher Young's modulus, tensile strength, and elongation at break are verified for the D-BNC tube as a result of the thicker fibres and a denser nano-fibre network. Permeability attainment was also successful, as no water leakage was detected, and there was an enhancement in burst pressure without any cytotoxic effects [277]. Moreover, ensuring the migration and proliferation of endothelial cells on the implant surface holds extreme importance in achieving biocompatibility. The BNC/chitosan/heparin composites significantly facilitated the adhesion and growth of human saphenous vein endothelial cells and endothelial progenitor cells (EPC). Conversely, the BNC/heparin composite exclusively exhibited these effects in the second cell type, EPC. Both variants hold promise for application in small-diameter vascular grafts, effectively minimizing the potential for thrombogenicity and augmenting biocompatibility [278]. In addition, a chemical crosslinking process was employed to incorporate heparin into BNC, functionalised with SF nanoparticles. The proliferation of endothelial cells, rapid endothelialization, minimal presence of inflammatory cells, and absence of degradability for 4 weeks were observed [279]. Incorporating 1% (w/v) fish gelatine resulted in rapid endothelialization, with hemolysis rates remaining below 1% (demonstrating hemocompatibility) and an enhanced level of biocompatibility [280].

Replacing blood vessels or vascular grafts smaller than 6 mm in diameter comprises challenges. However, several multifunctional BNC composites exhibit promising properties. BNC/chitosan composites demonstrated no allergic reactions and effectively suppressed inflammatory responses or excessive growth of regenerated muscle tissue. This fulfils the criteria for biocompatibility and non-cytotoxicity [281]. *In vivo* blood vessel regeneration was swiftly accomplished through *in situ* modification of BNC with potato starch. Potato starch particles at higher concentrations (2%, w/v) expanded during the fermentation process, resulting in an increase in pore size (~28 ± 6 μm) [282].

Corneal dysfunction culminates in vision loss, prompting the adoption of an artificial cornea as the optimal treatment approach. The demand for synthetic alternatives arises from donor scarcity. This transplantation technique demonstrates heightened efficacy owing to its non-vascular nature [283]. The artificial cornea should satisfy the following pre-requisites: biocompatibility, mechanical stability, comfort, rigid structure, transparency, and the ability to enhance cell adhesion and proliferation [284]. In this context, hyaluronic acid can be applied in corneal implants. Anisotropic properties and high transparency (40% higher than BNC) were achieved due to the incorporation of this agent. The chemically crosslinked BNC/hyaluronic acid composite demonstrated considerable cytocompatibility towards corneal stromal cells and suture strength comparable to the human eye [285]. The integration of this composite into BNC, without requiring a crosslinking agent, displayed several encouraging attributes. Mechanical properties and elasticity, high porosity, and excellent transmittance are some of the characteristics of the composite [286]. Beyond hyaluronic acid, incorporating PVA improves the optical properties through the expansion of interstitial spaces of BNC, promoting increased light transmission. Moreover, this inclusion supports the diffusion of oxygen and essential nutrients crucial for cellular growth while demonstrating minimal immunogenicity [287]. Therefore, the excellent ability to promote light transmission, high water content combined with UV protection establishes PVA as a viable option to replace non-biocompatible polymethyl methacrylate in corneal implants and contact lenses [110].

PP-based implants are applied surgically for the treatment of hernias. Nonetheless, a reduction in physicochemical properties, accelerated degradation in the human body, and its non-inert nature that fosters infections and inflammation decrease the efficacy of employing these synthetic polymers [288]. To mitigate associated biological risks, a novel biomaterial, BNC, was combined with chitosan and applied to a PP mesh. After 3 months of implantation, the composite favoured tissue remodelling and demonstrated a distinct absence of cytotoxicity. Unlike PP-based hernia meshes, this includes minimal irritation and no allergic reactions [289]. In addition to treating hernias, BNC can serve as a substitute for a perforated tympanic membrane because of its flexibility, biocompatibility, and transparency. However, no modification of BNC was identified for this specific application. PVA emerges as a plausible choice for modification to enhance light transmission [290].

Different alternatives have been explored to promote the regeneration of urological tissues, such as the case of urinary conduits - a critical component in managing bladder cancer treatment [290].

Keratocytes were cultured on a BNC/SF bi-layer scaffold. SF encouraged cell proliferation and migration, while BNC supported preserving epithelial cells, which play a crucial role in urethral reconstruction [291].

Repairing nerve injuries is a complex and crucial process characterized by the challenges of limited regenerative potential. An up-and-coming solution lies in applying neural implants, particularly highlighted by the BNC favourable compatibility with Schwann cells [292]. In addition to biological properties, nerve regeneration implants need effective electrical conductivity to facilitate nerve impulses. Thus, Wu *et al.* (2021) developed a 3D bioprinting scaffolds of BNC (0.3%)/alginate (5%)/gelatine methacrylate (5%) loaded with rat Schwann cell line (RSC96) that showed a good electrical conductivity ($6 \times 10^{-7}$ $S \cdot m^{-1}$). The effect of introducing RSC96 cells on neural regeneration was assessed, confirming the expression of numerous mRNA genes associated with axon growth, proliferation regulation, migration control, Schwann cell maturation, and myelination. Following 21 days of *in vivo* implantation, no indications of inflammation or toxicity were observed [293]. From a different perspective, rat sciatic nerve regeneration was assessed using an oxidized BNC composite functionalised with chitosan nanoparticles *(in situ)* containing nerve growth factors. The microporous composite exhibited a notable reduction of microbial proliferation, while the oxidation of BNC improved its biodegradability. Schwann cell adhesion and proliferation demonstrated similar results to commercial grafts, and nerve growth factors were responsible for evident nerve repair (10 mm in 4 weeks) [294]. The electrical signal between cells plays an important part in tissue regeneration. As a conductive material, nerve conduits are able to transmit electrical signals between cells in electroactive tissue, thus allowing nerve repair through the promotion of Schwann cells adhesion and proliferation to construct the connected belt when the Wallerian degeneration occurs. In peripheral nerve injury, this is especially important since it allows the bridge between the two ends of damaged nerves. Poly(3,4-ethylenedioxythiophene), a conductive polymer known as PEDOT, and that has gained a significant interest in tissue engineering due to its biocompatibility and electrical properties, has been used in combination with sulfonated nanofibres and BNC to create a transparent conductive membrane. This composite showed great biocompatibility, high conductivity, and appropriate mechanical strength to be used for peripheral nerve repair, according to *in vivo* tests on Sprague Dawley rats [295].

Overall, composites based on BNC modified with organic compounds present promising physicochemical and biological properties for replacing synthetic soft implants.

### 2.3.5. BNC mesh composites

In soft tissue repair materials, it is important to have implants with anti-adhesive characteristics to minimize complications caused by intraperitoneal adhesions. Anton-Sales *et al.* developed an anti-adherent reinforcement material to support hernia soft tissues by combining BNC with standard PP meshes. First, the authors confirmed the suitability of double layer BNC for abdominal wall reinforcement regarding mechanical properties (tear strength > 16 $N \cdot cm^{-1}$). Then, a hybrid material was developed by integrating PP meshes between the BNC layers and the anti-adhesion properties of BNC with an in vivo rabbit model following the implantation process were evaluated. The results showed a general good integration to the abdominal wall. Histological analysis showed an inflammatory response at the peri-implanted area presenting fibroplasia and infiltration of diverse cell types, such as macrophages, lymphocytes, and heterophilic granulocytes, among others. Nevertheless, the anti-adherent properties were clearly proved, underscoring its applicability in hernia repair solutions. The only identified issue was its sub-optimal mechanical behaviour, that may be surpassed by stacking dried BNC membranes or by the development of novel composites [102]. A similar approach was performed by Ludwicka *et al.* The obtained PP mesh coated with never-dried BNC did not negatively influence the mechanical properties of the commercial PP mesh, and it was envisioned less immunogenic reaction towards the composite by lowering mast cells adhesion and degranulation. PP mesh, pristine never-dried and the composite exhibited significantly less rat basophilic leukaemia mast cells (RBL-2H3) cell adhesion in comparison to TCP (roughly 3-fold less). Regarding mastocytes degranulation level (percentage of N-acetyl-β-d-hexosaminidase (HEX)), it was reduced from approximately 32% in PP mesh to 19% in the PP coated with BNC composite. However, the degranulation in pristine BNC was slightly lower [296]. Therefore, it is clear the role of BNC in suppressing mast cell degranulation. Mast cells are present in all smooth muscles, therefore they will be in contact with all indwelling devices. Mast cells degranulate once they are activated, releasing a plethora of inflammatory mediators present in them up to 200 granules per cell. These mediators are able to promptly unfold into a violent immunologic response [297]. In the study carried out by Zharikov et al. never-dried BNC membranes were implanted in the abdominal wall of dogs to study its efficiency in hernia repair. The anti-adhesive behaviour of BNC was compared with a commercial PP mesh. After 14 days of implantation, it was observed a capsule of loose connective tissue around the BNC, exhibiting good fixation to the anterior abdominal wall, and negligible adhesions between the BNC membrane and the underlying tissues. However, some moderate inflammatory infiltration was occurring due to

accumulation of cell elements at the interface of BNC and the abdominal wall tissues. After two months, the host formed novel and stable connective tissue and angiogenesis was observed. Furthermore, negligible intraperitoneal adhesions between the intestinal loops and the BNC membrane were detected. Within this period, the commercial PP mesh-based grafts where coarser and scar structures were observed, denoting the superior biocompatibility of BNC [298]. To reduce adhesion of intraperitoneal meshes, Guo *et. al.* prepared a PP-based mesh coated with a combination of BNC and chitosan for abdominal incisional hernia. This composite exhibited lower adhesion grades and inflammatory response compared to the control, with good strength and biocompatibility [299]. Cui *et al.* were able to reduce adhesion using an all-BNC double layer mesh of a nanoporous and a microporous BNC layer. The nanoporous layer possesses the anti-adhesive properties, whilst the microporous layer demonstrated tissue integration. The mechanical properties met the requirements for external abdominal hernia repair. Some of the recent biomedical applications using BNC meshes are present in Table 2.9.

**Table 2.9.** BNC based meshes

| Bacterium strain | Composite | Adequacy | Assays | Cells/Animal | Application | Reference |
|---|---|---|---|---|---|---|
| N.d. | PP/BNC/chitosan | In vivo | Histological and visual analysis | Sprague Dawley rats | Abdominal incisional area | [299] |
| *Komagataeibacter xylinus X-2* | BNC | In vitro | Cytocompatibility, cell proliferation and visual analysis | NIH3T3 cell line | Hernia repair | [300] |
| *Komagataeibacter xylinus* (NCIMB 5346) | BNC/PP | In vivo | Histological and visual analysis | n.d. | Abdominal wall reinforcement | [102] |
| *Medusomyces gisevii* Sa-12 symbiotico- culture | None | In vivo | Histological and visual analysis | n.d. | Abdominal wall reinforcement | [298] |
| *Komagataeibacter xylinus* (E25) | BNC/PP mesh | In vitro | Cell adhesion (PrestoBlue assay) and degranulation (HEX release) | Rat RBL-2H3 basophilic leukemia mast cells | Reconstructive surgery (e.g., hernioplasty) | [296] |

n.d. – not defined

# Chapter 3

## Functionalisation with organic agents[2]

[2] This chapter is based on the following publications:

Peer-reviewed articles:

Melro, L.; Alves, C.; Fernandes, M.; Fernandes, R. D. V.; Pereira, A.; Moldes, D.; Rodrigues, A. C.; Sencadas, V.; Mitu, B.; Satulu, V.; Lourenço, J.; Pace, G.; Martins, L.A.; Gómez Ribelles, J. L.; Salgado, A. J.; Padrão, J.; and Zille, A. "Bacterial Cellulose and Phenolic Compounds Composites for Medical Implants". Under review in Composites Part A.

# 3. Functionalisation with organic agents

## 3.1. Introduction

This chapter describes the two methodologies used to functionalise BNC with organic active agents, filtration and exhaustion. The resulting composites were characterised through thermal analysis, morphology, surface chemistry, antimicrobial and antioxidant activity.

To determine the most effective and suitable approach for achieving an efficient internalization of the organic active agents Kraft lignin (KL) and olive pomace (OP), two different strategies were adopted. The membranes were functionalised through *ex situ* methodologies filtration and exhaustion. The *in situ* method was not feasible as the KL isolation takes several different steps that include very acidic solvents, and OP is the direct grinding of the olive's kernel. Organic active agents KL (2 wt%) and OP (1 wt%) were incorporated into bacterial nanocellulose (BNC), in separate and together, to endow it with properties that are not intrinsic to the native biopolymer, namely antioxidant, antifungal, and antibacterial properties [235, 236]. Considering the difficult solubility in water of OP and of KL in particular, different solubilisation media were tested, prior to functionalisation, distilled water ($dH_2O$), NaOH (0.1 M), and buffers phosphate-buffered saline (PBS) and Britton-Robinson (BR). In the present work, KL and OP modified BNC composites were analysed to assess their potential as antimicrobial implants, and characterised accordingly for antimicrobial activity, swelling capacity, active agent release, chemical and physical characteristics, and thermal stability.

## 3.2. Materials

Cultures of *Komagataeibacter hansenii* (ATCC 53582 from Merck Life Science – Algés, Portugal) occurred in Hestrin-Schramm culture medium. The preparation included 20 $g{\cdot}L^{-1}$ glucose (Carlo Erba – Barcelona, Spain), 5 $g{\cdot}L^{-1}$ peptone (Himedia – Mumbai, India), 5 $g{\cdot}L^{-1}$ yeast extract (Merck Life Science – Algés, Portugal), 2.5 $g{\cdot}L^{-1}$ magnesium sulphate (Panreac AppliChem – Barcelona, Spain), 2.7 $g{\cdot}L^{-1}$ sodium phosphate anhydrous (Panreac AppliChem – Barcelona, Spain), and 1.15 $g{\cdot}L^{-1}$ citric acid monohydrate (Merck Life Science – Algés, Portugal).

The bacteria tested for the antimicrobial activity assays were *Staphylococcus aureus* (ATCC 6538) and *Pseudomonas aeruginosa* (ATCC 27853), fungi *Candida albicans* (ATCC 10231) and *Candida krusei* (ATCC 2159), and bacteriophages *Escherichia coli* (bacteriophage host) (ATCC 15597) and bacteriophage *Escherichia coli* MS2 (ATCC 15597-B1) were supplied from ATCC (Virginia, USA). Trypticase soy broth (TSB) and nutrient broth (NB) media were purchased from Merck Life Science,

Algés, Portugal. Agar was acquired from Liofilchem (Italy). All the media were prepared in $dH_2O$ and autoclaved at 121 °C for 20 min. #271 medium consisted in 10 $g \cdot L^{-1}$ tryptone (Panreac AppliChem – Barcelona), 1 $g \cdot L^{-1}$ yeast extract, 8 $g \cdot L^{-1}$ NaCl, 1 $g \cdot L^{-1}$ glucose, 0.294 $g \cdot L^{-1}$, calcium chloride ($CaCl_2$, AnalytiChem Belgium NV – Zedelgem, Belgium), and 10 $mg \cdot L^{-1}$ thiamine (Merck Life Science – Algés, Portugal).

Simulated body fluid (SBF) was prepared using 7.996 $g \cdot L^{-1}$ NaCl, 0.350 $g \cdot L^{-1}$ sodium bicarbonate ($NaHCO_3$, Merck Life Science – Algés, Portugal), 0.224 $g \cdot L^{-1}$ potassium chloride (KCl, Merck Life Science – Algés, Portugal), 0.228 $g \cdot L^{-1}$ potassium phosphate dibasic trihydrate ($K_2HPO_4.3H_2O$, Merck Life Science, Algés, Portugal), 0.305 $g \cdot L^{-1}$ magnesium chloride hexahydrate ($MgCl_2.6H_2O$, AnalytiChem Belgium NV – Zedelgem, Belgium), 4% (v/v) hydrochloric acid (HCl 1 M, Thermo Fisher Scientific Inc. – Massachusetts, USA), 0.278 $g \cdot L^{-1}$ $CaCl_2$, 0.071 $g \cdot L^{-1}$ sodium sulphate ($Na_2SO_4$, Panreac AppliChem – Barcelona, Spain), and 6.057 $g \cdot L^{-1}$ tris(hydroxymethyl)aminomethane ($(CH_2OH)_3CNH_2$, Thermo Fisher Scientific Inc. – Massachusetts, USA). The pH was adjusted to 7.4 using a 1 M solution of HCl.

Phosphate buffered saline (PBS) was prepared using 8.0 $g \cdot L^{-1}$ NaCl, 0.20 $g \cdot L^{-1}$ KCl, 1.44 $g \cdot L^{-1}$ disodium phosphate ($Na_2HPO_4$, anhydrous, AnalytiChem Belgium NV – Zedelgem, Belgium) and 0.24 $g \cdot L^{-1}$ monopotassium phosphate ($KH_2PO_4$, Panreac AppliedChem – Barcelona, Spain). The final pH was 7.4.

Britton-Robinson buffer was prepared through the dissolution in $dH_2O$ 2.75 $g \cdot L^{-1}$ of NaOH, 1.58 $g \cdot L^{-1}$ acetic acid ($CH_3COOH$), 2.57 $g \cdot L^{-1}$ orthophosphoric acid ($H_3PO_4$), and 1.62 $g \cdot L^{-1}$ boric acid ($H_3BO_3$), all purchased at Merck Life Science – Algés, Portugal. The final pH was 7.0.

For the antioxidant tests, 2,2-diphenyl-1-picrylhydrazyl (DPPH) was purchased by Alfa Aeser Gmbh (Massachusetts, USA) and ascorbic acid was obtained from VWR Chemicals BDH (Carnaxide, Portugal).

## 3.3. Methods

### 3.3.1. BNC processing

BNC production occurred under static culture conditions at 28 – 30 °C for approximately one week (Fig. 3.1) [301]. After this period, the *K. hansenii* cells were disrupted by sterilization using an autoclave (121 °C, 20 min). Purification procedures of the BNC membranes were performed by rinsing with $dH_2O$ followed by submersion in 1 M NaOH for 24 h. This procedure allows the

remotion of medium residues and cellular debris. Finally, the BNC membranes were abundantly rinsed with $dH_2O$ until the pH equalised with $dH_2O$. The never-dried BNC membranes were cut into 1 mm thick films, autoclaved in $dH_2O$ and stored in aseptic conditions until further use [13].



**Figure 3.1.** Cultivation of *K. hansenii* in Hestrin-Schramm culture medium.

### 3.3.2. Organic active agents

According to the procedure described in [302], the KL powder, kindly supplied by Ence (Pontevedra, Spain), was obtained from black liquor from the Kraft cooking of Eucalyptus globulus. The acidic precipitation of the black liquor was performed by using 4 M sulfuric acid until pH reduction to 2.5. Following 2 h under stirring at 50 °C, the precipitate was recovered through centrifugation. The isolated lignin was washed twice with acidified water at pH 2.5. To obtain the powder, the lignin was oven dried overnight at 60 °C, finally milled with a mortar and pestle and stored for UV protection. OP was collected from the Valpaços Oleiculture Cooperative winery in December 2021 and transported in a closed plastic container for approximately 42 h. Once in the laboratory, dehydration at 60 °C for 24 h followed. The moist OP was transformed into powder using an IKA® A10 basic mill equipped with an A 10.1 stainless steel cutter. The OP was then stored at −18 °C to ensure its conservation before use. To assess the solubility of KL and OP, different media/solvents were used, namely water, 0.1 M NaOH, PBS (pH 7.4), and BR (pH 7.0). Functionalisation was performed using separate formulations of 2 wt% KL, 1 wt% OP, and a combination of 2 wt% KL with 1 wt% OP at 37 °C and remained under stirring (200 revolutions per minute (rpm)) overnight. The visual analysis of the dispersions was possible through an optical microscope DM IL LED Fluo (Leica Microsystems, Carnaxide, Portugal) with a magnification of 100×. In addition, the selection of the best suiting media/solvent was also carried out by functionalising the 1 mm films through an exhaustion process. For this purpose, Ibelus C-720

(Pregitzer & Ca. Lda., Guimarães, Portugal) equipped with an infrared heating system with rotation at 50 rpm over 50 cycles, and temperature gradient of 2 °C·min$^{-1}$ was used with different formulations, at 37 °C to simulate the human body temperature, for approximately 16 h.

### 3.3.3. Functionalisation methodologies

Membranes were functionalised through *ex situ* methodologies filtration and exhaustion. To enhance the functionalisation process, membranes with 1 mm thicknesses were previously pressed at 5 kN for 30 seconds to remove residual water, before being placed in contact with the agent's dispersions. A ratio of BNC area/bioagent dispersion of 0.04 m$^2$·L$^{-1}$ for BNC/KL, BNC/OP, and BNC/KL/OP was used. After functionalisation, the KL, OP, and KL/OP functionalised BNC composites were rinsed three times with 100 mL of PBS under constant agitation for 1 minute to remove excess of the active agent from the BNC surface. The samples were then sterilised at (121 °C, 20 min) and stored until further use.

***Ex situ***

Vacuum filtration

For the filtration method a vacuum pump was used, with the BNC replacing the traditional paper filter. A volume of 30 mL of the bioactive agent are retained in the membrane through vacuum at 1 bar (Fig. 3.2). The never-dried membrane was placed inside the Büchner funnel, completely covering the available flat area.

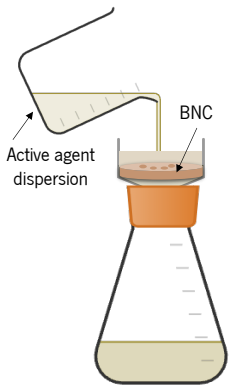



**Figure 3.2.** Schematic representation of BNC functionalisation through vacuum filtration.

Exhaustion

Organic and inorganic active agents were previously prepared before placing the BNC membranes inside the containers from the Ibelus C-720 dyeing equipment (Pregitzer Lda., Guimarães, Portugal) (Fig. 3.3). KL at 2 wt%, OP at 1 wt%, and a mixture of KL/OP (2:1 wt%) were suspended

in PBS solutions (200 mL). The BNC samples were left overnight (37 °C, 2 °C·min$^{-1}$, 50 rpm, cycles of 50 seconds).

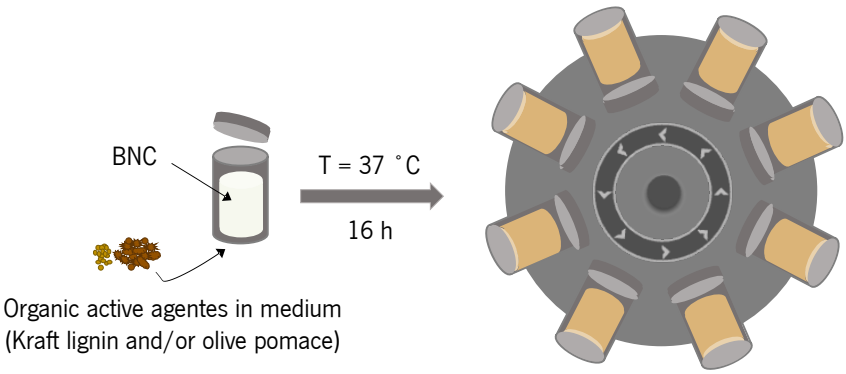



**Figure 3.3.** Schematic representation of BNC functionalisation through exhaustion using an Ibelus machine.

## 3.4. Characterisation

### 3.4.1. Size and morphology of KL and BNC composites

The KL and OP dispersions were examined using a scanning transmitted electron microscopy detector (STEM) with an ultra-high resolution field emission gun (FEI NOVA 200 Nano SEM), with an accelerating voltage of 15 kV (1.0 nm resolution). Dispersions were placed on Cu-C TEM grids (S160-4 AGAR). Regarding BNC composites, 1 × 1 cm samples with 3 mm of thickness were cut in liquid nitrogen and fixed with double-sided carbon tape on an aluminium metal support. Subsequently, the samples were covered, using a sputtering technique, with a 35 nm thick Au-Pd film (80/20%, w/w) using a high-resolution sputter coater (208HR Cressington Company, UK) and monitored by a high-resolution thickness controller (MTM-20, Cressington, UK).

Untreated BNC samples were prepared in a Quorum PP3010T (Quorum Technologies, England) cryofracture module before visualisation by Cryo-field emission scanning electron microscopy (Cryo-FESEM, Thermo Scientific SCIOS 2 FIB-SEM). Samples were attached to a specific support and fixed with a mix of Tissue-TEK O.C.T. and colloidal graphite to enhance electrical conductivity and improve imaging. Once prepared, the support was immersed in slush nitrogen to freeze the sample and immediately inserted into the cryofracture module. The sample was then fractured horizontally, sublimated for 15 minutes at –90 °C, and sputter-coated with platinum at 5 mA for 20 seconds. The sample was then ready to be inserted into the FESEM chamber to be visualised. Composite visualisation took place in a Carl Zeiss Ultra 55 (Carl Zeiss, Germany) field-emission

scanning electron microscope using the secondary electrons detector set at 1.5 kV. Ultra-high-resolution field emission gun – scanning electron microscope (FEG–SEM) (Field Electron and Ion Company, Hillsboro, Oregon) with an accelerating voltage of 10 kV, using both a secondary Everhardt-Thornley detector and at through lens detector in secondary electrons mode and under high vacuum conditions, were used to obtain the images of the samples.

### 3.4.2. Crystalline structure

The crystalline structure and phase purity of BNC were evaluated through X-ray diffraction (XRD) analysis on a 2×2 $cm^2$ freeze-dried BNC sample of 1 mm thickness. Samples were positioned on the diffractometer D8 Discover (Bruker, Karlsruhe) equipped with a CuK$\alpha$ source emitting radiation at $\lambda$ = 0.15406 nm. Diffraction spectra were acquired in the range of 2$\theta$ range between 10 to 30° with step size of 0.04° and a scanning speed of 1°·$min^{-1}$. The analysis was restricted to the 2$\theta$ = 14.8° (1 – 10), 2$\theta$ = 16.8° (110) and 2$\theta$ = 22.8° (200). The crystallinity index (CI) was determined using the Segal method [105] (Eq. 3.1), where $I_{200}$ represents the maximum intensity of the crystalline peak at 2$\theta \approx$ 22.8° and $I_{am}$ denotes the intensity of the amorphous region at 2$\theta \approx$ 18.2°.

$$CI(\%) = \frac{I_{200} - I_{am}}{I_{200}} \times 100 \qquad \text{(Equation 3.1)}$$

### 3.4.3. Pore size

The pore size of freeze-dried BNC was measured in 3 mm thickness samples instead of 1 mm due to lower associated error. Pore size was determined through capillary flow porometry using a Quantachrome 3Gwin-Pore Size porosimeter (Anton Paar, Graz, Austria) through bubble point analysis, following the American Society for Testing and Materials (ASTM) F316-03 standard (cylindrical model). Specimens with a diameter of 16 mm were evaluated, applying shape and size factors of 1.00 and 0.64, respectively, along with a pore tortuosity factor of 1.00. Prior to the measurements, BNC composites were immersed in a fluid of 1850 kg·$m^{-3}$ density at 23 °C, a surface tension of 16 dyn·$cm^{-1}$, and a zero-contact angle. Subsequently, the samples were inserted in the measurement chamber and securely sealed. A controlled pressure range of 2 to 14 bar was applied. The pore size was determined using the Porometer 3G series software based on the

Washburn Equation (Eq. 3.2), where P represents the pressure, $\gamma$ is the liquid's surface tension, and $\theta$ is the contact angle.

$$\text{Pore size} = \frac{4\,\gamma \cos\theta}{P} \qquad \text{(Equation 3.2)}$$

### 3.4.4. Surface area and adsorption isotherms

$N_2$ adsorption-desorption studies were performed with a specific surface area analyser (Gemini V-2380, Micromeritics Instrument Corporation), with nitrogen as the adsorbate gas at 77 K. Before conducting the analysis, the samples were degassed at 393 K under reduced pressure for 12 h. The specific surface area was obtained based on Brunauer, Emmett, Teller (BET) theory, from the linear region of the adsorption isotherm ($0.05<P/P_0<0.3$).

### 3.4.5. Chemical structure

The chemical composition of KL, OP and the BNC composites was obtained using a Shimadzu IRAffinity-1S Fourier transform infrared spectrophotometer (Shimadzu Corporation, Switzerland) equipped with a HATR 10 accessory with the horizontal attenuated total reflectance accessory and a diamond crystal (ATR-FTIR). KL at 2 wt% and OP at 1 wt% were previously dispersed in PBS overnight at 37 °C and dried in the oven at 40 °C for several days. The BNC composites (3 mm) were freeze-dried before characterisation. The samples were placed onto the crystal using air at 20 °C as background. All spectra were obtained by performing 45 scans at a spectral resolution of 8 $cm^{-1}$, over a 4000 – 400 $cm^{-1}$ range.

### 3.4.6. Surface chemistry

X-ray photoelectron spectroscopy (XPS) analyses of freeze-dried BNC composites (3 mm) were performed using an XPS analysis on a K-Alpha Thermo Scientific (ESCALAB™ XI+, East Grinstead, UK) spectrometer equipped with a 180° double focusing hemispherical analyser. Survey spectra were recorded at pass energy of 50 eV to determine the elemental composition of the BNC composites. Peak position was calibrated according to the standard C1s peak (284.7 eV) and O1s

(532.6 eV). High-resolution spectra were collected using an analysis area of ≈1 $mm^2$. Spectra were analysed for elemental composition for C1s and O1s, with binding energy regions measured at a pass energy of 20 eV to evaluate the elemental bonding state of the composites. The spectra acquisition and data processing were performed using the advanced Avantage data software (Thermo Avantage v5 9921, East Grinstead, UK). The least-squares peak analysis software, XPSPEAK (version 4.1, Prof. Raymond W.M. Kwok, Chinese University of Hong Kong), performed deconvolution into sub-peaks using the Gaussian/Lorentzian sum function and Shirley-type background subtraction. No tailing function was considered in the peak fitting procedure. The components of the various spectra were mainly modelled as symmetrical Gaussian peaks unless a certain degree of Lorentzian shape was necessary for the best fit. The best mixture of Gaussian–Lorentzian components was defined based on the instrument and resolution (pass energy) settings used as well as the natural line width of the specific core hole [303].

### 3.4.7. Thermal properties

The thermal properties of the developed freeze-dried composites (3 mm) were analysed using differential scanning calorimetry (DSC) and scanning thermogravimetric analysis (STA). The DSC thermograms were obtained using DSC-822e equipment (Mettler-Toledo International Inc, Switzerland). Samples with 5.9 ± 0.5 mg were placed in an aluminium pan. The samples were then heated from 25 to 450 °C, with a heating rate of 10 °C·$min^{-1}$, using a nitrogen flow rate of 200 mL·$min^{-1}$. The results were evaluated using LAB Mettler Star SW 8.1 software (Mettler-Toledo International Inc, Switzerland). The STA analyses of the developed freeze-dried composites (6.7 ± 1.6 mg) were conducted using the STA 7200 system from Hitachi (TA Instruments, Newcastle, UK). The thermal evaluation was performed within a temperature range of 25 to 1100 °C, under a controlled heating rate of 10 °C·$min^{-1}$ and a nitrogen flow rate of 200 mL·$min^{-1}$ to prevent oxidation. The thermogravimetric data were interpreted by examining the percentage of mass loss as a function of temperature, providing insights into the material's decomposition profile and thermal degradation behaviour.

### 3.4.8. Swelling profile

The functionalised BNC membranes were analysed according to their ability to absorb the body fluids present in the environment where they could be implanted. Therefore, swelling of the samples was determined before and after the functionalisation process. Briefly, functionalised samples of 16 mm in diameter were perforated with a nylon® yarn at one end and immersed in 7 mL of simulated body fluid (SBF) at 37 °C (physiological temperature) as exemplified in Fig. 3.4a, with a shaking speed of 50 rpm using a shaking bath VLSB18 (VWR Chemicals, Carnaxide, Portugal). Several periods were analysed, namely 1, 2, 4, 6, 24, 48, 72, 96, 120, 144, 168, 216, 288, 384, 504, 672, 1008, and 2184 h. Each time, the BNC membrane was removed from the medium and left standing vertically (1 minute) to drain excess SBF from the membrane surface (Fig. 3.4b).

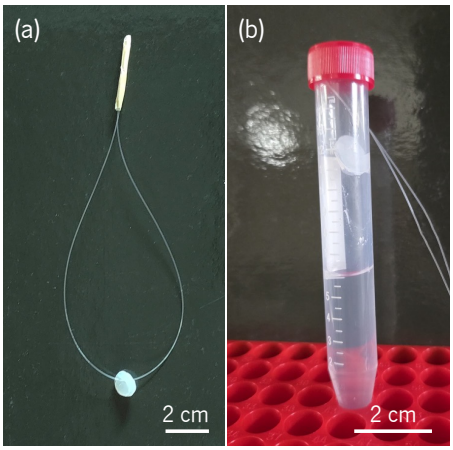



**Figure 3.4.** Demonstration of a BNC membrane (a) perforated with a polyamide filament, and (b) suspended vertically for excess medium drainage.

Subsequently, the membranes were weighed, and the swelling ratio (%) was determined using Eq. 3.3. In this experiment, five samples were tested for each specified condition.

$$\text{Swelling } (\%) = \frac{W_t - W_i}{W_i} \times 100 \qquad \text{(Equation 3.3)}$$

where $W_i$ is the initial weight, and $W_t$ is the weight for each analysis period.

### 3.4.9. Release profile

The KL and OP release rates from the BNC (1 mm thickness) were determined using SBF medium. Circular samples of 16 mm diameter were immersed in the different media at 37 °C with mild agitation (shaking speed of 50 rpm). Aliquots were collected over the same period as the swelling assay, and the KL and OP concentrations in solution were quantified using UV-vis spectroscopy (UV-vis 1800, Shimadzu, Switzerland). The release of the bioactive macromolecules was determined according to the calibration curve previously obtained in the UV-vis spectrometer. The coefficient of determination ($R^2$) were KL: y = 7.5195x + 0.0125, $R^2$:0.9999, OP: y = 3.3474x + 0.0039, $R^2$: 0.9999, and KL/OP: y = 2.5551x + 0.02, $R^2$: 1.000. Samples were retrieved fivefold. The release of KL and OP were determined using the absorbance value at 275 nm (KL), 280 nm (OP), and 275 nm (KL/OP) [304]. To investigate the kinetics of the drug release mechanism, the experimental data were fitted using semi-empirical and empirical mathematical models, including Korsmeyer-Peppas, Makoid-Banakar, Weibull, Logistic, Gompertz, and Probit models [305, 306]. The mathematical models of drug release profiles were evaluated using the DDSolver program [306].

### 3.4.10. Antimicrobial activity

For the evaluation of the antimicrobial activity of the organic compounds and the composites, bacteria *S. aureus* and *P. aeruginosa*, yeasts *C. albicans* and *C. krusei*, and bacteriophage *E. coli* MS2 were tested.

Bacteria and yeasts were cultured in TSB *(S. aureus, C. albicans,* and *C. krusei)* or NB (*P. aeruginosa*) and incubated overnight at 37 °C (bacteria) or 28 °C (yeasts) at 120 rpm. Bacterium *E. coli* host and bacteriophage *E. coli* MS2 were incubated at 37 °C in #271 medium.

The antimicrobial activity of BNC composites was assessed by release and contact assays. The assays were carried out using an initial concentration of bacteria of $1.0 \times 10^7$ colony forming units (CFUs)·$mL^{-1}$ and $1.0 \times 10^7$ plaque-forming units (PFUs)·$mL^{-1}$ of virus. Shake flask was adapted from ASTM-E2149-01 in which samples with an area of 2 $cm^2$ were immersed in 5 mL of the microorganism suspension and incubated at 37 °C (bacteria and virus) and 28 °C (yeasts) at 120 rpm for 4 h. Contact killing was adapted from AATCC 100-TM100 and 50 mL of the pre-established concentration of microorganisms was absorbed by the sample (4 $cm^2$) and incubated for 1 h. All samples were then immersed in 5 mL of either PBS (bacteria and yeasts) or #271 medium (virus).

After the required time of incubation, for both shake flask and contact killing methods, the microorganisms were serially diluted, cultured onto tryptic soy or #271 agar plates, and further incubated for another 16 h. Antimicrobial activity was reported quantitatively in terms of percentage microorganism reduction (Eq. 3.4) before and after contact with the samples [13].

$$\text{Log reduction } \left(\frac{\text{VC}}{\text{mL}}\right) = \text{Log}\left[\text{control}\left(\frac{\text{VC}}{\text{mL}}\right)\right] - \text{Log}\left[\text{sample}\left(\frac{\text{VC}}{\text{mL}}\right)\right] \quad \text{(Equation 3.4)}$$

Where VC means viable counts, and refers to CFU for bacterium, and PFU for virus particles.

### 3.4.11. Antioxidant properties

The antioxidant activity of the developed composites was analysed using the DPPH radical scavenging activity [307]. The experimental methodology was adapted from established protocols reported in previous studies [308-311]. The experimental approach was refined with slight adjustments to better align with the properties of the materials analysed. Composites with a diameter of 16 mm were immersed in 3 mL of a DPPH solution prepared in absolute ethanol at a concentration of 200 µM. The samples were incubated at 37 °C with a shaking speed of 75 rpm in the absence of light to prevent DPPH photodegradation. A DPPH solution in absolute ethanol served as the blank, while ascorbic acid (AA) at 2 wt% was used as the reference standard [312]. After the incubation periods (0.5, 1, 2, 4, 6, and 24 h), the solutions were analysed using a Shimadzu UV-2600 spectrophotometer (Shimadzu Europa GmbH, Duisburg, Germany) at a wavelength of 517 nm. The percentage of antioxidant activity was determined using Eq. 3.5, and all assays were performed in triplicate.

$$\text{Antioxidant Activity (\%)} = \frac{\text{Absorbance}_{\text{blank}} - \text{Absorbance}_{\text{sample at each time}}}{\text{Absorbance}_{\text{blank}}} \times 100 \quad \text{(Equation 3.5)}$$

## 3.5. Results and discussion

### 3.5.1. Media and functionalisation methodology selection

One of the main disadvantages of KL is its reduced solubility in neutral or low pH [234]. Hence, an initial test to evaluate filtration and exhaustion as the most adequate functionalisation methodology for BNC was performed using a basic solution (pH 9.0 – 10) of 0.1 M NaOH. Fig. 3.5 displays the heterogeneous distribution of KL on the filtered composites. Obvious surface sedimentation is observed (Fig. 3.5a Top), indicating that the KL was unable to completely penetrate the nanofibrous matrix of BNC (Fig. 3.5a Bottom). The vacuum filtration process appears to have caused fibre compaction and subsequent pore occlusion within the BNC structure, thereby preventing full matrix permeation. In contrast, the exhaustion process resulted in a more homogeneous functionalisation. In aqueous medium, the BNC remains at its maximum swelling capacity, facilitating the uniform impregnation of KL throughout the nanofibrous network (Fig. 3.5b). For this reason, the methodology selected for BNC functionalisation with KL was exclusively based on the exhaustion process.

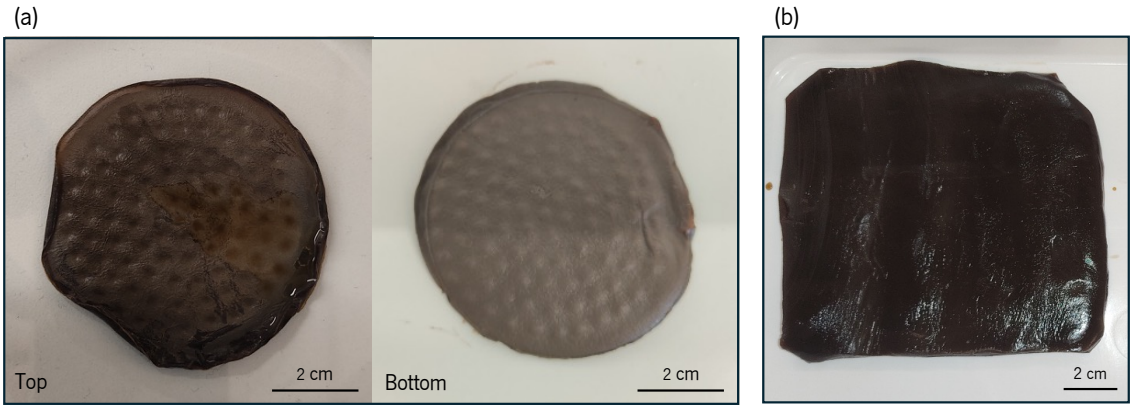



**Figure 3.5.** BNC/KL composites functionalised trough (a) filtration and (b) exhaustion approaches.

Considering that the cytotoxic nature of NaOH limits its suitability for implant applications [313], NaOH was reconsidered as a solvent for KL solubilisation. Despite being more soluble, OP is also partly insoluble in water. The solubility of the organic macromolecules KL and OP were thus tested in different media: distilled water ($dH_2O$), NaOH, and buffers PBS and BR. Additionally, a mixture of KL and OP was analysed to investigate potential synergistic effects between the two compounds. Optical microscopy images in Fig. 3.6 present the morphological characterisation of the solubility profiles. KL and OP exhibited poor solubility in $dH_2O$ (pH 6.5), presenting large agglomerates. In

contrast, nearly complete solubilisation of KL and OP was achieved in NaOH, due to the alkaline nature of the solvent pH (9.0 – 10)[234]. Furthermore, their solubility in both BR and PBS (pH 7.0 and 7.4, respectively) were comparable. Nonetheless, BR presents a considerable limitation due to its composition, which includes formic acid, a highly toxic compound, representing the simplest form of an organic acid [314, 315]. Hence, this evaluation was crucial for determining PBS as the medium to ensure the most effective functionalisation (Fig. 3.7). In addition, due to its biocompatibility with human body fluids and its non-toxic nature [316], PBS is an adequate choice for BNC functionalisation considering its intended biomedical application.

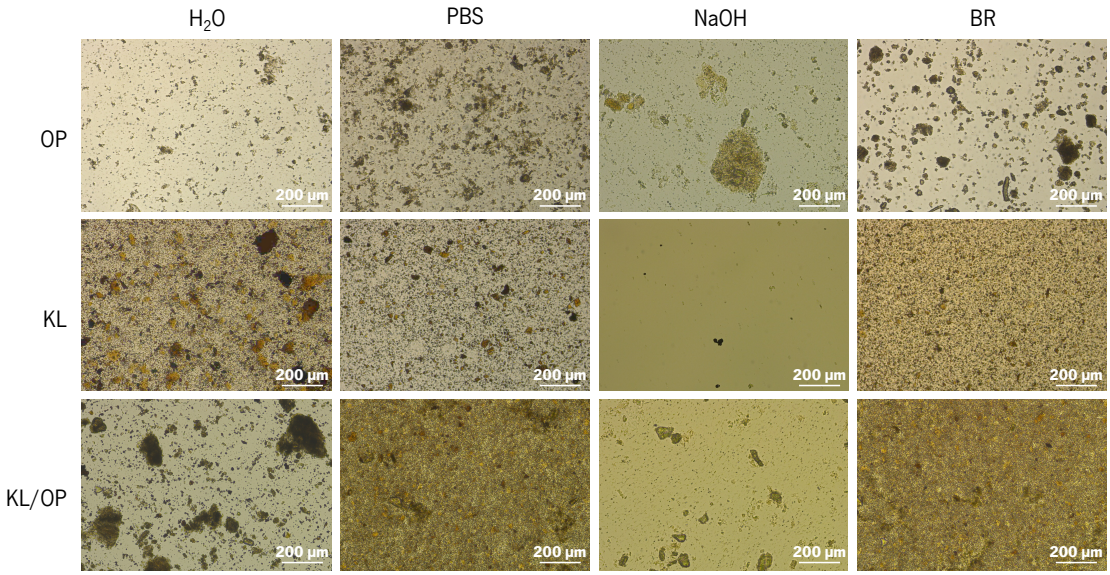



**Figure 3.6.** Microscopic images of the KL, OP, and KL/OP suspensions in $dH_2O$ (1 wt%), PBS, 0.1 M NaOH, and BR.

The uniformity and intense coloration of the PBS functionalised samples is presented in Fig. 3.7, demonstrating a good penetration of the organic macromolecules within the BNC membranes. This proves the suitability of the PBS as the solubilisation medium, particularly considering its non-toxicity and biocompatibility with the human body [316].

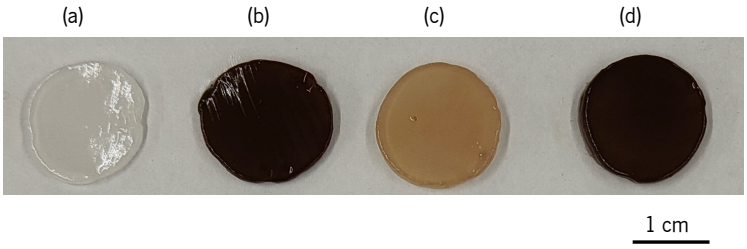



**Figure 3.7.** (a) pristine BNC, (b) KL, (c) OP, and (d) KL/OP functionalised BNC prepared using PBS as dispersion media of the biopolymers.

### 3.5.2. Size and morphology of KL and OP and BNC composites

The morphology of the KL, OP, and KL/OP was analysed by STEM images (Fig. 3.8a, c, e). The heterogeneous particle distribution is clear for all compounds which is corroborated by the histograms in Fig. 3.8b, d, f, evidencing partial dispersion. The prevalence of KL and KL/OP particles with an area lower than 0.3 μm² was close to 89 and 86%, showing that KL solubilisation is less effective than OP.

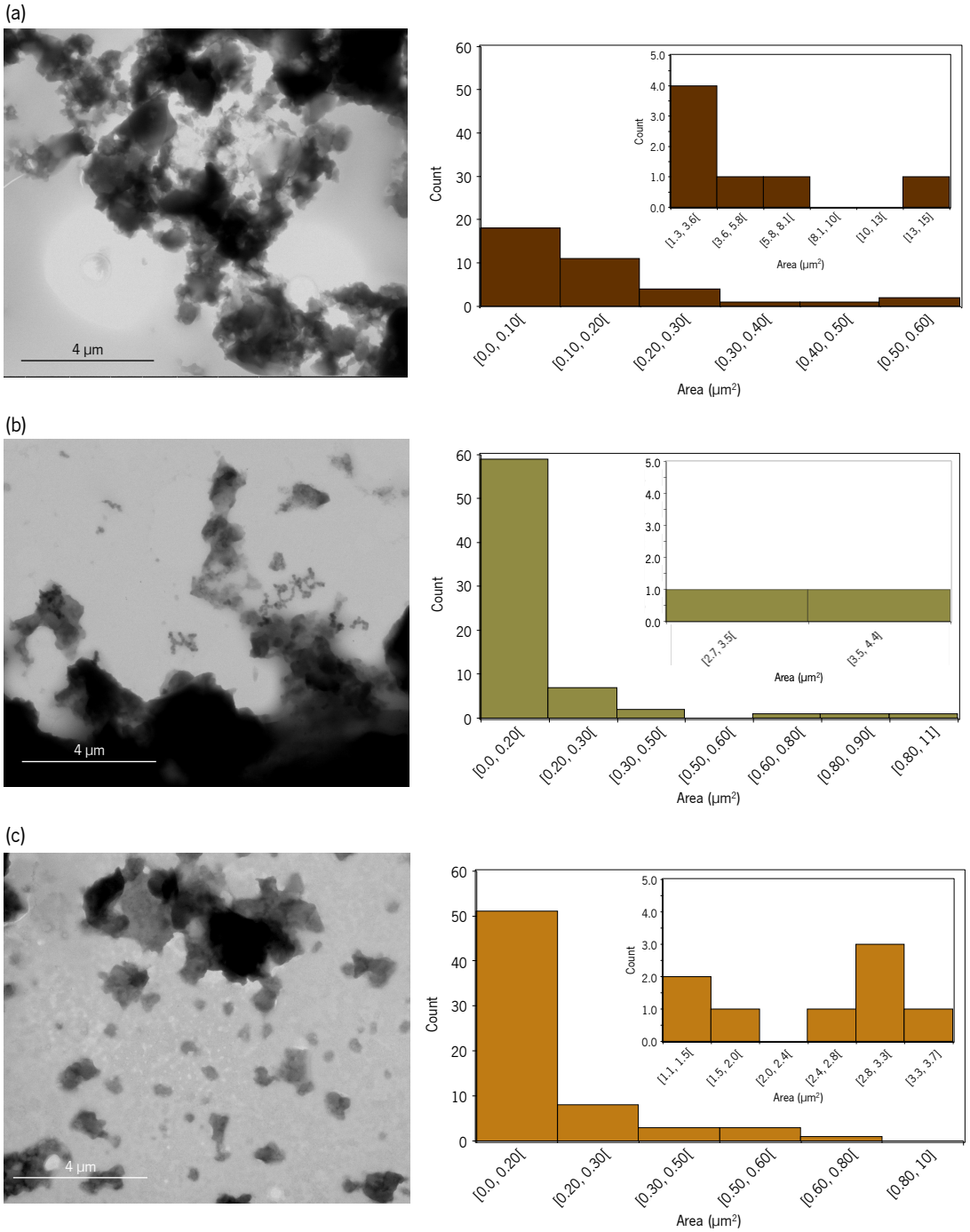



**Figure 3.8.** STEM image of (a) KL 2 wt%, (c) OP 1 wt%, and (e) KL/OP in PBS and particle area analysis of (b) KL, (d) OP, and (f) KL/OP.

The three-dimensional (3D) morphology of the BNC can be observed in the Cryo-FESEM images of the representative cross-section (Fig. 3.9a, b) and surface (Fig. 3.9c, d) of the membranes. The images show several layers of fibre entanglement, typical of BNC, which leads to its classification as a non-woven[317]. Fibre diameter (Fig. 3.9e), determined from the Cryo-FESEM images, ranged between 149 – 230 nm. These values are in line with the literature that report diameters between 70 – 150 nm [318] and 160 nm [319] for *K. hansenii* species. The inherent highly porous structure of native BNC can be observed, however, the incorporation of KL, OP, and the mixture KL/OP within the BNC matrix appears to have been limited. This may be attributed to the size and shape of the organic compounds [236, 320]. Cross-sectional SEM images (Fig. 3.10c, e, g) further confirm this observation, as the absence of the macromolecules within the fibrous network of BNC suggests that the functionalisation did not deeply permeate of the BNC matrix. The macromolecules aggregates are particularly large for KL (Fig. 3.10 d, h), suggesting a potential electrostatic interaction within the KL macromolecule, likely influenced by the lignin content. This is further supported by the cross-section images in Fig. 3.10e that suggests the absence of OP aggregates on the BNC surface. The highest influence of KL on the morphology of the BNC, namely a collapse in its structure and when compared to OP, is also visible in the cross-section images of the BNC/KL, BNC/OP, and BNC/KL/OP composites (Fig. 3.10d, f, h) [321].

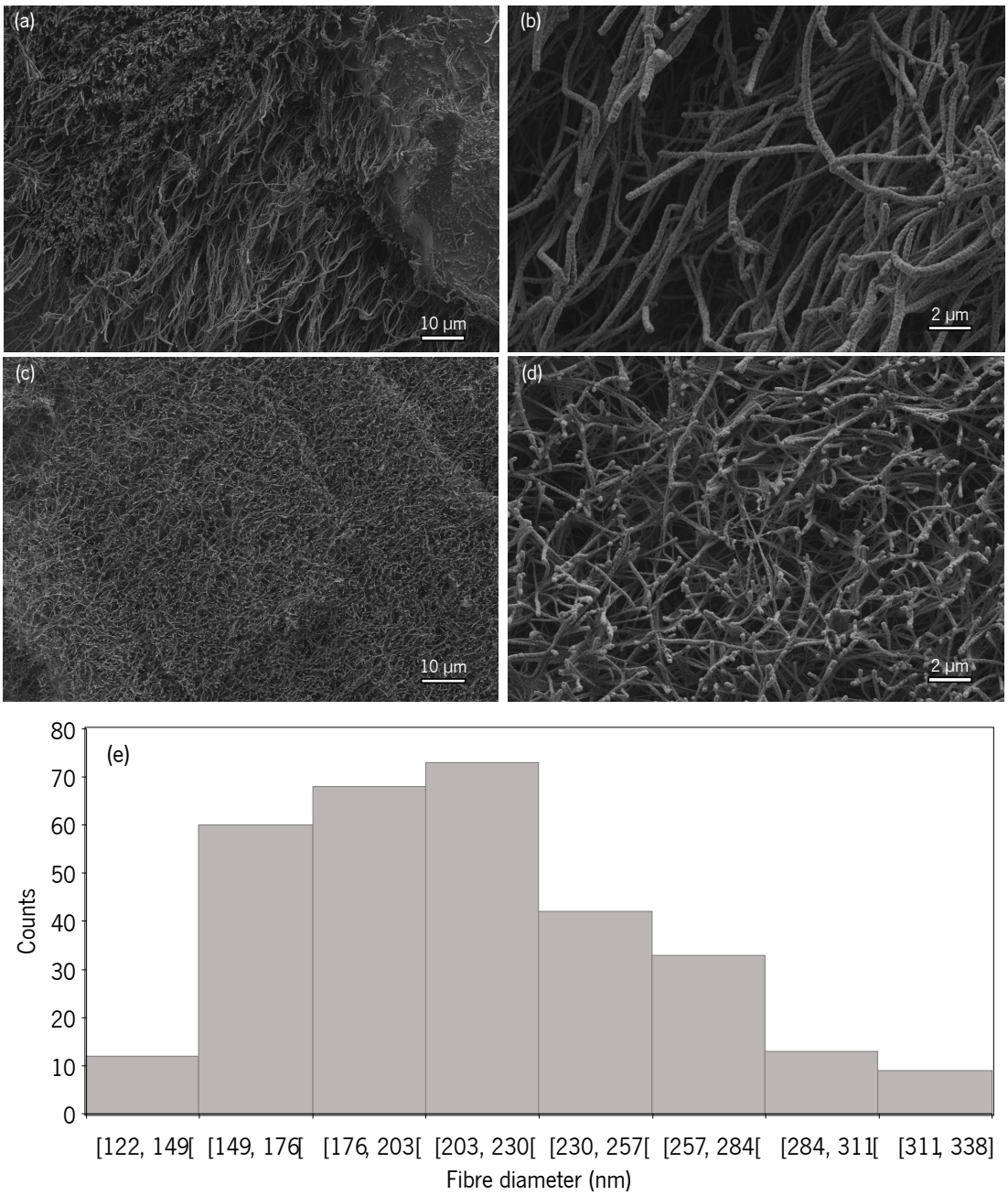



**Figure 3.9.** Cryo-FESEM image of the untreated never-dried samples: (a, b) cross-section, (c, d) surface; and (e) the histogram describing the estimated fibre diameter.

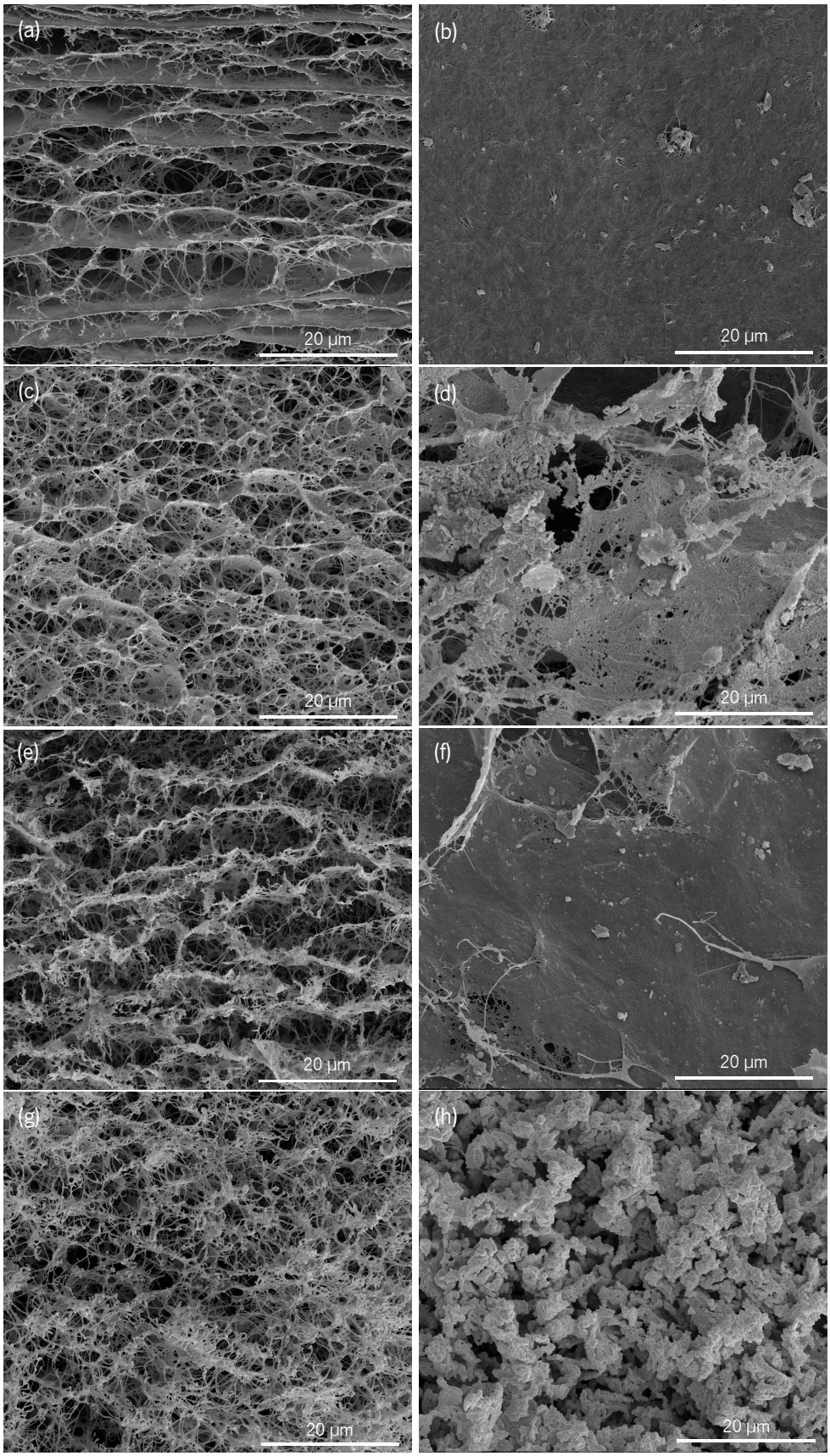



**Figure 3.10.** SEM images of the freeze-dried samples: cross-section of (a) BNC, (c) BNC/KL; (e) BNC/OP, and (g) BNC/KL/OP, and surface of (b) BNC, (d) BNC/KL, (f) BNC/OP, and (h) BNC/KL/OP.

### 3.5.3. Crystalline structure

The XRD pattern of the purified BNC exhibited characteristic reflections of native Cellulose I (Fig. 3.11) [54], with a prominent peak at $2\theta \approx 22.8°$ corresponding to the (200) lattice plane. The calculated CI was found to be 94%, a value rather similar to what has been reported in the literature for freeze-dried BNC [30]. This exceptional crystallinity confirms the high purity of the biosynthesised nanocellulose and the efficacy of the alkaline purification process in removing non-cellulosic bacterial biomass.

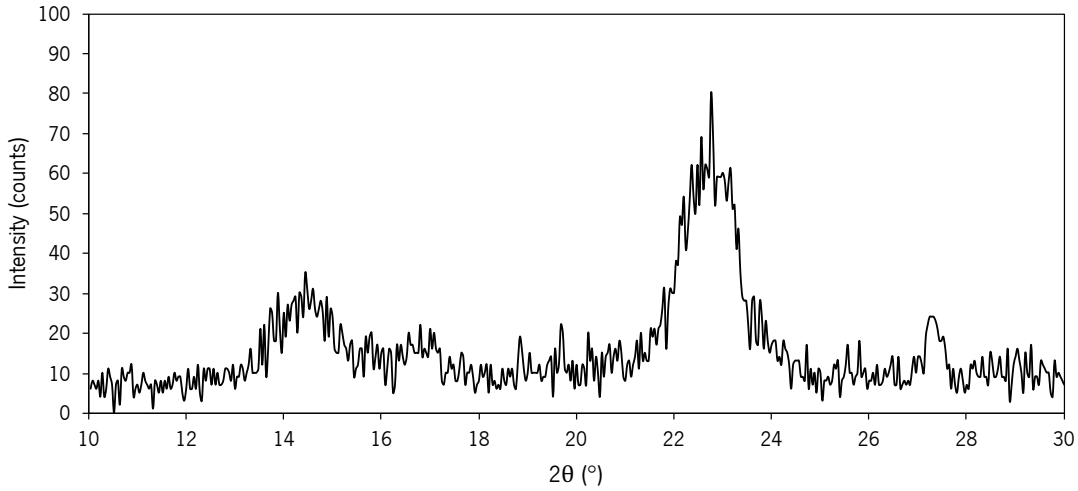



**Figure 3.11.** XRD diffractogram of untreated freeze-dried BNC.

### 3.5.4. Pore size

The influence of KL and OP on the BNC pore size was further analysed by capillary flow porometry technique. Their incorporation led to a decrease in average pore size of BNC, from 197 nm to 129 nm (BNC/KL), 46 nm (BNC/OP), and 108 nm (BNC/KL/OP), which may be attributed to pore obstruction. The pore size of the native BNC is in line with a macroporous structure, as reported in the literature, 0.0200 to 10.0 μm [322]. As mentioned above, considering the macromolecules areas displayed in the histograms of Fig. 3.8a–c, being smaller than 0.300 $\mu m^2$, it is expected that most of the particles cannot penetrate the 3D network of BNC (Fig. 3.10c, e, g). In the specific case of BNC/OP, the noticeable drastic pore size decrease may be justified by the smaller particle area of 178 nm (0.1 $\mu m^2$) that block the empty BNC pores, thus reducing their average diameter.

### 3.5.5. Surface area and adsorption isotherms

Besides pore diameter, the influence of the macromolecules on the surface area of BNC was evaluated by BET and $N_2$ adsorption-desorption isotherms (Fig. 3.12).

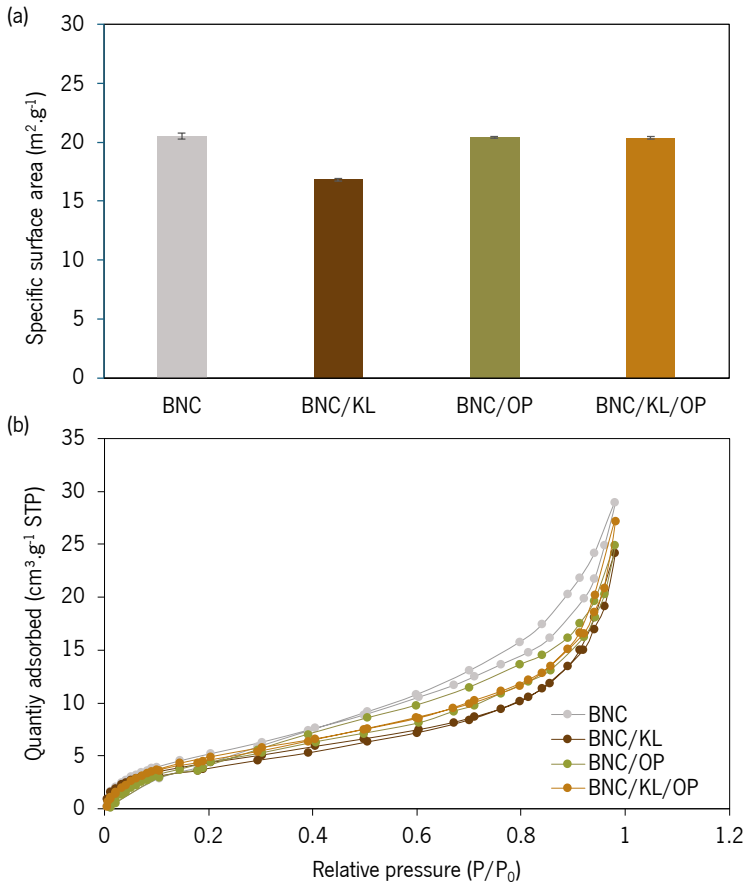



**Figure 3.12.** (a) BET surface area and (b) $N_2$ absorption/desorption isotherms of pristine and functionalised BNC.

The determined BET surface area of pristine BNC of 20.49 $m^2 \cdot g^{-1}$ (Fig. 3.12a), is in agreement with the literature values (between 20 and 200 $m^2 \cdot g^{-1}$) [323-326]. Differences in BET surface area values can be attributed to the bacterial strain used for production and the post-treatment of the membranes, including the drying method. A study by Adepu et al. demonstrated that the surface area was higher in freeze-dried samples compared to oven-dried samples due to structural collapse during thermal drying [327]. Upon incorporating KL (BNC/KL), a reduction in BET surface area was observed. This decline was attributed to the decreased availability of surface area as KL deposition on the BNC surface effectively blocked adsorption sites. For BNC/OP and BNC/KL/OP composites, surface area values remained comparable to those of the native BNC. For all samples, the adsorption/desorption curves overlapped in the region $0<P/P_0<0.5$ (Fig. 3.12b), suggesting

the presence of micropores with monolayer adsorption [328]. Further, a sudden increase was observed for $P/P_0$>0.9, and did not attain a stable status even at $P/P_0$=1, indicating that the $N_2$ gas trapped was due to capillary condensation of mesopores or macropores, at a relative pressure lower than its saturation pressure, and is a characteristic of slit-shaped pores [329]. Nonetheless, the presence of KL and OP led to lower adsorption values, in particular for BNC/KL.

### 3.5.6. Chemical structure

Structural analyses performed by ATR-FTIR (Fig. 3.13), show a large band at 3400 – 3200 $cm^{-1}$ attributed to O–H stretching vibrations, characteristic of the BNC pyranose ring, that is apparently unchanged in the BNC/KL and BNC/OP composites spectra [320]. This band became broader and more similar to the KL and OP in the BNC/KL/OP composite, likely due to the higher phenol content from the organic compounds that are able to mask the characteristic BNC band. Asymmetric and symmetric C–H stretching vibration bands of methylene groups (–$CH_2$–) in the cellulose structure are present as small absorption bands at 2916 and 2850 $cm^{-1}$ for BNC [330, 331]. Likely due to higher aliphatic content in OP, these bands are present as two better-defined peaks at 2924 and 2853 $cm^{-1}$ in the BNC/OP and BNC/KL/OP composites. In the same composites, a well-defined narrow peak at 1744 $cm^{-1}$ is attributed to the stretching vibrations of C=O from the carbonyl group of esters present in the triglyceride from OP, and the band at 1380 $cm^{-1}$ is attributed to the deformation of $CH_2$ groups. The presence of KL is identified at 1426, 1460, 1520, and 1600 $cm^{-1}$, due to aromatic skeletal vibrations combined with C–H in-plane deformation, C–H deformations of methyl and methylene, aromatic skeletal vibration breathing with C=O stretching, and C=O stretching (conjugated), respectively. Typical BNC bands are present at 1647 $cm^{-1}$ as a result of OH stretching (water absorption) and at 1427 $cm^{-1}$ due to C–H antisymmetric bending. Minor bands at 1410 and 1321 $cm^{-1}$ are due to C–H and O–H antisymmetric bending, at 1315 $cm^{-1}$ due to O–H in-plane bending, at 1203 $cm^{-1}$ due to symmetric stretching vibrations of sulfonic acid groups, at 1161 $cm^{-1}$ from C–O–C asymmetric stretching, and at 1053 $cm^{-1}$ due to C–O stretching. A strong intense peak at 1047 $cm^{-1}$ is from C–O–C stretching vibrations of the ether linkages between pyranose sub-units, at 898 $cm^{-1}$ from the stretching of the C–O–C at ß-(1→4)-glycosidic linkages, a small band at 771 $cm^{-1}$ results from bending peaks of $CH_2$, and at 740 $cm^{-1}$ is due to asymmetric stretching vibrations of sulfonic acid groups [320, 330].

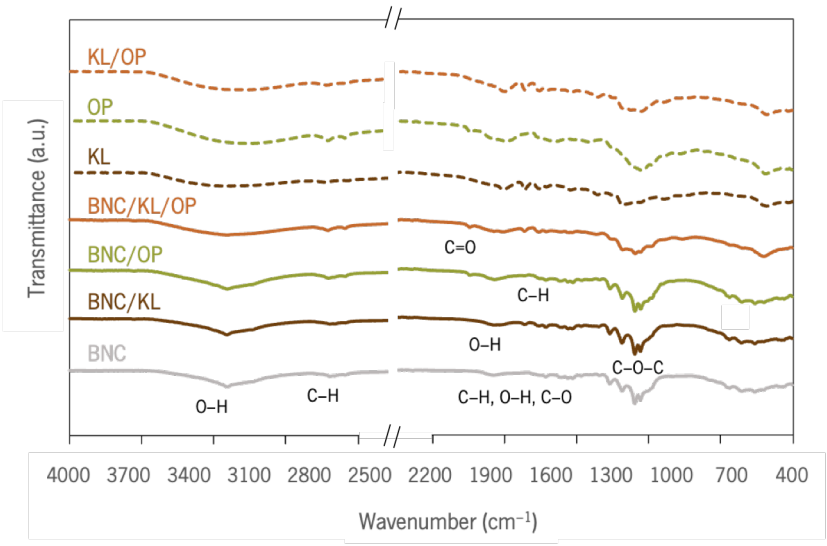



**Figure 3.13.** ATR-FTIR of the organic compounds, BNC and composites.

### 3.5.7. Surface chemistry (XPS)

The XPS survey spectra for BNC and BNC composites (Fig. 3.14) display a considerable presence on the surface of carbon (C1s) and oxygen (O1s) elements.

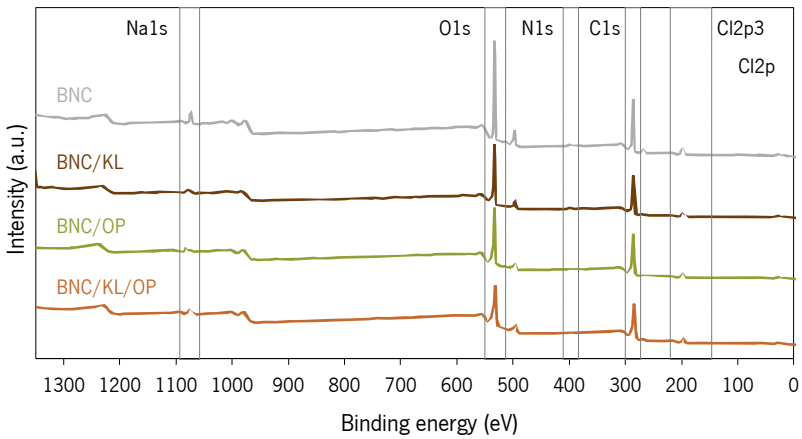



**Figure 3.14.** XPS survey spectra and high resolution.

As shown in Table 3.1, the incorporation of KL and/or OP leads to an increased atomic concentration of the C1s signal, while there is a slight decrease in the O1s concentration. The trend can be explained by the chemical structure of KL and OP, both of which are carbon-based [332, 333]. In addition, minor amounts of chlorine (Cl) and nitrogen (N) were detected in the samples, as well as small levels of sodium (Na) and silicon (Si) on the surface. The presence of these

elements may be a result of the NaOH-based purification process, which is known to affect the glass of the recipients used [334, 335]. Fig. 3.15a, b presents the C1s and O1s high resolution spectra aligned to the highest C–O–C peak, indicating the highest oxidation in the case of OP modification.

**Table 3.1.** Elemental atomic percentages on the surface of the samples from the XPS survey spectra.

| Atomic % | O1s | C1s | Cl2p | Na1s | N1s |
|---|---|---|---|---|---|
| BNC | 33.02 | 57.66 | 3.650 | 2.730 | 1.700 |
| BNC/KL | 31.58 | 64.05 | 3.170 | – | 1.210 |
| BNC/OP | 29.81 | 64.45 | 4.510 | – | 1.230 |
| BNC/KL/OP | 30.19 | 63.73 | 3.690 | 0.7400 | 1.150 |

The deconvolution of the C1s spectra is shown in Fig. 3.15c–f (further details are presented in Table 3.2). The BNC spectrum presented the three binding energy peaks: 284.7, 286.3 and 287.5 eV, attributed to C–H/C–C, C–O and O–C–O bonds, suggesting an elevated carbon content [336]. The incorporation of KL or/and OP led to an increase in the peak percentage atomic percent (PP At.%) corresponding to C–C/C–H bonds (Fig. 3.16a). The PP At.% increased from 26.28% in BNC to 27.83%, 32.35%, and 31.76%, in BNC/KL, BNC/OP, BNC/KL/OP, respectively. This is expected due to the large number of aromatic rings and aliphatic chains present in both KL and OP [204, 205]. The peaks referring to C–O bonds, which is the dominant peak for BNC at 286.5 eV, show a decrease in PP At.% after the functionalisation with OP and KL/OP. Contrarily, these bonds are present in higher percentages in the pristine BNC samples and have also increased with KL. The fact that they decrease could be the result of C–O signal dilution due to the introduction of more hydrocarbons. The peaks at around 288.0 – 288.5 eV correspond to O–C–O and C=O from acetal, hemiacetal, carboxylic or carbonyl groups [337]. The new peaks at higher binding energies of 289.0, 288.9, and 290.4 eV for KL, OP, and KL/OP composites are related to O=C–O groups of esterified hemicellulose [336]. The combination of KL/OP revealed shake-up satellite peaks due to p–p* transitions in aromatic rings [338]. The $\pi \rightarrow \pi^*$ is not expected in pristine BNC samples, thus it could be the result of airborne contamination or even drying [339]. In addition, even after purification, the BNC is unable to completely remove traces of medium and even of cells. Several elements that include double bonds, namely the peptidoglycan with C=O, that is visible in the SEM images, remains entangled in the BNC structure [328].

The increase from 3.55% in pristine BNC to 4.06% in BNC/KL of the π⟶π* transition indicates that lignin incorporation introduces additional aromatic functionalities. The lower π⟶π* contribution in BNC/OP (2.80%) suggests weakening or partial alteration of conjugated structures, while the pronounced increase in BNC/KL/OP (6.68%) reflects a synergistic effect between KL and OP, enhancing aromatic conjugation and π electron delocalisation [340]. Furthermore, environmental carbon contamination may contribute to this signal, generating shake-up satellites around 292 eV that mimic π⟶π* transitions [341]. In addition, partial structural rearrangements during drying or membrane processing may also be responsible. A broadening of the π⟶π* bond for the BNC/KL/OP composites is the result of the heterogeneous π-systems originating from the mixture [341].

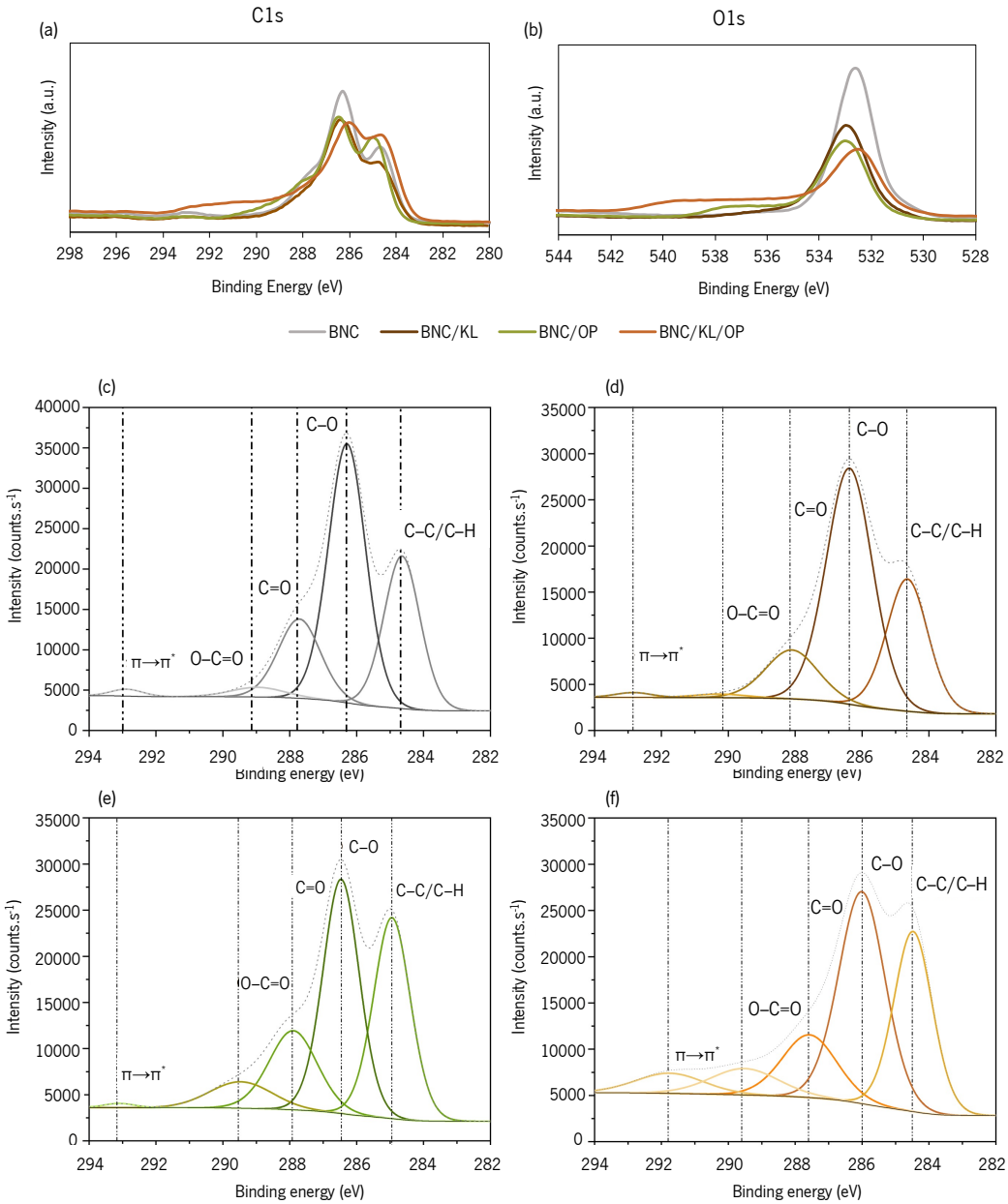



**Figure 3.15.** (a) C1s and (b) O1s spectra of BNC and their composites; and the peak deconvolution at the C1s region obtained for (c) BNC, and composites (d) BNC/KL, (e) BNC/OP, and (f) BNC/KL/OP.

**Table 3.2.** Deconvolution analysis of the C1s peaks of the sample.

| | **BNC** | **BNC/KL** | **BNC/OP** | **BNC/KL/OP** |
|---|---|---|---|---|
| | | C–C/C–H | | |
| Peak Position (eV) | 284.6 | 284.7 | 284.9 | 284.5 |
| FWHM (eV) | 1.270 | 1.450 | 1.290 | 1.350 |
| Area (counts·s$^{-1}$·eV$^{-1}$) | 26,129.7 | 22,611.1 | 30,676.0 | 28,721.7 |
| | | C–O | | |
| Peak Position (eV) | 286.2 | 286.4 | 286.5 | 286.0 |
| FWHM (eV) | 1.310 | 1.630 | 1.270 | 1.640 |
| Area (counts·s$^{-1}$·eV$^{-1}$) | 45,804.9 | 45,199.3 | 35,253.7 | 40,742.9 |
| | | C=O | | |
| Peak Position (eV) | 287.7 | 288.1 | 287.9 | 287.6 |
| FWHM (eV) | 1.470 | 1.840 | 1.690 | 1.920 |
| Area (counts·s$^{-1}$·eV$^{-1}$) | 15,745.3 | 10,584.6 | 15,704.0 | 14,170.1 |
| | | O–C=O | | |
| Peak Position (eV) | 289.0 | 290.3 | 289.5 | 289.5 |
| FWHM (eV) | 1.890 | 1.850 | 2.200 | 2.400 |
| Area (counts·s$^{-1}$·eV$^{-1}$) | 2,448.61 | 763.840 | 6,698.54 | 7,442.57 |
| | | $\pi \rightarrow \pi^*$ | | |
| Peak Position (eV) | 292.9 | 292.8 | 293.1 | 291.8 |
| FWHM | 1.110 | 1.290 | 1.050 | 2.400 |
| Area (counts·s$^{-1}$·eV$^{-1}$) | 1,027.37 | 725.050 | 499.870 | 5,577.81 |

Fig. 3.16b presents the O1s binding energy region spectra obtained for BNC and its composites. The BNC possesses its regular peaks, C=O around 531.2 eV, followed by the main peak of BNC, C–O at 532.0 eV, and by the O–C=O peak around 533.4 eV [342]. The high energy tails between 534.0 – 536.0 eV may be attributed to the presence of water molecules on the surface, in different bonding environments, namely as chemisorbed –OH and physisorbed $H_2O$. They also appear in BNC to a smaller extent. The contribution of the π -plasmons appears as a shoulder in O1s (typically 5360 – 538.0 eV), possibly due to O coupling with aromatic π-electrons, which are generated in aromatic materials, from both KL and OP. The fact that the combination of KL and OP induces the strongest tail intensity is due to the synergy among the aromatic structures originating from both compounds. This is in line with the highest intensity of the π–π* bond exhibited in the C1s binding energy region for the same BNC/KL/OP composite material. A similar signal broadening as that encountered in C1s binding energy also appears in this region. The highly energetic tail up to 540.0

eV suggests that some processes of inelastic losses may appear in the composite material, potentially caused by the sample heterogeneity.

Although XPS suggests changes in the chemical structure of the composites at the surface, overall, ATR-FTIR measurements evidence that the addition of KL or/and OP to BNC does not affect the intrinsic bulk characteristics of BNC, and the changes visible in the spectra are due to an increase in the macromolecules' content.

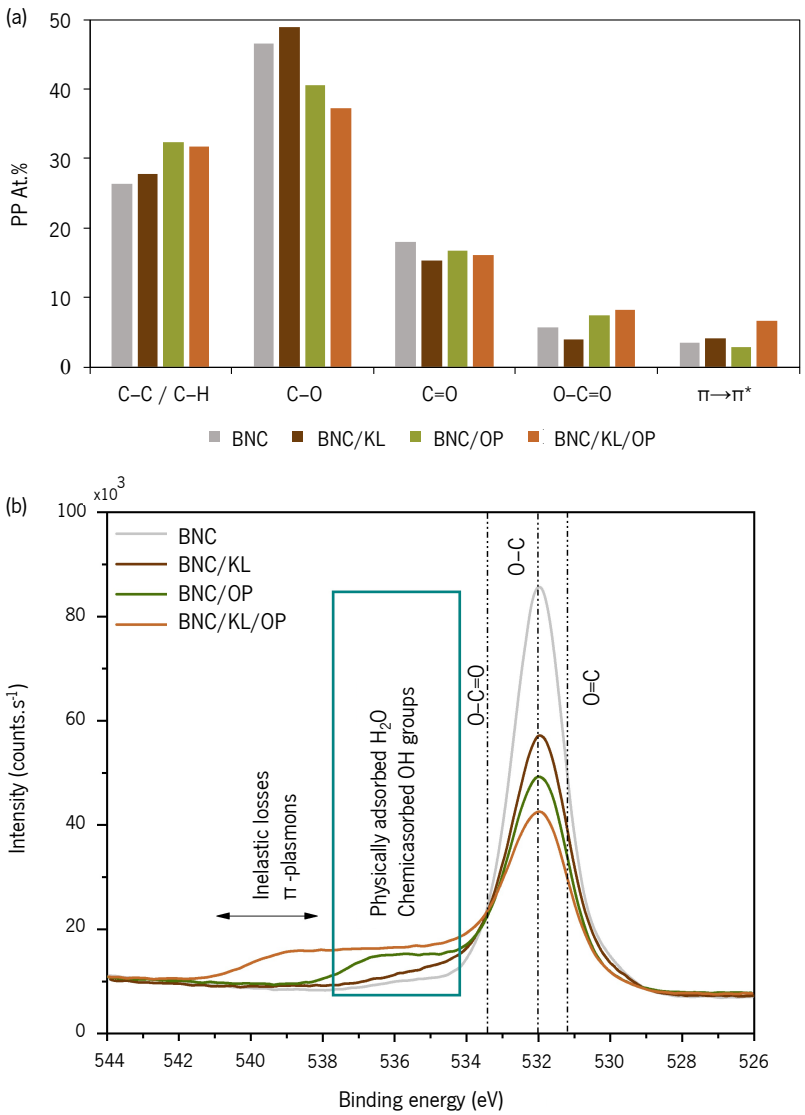



**Figure 3.16.** (a) Carbon bonds contribution for BNC and its KL/OP composites, and (b) the O1s binding energy region spectra obtained for BNC and its composites: BNC/KL, BNC/OP, and BNC/KL/OP.

### 3.5.8. Thermal properties

The thermal analysis of the freeze-dried BNC composites was evaluated through DSC thermograms (Fig. 3.17a), mass loss curves (Fig. 3.17b) and differential thermogravimetric (DTG) curves (Fig. 3.17c) obtained from STA. The DSC thermograms of untreated BNC exhibit two characteristic peaks: moisture release from the samples, either due to physically absorbed molecules or those chemically bound through hydrogen bonds (49.0 – 127 °C) (endothermic peak), and decomposition of cellulose (328 – 362 °C) (exothermic peak), as confirmed by thermogravimetric analysis (TGA). The DSC thermograms of BNC composites reveal two similar peaks, with a third peak corresponding to the decomposition of OP and KL near 200 °C [343]. The degradation profiles of cellulose and lignin are comparable, as evidenced by closely aligned exothermic peaks (344 – 349 °C), suggesting that KL and OP incorporation did not considerably affect the thermal properties of the BNC composites.

The TGA curves show two characteristic processes: (i) moisture loss present in the samples or due to hydrogen bonds, and (ii) depolymerisation of $\beta$-glucan polymer chains and oxidation of cellulose-based materials into carbonaceous residue [320, 344]. Although freeze-dried samples were analysed, residual water was detected due to dehydration and volatilisation within the polymer chain. Nevertheless, the water content remained low, from 4.0 – 7.0% between 25.0 – 105 °C, consistent with the DSC thermogram results [344]. A two-stage decomposition process was observed, with the total mass loss in this process being similar in all composites (~85%). Except for BNC/KL/OP, which exhibited a mass loss of 80%. Moreover, a considerably higher mass loss was observed in the second stage of decomposition, considering that the degradation of KL and OP occurs at temperatures of approximately 313 – 345 °C [345]. The incorporation of KL and OP individually did not affect the thermal properties of the composites, as their decomposition temperatures were similar to that of BNC. This may be attributed to the lack of covalent bonds between these compounds and BNC, and the presence of these biopolymers being limited to the surface of the BNC. The stable aromatic unit characteristic of KL could also contribute to thermal improvements, particularly regarding the maximum degradation temperature (340 °C). Nevertheless, this increase was relatively low, given that the other composites exhibited values ranging from 333 to 338 °C [346]. A higher residual content was obtained in the BNC/KL/OP composite, indicating the presence of a more crystalline structure, which resulted in slightly improved thermal resistance [344].

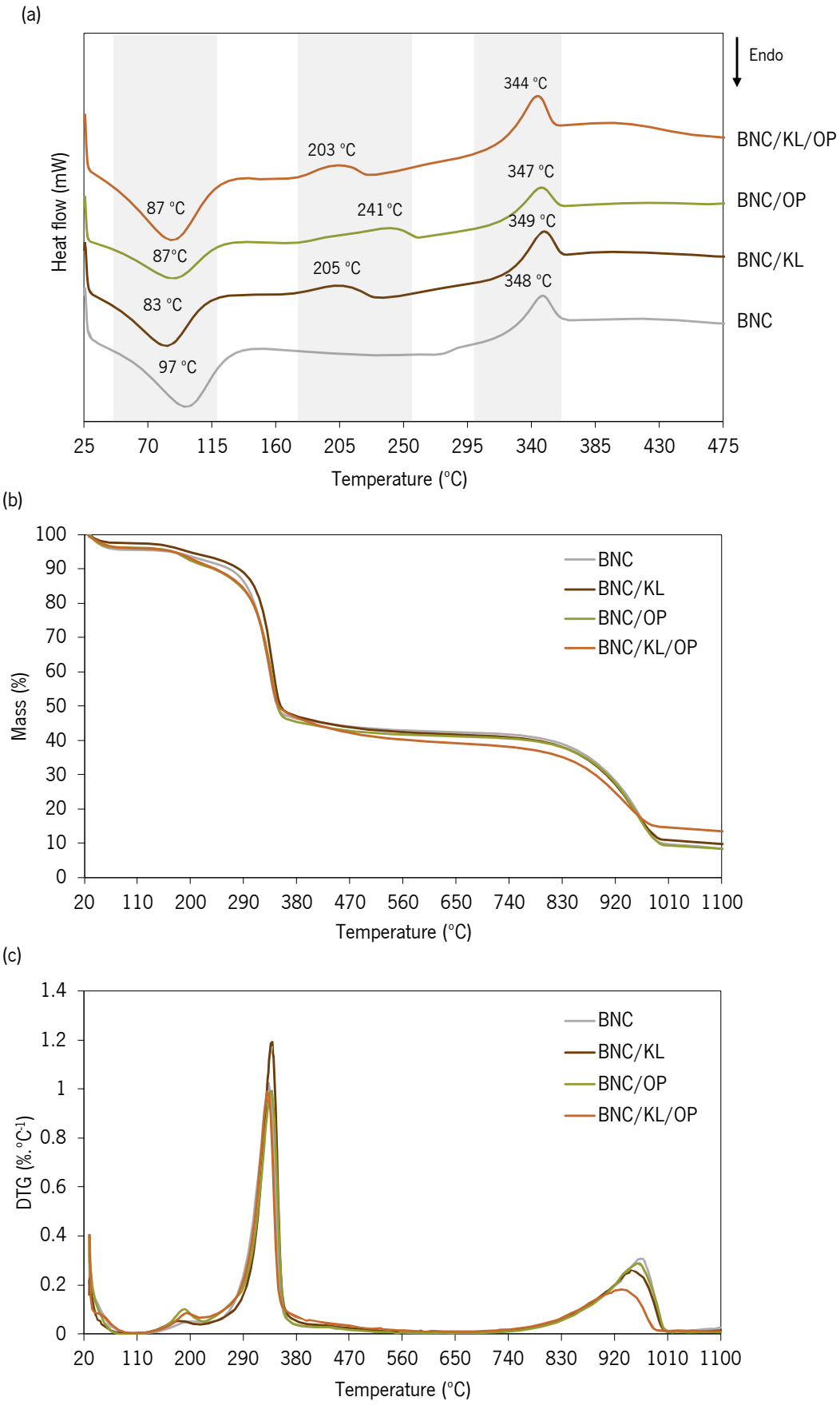



**Figure 3.17.** (a) DSC thermogram, (b) TGA curves, and (c) DTG curves of BNC composites.

The results provided by TGA, in combination with ATR-FTIR and XRD, show the high purity of the untreated BNC. XRD analysis revealed an exceptional crystallinity index of 94.0%, which was corroborated by ATR-FTIR spectroscopy, which showed an effective removal of bacterial proteins and hemicelluloses during the purification process (absence of bands at 1548 and 1730 $cm^{-1}$), while displaying the dominant C–O–C stretching vibrations at 1033 $cm^{-1}$ [347]. Furthermore, TGA confirmed the high thermal stability of untreated BNC, exhibiting a degradation temperature of 348 °C, characteristic of crystalline Cellulose I. Overall, these results demonstrate the purity of untreated BNC.

### 3.5.9. Swelling profile

The swelling behaviour of a material is often related to its hydrophilic properties and drug release in response to a biological fluid, thus influencing the biocompatibility of the implant [348]. The swelling ratio of BNC, and composites BNC/KL, BNC/OP, BNC/KL/OP was evaluated by measuring the swelling ratio in SBF medium. Fig. 3.18 illustrates the swelling curves for each sample. The high swelling behaviour of BNC which is governed by its inherent hydrophilicity and 3D structure, affords a water-holding capacity superior to that of most polysaccharides [349]. This characteristic significantly influences drug release in physiological fluids and dictates overall biocompatibility of the surgical implant [348]. The inherent hydrophobicity of KL and OP, coupled with the reduced pore dimensions detailed in Section 3.5.4., likely contributed to the observed reduction in the swelling of the composites. Fig. 3.19 illustrates the equilibrium swelling values observed for each condition. The composite BNC/KL/OP presents a higher swelling compared to the other composites, close to pristine BNC. The reduction in swelling may be attributed to the hydrophobicity of both KL and OP, other than a synergistic effect between the two macromolecules. Although their area, as evidenced in Fig. 3.8., are relatively large to fully permeate the BNC pores, they are still capable of entering the pores. This is supported by the pore size reduction from 197 nm (BNC) to 108 nm (BNC/KL/OP) (Section 3.5.4.). Consequently, despite diminishing swelling, the reduction is not as pronounced as in the case of BNC/OP.

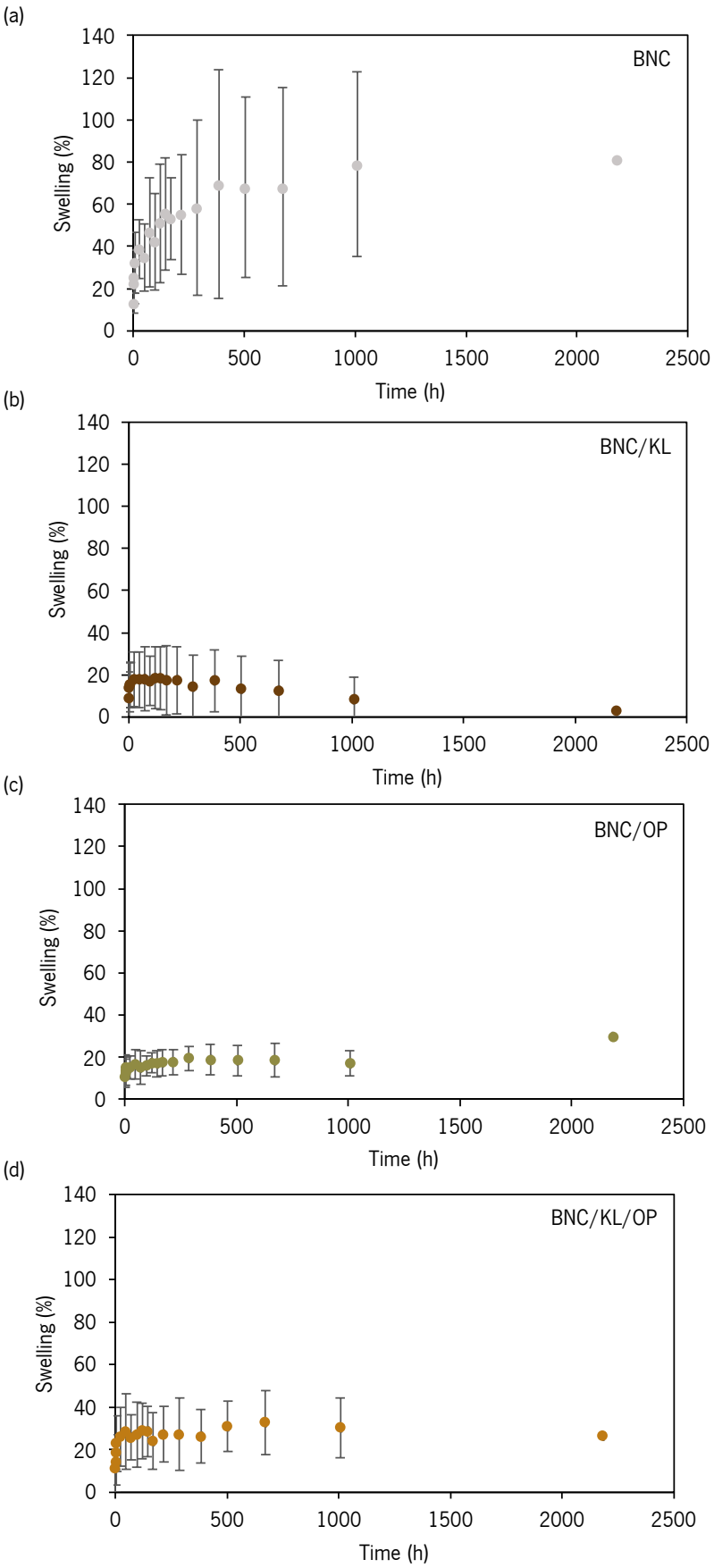



**Figure 3.18.** Swelling profile of (a) BNC and composites (b) BNC/KL, (c) BNC/OP, and (d) BNC/KL/OP in SBF.

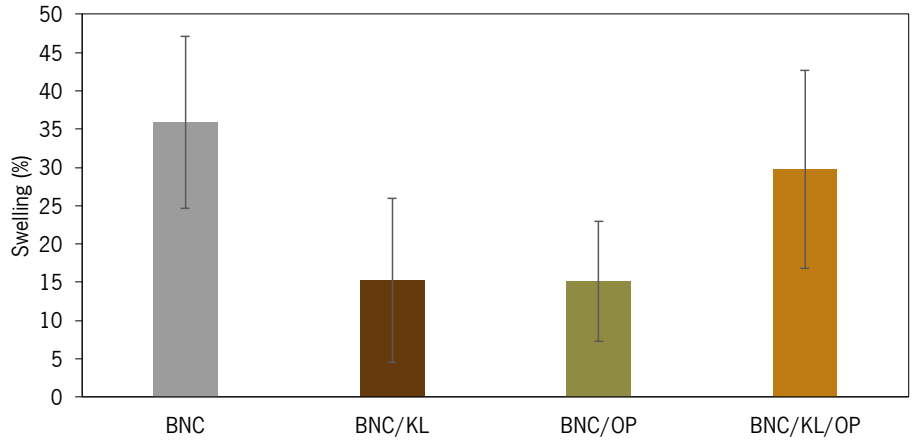



**Figure 3.19.** Swelling equilibrium in SBF.

### 3.5.10. Release profile

The release profile of KL, OP, and KL/OP is shown in Fig. 3.20. The release is sustained over time, and the highest release percentage is only slightly above 0.1%. This minimal percentage may be due to the large size of the organic particles being unable to enter the nanofibrous structure, due to the smaller pore size of the BNC, as confirmed in Fig. 3.8 and Fig. 3.10c, e, g. Moreover, despite the hydrophilicity and elevated swelling of BNC (as confirmed in Fig. 3.18a), which could suggest high release rates, the hydrophobic nature of KL and OP and their electrostatic interaction with BNC decreases their diffusion into the aqueous media [350]. The controlled release of the samples is beneficial since it improves patient compliance and reduces side effects, particularly toxic effects [351].

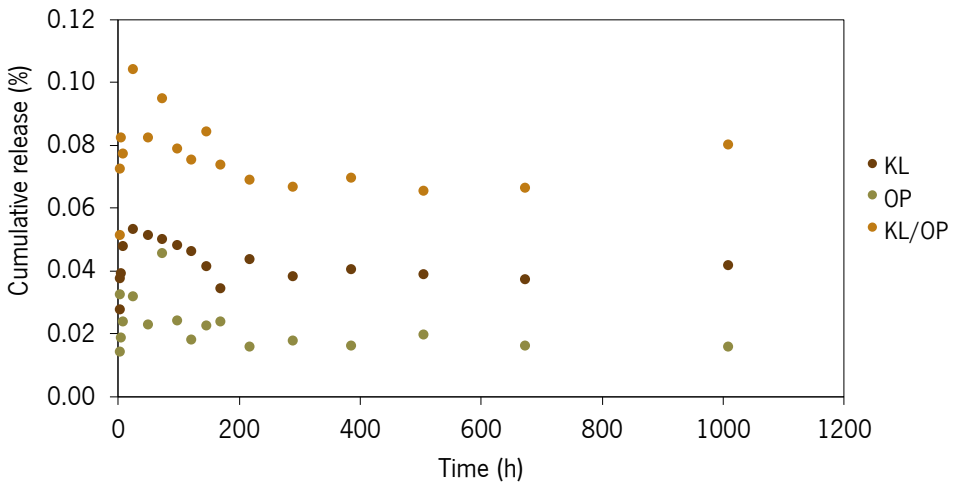



**Figure 3.20.** Cumulative drug release profiles of KL, OP, and KL/OP throughout 1008 h in SBF.

The fitted experimental data are presented in Table 3.3 and Fig. 3.21, and include Korsmeyer-Peppas, Makoid-Banakar, Weibull, Logistic, Gompertz, and Probit models, which apply a nonlinear least-squares curve-fitting technique [305, 306]. The drug release models' fitting quality was evaluated using the coefficient of determination ($R^2$) values and the Akaike Information Criterion (AIC), for which there is no absolute value. Instead, a comparison between the lowest AIC value indicates the better-fitting model [352]. The mathematical modelling results show that no model was able to adequately predict the release data obtained, due to the very low release percentages.

**Table 3.3.** Mathematical modelling results of experimental drug release data of BNC release models in SBF.

| Model | Parameters | KL | OP | KL/OP |
|---|---|---|---|---|
| Korsmeyer-Peppas $F=k\times t^n$ | *k* | 0.03900 | 0.02500 | – |
| | *n* | 0.01400 | -0.03800 | – |
| | $R^2$ | 0.002000 | 0.03500 | – |
| | AIC | -119.0 | -113.70 | – |
| Makoid-Banakar $F=k\times t^n\times e^{-kt}$ | kMB | 0.03700 | 0.02200 | 0.07000 |
| | *n* | 0.05400 | 0.03100 | 0.03400 |
| | *k* | 0.00000 | 0.001000 | 0.0000 |
| | $R^2$ | 0.2110 | 0.1930 | 0.1060 |
| | AIC | -121.0 | -114.7 | -98.93 |
| Weibull $F=100\times\left(1-e^{\left[\frac{-(t^\beta)}{\alpha}\right]}\right)$ | a | 2547 | 4051 | – |
| | b | 0.01600 | -0.03300 | – |
| | $R^2$ | 0.01600 | 0.02700 | – |
| | AIC | -117.3 | -11.56 | – |
| Logistic $F=100\times\frac{e^{[\alpha+\beta\times\log(t)]}}{1-e^{[\alpha+\beta\times\log(t)]}}$ | a | -7.837 | -8.285 | – |
| | b | 0.03300 | -0.08700 | – |
| | $R^2$ | 0.002000 | 0.03500 | – |
| | AIC | -119.0 | -113.7 | – |
| Gompertz $F=100\times e^{-\alpha\times e^{-\beta\times\log(t)}}$ | a | – | 8.279 | – |
| | b | – | -0.01000 | – |
| | $R^2$ | – | 0.03900 | – |
| | AIC | – | -113.8 | – |
| Probit $F=100\times\phi[\beta\times\log(t)]$ | a | – | -3.477 | – |
| | b | – | -0.02300 | – |
| | $R^2$ | – | 0.03700 | – |
| | AIC | – | -113.7 | – |

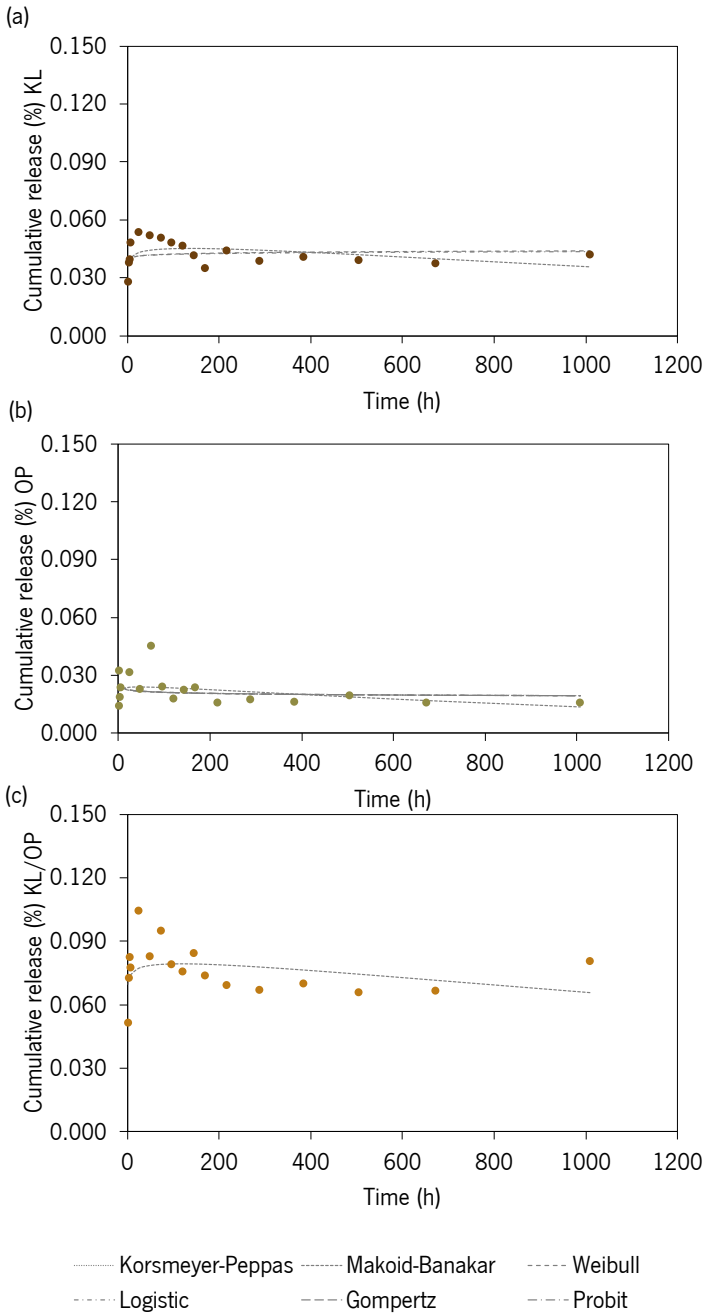



**Figure 3.21.** Fitting of the experimental drug release data of (a) KL, (b) OP, and (c) KL/OP from the BNC composites in SBF with Korsmeyer-Peppas, Makoid-Banakar, Weibull, Logistic, Gompertz, and Probit models.

### 3.5.11. Antimicrobial activity

The minimal inhibitory concentration of KL is depicted in Table 3.4. The potential of antibacterial activity of KL, particularly against the tested Gram-positive bacterium, *S. aureus*. The minimal bactericidal/virucidal activity (Table 3.5) corroborates these findings by displaying a relevant Log reduction against *S. aureus*, specifically by lignin without alkali treatment. As for the minimal

virucidal activity, the Log reduction is low with the exception of 1% KL treated with 0.1 M of NaOH. Interestingly, once the KL is incorporated into BNC, the BNC with the highest zone of inhibition against *S. aureus* is the one solubilised in 0.1 M NaOH. Nevertheless, the bactericidal activity against *E. coli* and the antiviral activity are negligible.

**Table 3.4.** Minimal inhibitory concentration of KL in $dH_2O$ and 0.1 M NaOH.

| Solvent media | | NaOH | | $dH_2O$ | |
|---|---|---|---|---|---|
| **Concentration** | | **1%** | **0.1%** | **1%** | **0.1%** |
| Log reduction ($CFU \cdot mL^{-1}$) | *S. aureus* | 1.80 | 1.90 | 3.80 | 2.90 |
| | *E. coli* | 0.600 | 0.000 | 0.900 | 0.000 |
| Log reduction ($PFU \cdot mL^{-1}$) | MS2 | 3.00 | – | 1.80 | – |

**Table 3.5.** Minimal bactericidal/virucidal concentration of KL in $dH_2O$ and 0.1 M NaOH.

| | | **BNC** | **BNC/KL (NaOH)** | **BNC/KL ($dH_2O$)** |
|---|---|---|---|---|
| ZoI (mm) | *S. aureus* | 0.000 | 13.2 | 8.50 |
| | *E. coli* | 0.000 | 0.000 | 0.000 |
| Log reduction ($PFU\ mL^{-1}$) | MS2 | 0.000 | 0.300 | 0.300 |

KL and OP antimicrobial activity has been thoroughly described and is attributed to the phenolic fragments holding a double bond in the Cα = Cβ position of the side chain and a methyl group in the γ position. These phenolic groups lead to bacteria's death when in contact with the cell membrane, prompting bacterial lysis [353, 354]. The assessment of the antimicrobial activity of the BNC composites was performed using the shake flask and the contact killing assays. According to Fig. 3.22a, no antimicrobial activity was observed using the shake flask methodology. This method is strongly dependent on the release of the bioactive compound. Despite the verified statistical differences, the statistical analysis was not discussed, considering the lack of activity (all results show log reduction lower than 1). These findings are in agreement with the controlled

release data (Fig. 3.20) that show a negligible release from the BNC substrates, likely due to the hydrophobic nature of KL and OP [350].

The contact killing results in Fig. 3.22b showed no antibacterial nor antifungal activity for neither sample. Regarding the antiviral activity, the MS2 bacteriophage seems to be vulnerable to BNC/OP, with log reductions of 4. The control obtained a 2 log reduction, which, despite being high for a control sample, does not invalidate the 4 log reduction for BNC/OP and BNC/KL/OP composites. The reason could be hypothetically attributed to the high electrostatic forces established between BNC and the virus. This is based on the results obtained with cotton knitted structures, where 1 log reduction was observed for control samples. In this case, the effect is enhanced due to the high surface area provided by the nanostructured BNC [355].

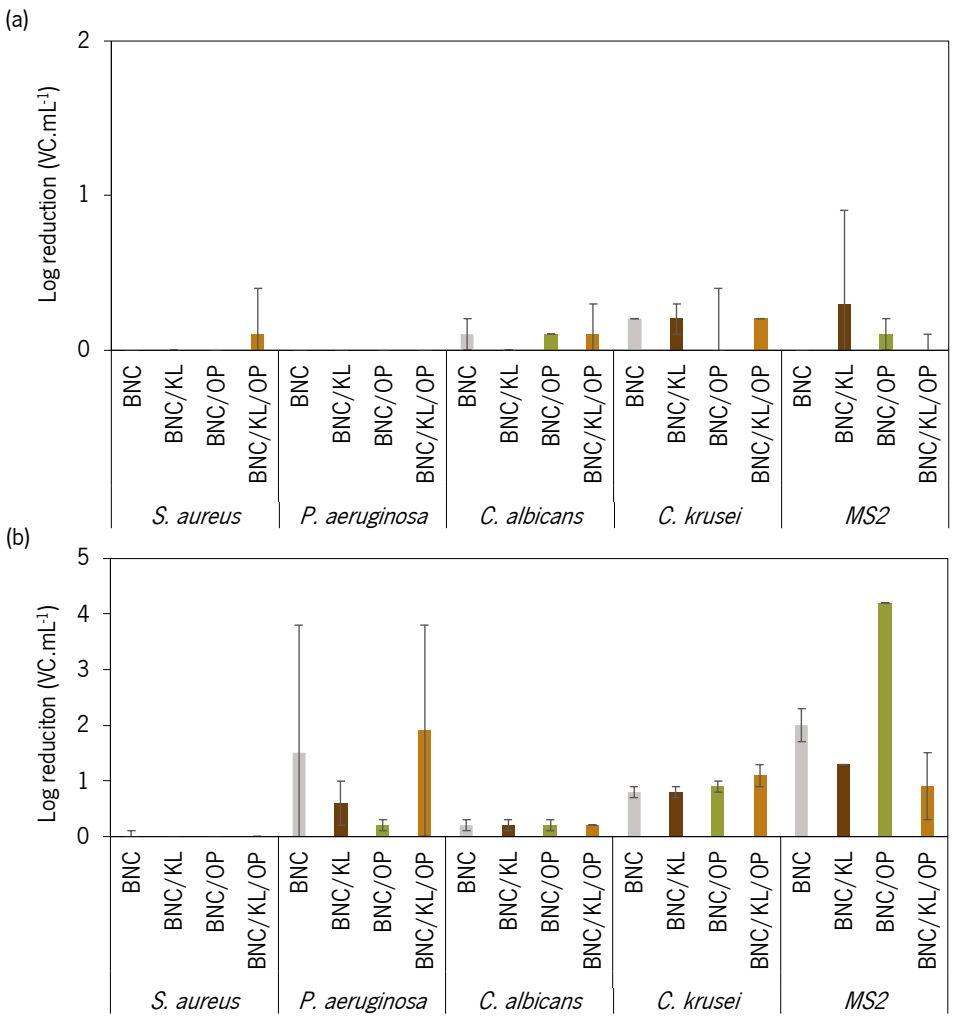



**Figure 3.22.** Antimicrobial activity: (a) shake flask and (b) contact killing of BNC and composites against *S. aureus*, *P. aeruginosa*, *C. albicans*, *C. krusei*, and MS2. VC stands for viable counts.

Other factors that could influence the antimicrobial activity are the surface charges of the bioactive agents. Gram negative bacteria have a higher negative surface charge, which could also explain the unexpected effectiveness against *P. aeruginosa*. The antimicrobial activity against Gram-positive bacteria can be justified by a higher electrostatic interaction and hydrogen bonding between the cell membrane and the KL moieties [356]. Despite the low antimicrobial activity obtained, liquor pulp precipitated lignins, as is the case with KL, are reported to be efficient against Gram-positive bacteria, like *S. aureus*, but not towards Gram-negative bacteria, as is the case with *P. aeruginosa*. In general, the reduced antibacterial efficiency of KL towards Gram-positive bacteria is due to the aliphatic –OH groups from the carbohydrates [353]. In addition, the difference in the antimicrobial activity of the different lignins may also be attributed to the recovery and preparation methods, pH and temperature [353]. Yang *et al.* reported antibacterial activity of lignin nanoparticles/polylactic acid against both Gram-positive and Gram-negative bacteria, suggesting that another influencing factor could be the size [357]. The stability of OP was discussed by Lammi *et al.*, who suggest that the OP grinding and drying process at 60 °C for 24 h may cause denaturation of the bioactive compounds [358]. Furthermore, other authors suggest that the thawing process, or even the period during which the OP remains at room temperature, may affect its properties. Hydrolysis of secoiridoids affects the concentration of the main phenols, thus altering the phenol constituents, which in turn affects the antibacterial activity [359, 360]. Antiviral activity with 2 log cannot be validated due to having the same values as the control sample.

Usually, a log reduction between 2 and 3 is required to be considered antimicrobial, it may also depend on the type of application [361]. Thus, according to the present results, no significant antimicrobial activity is verified. This may be due to the low release and size of the macromolecules. Although several authors in the literature state that KL has antimicrobial activity, it should be considered that this property is variable, since it depends on the source and isolation method. Furthermore, OP has shown bacteriostatic effect against different pathogens [362].

### 3.5.12. Antioxidant properties

The implantation of biomaterials into the human body induces an inflammatory response, primarily motivated by oxidative stress resulting from increased reactive oxygen species (ROS) production [363]. Therefore, implants should exhibit antioxidant activity to neutralise ROS and prevent the establishment of an oxidative environment that could compromise their long-term stability. KL and

OP possess methoxy and phenol groups in their structure, contributing to their antioxidant activity and reducing the ROS concentration [364-366]. Thus, the antioxidant activity of BNC composites was evaluated using the DPPH assay (Fig. 3.23).

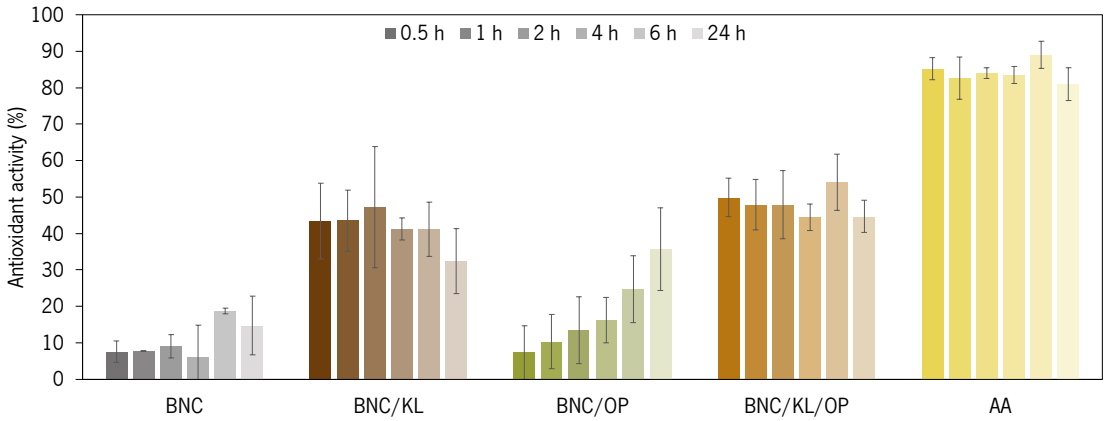



**Figure 3.23.** Antioxidant activity of BNC composites. AA was used solely as positive control.

BNC does not exhibit intrinsic biological properties; however, a residual antioxidant activity (below 20%) was observed, as reported in the literature [367, 368]. Following the incorporation of polyphenol agents, this biological property generally increased. KL reaches an initial boost compared to OP, which could, on one hand, be attributed to the larger particle size of KL that is more available at the BNC surface. On the other hand, BNC/OP presents a lower pore size, which indicates the presence of smaller OP particles inside the pores and greater phenolic content, both of which are believed to enhance diffusion efficiency [369]. DPPH is a small molecule (nearly 1 nm) thus, it is able to permeate through the pores of BNC interacting with KL and OP inside the BNC, despite the low release profile verified. Therefore, the antioxidant activity of BNC/OP increases over time, reaching a higher percentage at 24 h compared to BNC/KL. This may be justified by the lower diffusion of OP particles that required a longer period. Crugeira *et al.* demonstrated that BNC produced using OP hydrolysate as a substrate exhibited a more gradual release of phenolic compounds, which corresponded to an increased antioxidant activity of approximately 40% in DPPH assays [334]. However, the antioxidant activity of BNC/KL and BNC/KL/OP diminishes after 24 h. In the present study, a maximum activity of around 55% was achieved for both composites. This moderate activity is likely due to their larger particle size and lower porosity, which may limit the effective release of active compounds. This antioxidant activity

may help neutralise the ROS generated during inflammatory processes, which is particularly important for implants given the high incidence of post-operative complications.

## 3.6. Conclusions

The exhaustion methodology employed for BNC functionalisation resulted in only a partial incorporation of the organic active agents, KL and OP. The limited uptake was not a problem of methodology, but the particle size of the macromolecules. The more adequate solubilisation medium proved insufficient for achieving optimal functionalisation. Consequently, the resulting composites exhibited limited antimicrobial and antioxidant activities. In addition Kraft lignin in particular, is too heterogeneous as a consequence of its processing method. Thus its characterisation for potential application in biomedicine is thus limited. In addition, further studies are required for a fundamental knowledge of the impact of lignin on the human body.

# Chapter 4

## Functionalisation with inorganic agents[3]

[3] This chapter is based on the following future publications:

Peer-reviewed article:

Melro, L.; Fernandes, M.; Mehravani, B.; Ribeiro, A. I.; Mitu, B.; Satulu, V.; Rodrigues, A. C.; Gama, M.; Padrão, J.; Zille, A.; "BNC-based hernia mesh with prospective decrease of post-operative infections – Part I (*ex situ* and *in situ* production and characterization)".

# 4. Functionalisation with inorganic agents

## 4.1. Introduction

This chapter describes the three methodologies applied in the functionalisation of bacterial nanocellulose (BNC) with inorganic particles. The different methods were compared through characterization, namely thermal analysis, morphology, surface chemistry, and antimicrobial properties.

To understand the most adequate functionalisation methodology of BNC, both *ex situ* and *in situ* methods were tested. For the *ex situ* methodology in particular, filtration and exhaustion were chosen, having the active agents, metal particles been synthesised previously. For the *in situ* methodology, the particles were synthesised in the presence of the BNC membrane. Metal particles modified BNC composites were analysed to assess their potential as antimicrobial implants, and characterised accordingly for antimicrobial activity, swelling capacity, particle release, for chemical and physical characteristics, and thermal stability.

## 4.2. Materials

For the syntheses of the metal particles, all reagents were used as received and without further purification: tetrachloroauric (III) acid trihydrate ($HAuCL_4$), purchased from Thermo Fisher Scientific Inc. – Massachusetts, United Sates of America (USA); silver nitrate ($AgNO_3$) obtained from Solstice Advanced Materials – New Jersey, USA; sodium borohydride ($NaBH_4$) acquired at VWR Chemicals BDH – Carnaxide, Portugal; copper (II) sulphate pentahydrate ($CuSO_{4\cdot5}H_2O$), sodium hydroxide (NaOH), sodium hypophosphite monohydrate ($NaPO_2H_2$), ascorbic acid ($C_6H_8O_6$), tri-sodium citrate dihydrate ($C_6H_5Na_3O_7{\cdot}2H_2O$), and sodium chloride (NaCl), purchased at Merck Life Science – Algés, Portugal. Ultrapure water with a resistance of 0.055 MΩ cm was used in all the experiments. All the glassware was cleaned before and after syntheses with a solution of 7% (v/v) of nitric acid ($HNO_3$, Panreac AppliChem – Barcelona, Spain). For the Au nanoparticles synthesis, a mixture ratio of 3:1 (v/v) of hydrochloric acid (HCl, Thermo Fisher Scientific Inc. – Massachusetts, United Sates of America) and nitric acid ($HNO_3$, Panreac AppliChem – Barcelona, Spain), also named aqua regia, was used instead. All glassware was rinsed with distilled water ($dH_2O$) prior to the experiments.

Cultivation materials and methods of *Komagataeibacter hansenii* (ATCC 53582) and the preparation of simulated body fluid (SBF) are described in Section 3.2.

The bacteria tested for the antimicrobial activity assays were *Staphylococcus aureus* (ATCC 6538) and *Pseudomonas aeruginosa* (ATCC 27853) were supplied from American Type Culture Collection (ATCC, Virginia, USA). Trypticase soy broth (TSB) and nutrient broth (NB) media were purchased from Merck Life Science, Algés, Portugal. Agar was acquired from Liofilchem (Italy). All the media were prepared in distilled water ($dH_2O$) and autoclaved at 121 °C for 20 min. #271 medium contains 10 $g{\cdot}L^{-1}$ tryptone (Panreac AppliChem – Barcelona), 1 $g.L^{-1}$ yeast extract, 8 $g.L^{-1}$ NaCl, 1 $g.L^{-1}$ glucose, 0.294 $g.L^{-1}$, calcium chloride ($CaCl_2$, AnalytiChem Belgium NV – Zedelgem, Belgium), and 10 $mg.L^{-1}$ thiamine (Merck Life Science – Algés, Portugal).

## 4.3. Methods

### 4.3.1. Cultivation of *Komagataeibacter hansenii*

*K. hansenii* was cultivated according to Section 3.3.1.

### 4.3.2. Synthesis of Au nanoparticles

The first synthesis of Au nanoparticles (Fig. 4.1a) included mixing and boiling 13 mL of a 320 $mg{\cdot}L^{-1}$ stock solution of gentamicin sulphate solution (203 $mg.^{-1}L$), 2 mL of NaOH, 1 M), and 5 mL of $HAuCl_4$ (5 mM). For the *in situ* method, when the mixture turned red, the BNC was immediately immersed in the solution and kept for 1 h. Due to the presence of gentamycin, a potent broad-spectrum antibiotic, this synthesis was replaced by another, to ensure the antibacterial activity of the nanoparticles was only due to the nanoparticles, and not the antibiotic.

The second and final synthesis of Au nanoparticles was based on the method previously described by Zhao and co-workers (2012) [370]. Briefly, a round-bottom flask containing 10 mM of NaCl and 0.25 mM of $HAuCl_4$ in 100 mL of water was heated to boiling point. Subsequently, 0.7 mL of 5% (w/v) of reducing agent tri-sodium citrate dihydrate, was added and the dispersion was maintained under magnetic stirring at boiling temperature for 20 minutes and left at room temperature until cooled.

### 4.3.3. Synthesis of Ag nanoparticles

Ag nanoparticles were synthesised (Fig. 4.1b) based on the method described by Wan et al. (2013) [371] with some modifications. In brief, for the preparation of the 4 nm starter seeds, 20 mL of a 1% (w/v) tri-sodium citrate dihydrate solution was added to a round-bottom flask containing 75 mL of deionized water. This solution was heated to 70 °C under reflux. The heating was maintained for 15 minutes until further addition of 1.7 mL of 1% (w/v) $AgNO_3$, quickly followed by 2 mL of 0.1% (w/v) reducing agent $NaBH_4$, under constant intense magnetic stirring. The dispersion was kept at 70 °C for 1 h and cooled to room temperature before adjusting the final volume to 100 mL. For the synthesis of 20 nm Ag nanoparticles, 2 mL of the previously prepared citrate solution was boiled in another round-bottom flask containing 40 mL of deionized water for 15 minutes. Under intense magnetic stirring, 10 mL of the 4 nm Ag nanoparticles dispersion was added, followed by 1.7 mL of the $AgNO_3$ previously prepared. Magnetic stirring and heating were maintained for 1 h under reflux, after which the dispersion was cooled to room temperature.

### 4.3.4. Synthesis Cu and $CuO_2$ particles

The synthesis of Cu and $Cu_2O$ (Fig. 4.1c-d) is similar, with the difference being the use of NaOH to obtain $Cu_2O$ particles, instead of water, which is the case for Cu. According to Mehravani and co-workers (2022), 100 mL of deionized water or NaOH (0.044 M) were heated up to 65 °C under magnetic stirring. Then, 40 mL of copper sulphate ($CuSO_4$, 0.01 M), 30 mL of ascorbic acid ($C_6H_8O_6$, 0.06 M), and 30 mL of sodium phosphinate ($NaPO_2H_2$, 0.028 M) were quickly added. The temperature was increased to 85 °C and kept for 1h under magnetic stirring. Although ascorbic acid acts both as reducing and capping agent, in this case, it is the sodium phosphinate the main reducing agent, which also acts as a catalyst. In fact, by combining both, the oxidation was avoided and the velocity of the reaction increased [372].

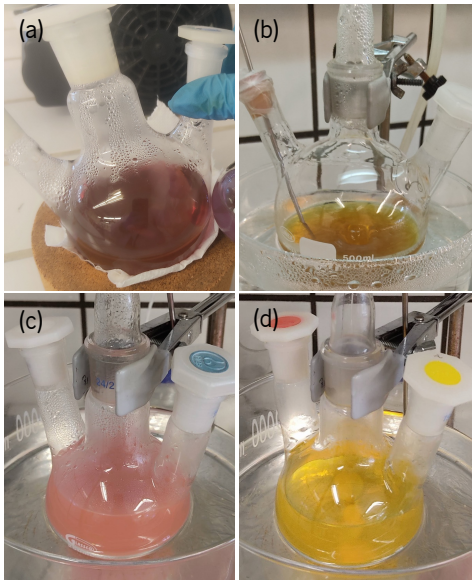



**Figure 4.1.** Syntheses of (a) Au, (b) Ag, (c) Cu, and ($Cu_2O$) particles.

### 4.3.5. Functionalisation methodologies

Different functionalisation strategies were employed to determine the most effective and suitable approach for achieving an efficient internalization of the active agents. Membranes were functionalised through *ex situ* methodologies including electrophoresis, filtration, and exhaustion, and through *in situ* synthesis. The aim was to ensure the most uniform functionalisation, the desired antimicrobial activity, while at the same time having a controlled release. To enhance the functionalisation process, membranes with 1 mm thicknesses were previously pressed at 5 kN for 30 seconds to remove excess water, before being placed in contact with the agent's dispersions. A ratio of BNC area/metal particles dispersion of 0.09 $m^2 \cdot L^{-1}$ was used for the *ex situ* functionalisations. After functionalisation, the metal particles functionalised BNC were rinsed with $dH_2O$ (0.02 $m^2 \cdot L^{-1}$) for 4 h under very mild magnetic stirring (100 rpm) to remove unattached metal particles and to neutralize the alkaline character of the functionalised BNC. The samples were then sterilised at (121 °C, 20 min) and stored until further use.

***Ex situ***

Electrophoresis was attempted but considering the negative charge of the developed metal particles and the negatively charged BNC [373], it did not work. Therefore, only vacuum filtration and exhaustion were considered as *ex situ* functionalisation methods.

Vacuum filtration

For the filtration method a vacuum pump was used, with the BNC replacing the traditional paper filter (Fig. 4.2). A volume of 30 mL of the bioactive agent are retained in the membrane through vacuum at 1 bar (Figure 4.2). The never-dried membrane was placed inside the Büchner funnel, completely covering the available flat area.

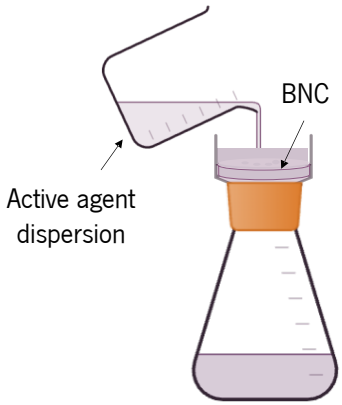



**Figure 4.2.** Schematic representation of BNC functionalisation through vacuum filtration.

Exhaustion

Inorganic agents were previously prepared before placing the BNC membranes inside the containers from the Ibelus C-720 dyeing equipment (Pregitzer Lda., Guimarães, Portugal) (Fig. 4.3). Metal particles (200 mL) remained in aqueous solution after being synthesised as described in the Sections 4.3.2 – 4.3.4. The BNC samples were left overnight (37 °C, 2 °C·min$^{-1}$, 50 rpm, cycles of 50 seconds).

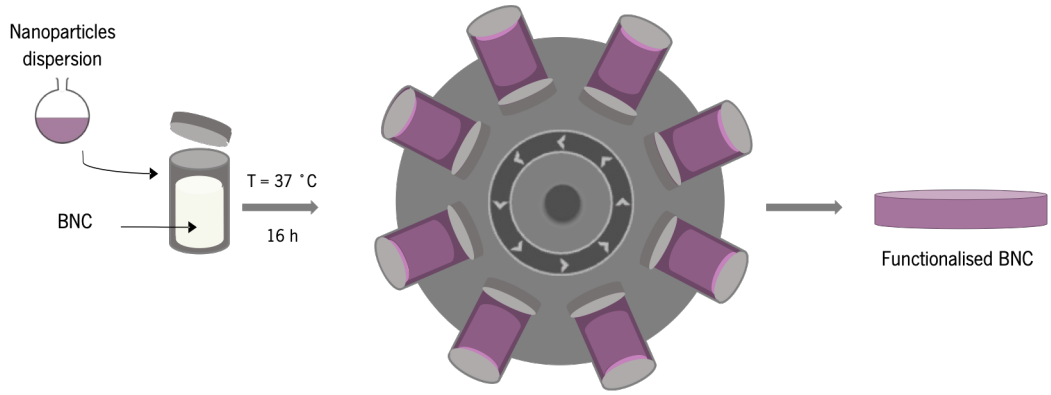



**Figure 4.3.** Schematic representation of BNC functionalisation through exhaustion using an Ibelus machine.

### *In situ*

In the present work, the *in situ* method was applied only in the functionalisation of the BNC with the metal particles. In brief, the particles synthesis was initiated as described in Sections 4.3.2 – 4.3.4, and immediately after the last compound is added to the solution, the BNC is introduced and the reaction left to react for the remaining time of the synthesis (Fig. 4.4). This method, in theory, promotes the entrapment of metal particles within the nanofibrous structure of the BNC, therefore preventing the particles leaching.

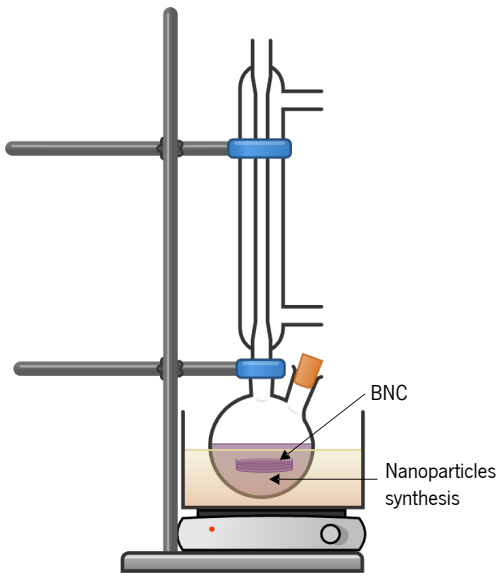



**Figure 4.4.** Schematic representation of BNC functionalisation through *in situ* synthesis of metal particles.

Prior to morphological, thermal, and chemical analyses, all samples were freeze-dried.

## 4.4. Characterisation

### 4.4.1. Charge and size of the particles

Size and agglomeration of metal particles was estimated using UV-vis spectroscopy (UV-vis 1800, Shimadzu, Switzerland). Dynamic light scattering (DLS), another non-invasive technique, is able to provide more accurately information about the size and size distribution of colloidal solutions by measuring the intensity of the laser light when scattered by molecules in solution. The scattering is correlated to the hydrodynamic radius, as in the Stokes–Einstein equation measuring fluctuations in light intensity over time that depend on the size of the particles and the viscosity of the medium. Particles of different size and aggregation status are recognized by their increasing hydrodynamic radius value and this value may vary in function of colloidal preparation method, solvent conditions, temperature, or time. The distribution coefficient (particle dispersion index, PDI) is an important data that reveals the uniformity of the experiment. A value below 0.05 indicates a monodisperse system, values between 0.08 – 0.7 suggest a moderate dispersion system, but if the superior to 0.7 it reveals a varied size distribution [374, 375]. Zeta potential measurements help to understand the electric charge on the surface of particles, allowing to predict the stability of a colloidal system. Therefore, the stability of colloidal metal particle suspensions and its grade of agglomeration can be determined through this technique. Also, the pH effect on the stability of the nanoparticle's suspensions can be determined through the zeta potential. The hydrodynamic size distribution, PdI and zeta potential of the metal particles dispersion were measured using a Zetasizer Nano ZS (Malvern Instruments, Malvern, UK). Data was collected after 30 scans at 25 ± 1 °C. The presented values were obtained by averaging measurements of three samples.

### 4.4.2. Morphology and elemental composition

The metal particles were examined using a scanning transmitted electron microscopy detector (STEM) with an ultra-high resolution field emission gun (FEI NOVA 200 Nano SEM), with an accelerating voltage of 15 kV (1.0 nm resolution). Dispersions were placed on Cu-C TEM grids (S160-4 AGAR). Regarding BNC composites, 1 × 1 cm samples with 1 mm of thickness were cut in liquid nitrogen and fixed with double-sided carbon tape on an aluminium metal support. Subsequently, the samples were covered, using a sputtering technique, with a 16.5 nm thick Au-

Pd film (80/20% by weight) using a high-resolution sputter coater (208HR Cressington Company, UK) and monitored by a high-resolution thickness controller (MTM-20, Cressington, UK).

Analyses of the surface and cross-section morphology of the BNC and BNC composites were also obtained through scanning electron microscopy (SEM) using a FlexSEM 1000 (Hitachi, Japan), with an acceleration voltage of 15 kV. Ultra-high-resolution field emission gun – scanning electron microscope (FEG–SEM) (Field Electron and Ion Company, Hillsboro, Oregon) with an accelerating voltage of 10 kV, using both a secondary Everhardt-Thornley detector and a Through Lens Detector in SE mode and under high vacuum conditions, were used to obtain the images of the metal particles and the BNC/metal particles. Elemental analysis was performed using energy dispersive spectrometer (EDS).

The size and area of the particles were determined using the microscope images with the aid of ImageJ 1.54g software (version Java 1.8.0_345, Wayne Rasband and contributor, National Institutes of Health, USA).

### 4.4.3. Chemical characterization

The BNC membranes were analysed by attenuated total reflectance-Fourier transform infrared (ATR-FTIR). A Shimadzu IRAffinity-1S FTIR spectrophotometer (Switzerland), coupled with a HATR 10 accessory with a diamond crystal, was used to record the films spectra. BNC films were dried overnight at 40 °C. The samples were placed onto the crystal using air at 20 °C. A background scan with no sample and no pressure was acquired before the spectra of the samples were collected. A total of 40 scans at a spectral resolution of 8 $cm^{-1}$, over a range 400 – 4000 $cm^{-1}$ were recorded.

X-ray photoelectron spectroscopy (XPS) is a quantitative technique for measuring the chemical composition of materials surface (depth of 50 – 70 Å) that also indicates the binding states of the elements. It is commonly used to characterize thin films and surface modifications [376, 377]. XPS analyses were performed on 1 mm thickness freeze-dried samples using K-Alpha Thermo Scientific (ESCALAB™ XI+, East Grinstead, UK) spectrometer equipped with a 180° double focusing hemispherical analyser. Survey spectra were recorded at pass energy of 50 eV to determine the elemental composition of the BNC composites. Peak position was calibrated according to the standard C1s peak (284.7 eV) and O1s (532.6 eV). High-resolution spectra were collected using an analysis area of ≈1 $mm^2$. Spectra were analysed for elemental composition for C1s and O1s, with binding energy regions measured at a pass energy of 20 eV to evaluate the

elemental bonding state of the composites. The spectra acquisition and data processing were performed using the advanced Avantage data software (Thermo Avantage v5 9921, East Grinstead, UK). The least-squares peak analysis software, XPSPEAK (version 4.1, Prof. Raymond W.M. Kwok, Chinese University of Hong Kong), performed deconvolution into sub-peaks using the Gaussian/Lorentzian sum function and Shirley-type background subtraction. No tailing function was considered in the peak fitting procedure. The components of the various spectra were mainly modelled as symmetrical Gaussian peaks unless a certain degree of Lorentzian shape was necessary for the best fit. The best mixture of Gaussian–Lorentzian components was defined based on the instrument and resolution (pass energy) settings used as well as the natural line width of the specific core hole [303].

### 4.4.4. Thermal analysis

Thermogravimetric analyses (TGA) were carried out in a Hitachi STA7200 (Tokyo, Japan). Samples (5 – 7 mg) were placed in platinum pans and tested from 25 to 600 °C with a heating rate of 10 °C·min$^{-1}$ and under a nitrogen flow rate of 200 mL·min$^{-1}$.

### 4.4.5. Swelling profile

The swelling degree (%) of the BNC samples was determined gravimetrically and was based on the average variation of the sample's wet weight, during the assay. The circular BNC films with a volume of 2.0 cm$^3$, were immersed in 5 mL of SBF. The assay was conducted at 37 °C under shaking at 110 rpm. At determined time intervals, the wet weight of the samples was recorded, after removing the excess of surface water by suspending the BNC in polypropylene wires for 1 minute (Fig. 3.4). The assay was conducted until weight stabilization (full swelling). Swelling degree was determined using the following equation:

$$\text{Swelling degree } (\%) = \frac{W_t - W_0}{W_0} \times 100 \qquad (3.5)$$

where $W_t$ is the weight of the sample at time t and $W_0$ denotes the initial weight of the BNC samples. Quintuplicates of each condition were used.

### 4.4.6. One-month release

Circular samples of 16 mm diameter and 1 mm thickness were immersed in SBF medium at 37 °C with mild agitation (shaking speed of 50 rpm). Aliquots were collected after 1 month. Considering the plasmonic properties of the metal particles, the particles concentration was quantified using ultraviolet-visible spectroscopy (UV-vis 1800, Shimadzu, Switzerland). Calibration curves were determined for extrapolation, Au: $y = 0.0076x + 0.0047$, $R^2 = 0.994$, Ag: $y = 0.0103x + 0.0079$, $R^2 = 0.9982$, Cu: $y = 0.0015x + 0.0125$, $R^2 = 0.9983$, Cu2O: $y = 0.0456x + 0.0029$, $R^2 = 0.9871$. However, due to the low release and insufficient equipment accuracy, samples were analysed through atomic absorbance spectroscopy (AAS) to determine the metal particle content in the membranes using a novAA® 350 AJ Analytical Instrumentation, and subsequently their release. Samples (triplicates) were removed from the medium after 1 month, left to dry, and then digested in piranha solution (0.6 : 1.0 (v/v) $H_2O_2$ : $H_2SO_4$) and neutralized with 3M NaOH. Piranha was used because it is able to completely dissolve BNC. Exceptionally, Au nanoparticles were not analysed due the impossibility of digestion of Au by piranha solution. *Aqua regia* can dissolve Au nanoparticles however, it cannot dissolve BNC and mixing both solutions is extremely dangerous.

### 4.4.7. Antimicrobial activity

The antibacterial efficacy of the functionalised BNC was assessed quantitatively according to the standard contact killing (American Society for Testing and Materials (AATCC) 100-TM100) and the shake flask (ASTM-E2149-01) methods. BNC samples were evaluated quantitatively following an adaptation of the standard AATCC 100-TM100. Bacteria inocula were prepared in TSB *(S. aureus)* and NB *(P. aeruginosa)* and incubated overnight at 37 °C and 120 rpm. Each test was carried out using an initial concentration of $1.0\times10^7$ colony-forming units (CFUs)·$mL^{-1}$.

For the contact-killing assay, samples with dimensions 2x2 cm were placed in contact with 20 µL of bacteria suspension in PBS at 37 °C for 1 h. Before contact with samples (0 h) and after contact with samples (1 h) the bacteria were serially diluted and cultured onto trypticase soy agar (TSA) and nutrient agar (NA) plates. In the case of the shake flask method, samples of 1x1 cm were incubated in 5 mL of bacteria suspension in PBS at 37 °C and 120 rpm. Like in the previous method, the bacteria were serially diluted before contact with samples (0 h) and after contact with samples (5 h) and cultured onto TSA and NA plates. Quantitative results were obtained by counting

the colonies of surviving bacteria on the agar plates. Antimicrobial activity was reported qualitatively in terms of log reduction, calculated as the ratio between the number of surviving bacteria colonies present on the agar plates, before and after contact with the BNC.

## 4.5. Results and discussion

### 4.5.1. Size and charge and of the particles

The assessment of the size and stability of the synthesised metal particles was performed after each synthesis through UV-vis. Due to their nanoscale, metal particles possess plasmonic properties. Hence, there is a characteristic peak in the UV-vis spectrum for each element and size. Thus, from the spectra, changes in the size or agglomeration can be inferred through a shift to lower wavelengths [378]. Fig. 4.5 shows the successful synthesis of the metal particles, indicating the wavelength at the maximum absorbance. Au and Ag nanoparticles exhibit the characteristic peaks at 527 and 402 nm, respectively [379, 380]. Cu particles have two surface plasmon resonance bands at approximately 500 and 600 nm. Bimetallic copper particles, $Cu_2O$, present a band at lower wavelengths compared to Cu particles, at 458 nm, which has been reported previously [381].

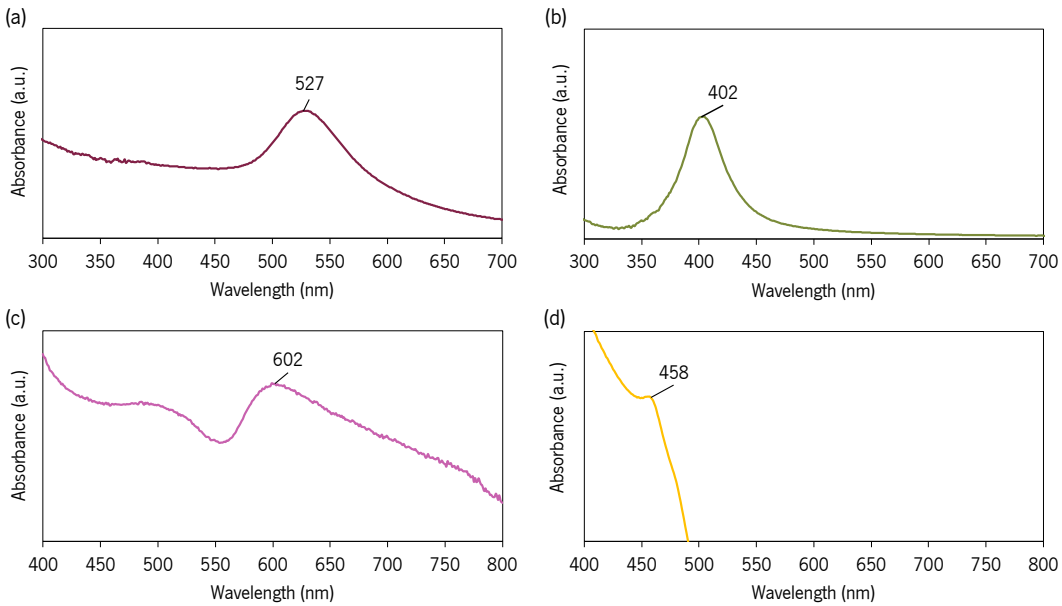



**Figure 4.5.** UV-vis spectra of (a) Au, (b), Ag, (c) Cu, and (d) $Cu_2O$ particles. The maximum absorbance is highlighted.

The DLS, zeta potential, and STEM analyses of the metal particles show that both Ag and Au present a more stable, circular and uniform distribution. According to DLS (Fig. 4.6), the

hydrodynamic diameter of Au is 30.9 ± 0.450 nm (PdI 0.550 ± 0.0100) and for Ag it is 23.9 ± 0.260 nm (PdI 0.550 ± 0.0200). These sizes are slightly larger than the STEM results (Fig. 4.7), 27.6 ± 2.80 nm and 17.9 ± 3.10 nm for Au and Ag, respectively. The reason for the higher diameter obtained through DLS is because DLS measures the hydrodynamic diameter, hence the Brownian motion of particles. In addition, aggregated particles are slower and often appear as larger size peak, higher Z-average size and/or broader PdI [382, 383]. Thus, the DLS measurements of the particles Cu (Z-ave: 35,958.7 ± 24,3350 nm, PdI 0.720 ± 0.260) and $Cu_2O$ (Z-ave: 981.9 ± 41.70 nm, PdI 0.150 ± 0.0300), were not considered for comparison with STEM (Fig. 4.7) due to the large agglomeration and lack of uniform spherical shape. Instead, the area of the particles was determined from the STEM images, that show agglomeration and random shapes and sizes of Cu and $Cu_2O$ particles. The areas of the metal particles (Fig. 4.8) show a much larger area for $Cu_2O$ particles, 3,658 ± 2,486 $\mu m^2$, whilst the least stable Cu particles obtained 1.613 ± 1.096 $\mu m^2$. These results are contradictory to zeta potential values since $Cu_2O$ particles obtained a zeta potential of -44.3 ± 4.32 mV for $Cu_2O$ and hardly negative values for Cu particles, 9.88 ± 1.85 mV. The zeta potential measurements of both Au and Ag, confirm the stability of these nanoparticles with very negative values of -41.5 ± 2.61 mV and -58.4 ± 2.11 mV, respectively.

The aqueous dispersion of particles was analysed by DLS and zeta potential after the *in situ* syntheses and compared to the synthesis of metal particles in the absence of BNC. The results show that the *in situ* syntheses lead to a loss of stability of the particles, and the average diameter increases for Au (34.89 ± 0.501 nm) and Ag (29.22 ± 0.04200 nm), the smaller and more stable nanoparticles, while PdI decreases slightly. Contrarily, the average diameter decreases considerably for Cu (5,976.3 ± 2,032.3 nm) and $Cu_2O$ (408.50 ± 117.40 nm), whilst PdI increases reaching 1.00 for Cu particles, demonstrating the high size variation of these particles, which is in accordance with the zeta potential.

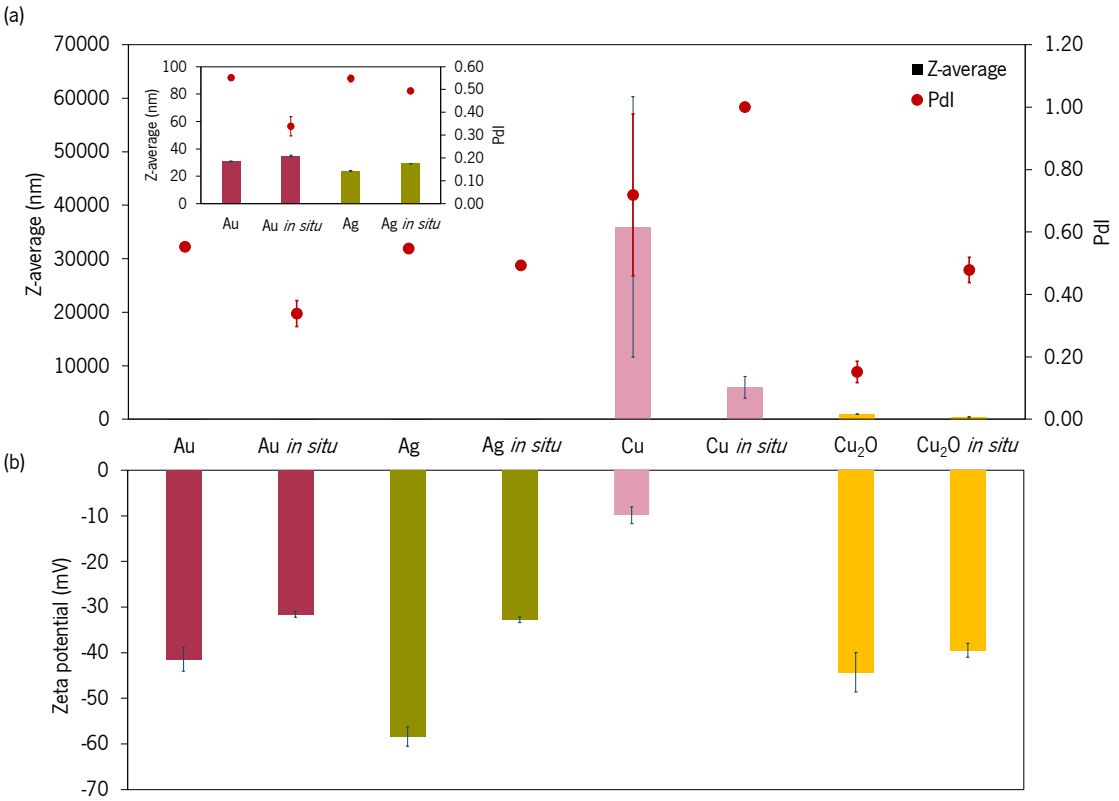



**Figure 4.6.** DLS measurements of (a) particle size and PdI and (b) zeta potential of the metal particles.

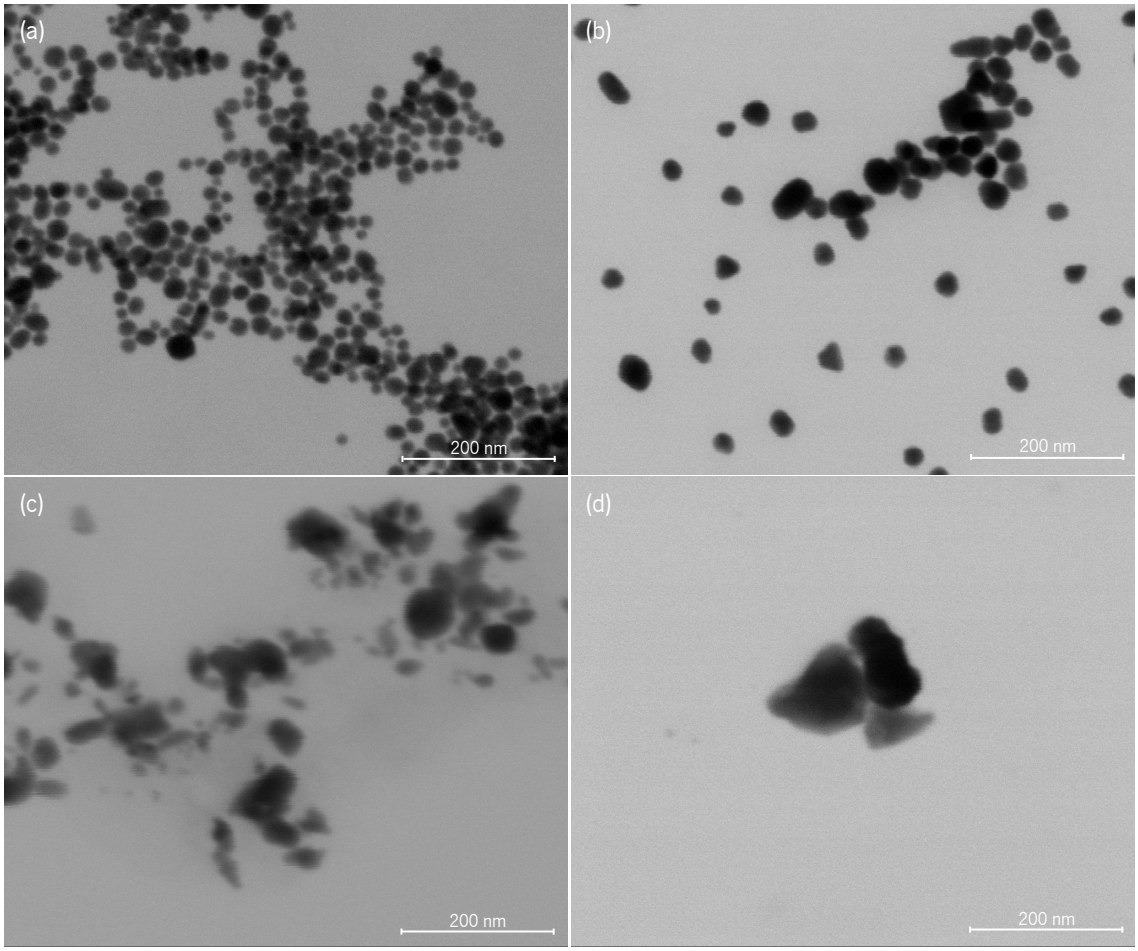



**Figure 4.7.** STEM images of metal particles (a) Au, (b) Ag, (c) Cu, and (d) $Cu_2O$.

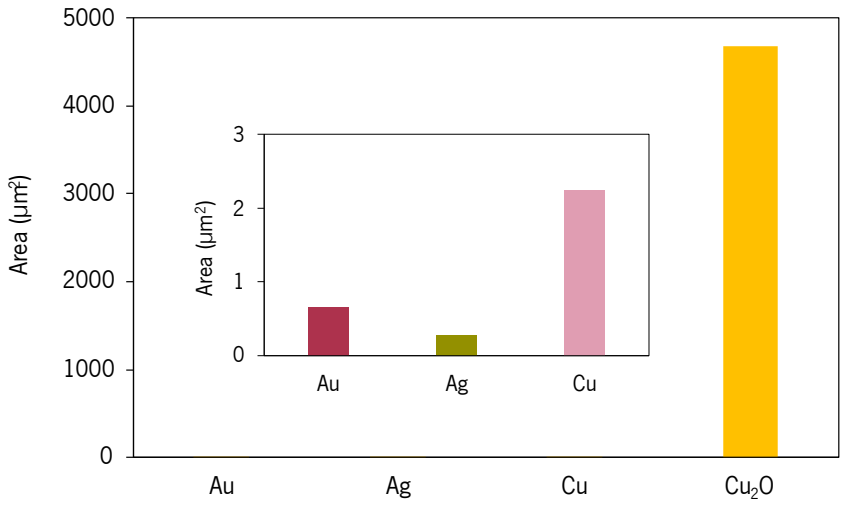



**Figure 4.8.** Area of the metal particles calculated through the STEM images.

### 4.5.2. Morphology and elemental composition

The vacuum filtered BNC samples, presented in Fig. 4.9, show the concentration of the metal particles where the pores of the Büchner funnel are, resulting in a heterogeneous functionalisation. In addition, the penetration of the metal particles within the nanofibrous structure of BNC is less effective. Nevertheless, both exhaustion and *in situ* methodologies result in seemingly similar functionalisation efficacy.

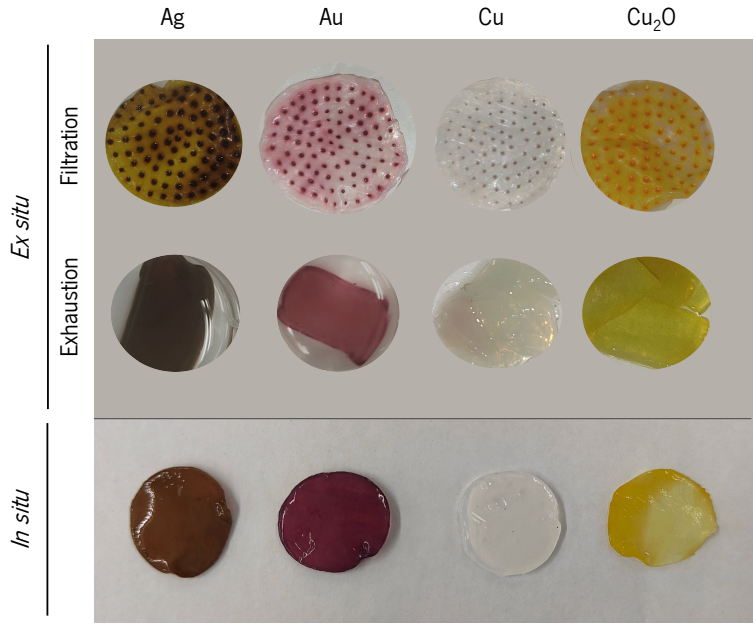



**Figure 4.9.** Functionalised BNC by *ex situ* methods: filtration and exhaustion, and *in situ*.

Through EDS (Fig. 4.10 – 4.13), the percentage of the atomic elements was determined in each BNC composite, by identifying the characteristic X-ray peaks and comparing the relative peak intensity of every element. Elemental mapping provides de spacial distribution of each element in each sample, which are in line with the elemental percentages. Elemental composition shows that through exhaustion method there is a higher percentage of the atomic element of the metal particle, suggesting a more efficient functionalisation. However, this result could indicate a higher deposition on the surface and is not accurate whether there was particle permeation.

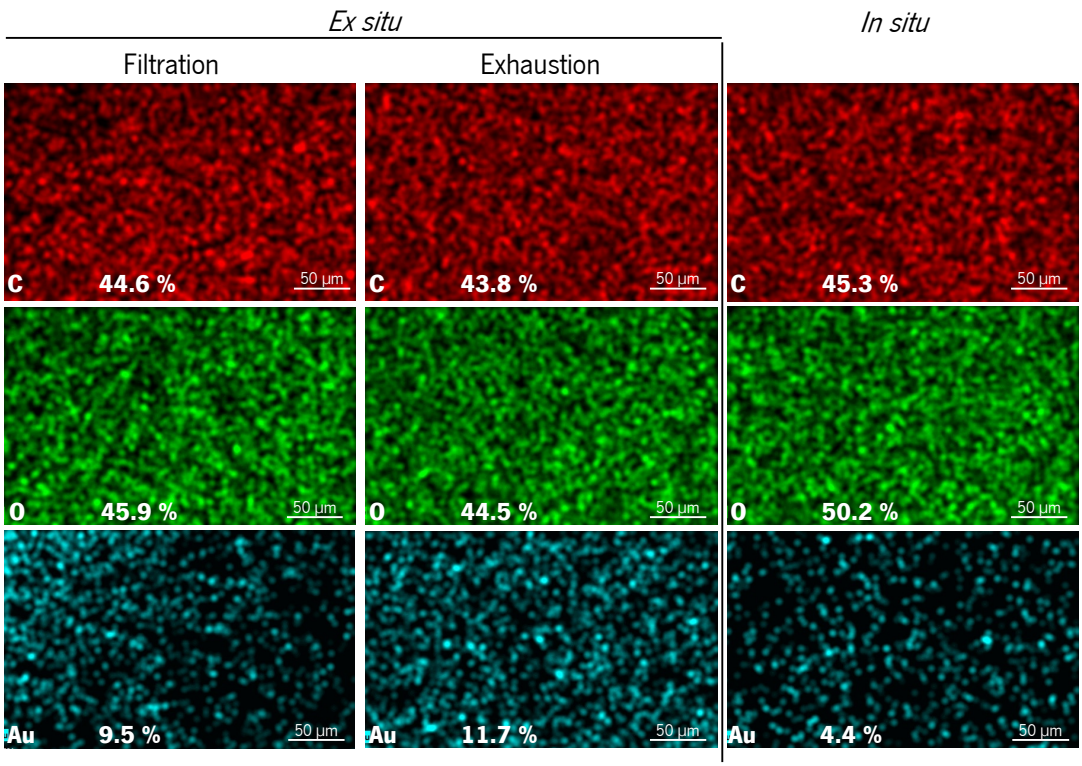



**Figure 4.10.** Mapping of BNC/Au nanocomposites and elemental mass % composition.

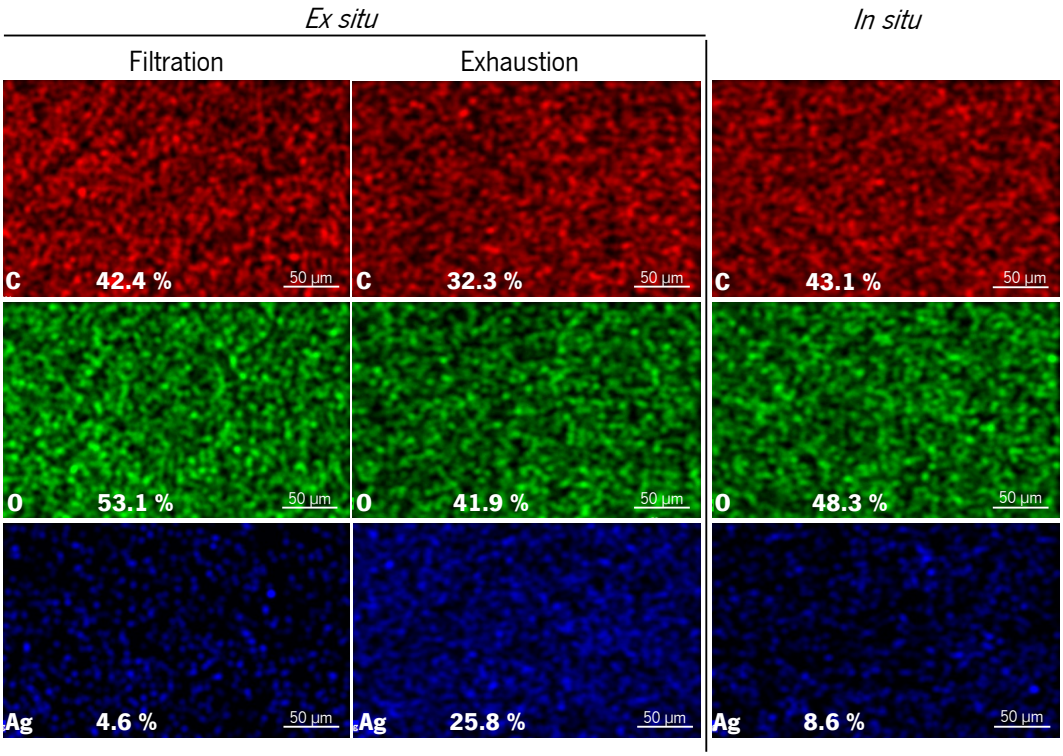



**Figure 4.11.** Mapping of BNC/Ag nanocomposites and elemental mass % composition.

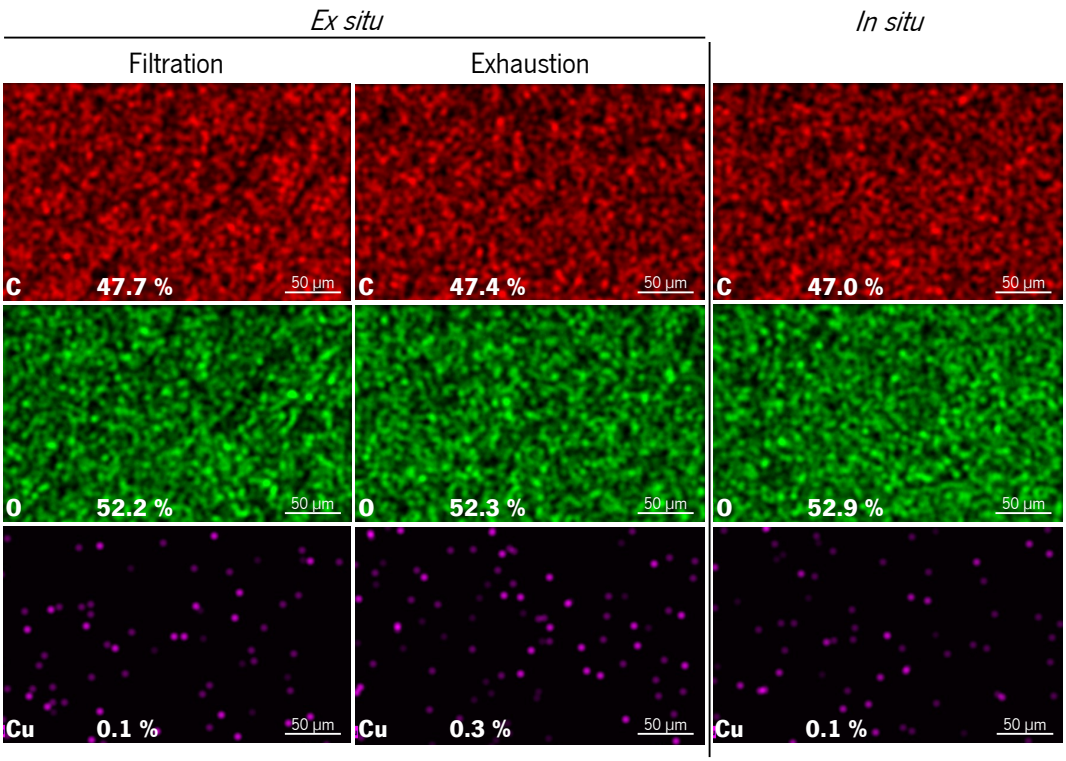



**Figure 4.12.** Mapping of BNC/Cu composites and elemental mass % composition.

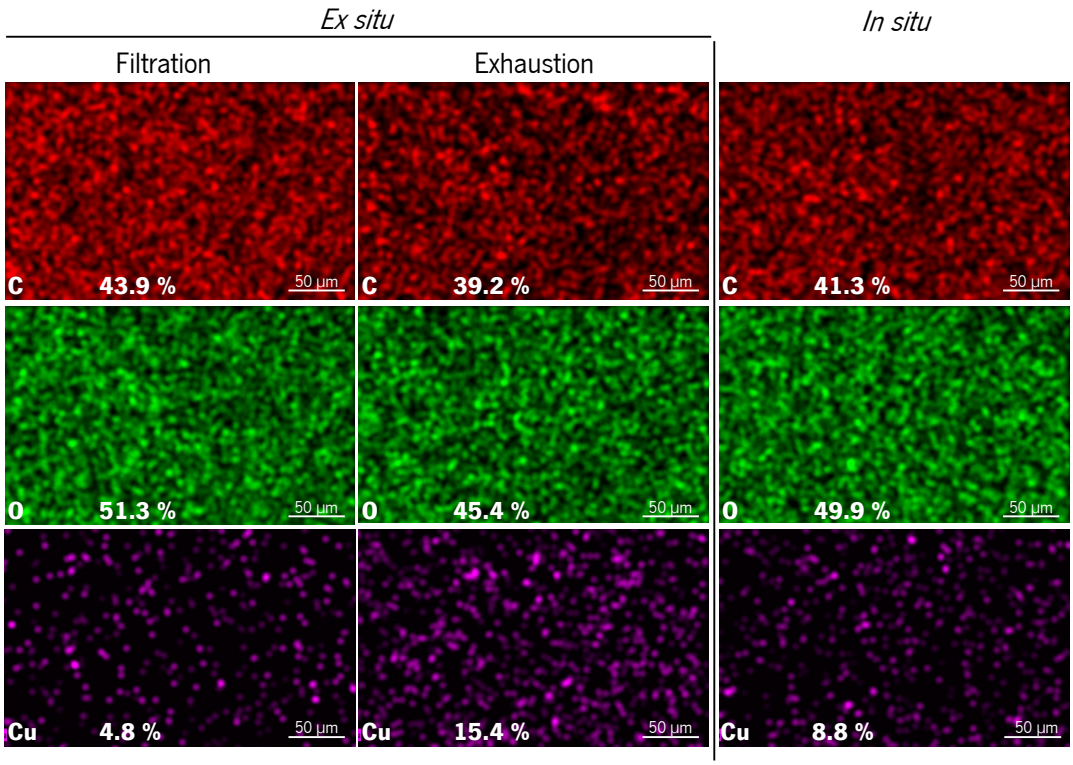



**Figure 4.13.** Mapping of BNC/$Cu_2O$ composites and elemental mass % composition.

### 4.5.3. Chemical composition

The surface chemistry was analysed by ATR-FTIR and the spectra are shown in Fig. 4.14. The characteristic broad band at 3340 $cm^{-1}$ of the stretching vibrations of –OH groups of BNC is maintained in the samples of the composites functionalised through the exhaustion method (Fig. 4.14b). For both filtration (Fig. 4.14a) and *in situ* (Fig. 4.14c) obtained samples, a very slight shift to lower wavenumbers, 3330 $cm^{-1}$, occurred. This suggests interactions between the metal ions and the –OH groups of BNC [384]. The low intensity band at 2890 $cm^{-1}$ from the aliphatic C–H stretching is present in all composites produced under the three different methodologies without significant changes [13]. Peaks at wavenumbers 1427, 1370, 1330, and 1057 $cm^{-1}$ correspond to $–CH_2$ bending vibrations, –CH bending vibration, OH in-plane bending, and C–O–C stretching of BNC, respectively [13, 101]. Peaks at 1157 $cm^{-1}$ and 895 $cm^{-1}$ correspond to in-plane asymmetric stretching and symmetric stretching of glycosidic bond (C–O–C) [101]. According to these results, interactions between the metal ions and the –OH groups of BNC seem to be the most significant changes in the composites, meaning that BNC maintains its characteristics.

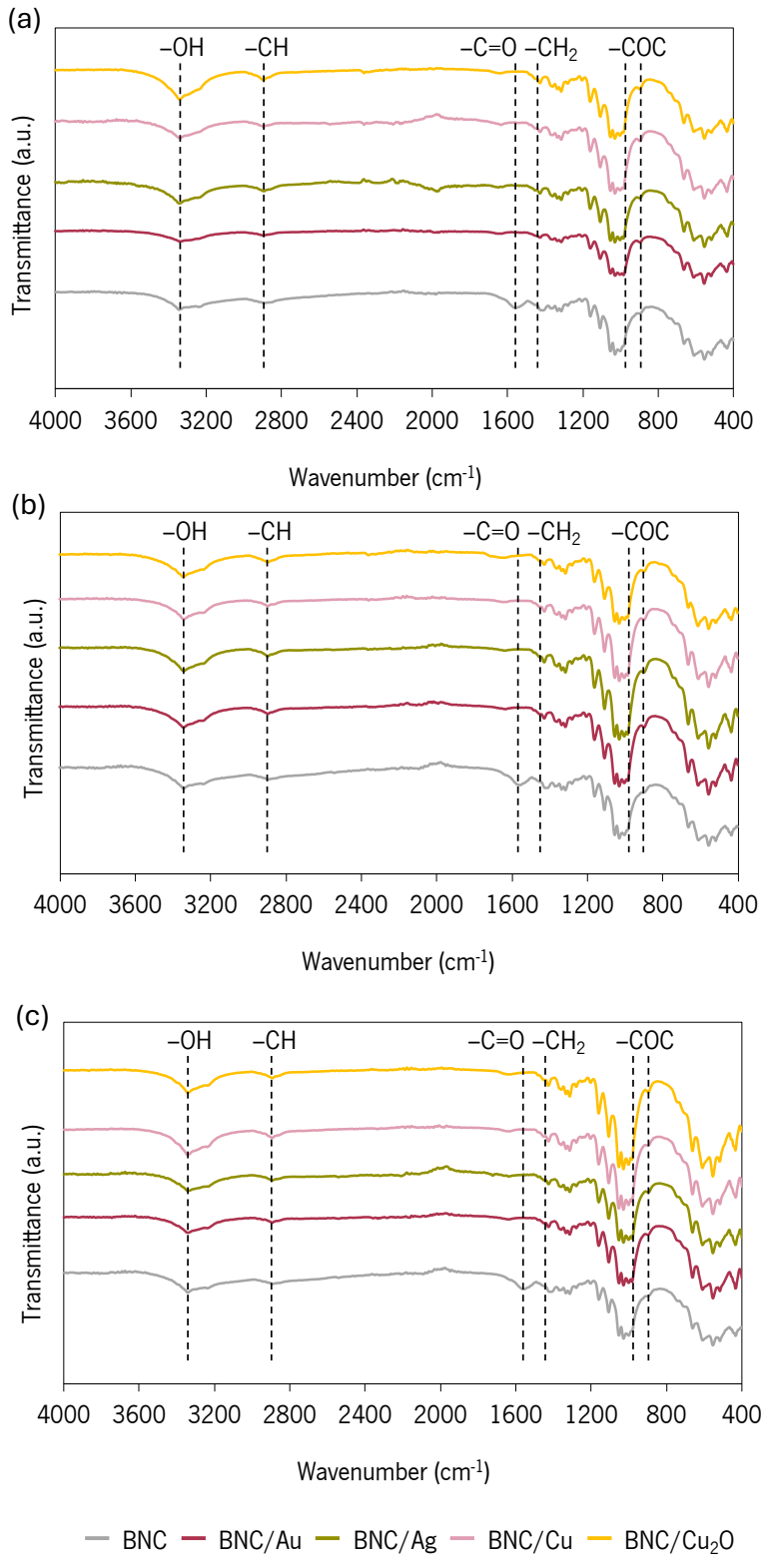



**Figure 4.14.** ATR-FTIR spectra of BNC/metal particle composites obtained through *ex situ* (a) filtration and (b) exhaustion, and (c) *in situ* methodologies.

### 4.5.4. Surface chemistry

XPS analysis was performed to investigate the surface chemical composition and oxidation states of the BNC composites. The survey spectra (Fig. 4.15) show the peaks attributed to C1s, O1s, Au4f, Ag3d, and Cu2p.

The spectra in Fig. 4.15a refer to the BNC/Au nanocomposite obtained by vacuum filtration, exhaustion, and *in situ* synthesis. According to the analysis, the typical Au4f peak appears at binding energies 83.60 and 83.80 eV ($Au^0$) for exhaustion and *in situ*, respectively [385]. It is however absent for filtration. This result suggests that the vacuum filtration is unable to retain the small Au nanoparticles (27.6 ± 2.80 nm) at the surface of the BNC, and as suggested by ATR-FTIR, no covalent bond was formed either. The BNC/Ag nanocomposite spectra in Fig. 4.15b, show the Ag3d peak at binding energies of 367.8 eV, assigned to AgO bonds all three functionalisation methodologies [386]. For BNC/Cu composites (Fig. 4.15c), the typical Cu2p peak appears at binding energies of 932.3 eV for *in situ*, related to Cu(0) or Cu(I) [387], but is absent for both *ex situ* functionalisation methodologies. The BNC/$Cu_2O$ spectra in Fig. 4.15d, shows Cu2p peak at binding energies 932.1 and 931.9 eV for filtration and *in situ*, respectively, but is absent in the samples functionalised through exhaustion. These results indicate that the *in situ* functionalisation is able to retain the particles at the surface of the BNC across all methodologies whilst the *ex situ* functionalisation, particularly vacuum filtration, results in partial or complete particle loss, considering the absence of Au4f and Cu2p peaks in these cases.

Regarding the BNC related peaks, in all samples, the C1s peak appears at the same binding energy of 286.3 eV, associated to C–O bonds, except for the BNC/$Cu_2O$ functionalised by vacuum filtration, with binding energy at 284.8 eV, related to C–C/C–H bonds [388]. The O1s peak is also rather similar between all samples with typical peaks at 532.4 – 532.6 eV, typical of O–C–O groups in cellulose, indicating the presence of oxygen-containing functional groups commonly found in cellulose [336, 388], except for the vacuum filtration functionalisation in the BNC/$Cu_2O$ composites, with binding energies of 531.2 eV. The shift towards lower binding energies in C1s for BNC/$Cu_2O$ obtained by vacuum filtration is chemically significant and may indicate increased electron density.

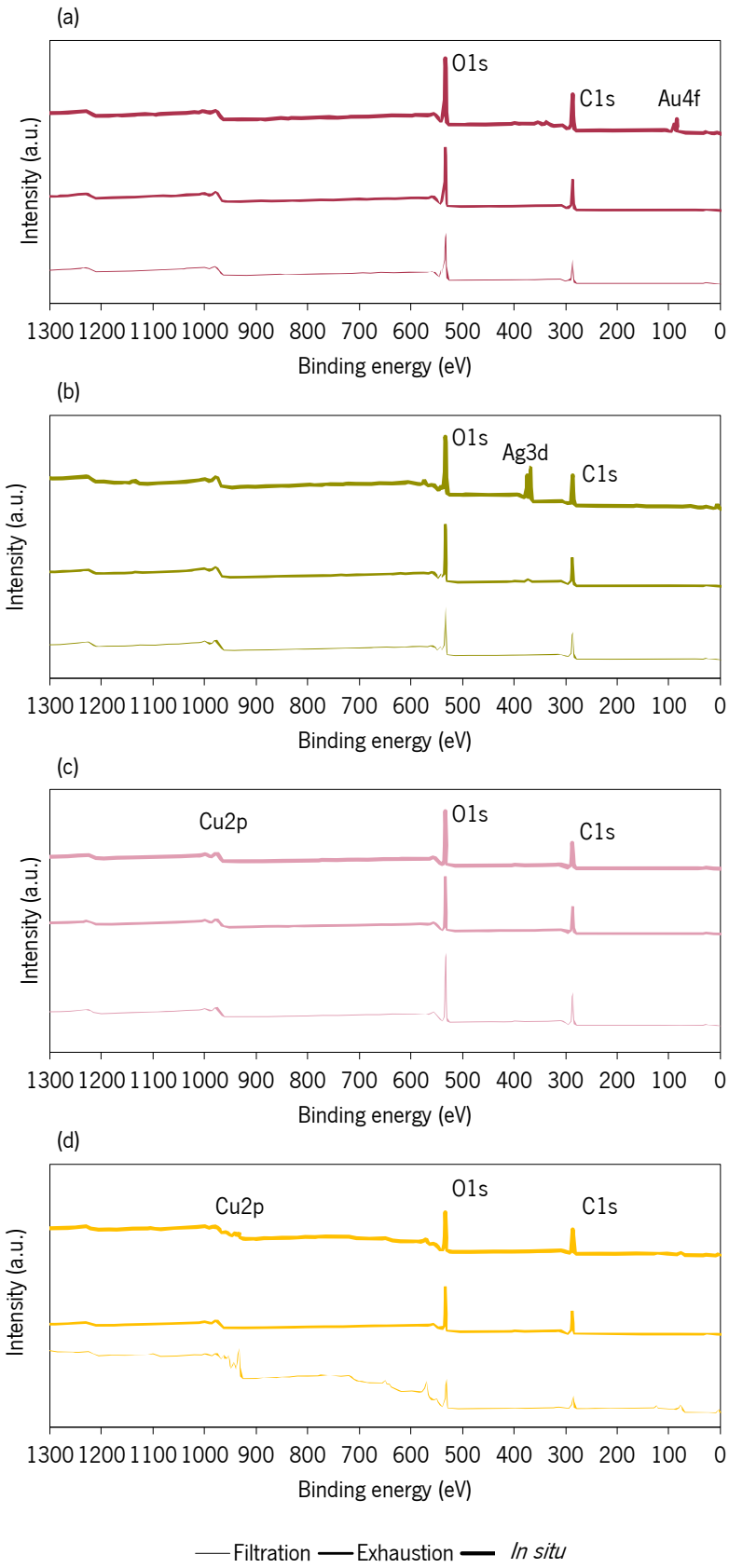



**Figure 4.15.** Survey spectra of (a) BNC/Au, (b) BNC/Ag, (c) BNC/Cu, and (c) BNC/$Cu_2O$ composites.

The atomic percentages of the BNC composites displayed in Table 4.1 show a higher percentage of the metal particles in the samples functionalised *in situ* (0.10 – 3.3%), with the exception of the BNC/$Cu_2O$ composite prepared via the vacuum filtration methodology (14.9%). The percentage of C1s is always superior to O1s.

**Table 4.1.** Atomic percentages (%) of C1s, O1, Auf4, Ag3d, and Cu2p3 in the functionalised BNC composites.

| Composite | Method | C1s | O1s | Au4f |
|---|---|---|---|---|
| | Filtration | 57.4 | 42.6 | 0.0 |
| **BNC/Au** | Exhaustion | 59.7 | 40.3 | 0.1 |
| | In situ | 61.2 | 37.7 | 1.1 |
| | | **C1s** | **O1s** | **Ag3d** |
| | Filtration | 58.8 | 41.1 | 0.1 |
| **BNC/Ag** | Exhaustion | 58.2 | 41.5 | 0.3 |
| | In situ | 60.2 | 36.5 | 3.3 |
| | | **C1s** | **O1s** | **Cu2p3** |
| | Filtration | 59.0 | 40.9 | 0.0 |
| **BNC/Cu** | Exhaustion | 60.4 | 39.6 | 0.0 |
| | In situ | 59.4 | 40.6 | 0.1 |
| | | **C1s** | **O1s** | **Cu2p3** |
| | Filtration | 47.4 | 37.7 | 14.9 |
| **BNC/$Cu_2O$** | Exhaustion | 60.6 | 39.4 | 0.0 |
| | In situ | 61.1 | 36.7 | 2.3 |

### 4.5.5. Thermal analysis

STA was used to determine if the metal particles influenced the thermal degradation of BNC. Overall, the results in Fig. 4.16 show similar thermal stability profiles between the three different methodologies applied in the functionalisation of BNC. Particular similarity to pristine BNC was found for *in situ* functionalised composites, except for BNC/Ag. In this case, the highest similarity was found for composites obtained through filtration. According to Fig. 4.17, the *in situ* functionalisation results in the most stable weight loss up until 320 °C, reaching a maximum of 5.0% for the *in situ* BNC/Ag, from 35.0 – 100 °C. From 100 – 320 °C a maximum of weight loss is verified for BNC/$Cu_2O$ exhaustion reaching 23%, with the *in situ* samples being the most stable with the lowest maximum weight loss under 10%. Pristine BNC loses 5 and 6% in weight from 35.0 – 100 °C and 100 – 320 °C, respectively. The DTG curves (Fig. 4.16 e–h) show a single

degradation peak around 360 °C which corresponds to the breakdown of glycosidic linkages hence depolarisation of cellulose chains thus, the principal decomposition of high-purity cellulose [389]. Overall, the *in situ* methodology seems to have preserved the thermal resistance of BNC, thus suggesting that inter- and intramolecular hydrogen bonding in the cellulose structure was unchanged [389]. This is particularly important due to the thermal sterilisation that BNC undergoes at 121 °C.

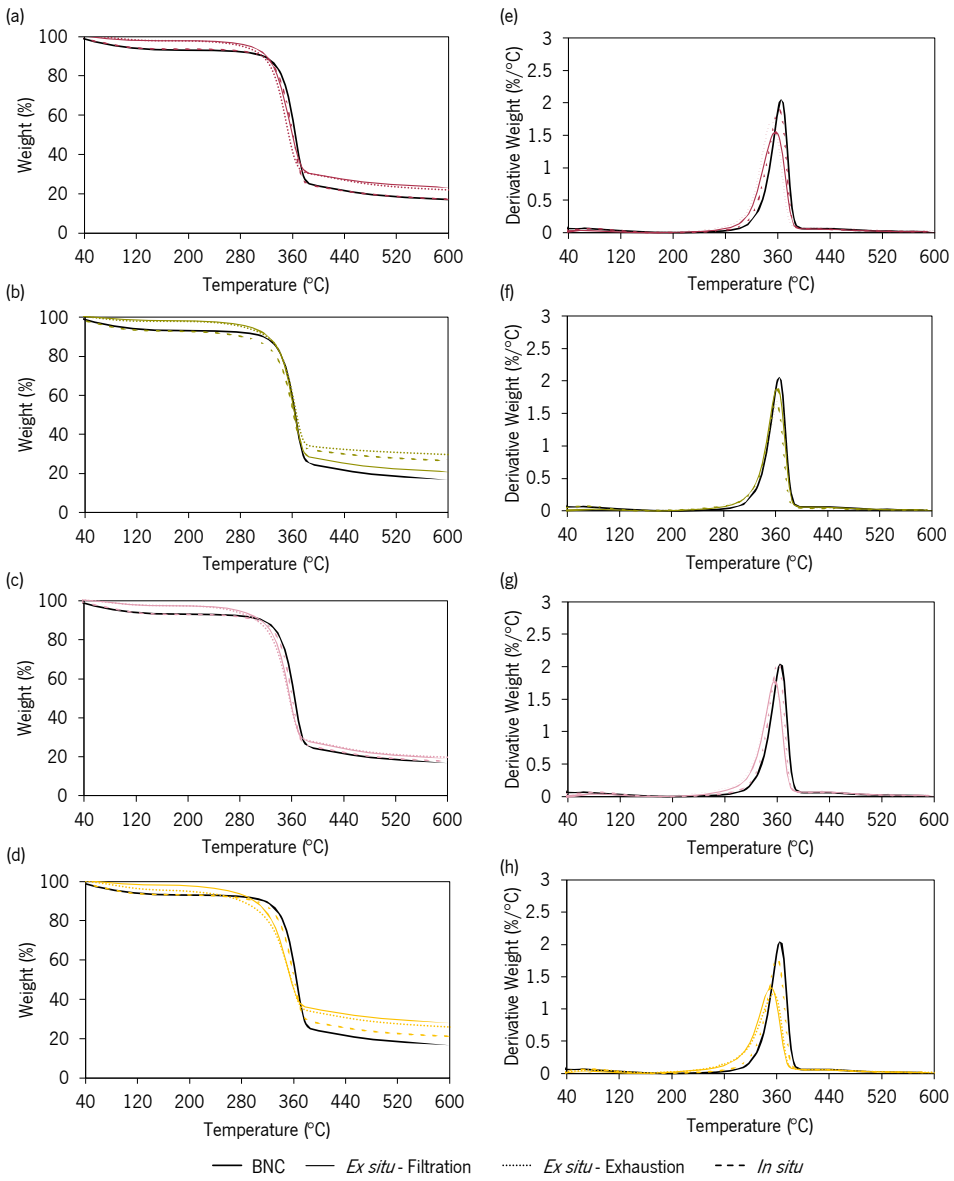



**Figure 4.16.** Thermal analysis spectra relating to the weight loss of (a) BNC/Au, (b) BNC/Ag, (c) BNC/Cu, and (d) BNC/$Cu_2O$ composites obtained through *ex situ* – filtration, *ex situ* – exhaustion, and *in situ* syntheses. The derivative weight loss is presented for (e) BNC/Au, (f) BNC/Ag, (g) BNC/Cu, and (h) BNC/$Cu_2O$ composites.

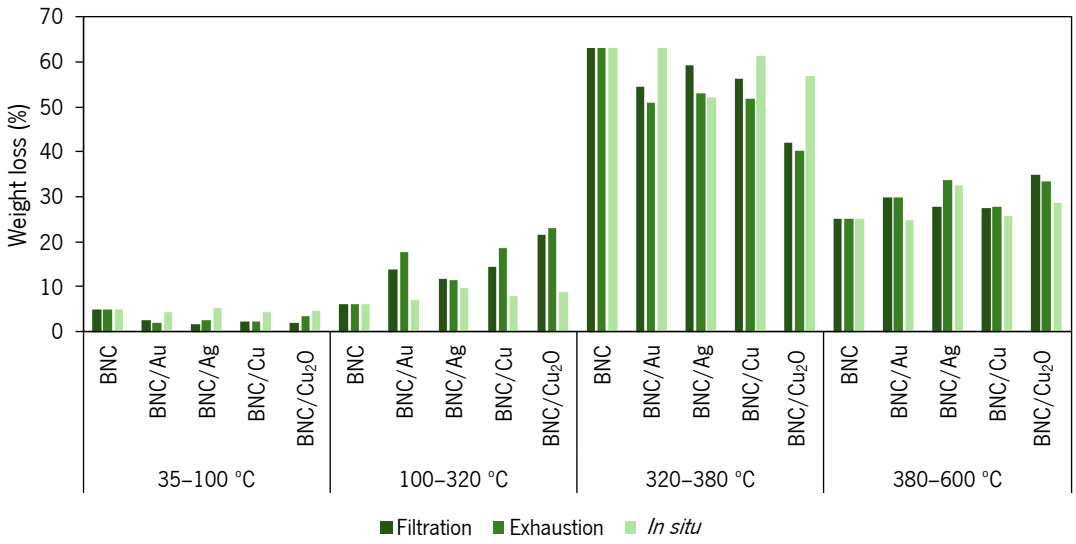



**Figure 4.17.** Weight loss percentage for each composite at different temperature stages.

### 4.5.6. Swelling profile

The swelling behaviour of the BNC composites (Fig. 4.18) in SBF at 37 °C was studied to evaluate the release profile of the metal particles according to the three functionalisation methodologies applied. Pristine BNC membranes in the never-dried state were used as a control. Besides the intrinsic hydration capacity of BNC, the 3D structure of the polymer network influences the swelling behaviour. Higher porosity and pore size lead to a more efficient water diffusion and swelling capacity. In addition, the density of the fibrous network influence swelling, translating into a slower diffusion and swelling capacity [352]. The non-functionalised BNC appear to stabilise after 144 h (6 days) reaching around 60% swelling. The samples prepared via vacuum filtration (Fig. 4.18a) produced a similar behaviour, except for Au, which showed a higher swelling degree of 63% after 96 h. The Ag, Cu, and $Cu_2O$ seem to induce a similar behaviour between them, demonstrating a considerable drop in swelling capacity, and stabilising after 24 h, reaching around 24%, 27%, 17% swelling, respectively. The exhaustion method (Fig. 4.18b) produced samples with slightly higher variations between them, with the Ag samples reaching 46% swelling at 24 h, reaching approximately 60%. At swelling equilibrium. The remaining samples only increased swelling up to 12%, 21%, and 27%, for Au, Cu, and $Cu_2O$, at equilibrium (t144 h). For the *in situ* methodology (Fig. 4.18c), the BNC/$Cu_2O$ membranes behaved similarly to BNC, with approximately 60% of swelling. Through this functionalisation, BNC/Au, BNC/Ag, and BNC/Cu have an equilibrium swelling of approximately 20%. According to the results obtained, both the functionalisation

methodology and the metal particles influence the swelling capacity of BNC, never reaching an equilibrium swelling percentage superior to pristine BNC.

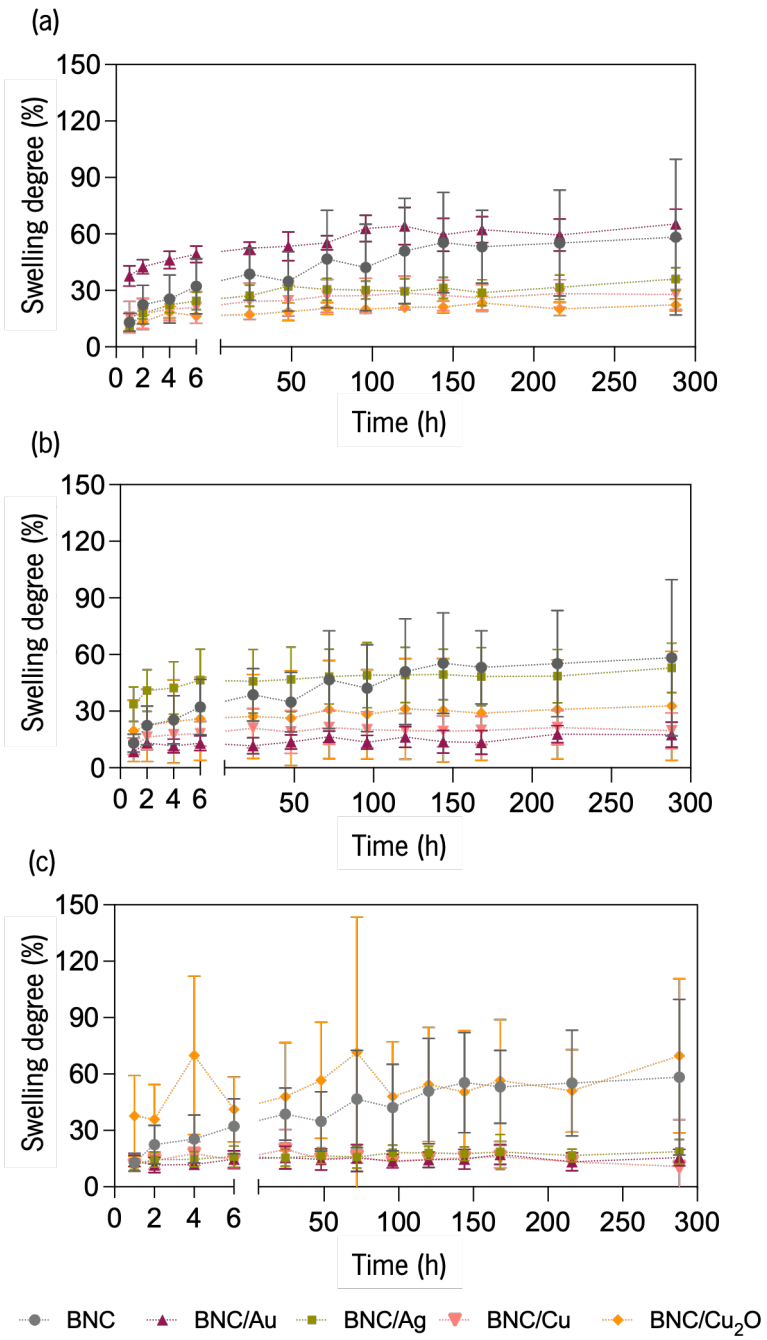



**Figure 4.18.** Swelling behaviour of BNC composites obtained through (a) *ex situ* – filtration, (b) *ex situ* – exhaustion, and (c) *in situ* syntheses.

### 4.5.7. One-month release

A comparison of the release of the metal particles of the different functionalisation methodologies is presented in Fig. 4.19. Au nanoparticles were not analysed due to the required digestion procedure digestion. Piranha solution is unable to digest Au nanoparticles and aqua regia solution, required for Au nanoparticles digestion, is unable to degrade BNC. The release percentage after one month is higher for the $Cu_2O$ particles independent of functionalisation methodology, an average of 73.2 ± 13.7%. According to the swelling assay, the BNC/$Cu_2O$ composite obtained by *in situ* functionalisation, presents the highest swelling, which agrees with the release (70.6 ± 4.70%). The release of Cu is also similar between the different functionalisations, an average of 54.6 ± 3.40%. Ag release presented similar release values for filtration (54.5 ± 8.60%) and *in situ* (48.0 ± 23.3%), while lower release was obtained for the exhaustion (34.8 ± 15.3%) methodology. This is the lowest release obtained of all samples and characterisation approaches, which is not corroborated by the swelling profile since the exhaustion of BNC/Ag is the highest in this methodology.

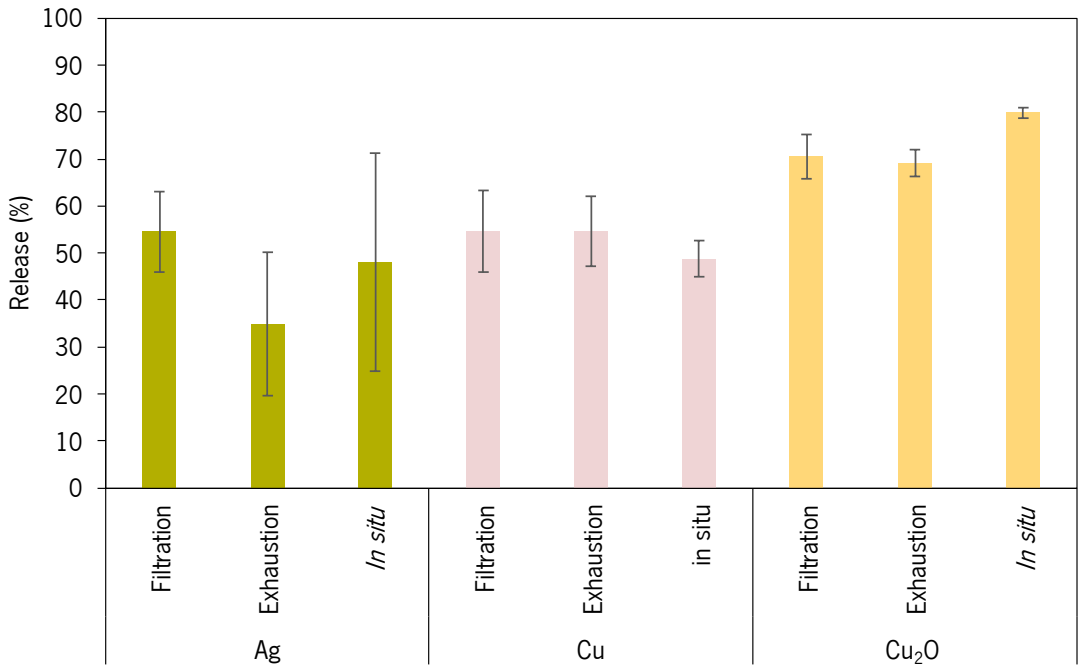



**Figure 4.19.** One-month release of Ag, Cu and $Cu_2O$ particles from the respective composites obtained from *ex situ* and *in situ* methods after 1 month.

### 4.5.8. Antimicrobial activity

The antibacterial activity of the metal particles was assessed through contact killing and shake flask methods. The contact killing (Fig. 4.20a) shows that both BNC/Cu and BNC/$Cu_2O$ composites present moderate disinfectant effect against *S. aureus* for all three functionalisation methodologies. The same copper-based composites present moderate disinfectant activity against *P. aeruginosa*, except BNC/Cu obtained through exhaustion which is a weak decontaminant. BNC/Ag is a weak decontaminant against *P. aeruginosa* when functionalised through both the *ex situ* methodologies. This shows that the composites are effective upon contact. However, the results of the shake flask (Fig. 4.20b) show that the composites are also effective upon release of the particles with the BNC/Ag nanocomposites presenting sterilizing effect against *P. aeruginosa*. BNC/Cu and BNC/$Cu_2O$ also have a very similar activity, except for BNC/Cu functionalised by exhaustion and in situ, which suggests more entrapment of the particles and lower release, which is not in line with the release of Cu. A log reduction of 5 against *S. aureus* has been reported using the same *in situ* synthesis of Cu and $Cu_2O$ particles in the presence of a textile fabric. In the case of Gram negative *E. coli*, Cu and $Cu_2O$ functionalised fabrics were slightly more efficient, with Log reduction of 6 [372]. A similar activity of the same composites is verified against *S. aureus*, except for BNC/Ag, exhaustion and in situ, that are strong decontaminant.

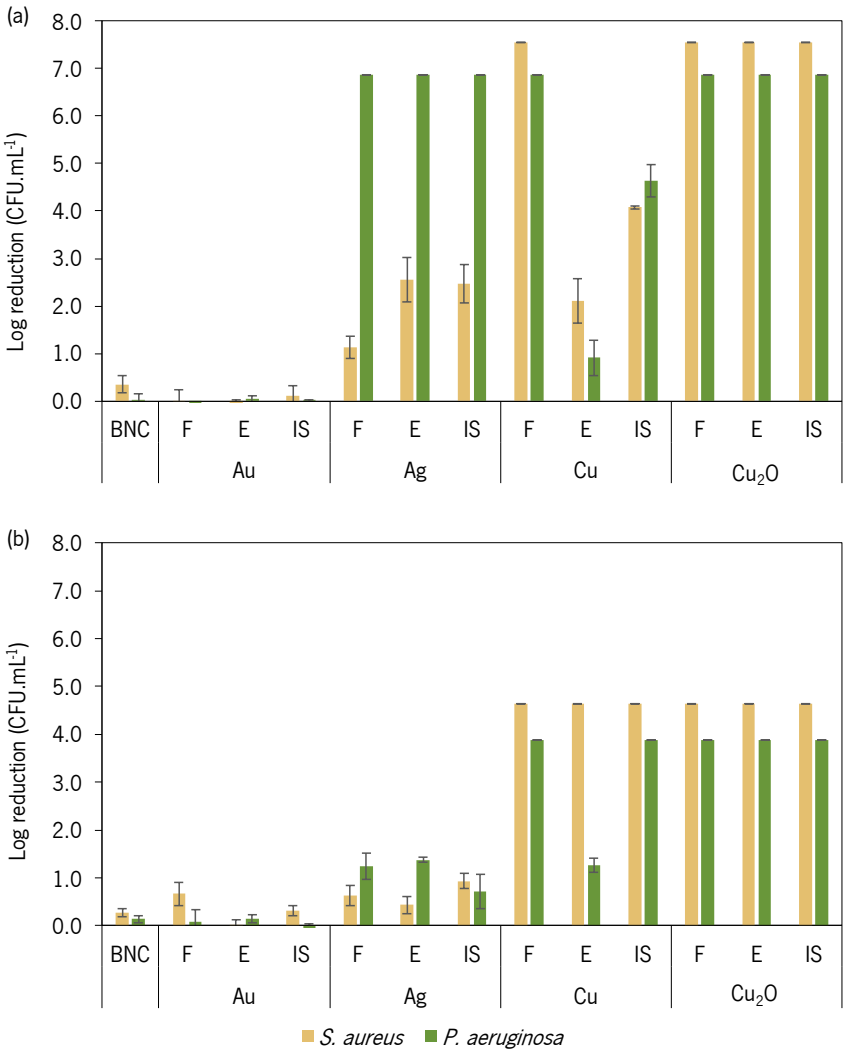



**Figure 4.20.** Antibacterial activity (a) contact killing and (b) shake flask of BNC and BNC composites obtained through *ex situ* (F) filtration and (E) exhaustion, and (IS) *in situ* methodologies.

## 4.6. Conclusions

Of the different methodologies applied, both exhaustion and *in situ* presented the best results. Considering their similarly, the *in situ* methodology was chosen due to the reduced steps necessary for the functionalisation of BNC. In terms of physical-chemical analyses, the composites were not affected by the functionalisation, suggesting no formation of bonds, despite the confirmation of the particles within the BNC. The highest release occurs for $Cu_2O$, which justifies the antibacterial activity verified. Theoretically, metal particles have a higher potential for maintaining long-term activity in comparison to biological agents. This is a clear advantage considering the purpose of this work.

# Chapter 5

## BNC mesh composites[4]

[4] This chapter is based on the following future publication:

Peer-reviewed article:

Melro, L.; Fernandes, M.; Campos, T.; Mehravani, B.; Ribeiro, A. I.; Mitu, B.; Satulu, V.; Fernandes, N.; Carvalho, O.; Faria, C.; Ferreira, F.; Pereira, F.; Dourado, N.; Silva, J. P.; Carvalho, F.; Padrão, J.; Zille, A.; "BNC-based hernia mesh with prospective decrease of post-operative infections – Part II (biological activity and mechanical properties)".

# 5. BNC mesh composites

## 5.1. Introduction

This chapter presents the composite BNC mesh, obtained by *in situ* methodology, and their antimicrobial, cellular and mechanical characterisation.

Common treatment for hernia repair includes the introduction of a polypropylene (PP) or polyester patch that generally induce inflammatory response. Besides the material origin, the design of meshes is a critical factor in promoting tissue integration, enhancing mechanical properties, flexibility and reducing postoperative complications [14]. A BNC mesh was produced with the aid of a template and was functionalised with antimicrobial agents, namely metal particles. It is known that the drying process of BNC results in stronger bonding, higher fibre packaging, enhanced crystallinity, and eventually higher Young's modulus [101]. For this reason, metal particles functionalised BNC-based meshes were characterised in the never-dried (hydrated) and rehydrated states. The expected enhancement of their mechanical properties was verified, and the eventual influence of the swelling capacity and metal particle release, antimicrobial activity, and cellular activity.

## 5.2. Materials

Cultivation materials and methods of *Komagataeibacter hansenii* (American Type Culture Collection (ATCC) 53582 and the preparation of simulated body fluid (SBF) and phosphate buffered saline (PBS) are described in Section 3.2. The antibacterial activity assays were performed with the same materials as reported in Section 4.2.

For the cell culture and cell assays the following reagents were used: Dulbecco's modified Eagle's medium (DMEM/F12 (1:1) with stable glutamine, 1.2 $g \cdot L^{-1}$ $NaHCO_3$), fetal bovine serum (FBS) supreme heat inactivated, penicillin-streptomycin (10.000 $U \cdot mL^{-1}$ Streptomycin) sterile-cell culture grade, and trypsin 0.25% in phosphate buffered saline (PBS), without Ca and Mg, sterile-cell culture grade, all purchased from Biotecnómica (São Mamede Infesta, Portugal). Reagent 3-(4,5-dimethylthiazol-2-yl)-5-(3-carboxymethoxyphenyl)-2-(4-sulfophenyl)-2H-tetrazolium (MTS) MTS Kit (Cell Proliferation) (Colorimetric), was purchased from Abcam Limited (Cambridge, UK) Hanks balanced salt solution (HBSS) was obtained from Thermo Fisher Scientific Inc. (Massachusetts, USA). Neutral red (NR), thiazolyl blue tetrazolium bromide (MTT, 98%), dimethyl sulphoxide

analytical reagent (DMSO, dehydrated max. 0.03% $H_2O$), and the reagents for the lysis solution, ethanol and glacial acetic acid, were obtained from Merck Life Science (Algés, Portugal). NCTC clone 929 (L cell, L-929, derivative of Strain L) was purchased from ATCC (Virginia, USA).

## 5.3. Methods

### 5.3.1. BNC mesh production

The BNC membranes were obtained by cultivating *K. hansenii* (ATCC 53582) under static culture conditions and according to Section 3.3.1.

A first attempt at designing macropores onto a BNC membrane was performed using a $CO_2$ Light Amplification by Stimulated Emission of Radiation (LASER) machine, at 10.9 nm, with power of 5 mA, and speed of 5.0 – 20 mm.$s^{-1}$, with 4 – 6 passages. The pattern of the pores was previously drawn in Autodesk Fusion 360. Another attempt using a Chongqing Bende Machinery Co., Ltd. $CO_2$ laser, with a 10.6 µm wavelength, spot size of 200 µm, 20 kHz of pulse frequency and a maximum power of 50 W, with speed of 10.0 – 500 mm·$s^{-1}$, and several different passages was performed without success. For this latter machine, the patter was previously drawn on EzCad 2.5.3. Fig. 5.1 shows the resulting pattern on BNC membranes. As is visible, the patterning is not uniform, particularly if the distance between holes is too narrow. There is overlapping, and because the membranes need to be constantly rehydrated so it does not burn, even if fixed, displacement always occurs, thus making the number of passages unsuccessful.

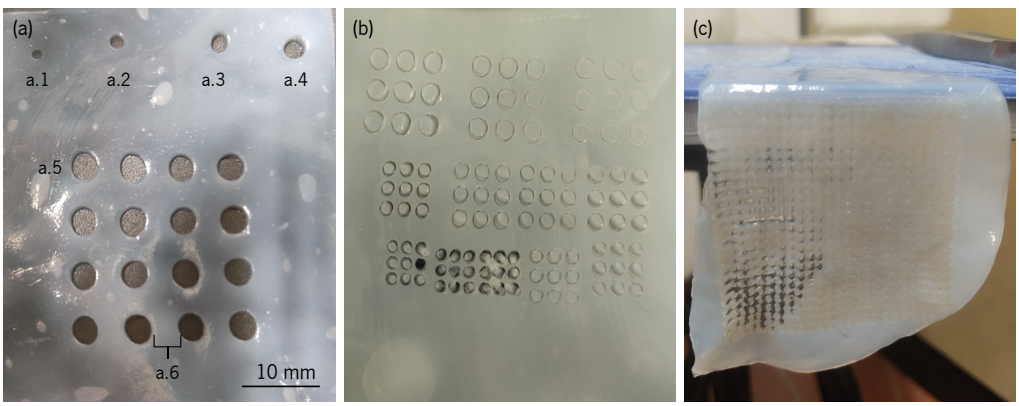



**Figure 5.1.** LASER patterned BNC membranes obtained from (a) $CO_2$ LASER with hole diameters of (a.1) ⌀ 1.0 mm, (a.2) ⌀ 1.5 mm, (a.3) ⌀ 2.0 mm, (a.4) ⌀ 2.5 mm, and ⌀ 3.0 mm, and (a.6) interspace between holes of 3.0 mm; and obtained from (b, c) Bende LASER showing the heterogeneous cutting of BNC.

The second attempt was to cultivate *K. hansenii* in the presence of a template. In this case, an important factor needed to be taken into account, the sterilizability of the template material. It should sustain autoclaving temperatures of 121 °C for 20 minutes, and should be inert, so it does not interfere with the bacteria cultivation, thus BNC production. Different templates were discussed for three-dimensional (3D) printing. The idealised templates included different pore sizes (0.1 mm, 1 mm and 3 mm) and different distances between pores. However, since the static BNC production occurs at the surface of the culture medium, a large aspect ratio was required, which hindered its production. In addition, the materials able to sustain the autoclaving procedure, such polytetrafluoroethylene or polysiloxane, are difficult to print with [390]. Thus, a metal-based template was built, as shown in Fig. 5.2. The resulting membrane from the fermentation does not have a desired pattern since its extraction tends to damage the design and is very limiting in terms of size.

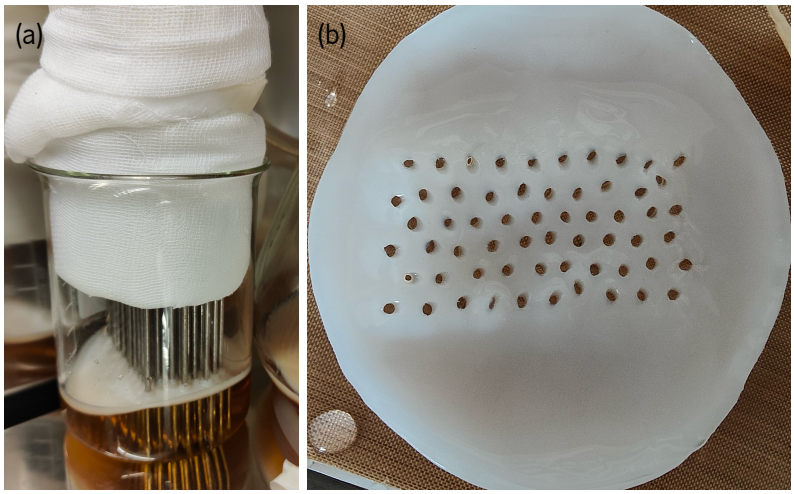



**Figure 5.2.** (a) Metal-based template used during BNC production and (b) resulting washed membrane.

Finally, through the inclusion of a commercial silicon template inside the fermentation recipient, as shown in Fig. 5.3, four days were enough for the growth of the BNC mesh. A uniform patterned BNC mesh was obtained. The specifications are presented in Table 5.1. and include commercial PP-based meshes (Fig. 5.4): (a) Optilene B. Braun-Portugal (60 $g \cdot m^{-2}$), (b) Ethicon Ultrapro Advanced (28 $g \cdot m^{-2}$), and (c) Optilene Mesh Elastic B. Braun-Portugal (48 $g \cdot m^{-2}$).

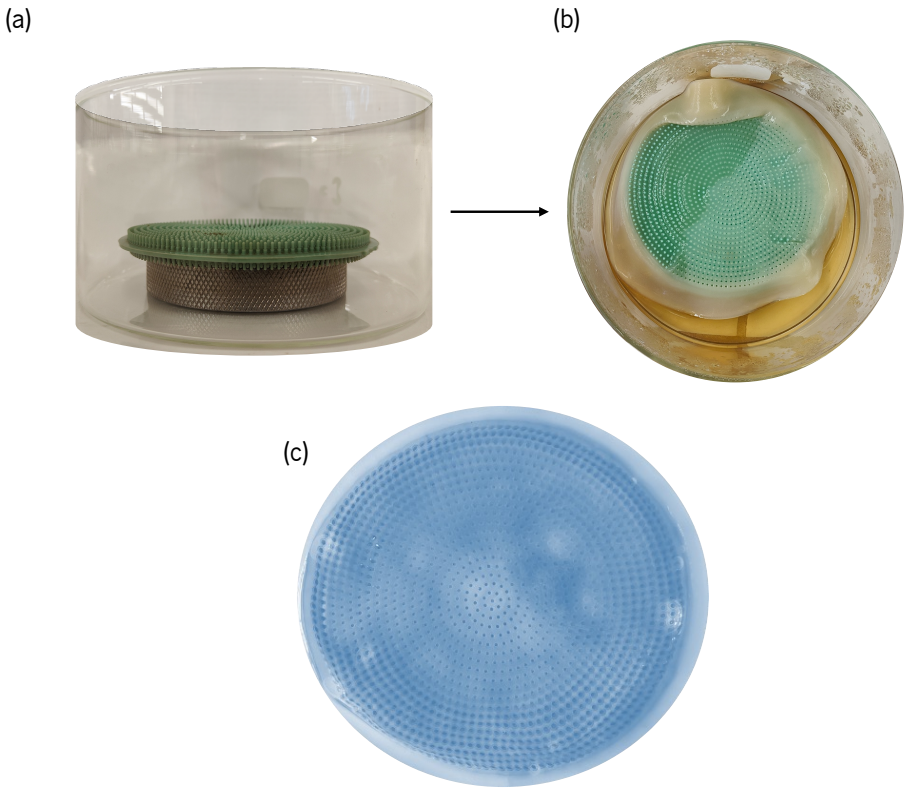



**Figure 5.3.** (a) Template used to create BNC meshes, (b) cultivation of *K. hansenii* in the presence of the template and (c) resulting BNC mesh.

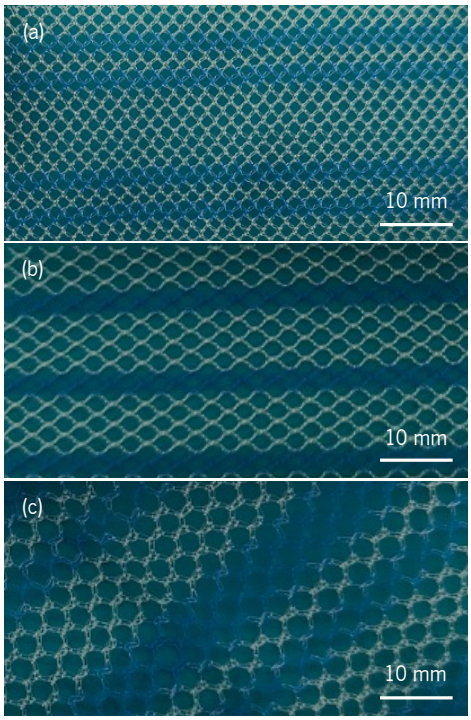



**Figure 5.4.** Commercial polypropylene meshes: (a) Optilene B. Braun-Portugal (60 g·m$^{-2}$), (b) Ethicon Ultrapro Advanced (28 g·m$^{-2}$), and (c) Optilene Mesh Elastic B. Braun-Portugal (48 g·m$^{-2}$).

**Table 5.1.** Dimensions of pore and interspace between pores of BNC and commercial PP-based meshes.

| | **Diameter (mm)** | **Interspace (mm)** |
|---|---|---|
| BNC hydrated | 1.13 ± 0.0700 | 1.58 ± 0.0800 |
| BNC rehydrated | 0.970 ± 0.0600 | 1.63 ± 1.28 |
| Optilene | 1.25 ± 0.0500 | 0.500 ± 0.0600 |
| UltraPro Ethicon | 2.41 ± 0.0520 | 0.400 ± 0.0400 |
| Optilene Mesh Elastic | 2.81 ± 0.000 | 0.600 ± 0.0700 |

### 5.3.2. Functionalisation *in situ*

The *in situ* functionalisation of the BNC meshes with particles of gold (Au), silver (Ag), copper (Cu), and copper oxide ($Cu_2O$) were prepared as described in Sections 4.3.2 – 4.3.5, with the only difference being the introduction of a BNC mesh instead of a BNC membrane. The resulting BNC-based meshes are presented in Fig. 5.5.

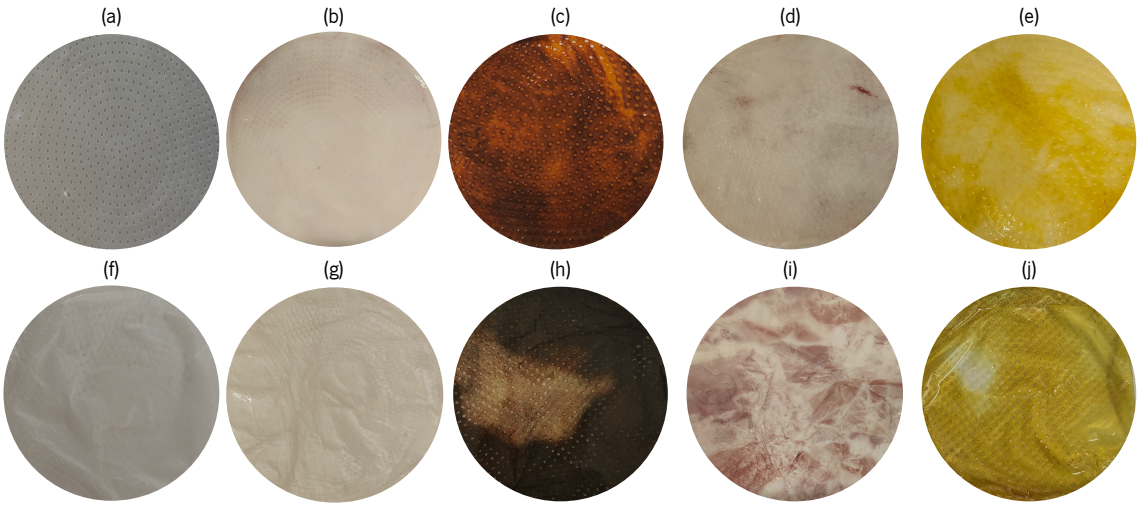



**Figure 5.5.** Images of never-dried BNC meshes: (a) BNC, (b) BNC/Au, (c) BNC/Ag, (d) BNC/Cu, (e) BNC/$Cu_2O$, and rehydrated BNC meshes: (f) BNC, (g) BNC/Au, (h) BNC/Ag, (i) BNC/Cu, and (j) BNC/$Cu_2O$.

## 5.4. Characterisation

### 5.4.1. Morphology

BNC composites, 1 × 1 cm samples with 1 mm of thickness were cut in liquid nitrogen and fixed with double-sided carbon tape on an aluminium metal support. Subsequently, the samples were covered, using a sputtering technique, with a 16.5 nm thick Au-Pd film (80/20% by weight) using a high-resolution sputter coater (208HR Cressington Company, UK) and monitored by a high-resolution thickness controller (MTM-20, Cressington, UK). Elemental analysis was performed using x-ray energy dispersive spectrometer (EDS). Cell morphology was assessed via SEM using a FlexSEM 1000 (Hitachi, Japan), with an acceleration voltage of 15 kV.

### 5.4.2. Swelling profile

The swelling degree (%) of the BNC samples was determined gravimetrically and was based on the average variation of the sample's wet weight, during the assay. The circular BNC samples with a volume of 2.0 $cm^3$, were immersed in 5 mL of SBF. The assay was conducted at 37 °C under shaking at 120 rpm. At determined time intervals, the wet weight of the samples was recorded, after removing the excess of surface water by suspending the BNC in polypropylene wires for 1 minute (Fig. 3.4). The assay was conducted until weight stabilization (full swelling). Swelling degree was determined using Eq. 5.1:

$$\text{Swelling degree } (\%) = \frac{W_t - W_0}{W_0} \times 100 \qquad \text{(Equation 5.1)}$$

where $W_t$ is the weight of the sample at time t and $W_0$ denotes the initial weight of the BNC samples. Quintuplicates of each condition were used. The rehydrated samples were dried at 40 °C overnight and immersed in water for 24 h before sterilisation.

### 5.4.3. Release profile

The release profile was performed as reported in section 4.4.6., with the exception that samples were collected after 1, 3, and 6 months.

### 5.4.4. Antibacterial activity

The antibacterial efficacy of the functionalised BNC was assessed quantitatively according to the standard contact killing (AATCC 100-TM100) and the shake flask (American Society for Testing and Materials (ASTM)-E2149-01) methods. Bacteria inocula were prepared in trypticase soy broth (TSB) *(S. aureus)* and NB *(P. aeruginosa)* and incubated overnight at 37 °C and 120 rpm. Each test was carried out using an initial concentration of $1.0 \times 10^7$ colony-forming units (CFUs)·mL$^{-1}$. This excludes the 24 h shake flask, for which concentrations of $1.0 \times 10^5$ CFUs·mL$^{-1}$ were prepared. For the contact-killing assay, samples with dimensions 2 x 2 cm were placed in contact with 20 µL of bacteria suspension in PBS at 37 °C for 1 h. Before contact with samples (t0 h) and after contact with samples (t1 h) the bacteria were serially diluted and cultured onto trypticase soy agar (TSA) and nutrient agar (NA) plates. In the case of the shake flask method, and for the 24h contact, samples of 1 x 1 cm were incubated in 5 mL of bacteria suspension in Mueller-Hinton broth (MHB) at 37 °C and 120 rpm. Like in the previous method, the bacteria were serially diluted before contact with samples (t0 h) and after contact with samples (t5 h and t24 h) and cultured onto TSA and NA plates.

Quantitative results were obtained by counting the colonies of surviving bacteria on the agar plates. Antimicrobial activity was reported quantitatively in terms of log reduction, calculated as the ratio between the number of surviving bacteria colonies present on the agar plates, before and after contact with the fabric.

### 5.4.5. Cell adhesion and viability

The potential cytotoxicity of the BNC/metal particles meshes and cell adhesion were evaluated using fibroblasts L929 cell line, according to International Organisation for Standardisation (ISO) 10993-5: Biological evaluation of medical devices - Part 5: Tests for in vitro cytotoxicity. The chosen viability assays for adhered cells were the NR, MTT, and MTS. Cell incubation time for the assays were 24 h and 168 h. Considering the application of the meshes as implant, a maximum viable time of *in vitro* incubation time of 168 h was performed. Fibroblasts are important for cell viability in this study, since they are the most common cells of connective tissue in animals, producing the structural framework of tissues. Besides, they are responsible for the synthesis of extracellular matrix and collagen, thus playing a critical role in wound healing.

The L929 cell medium was prepared by adding 6.68 g DMEM and 1.85 g $NaHCO_3$ to 445 mL of $dH_2O$, and the pH adjusted to 7.2 – 7.3. This solution was then filtered in a flux chamber, whilst 50 mL of FBS and 5 mL of Pen/Strep + Amp B (1%) were being added. The final pH was between 7.2 – 7.4.

The BNC mesh sample dimensions were 0.5 mm thick with a diameter of 10 mm. Prior to the essays, half of the samples were dried in an oven overnight (16 h) at 40 °C and immersed in SBF for another 6 h. The excess SBF was removed, and all samples were autoclaved and stored before being tested. Cells were seeded on top of each non-functionalised mesh (Optilene 60 $g \cdot m^{-2}$, BNC H – hydrated BNC mesh, and BNC R – rehydrated BNC mesh), and functionalised BNC meshes (BNC/Ag H and BNC/Ag R – Ag functionalised BNC meshes in the hydrated and rehydrated states, BNC/Cu H and BNC/Cu R – Cu functionalised BNC meshes, and finally, BNC/$Cu_2O$ H and BNC/$Cu_2O$ R – $Cu_2O$ functionalised BNC meshes (Fig. 5.4 and Fig. 5.5). L929 fibroblasts were incubated in DMEM at 37 °C in a 5% $CO_2$ humidified atmosphere. Cells grown directly on the polystyrene surface were used as control.

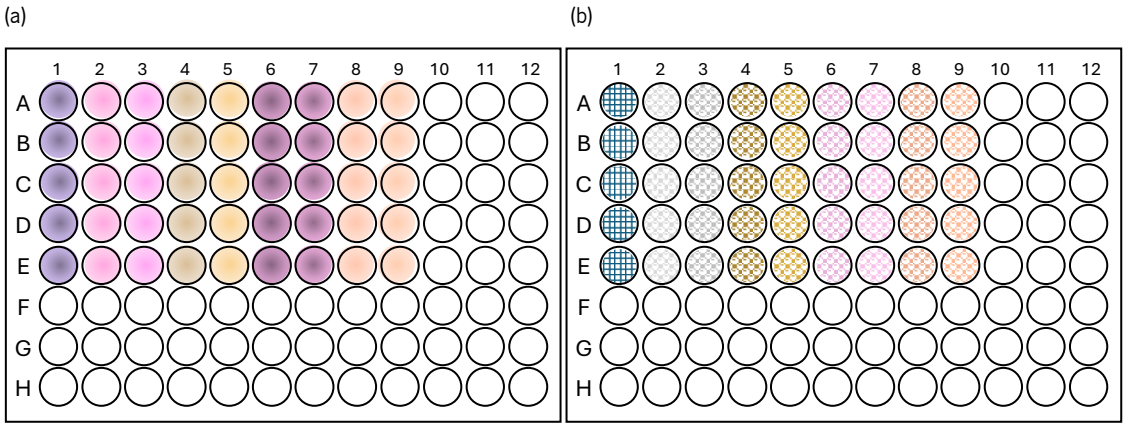



**Figure 5.6.** Schematic representation of the (a) cell seeding with samples and medium, and (b) the meshes transference to a new plate. Columns refer to 1. Optilene, 2. BNC H, 3. BNC R, 4. BNC/Ag H, 5. BNC/Ag R, 6. BNC/Cu H, 7. BNC/Cu R, 8. BNC/$Cu_2O$ H, 9. BNC/$Cu_2O$ R.

To initiate the assay, five samples of each condition of meshes were placed in wells of 96-well plates before seeding the cells ($1 \times 10^5$ $cell \cdot mL^{-1}$) (Fig. 5.6a). This was performed for each assay (NR, MTT, and MTS) and for the two timepoints, 24 h and 168 h. For cell counting, the total number of fibroblasts were quantified in a Neubauer chamber, using trypan blue (ratio 1:1) to distinguish viable from non-viable (blue) cells. After incubation at 37 °C in a 5% $CO_2$ humidified

atmosphere for 24 h, the membranes of each plate relative to the intended assay and timepoint, were transferred to another 96-well plate to perform the cell viability assays of adhered cells (Fig. 5.6b). Control wells containing only cells were maintained on the original plate after medium was removed. Then, the testing solutions were added to the membranes according to the description below. This protocol was replicated for the 168 h time point. In addition to assessing cell adhesion, the MTS assay was employed to evaluate the influence of the meshes on cell proliferation. Following mesh removal, the wells were treated in parallel with the cell controls, the culture medium was removed and replaced with the MTS testing solution (DMEM/MTS).

Neutral Red (NR) uptake assay

The NR assay relies on the ability of viable cells to incorporate and bind the supravital cationic dye NR. Once having crossed the cell membrane through non-ionic diffusion, the NR dye accumulates in the lysosome of viable cells.

The preparation of 40 mL of NR solution (50 µg·mL$^{-1}$) included adding 606 µL of 3.3 g·L$^{-1}$ NR solution to 39.39 mL of HBSS. For the preparation of 100 mL of the lysis solution, 50 mL of ethanol and 1 mL glacial acetic acid were added to 49 mL $dH_2O$. Both solutions were stored.

To initiate the assay, 100 µL of the NR testing solution, containing 1.5% of NR (50 µg.mL$^{-1}$) in cell culture medium, were added to each mesh/well. After 1 h incubation at 37 °C in a 5% $CO_2$ atmosphere, the medium was removed and the meshes/wells were washed with 200 µL of HBSS, and 150 µL of the lysis solution were added. The plates were protected from the light and placed on a shaker for 15 minutes for complete homogenization. Then, 100 µL of this solution were transferred to a new microplate. The absorbance was read in a spectrophotometer at 540/690 nm. For cell viability assessment, cellular metabolic activity was calculated according to Eq. 5.2 where $Absorbance_{sample}$ stands for the absorbance of the cells that were in contact with the meshes and $Absorbance_{control}$ stands for the absorbance of the cells in the absence of the meshes.

$$\%=\frac{Absorbance_{sample}}{Absorbance_{control}}\times 100 \qquad \text{(Equation 5.2)}$$

MTT assay

The MTT, a yellow tetrazole (3-(4,5-dimethylthiazol-2-yl)-2,5-diphenyltetrazolium bromide), is reduced by active reductase enzymes of living cells forming an insoluble purple formazan crystals. To prepare a 40 mL MTT solution (5 $mg \cdot mL^{-1}$), 200 mg of MTT were added to 40 mL of HBSS, and sonicated until complete dissolution. The solution was then sterilized by filtration using a membrane with a porosity of 0.22 µm. Finally, 5 mL aliquots were prepared and stored at -20 °C protected from light, until further use. Prior to the assay, a solution of 10% MTT in cell culture medium was prepared and kept safe from light. 100 µL of the MTT testing solution were added to each mesh/well. After 2 h incubation at 37 °C in a 5% $CO_2$ atmosphere, the solution was replaced by 120 µL of DMSO. The plates were protected from the light and placed on a shaker for 15 minutes. 100 µL of each well were transferred to another microplate and the absorbance read at 550/690. For cell viability assessment, cellular metabolic activity was calculated according to Eq. 5.2. Cell images of the 24 h cell seeding on the microplates were obtained from Automated Microscope and Live Cell Imager - BioTek Lionheart FX (Agilent, California, USA).

MTS assay

The MTS assay is based on the conversion of the tetrazolium salt MTS by NADPH-dependent dehydrogenases, active in viable cells, to a purple formazan in the presence of phenazine methosulfate. 120 µL of a solution containing 10% MTS in cell culture medium were added to the meshes/wells and incubated for 3 h at 37 °C in a 5% $CO_2$ atmosphere. An extra 120 µL of this solution were added to empty wells used as blank control for cell metabolic activity calculations. Then, 100 µL were transferred from each well to a new microplate. For cell viability assessment, cellular metabolic activity was calculated according to Eq. 5.2.

### 5.4.6. Mechanical properties

The evaluation of the mechanical properties was performed by first comparing a BNC membrane with a BNC mesh (porous structure). Afterwards, the BNC meshes in the hydrated and rehydrated states (Fig. 5.5) were compared with commercial polypropylene (PP)-based meshes (Fig. 5.4).

### Experimental characterization

For tensile strength testing, samples of 0.5 mm thickness were cut into a rectangular shape using a puncher with an area of 1,54 $mm^2$ (27 mm X 57 mm). The test specimens were placed on a paper to prevent distortion and ensure a correct and adequate placement of the specimen between the equipment grips. Before the assay, the paper was cut in the centre and completely removed, apart from where the tensile grips were holding both paper and BNC. To prevent sample slipping during experiments, a small piece of sandpaper was glued inside the grips (Fig. 5.7). Samples were subjected to a tensile strength using a servo-electrical testing machine (Micro-Tester INSTRON 5848), a 5 kN cell load with crosshead displacement rate set to 1 $mm \cdot sec^{-1}$ and gauge length of 35 mm. A minimum of 5 specimens were used. Uniaxial tensile tests were conducted using TA.XT Plus Texture Analyzer Exponent software (version 6.1.16 – Stable Micro Systems, Surrey, UK). Commercial meshes presented higher elasticity hence, the assays were performed using a strength tester equipment (Hounsfield HSK100, Salfords, UK). Minimum two specimens of each mesh (10 mm width, 0.48 mm thickness) with a 35 mm distance between the clamps were then submitted to tensile testing at a constant speed of 1 $mm \cdot sec^{-1}$. Elastic modulus, $E$ (MPa) and Poisson's ratio ($\nu$) were calculated from the obtained stress-strain curves.

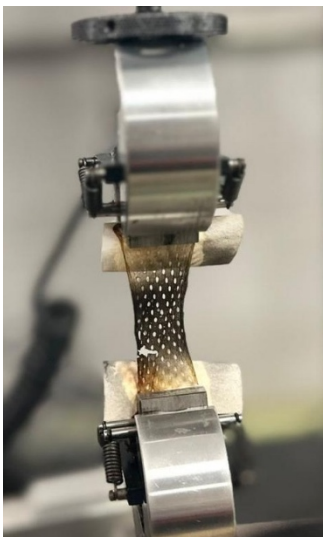


**Figure 5.7.** Tensile testing setup of the BNC sample.

The experimental procedure was structured in two distinct stages. Initially, continuous BNC membranes were tested to isolate the inherent mechanical response of the material, free from geometrical discontinuities. This baseline characterisation is essential, as it establishes reference

values for parameters such as *E*, tensile strength and strain at failure. Subsequently, BNC structures with controlled porosity, designed to mimic the architecture of hernia repair meshes, were evaluated. This second stage aimed to assess how geometric features such as pore size, ligament thickness and structural connectivity influence the global mechanical response. By comparing membranes and mesh-like structures, it becomes possible to decouple material-driven behaviour from structure-driven effects.

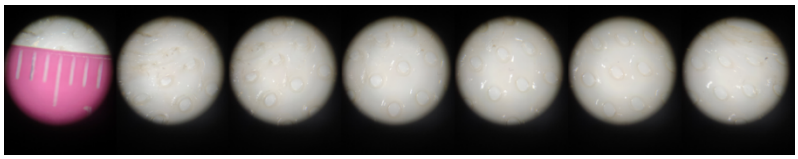


**Figure 5.8.** Images of the BNC meshes used as reference for building the numerical model.

### Numerical study

In parallel with the experimental work, a finite element modelling (FEM) framework was developed to reproduce the mechanical behaviour of both BNC membranes and porous structures. The numerical models were constructed using geometries that replicate the real dimensions of the tested specimens (Fig. 5.8). This ensures direct comparability between experimental and simulation results. For the discretization, quadratic tetrahedral elements (C3D10) were employed, allowing accurate representation of both the global deformation and local stress concentrations, particularly in regions of geometric complexity such as pore boundaries in the mesh structures. Boundary conditions were defined to replicate the experimental setup as closely as possible. One extremity of the model was fully constrained, while a displacement-controlled load was applied to the opposite end, reproducing the uniaxial tensile loading conditions (Fig. 5.9).

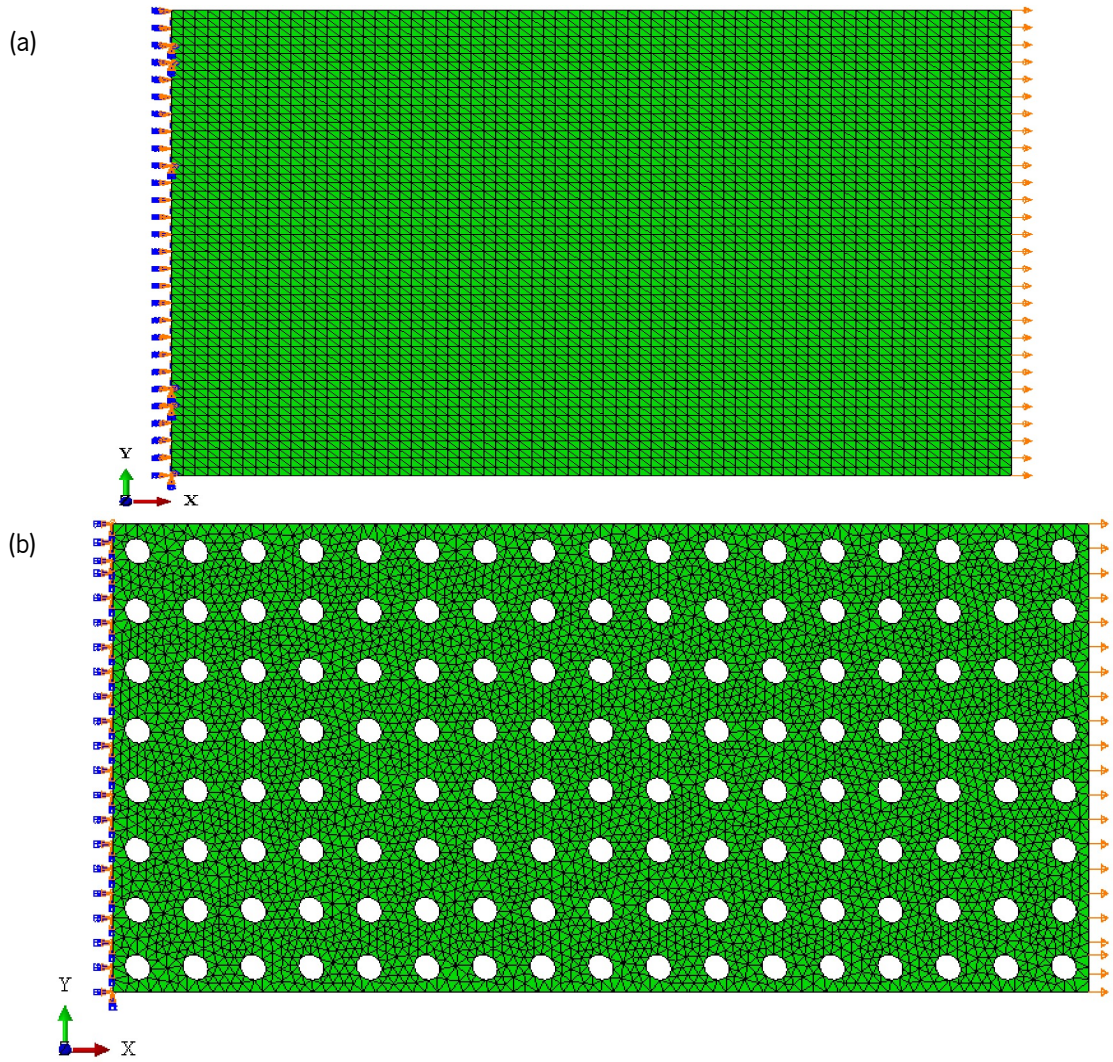



**Figure 5.9**. Finite Element model showing the used boundary conditions a) BNC membrane; b) BNC structure.

For the mesh, elements were fitted to the type of analysis, C3D10. Initial inputs to the material properties were Young's modulus 10 MPa and Poisson's ration 0.1. An incremental displacement was defined equivalent to the experimental testing, 60 mm·min$^{-1}$.

From the simulation, force vs displacement curves were obtained for the model. For the fitting of the elastic properties, both experimental and simulation results were compared. Young's modulus and Poisson's ratio were subsequently refined through an iterative inverse identification procedure, in which the numerical force-displacement response was compared to the experimental curves. The material parameters were progressively adjusted until a satisfactory agreement between simulation and experimental data was achieved, thus ensuring that the model accurately captured the mechanical behaviour of the material.

## 5.5. Results and discussion

### 5.5.1. Morphology

SEM images presented in Fig. 5.10 and Fig. 5.11 show the surface and cross-section of BNC composites. A much larger deposition of particles is visible on the surface compared to the inside of the BNC membrane, suggesting that, despite the small size of the particles (Table 5.2), their incorporation within the nanocellulose fibrous entanglement is limited. Despite this, the presence of particles is perceptible in the SEM images (Fig. 5.11). In addition, $Cu_2O$ particles are the most abundant on the surface. The oxygen present on the $Cu_2O$ particles may have contributed to an increase in interactions with the –OH groups of BNC, as suggested by Mira-Cuenca and co-workers, that state that the strong attachment of superparamagnetic iron oxide nanoparticles (SPIONs) coated fibres and the BNC surface are due to hydrogen bonding [391]. However, the expected concentration of the particles' syntheses calculated from the theoretical concentrations (Au: 49.0 $mg \cdot L^{-1}$; Ag: 221 $mg \cdot L^{-1}$; Cu 127 $mg \cdot L^{-1}$; $Cu_2O$ 286 $mg \cdot L^{-1}$) are in line with what can be observed in the electronic microscopy images, higher particle concentration for $Cu_2O$, followed by Ag.

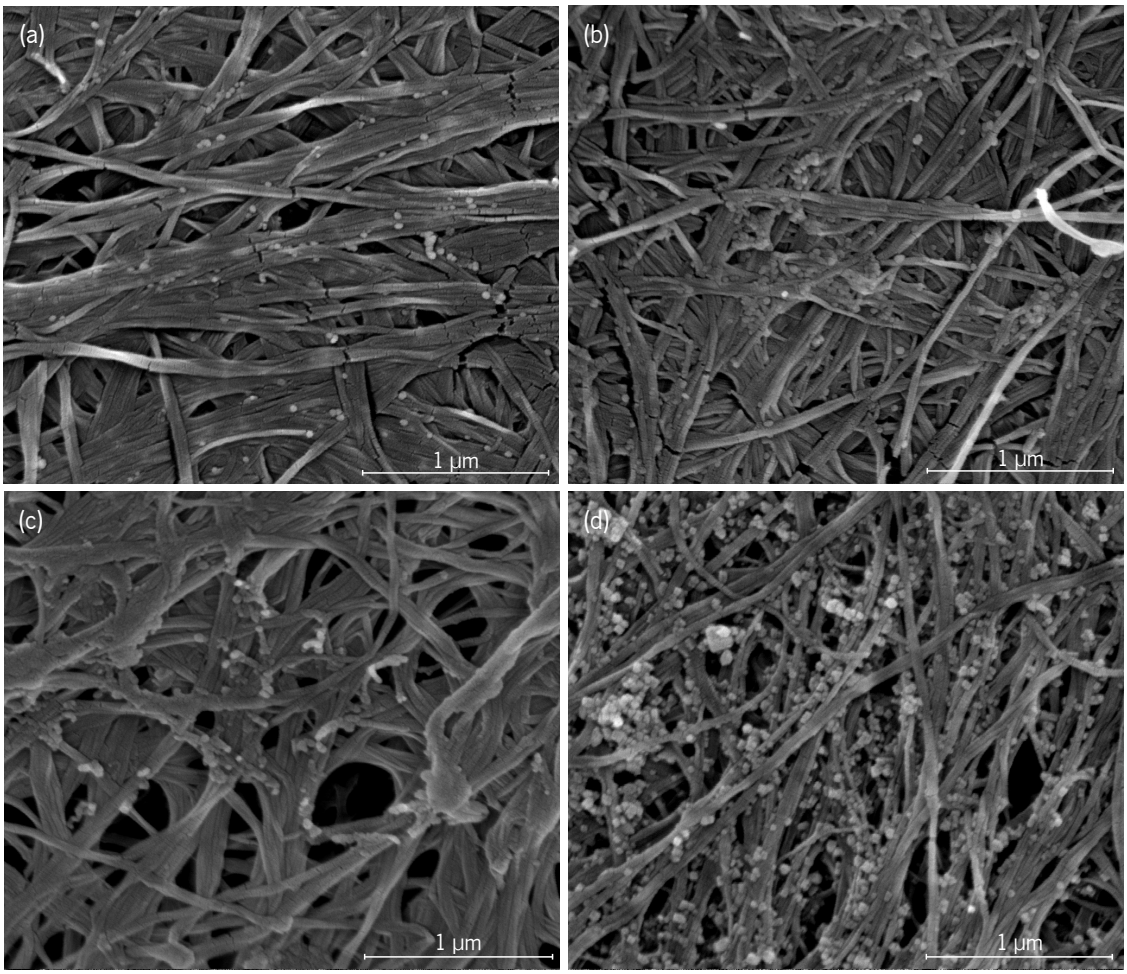



**Figure 5.10.** SEM images of the surface of the BNC composites (a) BNC/Au, (b) BNC/Ag, (c) BNC/Cu, and (d) BNC/$Cu_2O$, displaying the particles.

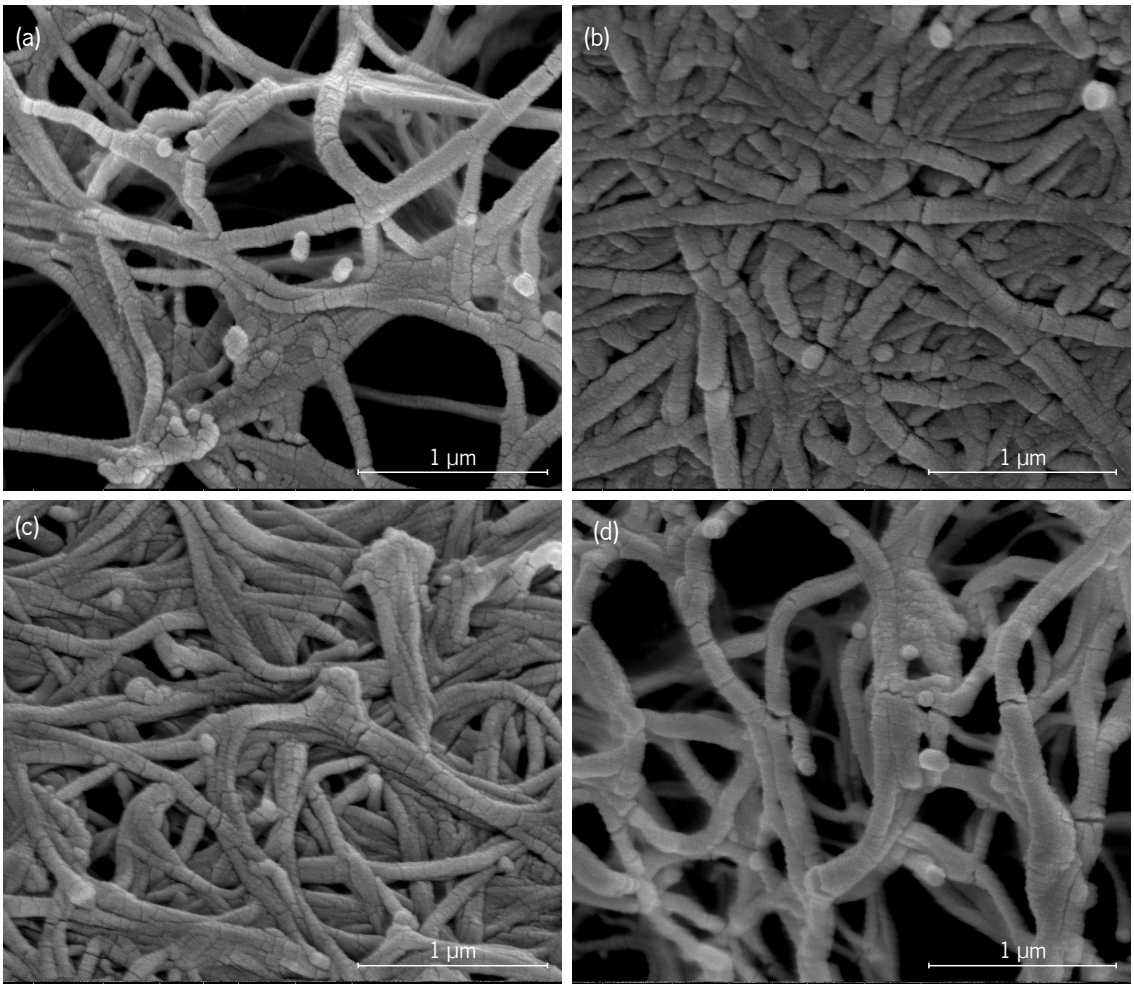



**Figure 5.11.** SEM images of the cross-section of the BNC composites (a) BNC/Au, (b) BNC/Ag, (c) BNC/Cu, and (d) BNC/$Cu_2O$, displaying the particles.

**Table 5.2.** Size of the particles on the BNC composites surfaces and interior.

| | **Au** | **Ag** | **Cu** | **$Cu_2O$** |
|---|---|---|---|---|
| | | *Surface* | | |
| **Diameter (nm)** | 35.5 ± 4.30 | 46.6 ± 13.1 | 82.2 ± 26.2 | 49.2 ± 6.77 |
| | | *Cross-section* | | |
| **Diameter (nm)** | 93.5 ± 12.7 | 128 ± 15.0 | 96.2 ± 20.7 | 98.1 ± 14.5 |

### 5.5.2. Swelling profile

The swelling behaviour of the BNC membranes in SBF at 37 °C (Fig. 5.12) was studied to evaluate the release profile of the metal particles in the hydrated and rehydrated states of the BNC, and to estimate the BNC expansion once implanted.

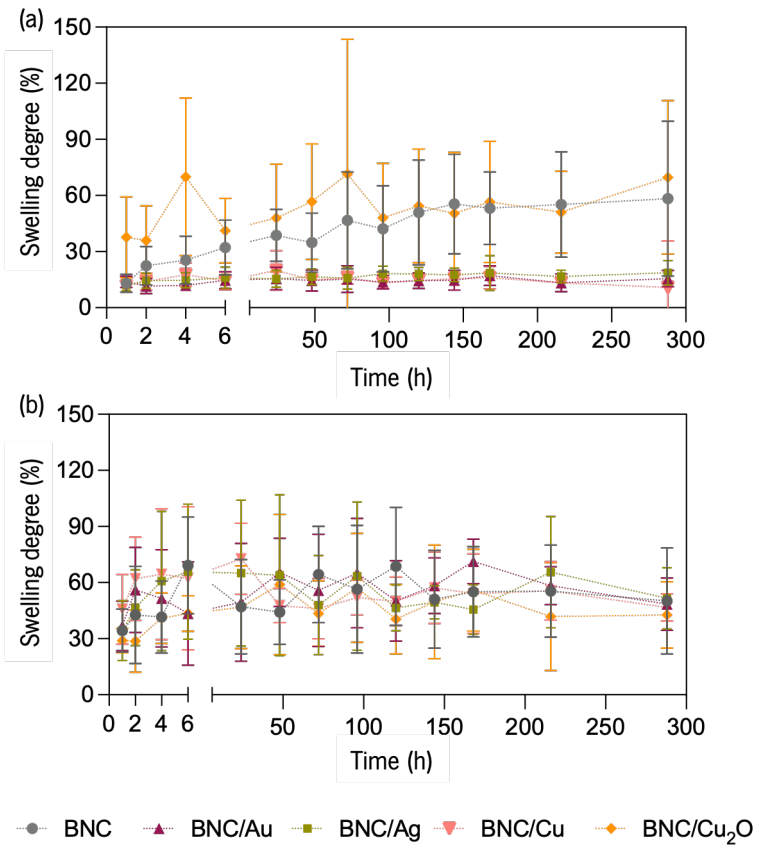



**Figure 5.12.** Swelling behaviour of BNC composites in the (a) hydrated and (b) rehydrated states.

Hydrated and rehydrated pristine BNC appear to stabilise after 144 h (6 days) reaching 55 and 51% of swelling, respectively. The high swelling of BNC is expected due to the hydration capacity of BNC. Its 3D nanofibrous porous structure allows a faster water diffusion and swelling capacity [352]. BNC functionalised with Ag and Cu seem to produce similar behaviour, demonstrating a considerable drop in swelling capacity, stabilising after 6 h, and reaching around 15% swelling. This drop in swelling capacity may be associated with the size of the Ag nanoparticles (17.9 ± 3.10 nm) and the BNC pore size (197 nm) that fill the empty pores inhibiting the entrance of water molecules. Differently, the agglomerates of Cu particles (Z-ave: 35,958.7 ± 24,3350 nm), are likely washed away, and the pores of BNC are likely filled with smaller Cu particles (PdI 0.72 ± 0.26) and salts that results from the instability of the reaction, re-oxidation from the metallic ($Cu^0$) to the

cuprous state ($Cu^{+}$ or $Cu^{2+}$). Different to the other particles, the $CuO_2$ functionalised samples exhibited a swelling of 50% after 144 h, similar to never-dried BNC control. Due to their large size, $Cu_2O$ (Z-ave: 981.9 ± 41.70 nm) are likely unable to permeate the pores of BNC, and because they are stable, their size variation is not considerable (PdI 0.15 ± 0.030), which could justify the similar behaviour to BNC. As stated above, the collapse of the fibrous structure that results from the oven-drying process, considerably reduces the recovery capacity of BNC, influencing the water retention capacity [352]. The drying process increases the proximity of the fibres, promoting the formation of hydrogen bonding. The resulting higher aggregation of the 3D structure of BNC, results in less permeability [13]. Nonetheless, it should be noted that the broad range of values displayed by rehydrated samples showed a swelling between 45 – 70%, which reduces the robustness of the results. The literature reports swelling percentages of 364.9% for a rehydrated 0.02 mm thick BNC with an area of 3 x 3 $cm^2$ [392].

### 5.5.3. Release profile

The cumulative release of the metal particles (Fig. 5.13) shows no noteworthy difference between hydrated and rehydrated BNC composites.

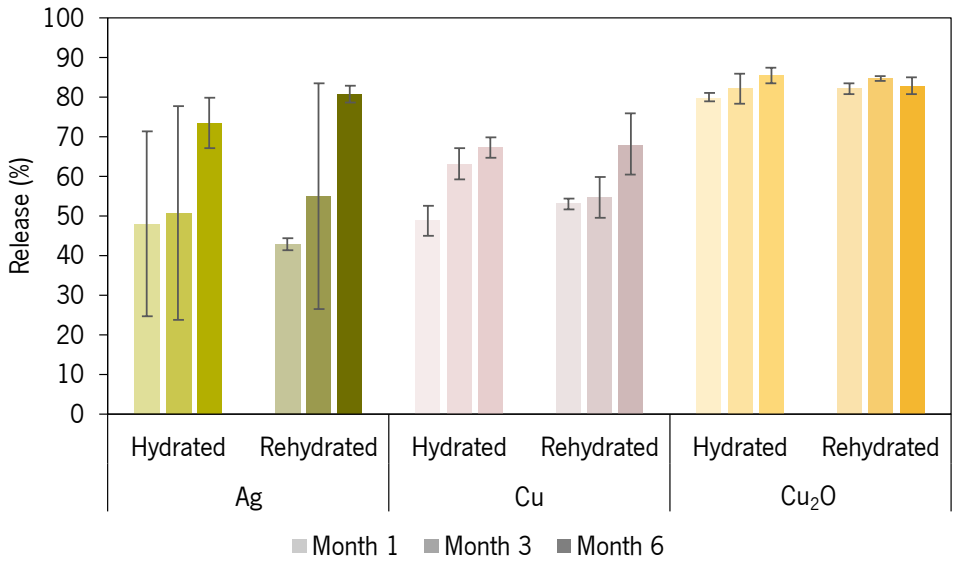



**Figure 5.13.** Cumulative release profiles of the metal particles after 1, 3, and 6 months.

For Ag and Cu particles, the release after 1 month gets an average of 45 ± 3.8 % for Ag and 51 ± 3.0% for hydrated and rehydrated composites, reaching its highest value after 6 months with averages of 77 ± 5.0% and 67 ± 0.60% for Ag and Cu, respectively. The release of $Cu_2O$ after the first month is higher (81 ± 1.5%) than in the case of Ag and Cu particles. This behaviour is somewhat maintained throughout the 6 months, with an average percentage of 84 ± 2.0%. The higher release percentage for $Cu_2O$ may be attributed to particle agglomeration (Fig. 4.7) that prevents it from entering the nanofibrous structure of the BNC. Their substantial presence at the surface of BNC (Fig. 5.10), may have contributed for the higher release percentages, particularly during the first month, despite an expected increase in interactions between the oxygen of the $Cu_2O$ particles and the –OH groups of BNC [391].These results agree with the swelling profile (5.12a), with the BNC/$Cu_2O$ having a similar behaviour as BNC, with an equilibrium swelling of approximately 50%. Differently, BNC/Ag and BNC/Cu have much lower swelling values, around 20%.

### 5.5.4. Antibacterial activity

The contact killing assays (Fig. 5.14) demonstrated the effectiveness upon contact of Cu-based particles against both *S. aureus* and *P. aeruginosa*, presenting moderate disinfectant activity. No obvious differences were detected between hydrated and rehydrated stated among these samples. These results confirm the presence of Cu particles on the surface of BNC (Fig. 5.10). Hydrated BNC/Ag nanocomposites showed to be moderate disinfectant only against *P. aeruginosa.* No activity was verified against *S. aureus*, nor from rehydrated BNC/Ag. The commercial Optilene (60 $g \cdot m^{-2}$) mesh and the BNC/Au nanocomposites showed no antimicrobial activity. The lack of antimicrobial activity of pristine BNC, either hydrated or rehydrated, was also confirmed.

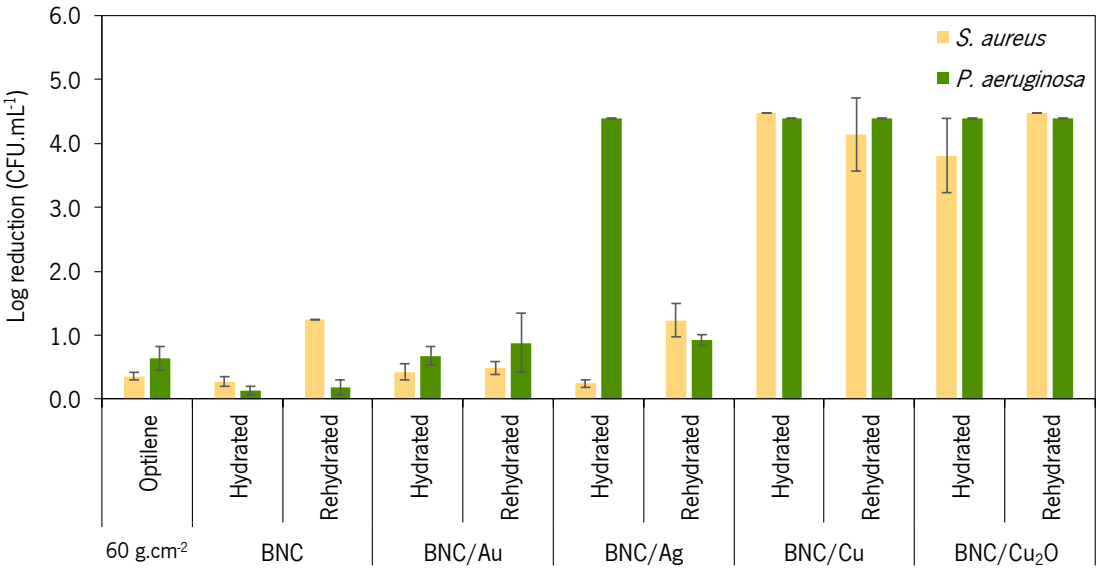



**Figure 5.14.** Contact killing results of BNC and its composites in the hydrated and rehydrated states, and commercial Optilene 60 g·m$^{-2}$ mesh.

The shake flask assay (Fig. 5.15) confirms the lack of antimicrobial activity of BNC/Au nanocomposites and Optilene meshes at 5h and 24h. Despite an expected higher antimicrobial effect of Cu-based composites against *S. aureus*, due to the release of $Cu^{2+}$ ions that are able to bind to the negatively charged Gram positive species [393], Cu-based composites presented sterilizing effect against *P. aeruginosa* and strong disinfectant activity against *S. aureus* at 5h (Fig. 5.15a). However, this effect decreases substantially at 24h, completely losing its activity. BNC/Ag nanocomposite showed weak decontaminant activity against *P. aeruginosa* at 5h in both hydrated and rehydrated states, losing this activity for the rehydrated state at 24h (Fig. 5.15b). The loss of antimicrobial activity at 24h after sterilizing effect may be a consequence of lower particle release that were unable to fight the remaining bacteria, allowing its proliferation in MHB medium.

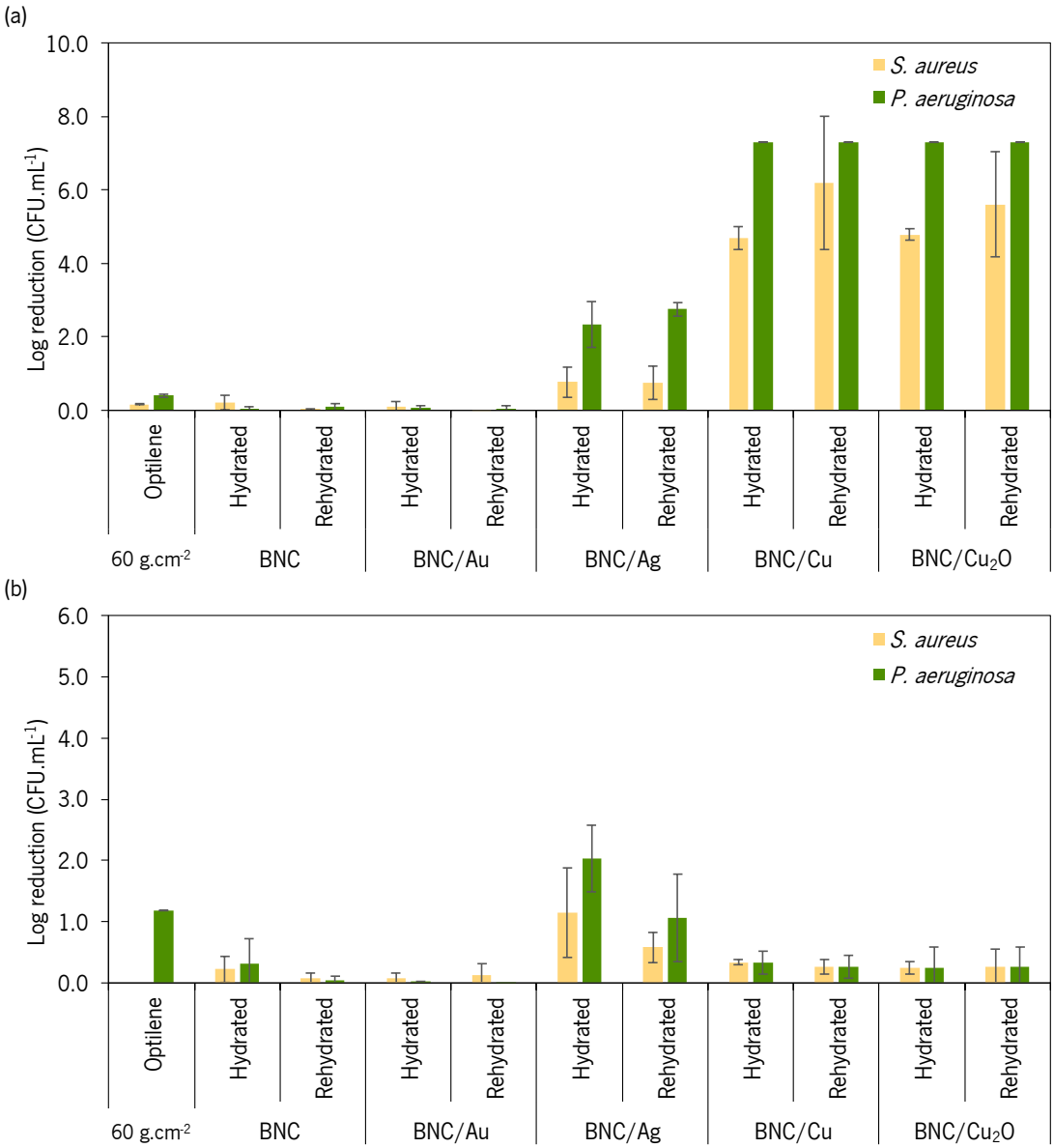



**Figure 5. 15.** Shake Flask results at (a) 5h and (b) 24h for BNC and its composites in the hydrated and rehydrated states, and commercial Optilene 60 g·m$^{-2}$ mesh.

### 5.5.5. Cellular adhesion

Considering the lack of antimicrobial activity of Au nanoparticles, the following characterization was performed with Ag, Cu, and $Cu_2O$ particles functionalised BNC meshes. Fig. 5.16 shows microscopy images obtained from Lionheart equipment, of the wells from the 24 h seeding of L929 cells on a microplate in the presence of the meshes, and after mesh removal. Fig. 5.16a evidences the normal cell growth of the control samples (without mesh), similar to the well that previously contained the Optilene mesh (Fig. 5.16b). The pristine BNC in the hydrated and rehydrated states

(Fig. 5.16 c, d) seem to affect similarly the cell growth with comparable morphology as for the control but less density in the centre. This may be attributed to the larger contact area of BNC meshes compared to commercial Optilene meshes. The BNC-based functionalised meshes show less cell density, with different morphology, suggesting that the metal particles have an influence on cell proliferation.

Inverted microscopy imagens (Fig. 5.17) of the wells of L929 cell seeding on the meshes after 24h corroborate what is stated above, that the particles influence negatively cell proliferation.

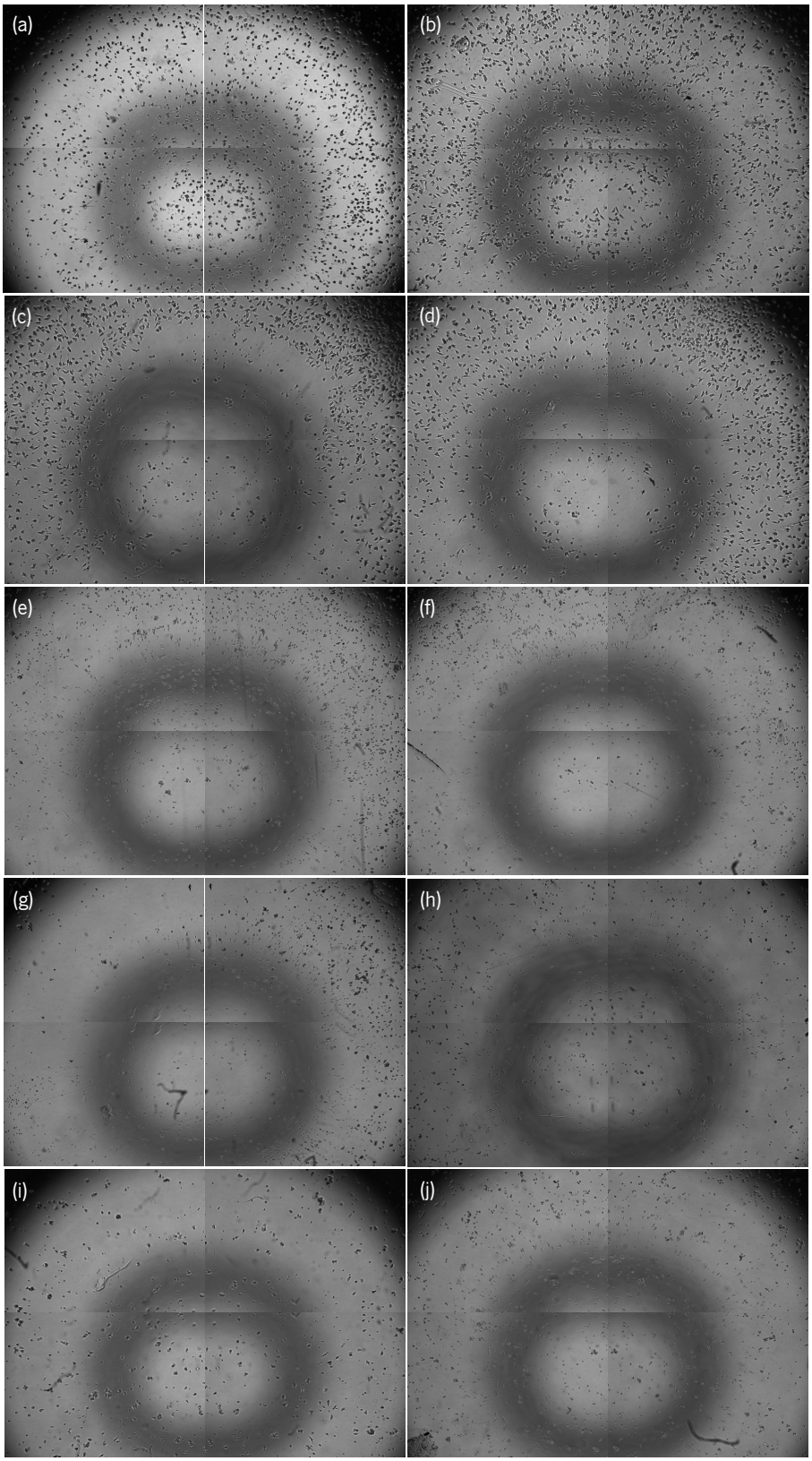



**Figure 5.16.** Lionheart images of the 96-well plates of the 24 h seeding of L929 cells: (a) control cells, (b) Optilene commercial mesh; (c) hydrated BNC, (e) hydrated BNC/Ag, (g) hydrated BNC/Cu, (i) hydrated BNC/$Cu_2O$, (d) rehydrated BNC, (f) rehydrated BNC/Ag, (h) rehydrated BNC/Cu, and (j) rehydrated BNC/$Cu_2O$.

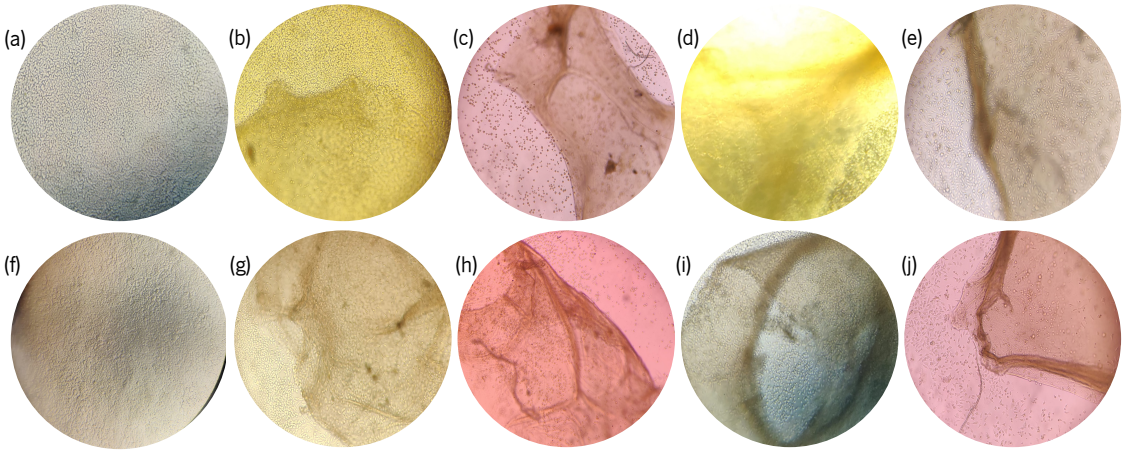



**Figure 5.17.** Microscopy images of cell proliferation from an inverted microscope (Kern®, Albstadt, Germany) after 168 h incubation of L929 cells in DMEM: (a) Control L929, hydrated meshes: (b) BNC, (c) BNC/Ag, (d) BNC/Cu, and (e) BNC/$Cu_2O$; (f) Optilene commercial mesh; and rehydrated meshes: (g) BNC, (h) BNC/Ag, (i) BNC/Cu, and (j) BNC/$Cu_2O$.

## L929 cellular adhesion onto the mesh

NR assay

The cell adhesion on the meshes was first analysed through the NR assay. Fig. 5.18 shows the metabolic activity of the adhered cells per area of contact mesh. The results suggest a higher cell metabolism for BNC/Ag meshes, hence, higher adhesion. However, these results are contradictory to what is visible in Fig. 5.16 – 5.17, that show an alteration in cell morphology with the presence of Ag nanoparticles. For this reason, the influence of NR and MTT (an alternative assay for cell metabolism), was tested in the presence of the BNC composites. Table 5.3 shows the absorbances of NR and MTT after the functionalised meshes were immersed in DMEM/NR medium or DMEM/MTT. The absorbances suggest the influence of the particles on the values obtained for the samples immersed in DMEM/NR.

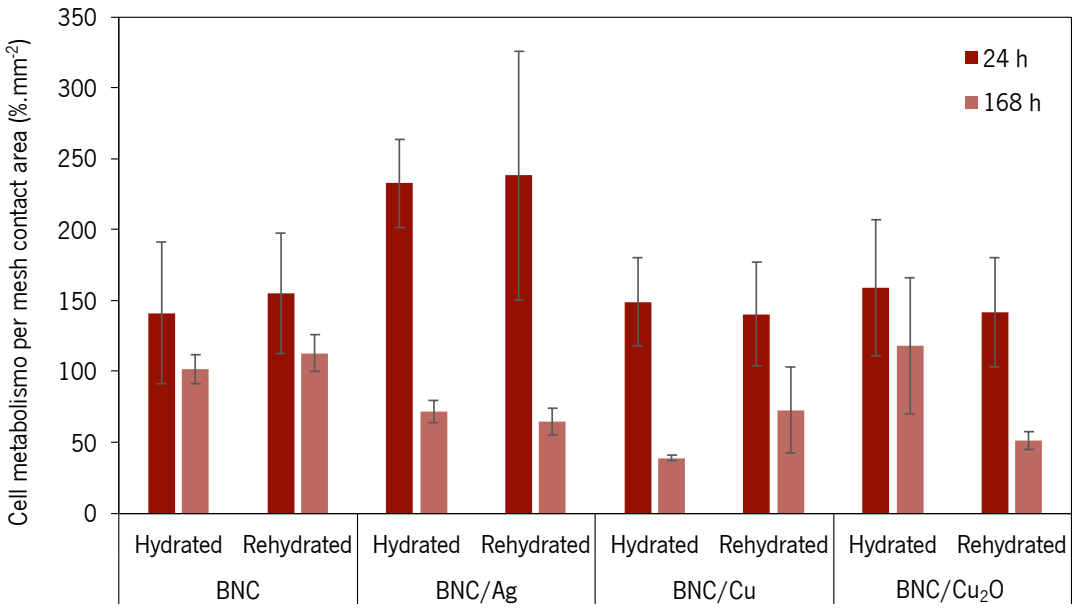



**Figure 5.18.** NR assay of adhered cells metabolism per contact area of mesh.

**Table 5.3.** Interference of NR and MTT on the metal particles functionalised meshes in the hydrated and rehydrated states.

| Absorbance at 540 nm | **NR** | **MTT** |
|---|---|---|
| BNC/Ag Hydrated | 0.118 ± 0.0320 | 0.0790 ± 0.00400 |
| BNC/Cu Hydrated | 0.106 ± 0.0160 | 0.0660 ± 0.00600 |
| BNC/Cu Rehydrated | 0.144 ± 0.0590 | 0.0640 ± 0.00100 |
| BNC/$Cu_2O$ Rehydrated | 0.123 ± 0.00800 | 0.0580 ± 0.00200 |
| BNC/$Cu_2O$ Rehydrated | 0.108 ± 0.00100 | 0.0690 ± 0.00100 |

MTT assay

Considering the results obtained in Table 5.3, MTT assays were performed. Fig. 5.19 evidences the metabolic activity of adhered L929 cells onto the meshes. After 24 h of seeding, the cell growth is between 40 – 60% but decreases substantially after 7 days of seeding to less than 20%. Contrary to the majority of the meshes, hydrated and rehydrated BNC meshes decrease cell metabolism to > 50%. Again, this is not verified in Fig. 5.16 and Fig.5.17, particularly the case of BNC/Ag nanocomposites after 24 h, that according to MTT reaches 70% of cell metabolism per area of mesh, whilst in the figures mentioned above, the cell morphology and proliferation is clearly affected.

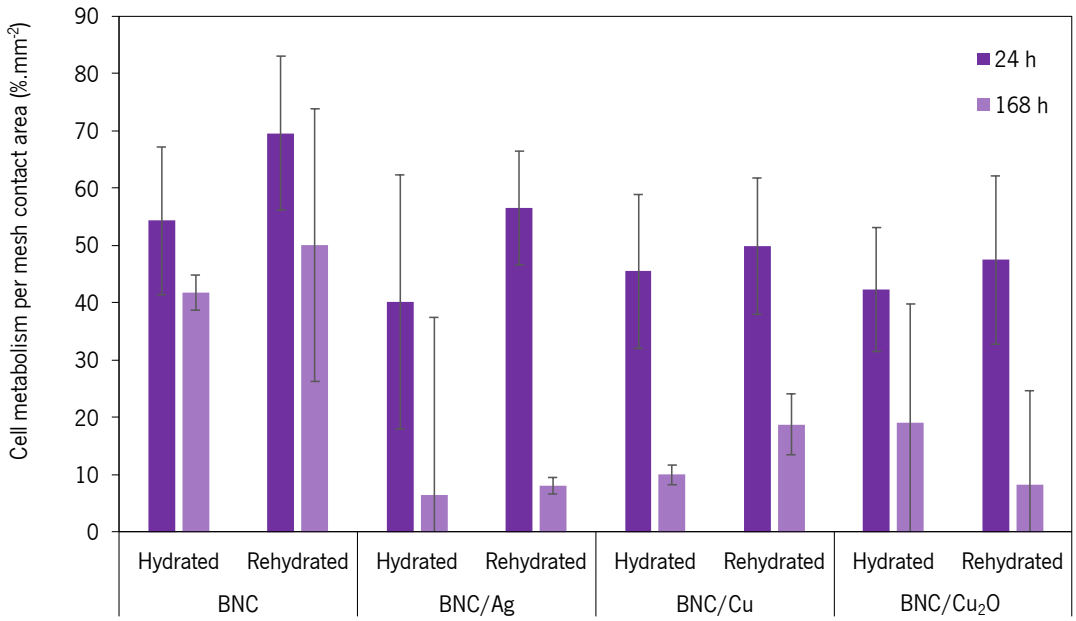



**Figure 5.19.** Cell metabolism per contact area of mesh through the MTT assay.

MTS assay

The MTS assay was used to verify both the cell adhesion onto the meshes and the influence of the composite meshes on the cell metabolic activity, according to the description in Section 5.4.5. The influence of the particles on the absorbances of the MTS/DMEM medium was verified by adding the mixture to the meshes and incubating for 24 h (Table 5.4). Since considerably lower values were obtained from the microplate readings for Cu-based composites, the average values of the three measurements of each sample were subtracted to the readings of the assays. The resulting cellular metabolic activity is presented in Fig. 5.20.

**Table 5.4.** Absorbance values obtained after a 24 h incubation of the meshes in DMEM/MTS.

| Absorbance at 540 nm | **MTS** |
|---|---|
| Optilene | 0.225 |
| BNC Hydrated | 0.186 |
| BNC Rehydrated | 0.211 |
| BNC/Ag Hydrated | 0.219 |
| BNC/Ag Rehydrated | 0.231 |
| BNC/Cu Hydrated | 0.158 |
| BNC/Cu Rehydrated | 0.203 |

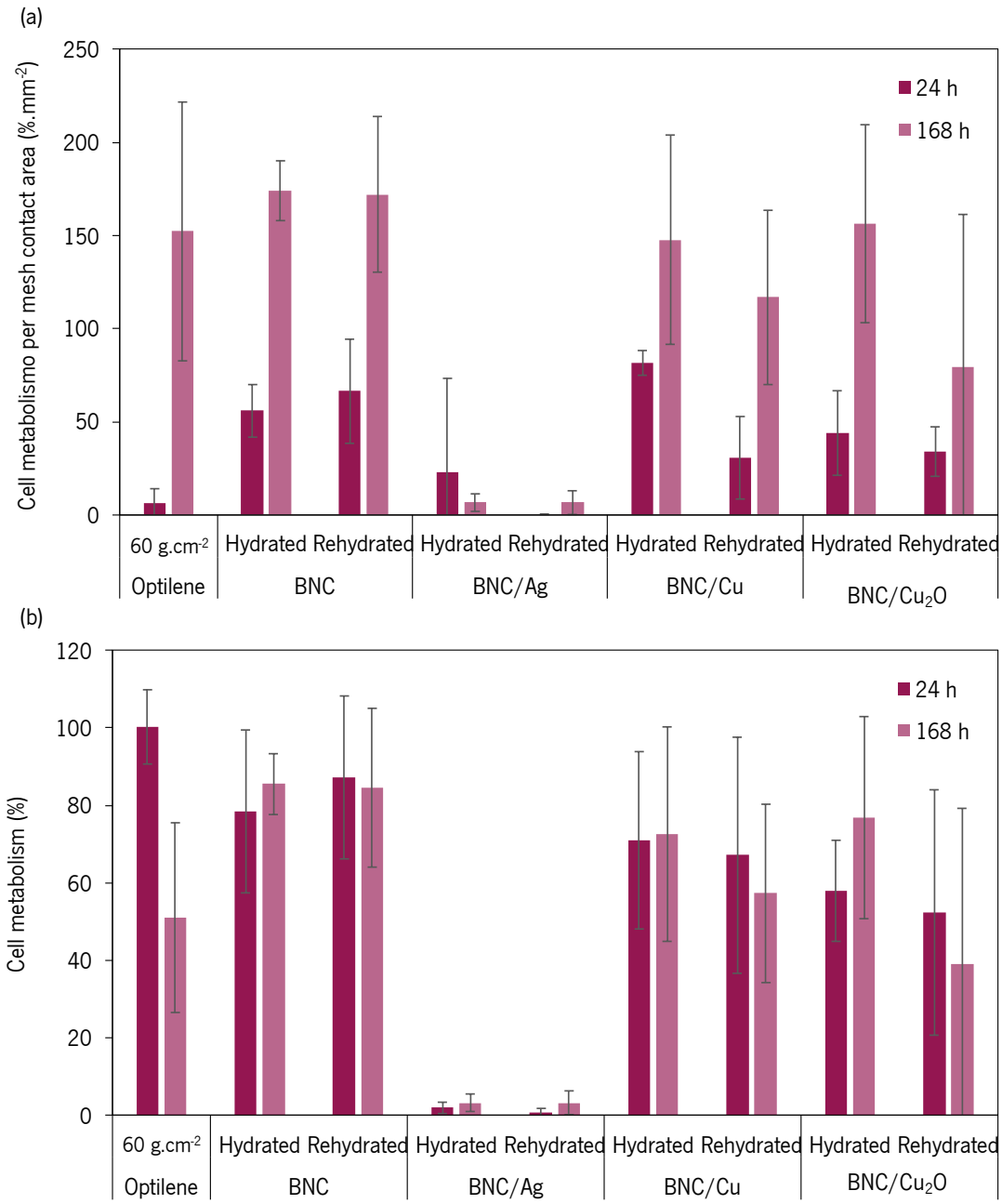



**Figure 5.20.** MTT assay of L929 (a) cell metabolism (%) of adhered cells per area of mesh contact ($mm^2$) and (b) influence of meshes on cell metabolism.

It is clear that BNC/Ag meshes present toxicity, which could be attributed to concentration. Another explanation may the due to the precipitation, in biological media, of toxic $Ag^+$ ions, that precipitate as silver chloride [394]. The majority of the meshes present a cell adhesion comparable to the commercial mesh, except for rehydrated BNC/$Cu_2O$ meshes. According to Fig. 5.20b, cell metabolism was not affected by the presence of BNC-based meshes, and the results are similar to commercial PP-based Optilene.

SEM images (Fig. 5.21) of the cells on the meshes after seeding of 168 h show different morphologies for cells adhered onto hydrated and rehydrated meshes.

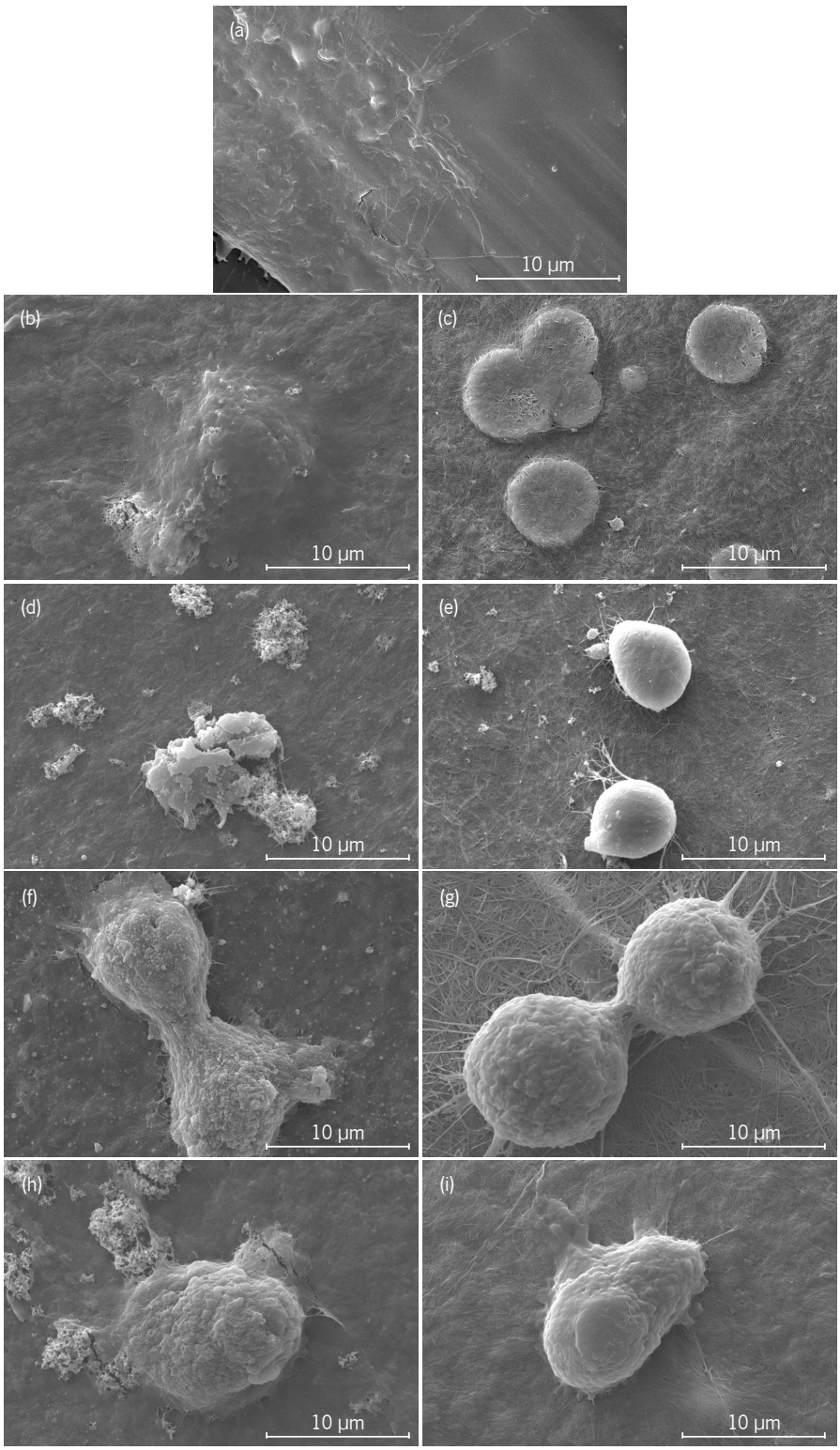



**Figure 5.21.** SEM images of L929 cells adhesion to the meshes after 168 h: (a) Optilene, (b) hydrated BNC, (c) rehydrated BNC, (d) hydrated BNC/Ag, (e) rehydrated BNC/Ag, (f) hydrated BNC/Cu, (g) rehydrated BNC/Cu, (h) hydrated BNC/$Cu_2O$, and (i) rehydrated BNC/$Cu_2O$.

The morphology of cells adhered onto hydrated meshes seems to have been affected. An explanation may be due to osmotic shock since the hydrated BNC are firstly stored in $dH_2O$ and only prior to the assay are immersed in SBF before sterilization. The rehydrated meshes are dried and rehydrated directly in SBF, hence the ionic levels avoid the osmotic shock [395].

### 5.5.6. Mechanical properties

The tensile preparation and response of the BNC membrane are presented in Fig. 5.22 – 5.23. The experimental load–displacement curves obtained from multiple specimens are compared with the corresponding numerical fitting. For the BNC membrane, a consistent and reproducible behaviour was observed across all tested samples, characterised by a smooth and continuous increase in load with displacement (Fig. 5.24). The curves exhibit a clearly defined linear region in the initial stages of deformation, indicating a predominantly elastic response within the tested range.

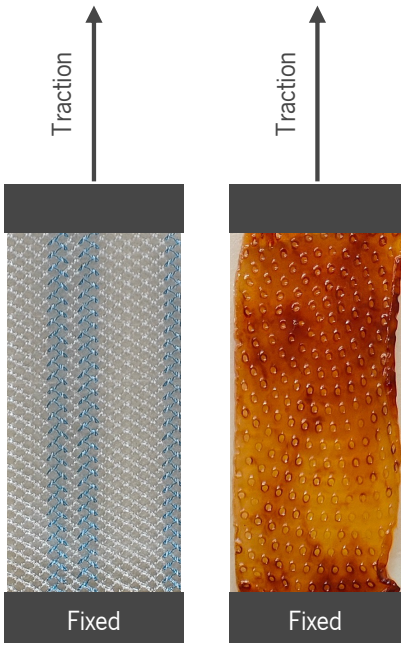



**Figure 5.22.** Example of the traction applied to a commercial and a BNC functionalised mesh.

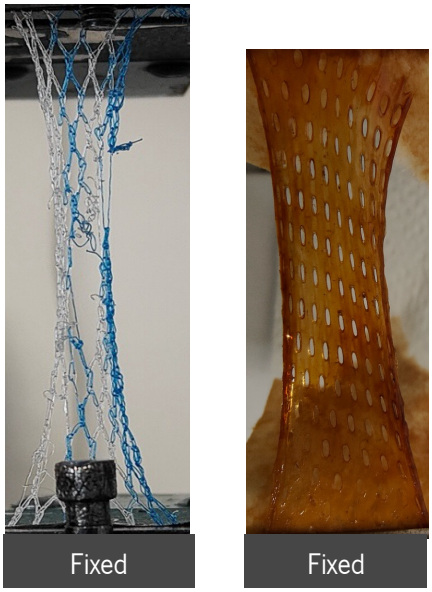



**Figure 5.23.** Example of the deformation of the specimens after traction was applied.

The numerical model showed good agreement with the experimental data, accurately capturing the slope of the load–displacement curves. The fitting procedure resulted in an estimated $E$ of approximately 0.5 MPa and a Poisson's ratio close to 0.01, which remained consistent across all samples. This agreement confirms the adequacy of the adopted linear elastic model to describe the initial mechanical behaviour of the BNC membrane under tensile loading.

A consistent mechanical distinction was found between BNC membranes and BNC meshes. Membranes showed smoother, more continuous load–displacement curves and lower stiffness (see Figure 5.24), reflecting their homogeneous and planar structure. Meshes consistently displayed higher stiffness and load-bearing capacity. This contrast highlights the importance of architecture in modulating the mechanical response (Fig. 5.25 and 5.26), even when chemical composition and hydration state are identical. Commercial meshes present higher elasticity (Fig. 5.27) compared to BNC meshes (Fig. 5.28).

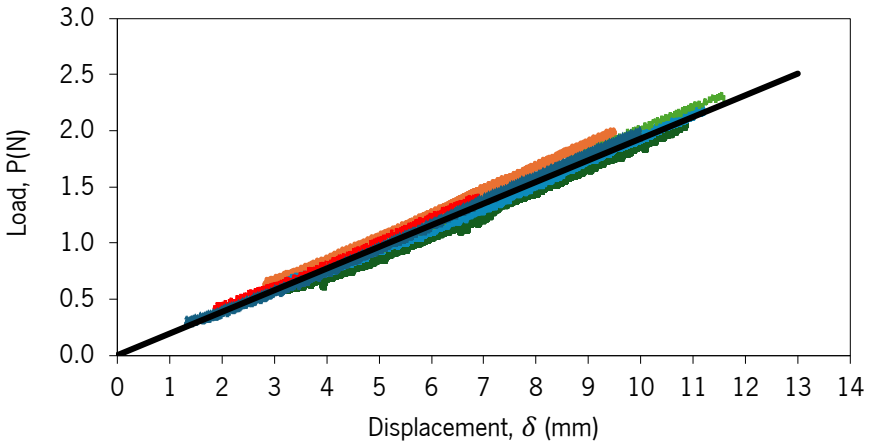



**Figure 5.24.** Numerical fitting of the 1 mm thick BNC membrane performed for 7 measurements using *E* of 0.5 MPa and Poisson's ratio of 0.01.

## Model Fitting

All samples showed a clearly defined linear elastic region in the initial stages of loading. Numerical fits (based on linear elasticity models) aligned well with the experimental curves, reinforcing the reliability of modulus estimates. In all cases, the Poisson's ratio remained close to 0.01, suggesting minimal lateral strain and near uniaxial deformation behaviour.

The consistency between experimental and numerical responses supports the reliability of the identified material parameters. The low Poisson's ratio suggests limited transverse deformation, indicating that the material undergoes predominantly uniaxial elongation during the initial loading stage. This behaviour is in line with the expected response of a hydrated nanofibrous network, where deformation is primarily accommodated through fibre reorientation and progressive load transfer along the tensile direction.

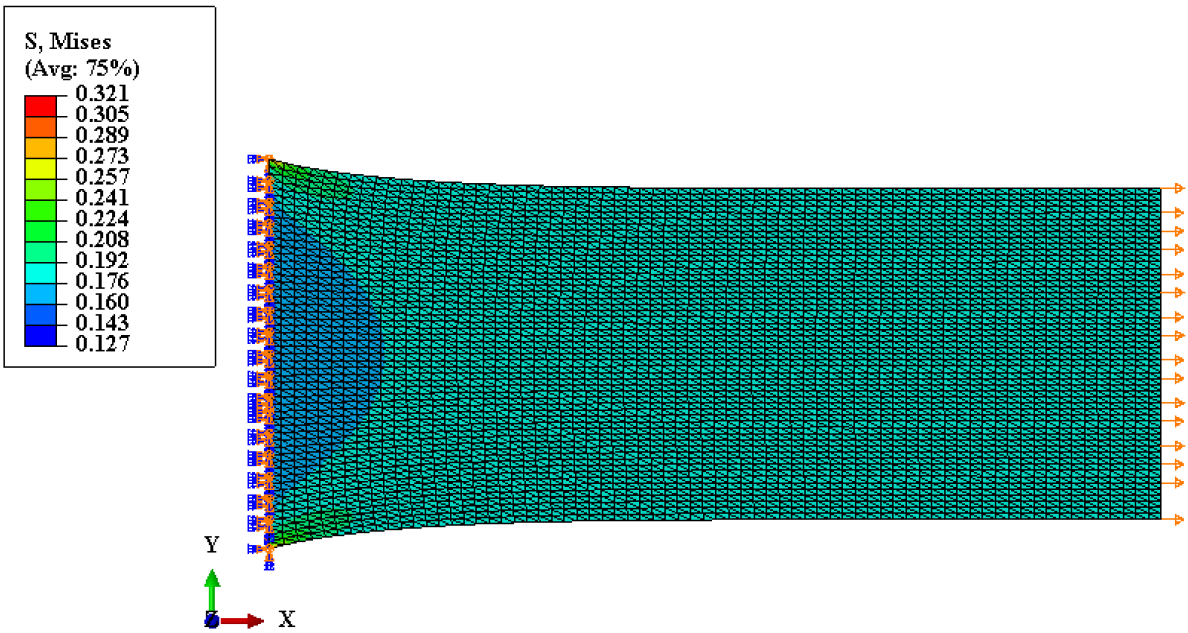



**Figure 5.25.** Deformed model of the BNC membrane with boundary conditions.

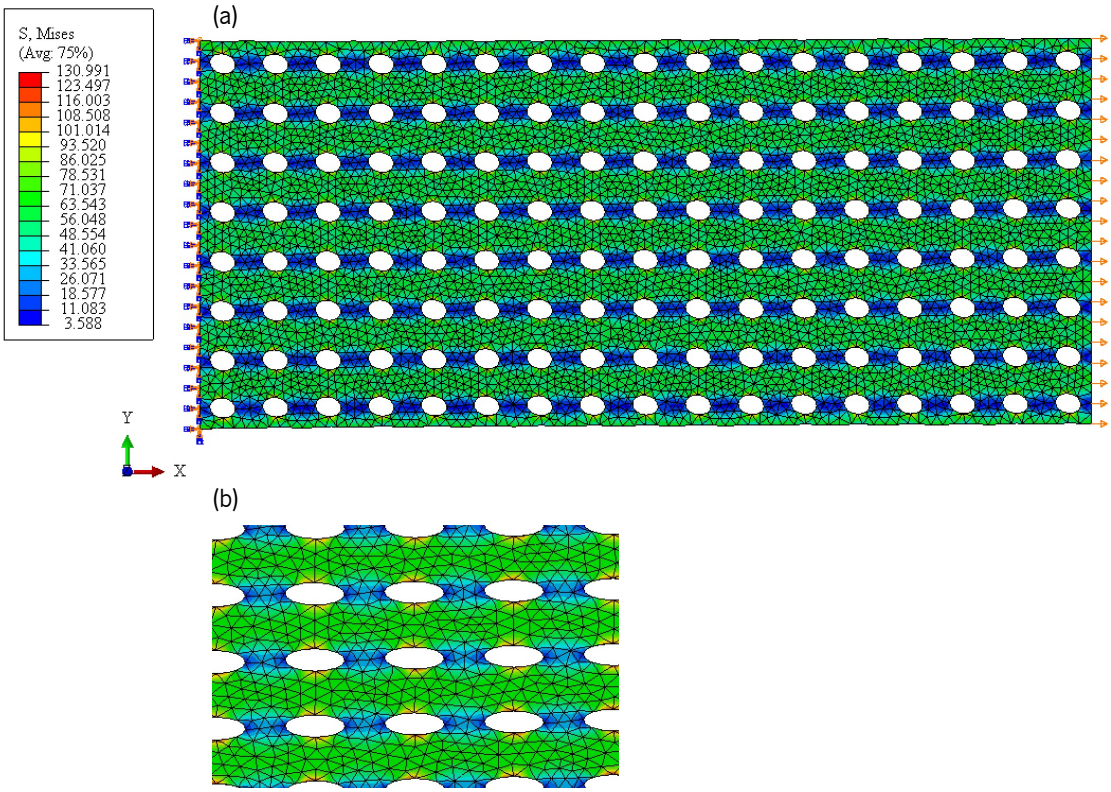



**Figure 5. 26.** Deformed model of the (a) BNC mesh and (b) a magnified image of the deformation of the holes.

Due to its nanofibrous structure, the mechanical behaviour of BNC can be described as a progressive deformation process involving different stages. Initially, a gradual alignment of the randomly oriented fibres occurs under tensile loading, followed by an increase in stiffness associated with load transfer along the aligned fibrils, and finally by fibre stretching at higher deformation levels [396]. This behaviour is reflected in the load–displacement response (Fig. 5.28), where an initial quasi-linear region is observed.

For the BNC membrane, the $E$ obtained from the numerical fitting was approximately 0.5 MPa. This relatively low value indicates a highly compliant behaviour, which can be attributed to the hydrated state of the material and the presence of a loosely connected fibrillar network. In such conditions, deformation is primarily accommodated through fibre reorientation and sliding mechanisms rather than immediate load-bearing through a dense structure.

It should be noted that this value is significantly lower than those reported in the literature for BNC, which are typically obtained for dried or structurally densified samples. The difference highlights the strong influence of hydration state, thickness, and internal porosity on the mechanical response of BNC, and suggests that direct comparison between studies must consider these factors carefully.

With the introduction of a porous architecture, a substantial increase in stiffness was observed, with the $E$ rising to approximately 12.0 MPa for the hydrated BNC mesh. This increase indicates that the organisation of the material into a structured network plays a dominant role in defining the global mechanical response, enabling more efficient load transfer through the system. This shows that the geometric factor of the network is enough to increase stiffness by more than 200 times of hydrated BNC. This represents passive (no additives) but highly effective optimization. Regarding the influence of rehydration, that is the collapse and partial recovery of the fibrous structure, further increase to ~16.0 MPa was verified for the rehydrated BNC mesh. This growth of approximately 32% greater than the hydrated membrane reinforces the effectiveness of the rehydration cycle as a structural densification method. The dehydration-rehydration significantly increased the $E$ across all tested samples (Table 5.6). Apart from BNC/Ag nanocomposites, there was an improvement in $E$ besides pristine BNC. BNC/Cu composites improved $E$ from 10 to 17.5 MPa when in the hydrated and rehydrated states, respectively, as did BNC/$Cu_2O$ with an increase from 11.5 to 20.5 MPa. The Ag functionalised nanocomposites showed an opposite behaviour to the remaining with a slight decrease from 15.5 MPa to 13.0 MPa. This may be due to the smaller size of Ag nanoparticles or water affinity that enables water absorbance which leads to higher residual water

that mechanically cushions the structure, making it more elastic and less rigid. These results confirm that physical post-processing (rehydration) is a viable and effective strategy to enhance BNC network performance.

Regarding the functionalisation with metallic particles, the impact on the mechanical properties provided different results. Ag enhanced stiffness under hydrated conditions (highest $E$ among hydrated samples), indicating potential for improved fibre-particle interactions. Cu resulted in lower initial stiffness, but greater gain after rehydration, suggesting latent reinforcement potential activated by structural rearrangement. $Cu_2O$ provided a balanced and strong mechanical response, with both hydrated and rehydrated samples showing high modulus values. These observations demonstrate that the type of additive affects not only the base stiffness but also the response to hydration changes.

Some variability was observed in replicate tests, especially in samples with metallic additives. This may result from heterogeneous particle dispersion, affecting local stiffness or differences in hydration levels, particularly in network regions with higher surface area. Despite this, the general trends were consistent, and all variations remained within reasonable experimental ranges.

Considering the tensile strength required to sustain a maximum abdominal pressure of approximately 0.023 MPa is lower than 0.16 MPa, BNC may be an alternative to hernia repair. In addition, inguinal hernias are subject to relatively low mechanical pressures, benefiting from light-weight meshes, providing the necessary support without pain or foreign body sensation [2, 14].

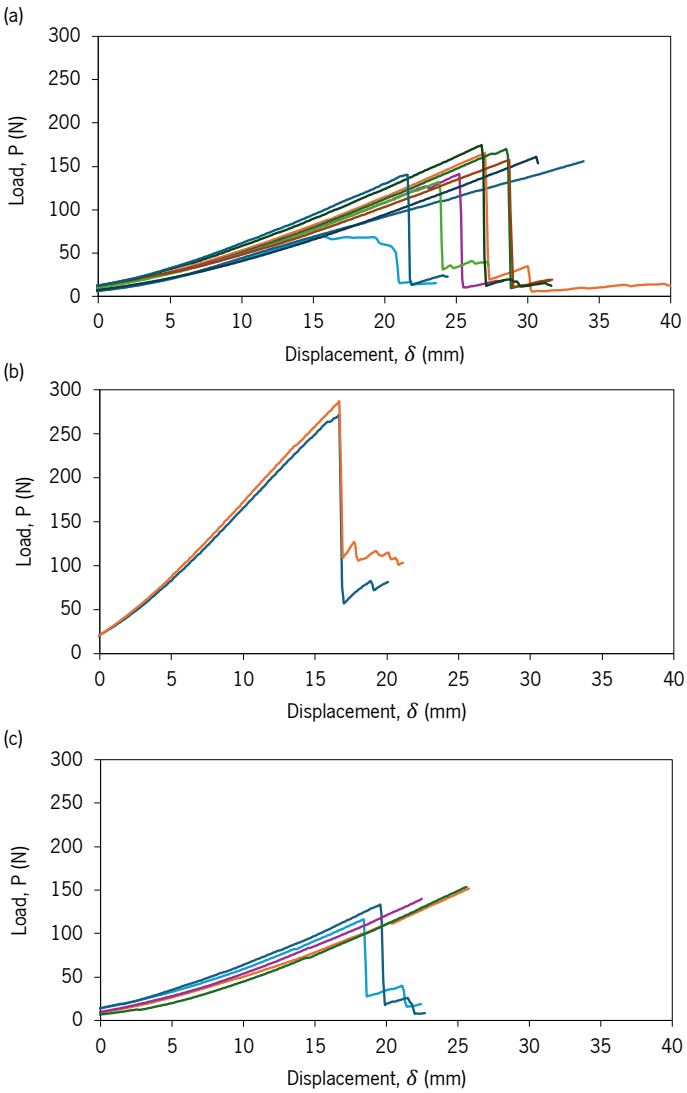



**Figure 5.27.** Graphics of the load vs displacement curves and the corresponding fitting of the commercial meshes: (a) Optilene B. Braun-Portugal, (b) Ethicon Ultrapro Advanced, and (c) Optilene Mesh Elastic B. Braun-Portugal.

Differences between the commercial meshes were also observed. Optilene Mesh Elastic presented the highest slope among the tested samples, indicating greater stiffness, while Ultrapro Advanced showed a slightly more compliant behaviour, with lower load values at equivalent displacements. These variations are consistent with differences in mesh density, filament thickness, and structural design. For the Ultrapro Advanced mesh, only two replicates were available, which may contribute to the reduced variability observed. Commercial meshes exhibited abrupt failure following a linear response, whereas BNC-based structures showed more progressive deformation prior to failure, indicating higher deformability.

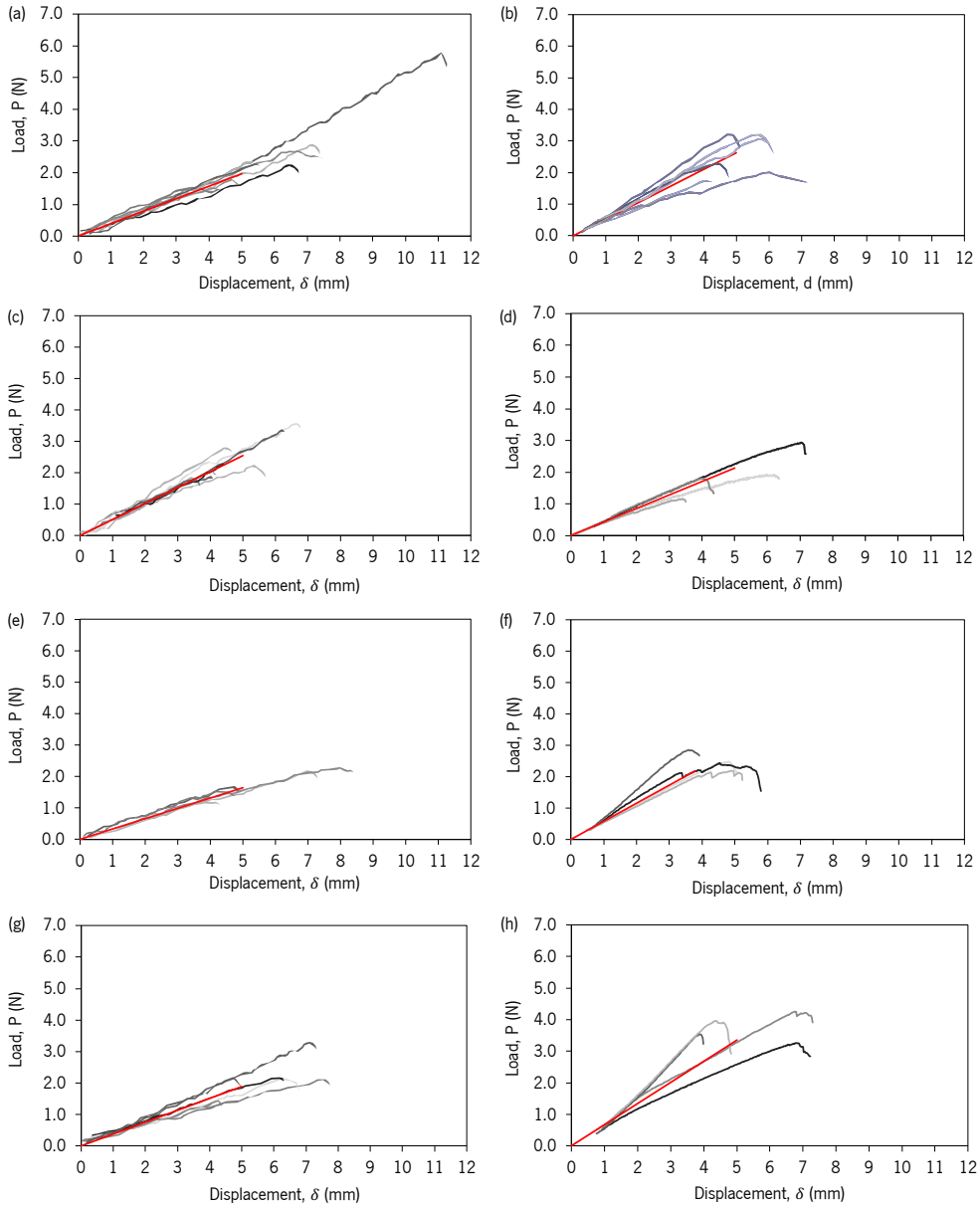



**Figure 5.28.** Graphics of the load vs displacement curves and the corresponding numerical fitting of the meshes: hydrated (a) BNC, (c) BNC/Ag, (e) BNC/Cu, (g) BNC/$Cu_2O$ hydrated, and rehydrated (b) BNC, (d) BNC/Ag, (f) BNC/Cu, (h) BNC/$Cu_2O$.

The comparison between the experimental curves and the corresponding numerical fits in Figure 5.28 shows that the model was able to reproduce the initial slope of the load–displacement response for all tested mesh configurations with reasonable accuracy. This indicates that the adopted numerical approach is adequate to estimate the apparent elastic response of the BNC-based structures in the initial loading regime. The agreement was generally stronger in the early stages of deformation, whereas larger deviations were observed at higher displacements and close to failure. This behaviour is expected, since the numerical fitting was based on a simplified elastic

description and does not explicitly account for local damage, progressive ligament rupture, pore distortion, or other structural nonlinearities that may arise during tensile loading.

**Table 5.5.** Comparison of the elastic modulus *(E)* of the commercial meshes.

| Sample | Elastic modulus (*E*, MPa) |
|---|---|
| Optilene 60 g·m$^{-2}$ | 164 |
| Ultrapro Ethicon 28 g·m$^{-2}$ | 170 |
| Optilene 48 g.m$^{-2}$ | 520 |

**Table 5.6.** Comparison of the elastic modulus *(E)* and Poisson's ratio of BNC membrane and hydrated and rehydrated functionalised BNC meshes.

| | | Elastic modulus *(E)* | Poisson's ration |
|---|---|---|---|
| BNC membrane | | 0.5 | 0.01 |
| **Hydrated meshes** | BNC | 12.0 | 0.01 |
| | BNC/Ag | 15.5 | |
| | BNC/Cu | 10.0 | |
| | BNC/$Cu_2O$ | 11.5 | |
| **Rehydrated meshes** | BNC | 16.0 | 0.01 |
| | BNC/Ag | 13.0 | |
| | BNC/Cu | 17.5 | |
| | BNC/$Cu_2O$ | 20.5 | |

The *E* of commercial PP-based meshes presented in Table 5.5 show mush higher values than the ones obtained for BNC meshes (Table 5.6). The Optilene (60 g·m$^{-2}$) whose mesh is tighter than that of Optilene Mesh Elastic (48 g·m$^{-2}$), presents an *E* of 164 MPa, circa 10 times higher than BNC. Optilene Mesh Elastic, with a wider mesh obtained 520 MPa. This later mesh may be considered a light-weight mesh, which is characterised by reduced inflammatory reaction and greater elasticity and flexibility. Thus, depending on the size of the defect, BNC-based meshes are sufficient for abdominal support, but need improvement if to be compared to current commercial meshes. The different bacteria strains are known to produce BNC with distinct morphology, density, crystallinity and porosity, which ultimately affect the final properties of BNC. Thus, a selection of BNC producing strain could be an alternative to produce BNC with superior mechanical properties. Carbon source selection is another important factor that impact BNC properties, although in this

study the selected medium Hestrin-Schramm is the most appropriate and carbon rich medium. Besides production, changes to the BNC may be done through chemical modification. Oxidation, acetylation, etherification, are able to modify the –OH groups of BNC with different functional groups increasing intermolecular interactions [397]. By changing the degree of substitution, further improvement of the mechanical properties is possible [398, 399]. The functionalisation with polymers adds a plasticising effect to the BNC by enabling strong interaction between the fibrils, avoiding the concentration of stress by sharing it between polymer and BNC. Metal particle reinforcement is another option for increasing the mechanical properties with BNC acting as both carrier and stabiliser [397]. An increase in *E* with the incorporation of metal particles was confirmed in this study for rehydrated meshes. These results demonstrate that the mechanical performance of BNC is primarily governed by structural organisation rather than intrinsic material properties, highlighting the potential of architecture-driven design for tailored biomedical applications.

## 5.6. Conclusions

The BNC mesh obtained was functionalised using *in situ* approach and showed excellent antimicrobial activity, both upon contact and release. In particular for both Cu-based particles and against *P. aeruginosa*. Cellular assays showed that BNC does not seem to affect the cell morphology and proliferation. On the contrary, Ag nanoparticles proved to be highly cytotoxic, possibly because the release it not in the form $Ag^{+}$, but as nanoparticle instead. $Cu_2O$ seems to be slightly more cytotoxic than Cu particles, although neither are considerably cytotoxic. The porous architecture and the introduction of metal particles proved to be beneficial in terms of stiffness in particular for hydrated BNC meshes, in comparison with the BNC membrane in the hydrated state.

# Chapter 6

## General conclusions and future perspectives

# 6. General conclusions and future perspectives

## 6.1. General conclusions

The project aimed at developing a BNC-based mesh to potentially replace current commercial plastic mesh devices. For this purpose, BNC was initially submitted to three different functionalisation methodologies: *ex situ* filtration and exhaustion, and *in situ*. Organic active agents, Kraft lignin (KL) and olive pomace (OP), two byproducts from the paper and olive oil industry, were used for their antimicrobial and antioxidant properties to functionalise BNC though *ex situ*. Inorganic metal particles gold (Au), silver (Ag), copper (Cu), and copper oxide ($Cu_2O$), substantially known for their antimicrobial properties were chosen for all three functionalisation approaches. The resulting KL, OP, and a mixture of KL/OP composites were characterised in terms of morphological (SEM, BET, porosity), chemical (ATR-FTIR, XPS), and thermal properties (TGA, DSC) evidencing no significant alterations to the original BNC structure. Despite no obvious formation of bonds between the BNC and the organic active agents, the presence of KL, OP, and KL/OP within the nanofibrous structure of BNC was verified even if partial. This was likely a consequence of the particle size, due to agglomeration, and small pore size of the BNC. As a consequence, the release profile was almost insignificant, hence the antimicrobial and antioxidant activities of the composites were also limited. The introduction of metal particles withing the BNC matrix was tested with both the exhaustion and *in situ* process presenting similar outcomes in terms of morphological, chemical, and thermal properties, showing no seeming alterations to the composite compared to pristine BNC, and similar antimicrobial activity. However, due to the simpler and faster one way method of the *in situ* functionalisation, this procedure was chosen for the next nest, the development of the BNC mesh. The release profile of the particles are in agreement with the antibacterial activity. Both BNC/Cu and BNC/$Cu_2O$ composites presented excellent antimicrobial activity upon contact for 1 h and release after 5 h. This effect is lost after 24h. The cellular assays show that BNC does not influence the morphological and proliferation of the cells, but the presence of the particles, in particular Ag, does have a damaging influence. The mechanical properties were analysed showing that with the introduction of pores, some properties are affected. Membranes displayed lower stiffness whilst meshes consistently displayed higher stiffness and load-bearing capacity. The elastic modulus *(E)* of commercial PP-based meshes present values around 10 times higher than BNC meshes. The dehydration-rehydration significantly increased *E*. Considering the

highest intraabdominal pressure and the *E* of the abdominal wall, BNC-based meshes are sufficient for abdominal support, depending on the size of the defect, but need improvement if to be compared to current commercial meshes.

## 6.2. Future perspectives

Based on the results from the present work, the following suggestions are presented for future work:

- Introduce new mesh designs on the BNC, namely different pore sizes and distances, and different shapes, in particular the honeycomb structure;
- Adjust and evaluate the influence of the concentration of the metal nanoparticles, particularly on the antimicrobial and cellular assays;
- Evaluate long-term antimicrobial activity of the functionalised meshes (1, 3, 6 months post-synthesis) – product shelf-life;
- Analyse the biofilm adherence onto the BNC mesh;
- Improve the mechanical properties of the BNC mesh both by passively changing its design, and actively through the functionalisation and modification of the BNC.

# References

1. Gilbert, A.I., J. Young, and R. Azuaje, *Overview of Modern Surgical Techniques in Inguinal Hernia Repair*, in *Textbook of Hernia*. 2017. p. 41-42.
2. Brown, C.N. and J.G. Finch. "Which mesh for hernia repair?". *The Annals of The Royal College of Surgeons of England* 2010, 92 (4), 272-278. DOI: 10.1308/003588410x12664192076296.
3. McCormack, K., N. Scott, P.M.N.Y.H. Go, et al. "Laparoscopic techniques versus open techniques for inguinal hernia repair". *Cochrane Database of Systematic Reviews* 2003. DOI: 10.1002/14651858.Cd001785.
4. Liu, P., K. Fu, X. Zeng, et al. "Fabrication and Characterization of Composite Meshes Loaded with Antimicrobial Peptides". *ACS Applied Materials & Interfaces* 2019, 11 (27), 24609-24617. DOI: 10.1021/acsami.9b07246.
5. Talley, A.D., B.R. Rogers, V. Iakovlev, et al. "Oxidation and degradation of polypropylene transvaginal mesh". *Journal of Biomaterials Science, Polymer Edition* 2017, 28 (5), 444-458. DOI: 10.1080/09205063.2017.1279045.
6. Sternschuss, G., D.R. Ostergard, and H. Patel. "Post-Implantation Alterations of Polypropylene in the Human". *Journal of Urology* 2012, 188 (1), 27-32. DOI: 10.1016/j.juro.2012.02.2559.
7. Nie, Y., Y. Xiong, L. Guan, et al. "Laparoscopic fixation of biological mesh at hiatus with glue and suture during hiatal hernia repair". *BMC Surgery* 2021, 21 (1). DOI: 10.1186/s12893-021-01151-0.
8. Robinson, T.N., J.H. Clarke, J. Schoen, et al. "Major mesh-related complications following hernia repair". *Surgical Endoscopy* 2005, 19 (12), 1556-1560. DOI: 10.1007/s00464-005-0120-y.
9. Buell, J.F., D. Sigmon, C. Ducoin, et al. "Initial Experience With Biologic Polymer Scaffold (Poly-4-hydroxybuturate) in Complex Abdominal Wall Reconstruction". *Annals of Surgery* 2017, 266 (1), 185-188. DOI: 10.1097/sla.0000000000001916.
10. Janet, J., S. Derbal, S. Durand Fontanier, et al. "C-reactive protein is a predictive factor for complications after incisional hernia repair using a biological mesh". *Scientific Reports* 2021, 11 (1). DOI: 10.1038/s41598-021-83663-6.
11. Cannon, R.E. and S.M. Anderson. "Biogenesis of Bacterial Cellulose". *Critical Reviews in Microbiology* 2008, 17 (6), 435-447. DOI: 10.3109/10408419109115207.
12. Gonçalves, S., J. Padrão, I.P. Rodrigues, et al. "Bacterial cellulose as a support for the growth of retinal pigment epithelium". *Biomacromolecules* 2015, 16 (4), 1341-1351. DOI: 10.1021/acs.biomac.5b00129.
13. Padrão, J., S. Gonçalves, J.P. Silva, et al. "Bacterial cellulose-lactoferrin as an antimicrobial edible packaging". *Food Hydrocolloids* 2016, 58, 126-140. DOI: 10.1016/j.foodhyd.2016.02.019.
14. Antoniadi, E., N. Ferreira, M. Vaz, et al. "Innovative Strategies in Hernia Mesh Design: Materials, Mechanics, and Modeling". *Materials* 2025, 18 (15). DOI: 10.3390/ma18153509.
15. Baylón, K., P. Rodríguez-Camarillo, A. Elías-Zúñiga, et al. "Past, Present and Future of Surgical Meshes: A Review". *Membranes* 2017, 7 (3). DOI: 10.3390/membranes7030047.
16. California, H.C.o.S. *Abdominal / Ventral Hernia*. 2026 [cited 2025 August 22].
17. Wang See, C., T. Kim, and D. Zhu. "Hernia Mesh and Hernia Repair: A Review". *Engineered Regeneration* 2020, 1, 19-33. DOI: 10.1016/j.engreg.2020.05.002.

18. Smith, S.M., A.A. Khoja, J.H.W. Jacobsen, et al. "Mesh versus non-mesh repair of groin hernias: a rapid review". *ANZ Journal of Surgery* 2022, 92 (10), 2492-2499. DOI: 10.1111/ans.17721.
19. Chen, N., M. Lv, Y. Chen, et al. "Investigation of risk factors and predictive model development for the progression of incarcerated inguinal hernia to strangulation". *Hernia* 2025, 29 (1). DOI: 10.1007/s10029-025-03480-y.
20. Giuntoli, G., G. Muzio, C. Actis, et al. "In-vitro Characterization of a Hernia Mesh Featuring a Nanostructured Coating". *Frontiers in Bioengineering and Biotechnology* 2021, 8. DOI: 10.3389/fbioe.2020.589223.
21. Huerta, S. and A.M. Garza. "A Systematic Review of Open, Laparoscopic, and Robotic Inguinal Hernia Repair: Management of Inguinal Hernias in the 21st Century". *Journal of Clinical Medicine* 2025, 14 (3). DOI: 10.3390/jcm14030990.
22. Eurostat. *Surgical operations and procedures statistics*. 2024 [cited 2026 January 7]; Available from: https://ec.europa.eu/eurostat/statistics-explained/index.php?title=Surgical_operations_and_procedures_statistics#Number_of_surgical_operations_and_procedures.
23. Billroth, T., *The Medical Sciences in the German Universities: A Study in the History of Civilization*. 1924: New York: The Macmillan company. 292.
24. Shiroud Heidari, B., J.M. Dodda, L.K. El-Khordagui, et al. "Emerging materials and technologies for advancing bioresorbable surgical meshes". *Acta Biomaterialia* 2024, 184, 1-21. DOI: 10.1016/j.actbio.2024.06.012.
25. Navalyal, S.R., P.K.H. Kumar, P. Hoogar, et al. "A Study on the Comparison of Hernia Repair Potcomes: Mesh Versus Non-Mesh Techniques in Inguinal Hernia Surgery". *European Journal of Cardiovascular Medicine* 2025, 15 (3), 935-939. DOI: 10.5083/ejcm/25-03-161.
26. Fadaee, N., D. Huynh, Z. Khanmohammed, et al. "Patients With Systemic Reaction to Their Hernia Mesh: An Introduction to Mesh Implant Illness". *Journal of Abdominal Wall Surgery* 2023, 2. DOI: 10.3389/jaws.2023.10983.
27. Özant, A. and K. Arslan. "Synthetic Meshes in Hernia Surgery". *Cyprus Journal of Medical Sciences* 2023, 8 (1), 1-7. DOI: 10.4274/cjms.2022.2021-217.
28. Hernandez, J.L. and K.A. Woodrow. "Medical Applications of Porous Biomaterials: Features of Porosity and Tissue-Specific Implications for Biocompatibility". *Advanced Healthcare Materials* 2022, 11 (9). DOI: 10.1002/adhm.202102087.
29. Kalaba, S., E. Gerhard, J.S. Winder, et al. "Design strategies and applications of biomaterials and devices for Hernia repair". *Bioactive Materials* 2016, 1 (1), 2-17. DOI: 10.1016/j.bioactmat.2016.05.002.
30. Klinge, U., K. Junge, M. Stumpf, et al. "Functional and morphological evaluation of a low-weight, monofilament polypropylene mesh for hernia repair". *Journal of Biomedical Materials Research* 2002, 63 (2), 129-136. DOI: 10.1002/jbm.10119.
31. Turner, T. *Hernia Mesh: Complications, Recalls & FIM-DE-SEMANA safety Warnings*. 2025 [cited 2025 20/01]; Cassandra L. :[Available from: https://www.drugwatch.com/hernia-mesh/.
32. Klinge, B.K.M.M.U. "Foreign Body Reaction to Meshes Used for the Repair of Abdominal Wall Hernias". *The European Journal of Surgery* 1999, 165 (7), 665-673. DOI: 10.1080/11024159950189726.
33. Goldstein, H.S. "Selecting the right mesh". *Hernia* 1999, 3 (1), 23-26. DOI: 10.1007/bf01576737.

34. Ghosh, S., *Composite nonwovens in medical applications*, in *Composite Non-Woven Materials*. 2014. p. 211-224.
35. Guillaume, O., A.H. Teuschl, S. Gruber-Blum, et al. "Emerging Trends in Abdominal Wall Reinforcement: Bringing Bio-Functionality to Meshes". *Advanced Healthcare Materials* 2015, 4 (12), 1763-1789. DOI: 10.1002/adhm.201500201.
36. Leber, G.E. "Long-term Complications Associated With Prosthetic Repair of Incisional Hernias". *Archives of Surgery* 1998, 133 (4). DOI: 10.1001/archsurg.133.4.378.
37. Rastegarpour, A., M. Cheung, and M. Vardhan. "Surgical mesh for ventral incisional hernia repairs:Understanding mesh design". *Plastic Surgery* 2016, 24 (01). DOI: 10.4172/plastic-surgery.1000955.
38. Deeken, C.R., M.S. Abdo, M.M. Frisella, et al. "Physicomechanical Evaluation of Polypropylene, Polyester, and Polytetrafluoroethylene Meshes for Inguinal Hernia Repair". *Journal of the American College of Surgeons* 2011, 212 (1), 68-79. DOI: 10.1016/j.jamcollsurg.2010.09.012.
39. Liu, W., Y. Xie, Y. Zheng, et al. "Regulatory science for hernia mesh: Current status and future perspectives". *Bioactive Materials* 2021, 6 (2), 420-432. DOI: 10.1016/j.bioactmat.2020.08.021.
40. Haigh, J.N., T.R. Dargaville, and P.D. Dalton. "Additive manufacturing with polypropylene microfibers". *Materials Science and Engineering: C* 2017, 77, 883-887. DOI: 10.1016/j.msec.2017.03.286.
41. Guillaume, O., R. Pérez-Tanoira, R. Fortelny, et al. "Infections associated with mesh repairs of abdominal wall hernias: Are antimicrobial biomaterials the longed-for solution?". *Biomaterials* 2018, 167, 15-31. DOI: 10.1016/j.biomaterials.2018.03.017.
42. Fine, A. "Laparoscopic Repair of Inguinal Hernia with Biomimetic Matrix". *JSLS : Journal of the Society of Laparoendoscopic Surgeons* 2012, 16 (4), 564-568. DOI: 10.4293/108680812x13462882737050.
43. Parshikov, V.V., V.A. Khodak, V.V. Petrov, et al. "Tension-Free Repair of Abdominal Wall Hernias Using Glue in Experiment". *Modern Technologies in Medicine* 2013, 5(2), 14-19.
44. Singhal, P., W. Small, E. Cosgriff-Hernandez, et al. "Low density biodegradable shape memory polyurethane foams for embolic biomedical applications". *Acta Biomaterialia* 2014, 10 (1), 67-76. DOI: 10.1016/j.actbio.2013.09.027.
45. Patrick, C.W. "Tissue engineering strategies for adipose tissue repair". *The Anatomical Record* 2001, 263 (4), 361-366. DOI: 10.1002/ar.1113.
46. Tandon, A., K. Shahzad, S. Pathak, et al. "Parietex™ Composite mesh versus DynaMesh®-IPOM for laparoscopic incisional and ventral hernia repair: a retrospective cohort study". *The Annals of The Royal College of Surgeons of England* 2016, 98 (8), 568-573. DOI: 10.1308/rcsann.2016.0292.
47. Gómez-Gil, V., G. Pascual, and J. Bellón. "Biomaterial Implants in Abdominal Wall Hernia Repair: A Review on the Importance of the Peritoneal Interface". *Processes* 2019, 7 (2). DOI: 10.3390/pr7020105.
48. Huber, A., A.V. Boruch, A. Nieponice, et al. "Histopathologic host response to polypropylene-based surgical mesh materials in a rat abdominal wall defect model". *Journal of Biomedical Materials Research Part B: Applied Biomaterials* 2012, 100B (3), 709-717. DOI: 10.1002/jbm.b.32503.
49. Lee, C.H., H. Kim, I.W. Han, et al. "Effect of polylactic film (Surgi-Wrap) on preventing postoperative ileus after major hepato-pancreato-biliary surgery". *Annals of Hepato-Biliary-Pancreatic Surgery* 2016, 20 (4). DOI: 10.14701/ahbps.2016.20.4.191.

50. Huang, K., X. Ding, B. Lv, et al. "Reconstruction of large-size abdominal wall defect using biodegradable poly-p-dioxanone mesh: an experimental canine study". *World Journal of Surgical Oncology* 2014, 12 (1). DOI: 10.1186/1477-7819-12-57.
51. Stoikes, N.F.N., J.R. Scott, A. Badhwar, et al. "Characterization of host response, resorption, and strength properties, and performance in the presence of bacteria for fully absorbable biomaterials for soft tissue repair". *Hernia* 2017, 21 (5), 771-782. DOI: 10.1007/s10029-017-1638-3.
52. Ruiz-Jasbon, F., J. Norrby, M.L. Ivarsson, et al. "Inguinal hernia repair using a synthetic long-term resorbable mesh: results from a 3-year prospective safety and performance study". *Hernia* 2014, 18 (5), 723-730. DOI: 10.1007/s10029-014-1249-1.
53. Hjort, H., T. Mathisen, A. Alves, et al. "Three-year results from a preclinical implantation study of a long-term resorbable surgical mesh with time-dependent mechanical characteristics". *Hernia* 2011, 16 (2), 191-197. DOI: 10.1007/s10029-011-0885-y.
54. Clemens, M.W., S. Downey, F. Agullo, et al. "Clinical Application of a Silk Fibroin Protein Biologic Scaffold for Abdominal Wall Fascial Reinforcement". *Plastic and Reconstructive Surgery Global Open* 2014, 2 (11). DOI: 10.1097/gox.0000000000000217.
55. Lake, S.P., N.F.N. Stoikes, A. Badhwar, et al. "Contamination of hybrid hernia meshes compared to bioresorbable Phasix™ Mesh in a rabbit subcutaneous implant inoculation model". *Annals of Medicine and Surgery* 2019, 46, 12-16. DOI: 10.1016/j.amsu.2019.08.004.
56. Messa, C.A., G. Kozak, R.B. Broach, et al. "When the Mesh Goes Away". *Plastic and Reconstructive Surgery - Global Open* 2019, 7 (11). DOI: 10.1097/gox.0000000000002576.
57. Ward, K.C., K.P. Costello, S. Baalman, et al. "Effect of acellular human dermis buttress on laparoscopic hiatal hernia repair". *Surgical Endoscopy* 2014, 29 (8), 2291-2297. DOI: 10.1007/s00464-014-3946-3.
58. Sun, L., J. Chen, and Y. Shen. " Randomized Controlled Trial Of Lichtenstein Repair Of Indirect Inguinal Hernias With Two Biologic Meshes From Porcine Small Intestine Submucosa ". *Therapeutics and Clinical Risk Management* 2019, Volume 15, 1277-1282. DOI: 10.2147/tcrm.S208185.
59. Young, D.A., K.C. McGilvray, N. Ehrhart, et al. "Comparison ofin vivoremodeling of urinary bladder matrix and acellular dermal matrix in an ovine model". *Regenerative Medicine* 2018, 13 (7), 759-773. DOI: 10.2217/rme-2018-0091.
60. Young, D.A., N. Jackson, C.A. Ronaghan, et al. "Retrorectus repair of incisional ventral hernia with urinary bladder matrix reinforcement in a long-term porcine model". *Regenerative Medicine* 2018, 13 (4), 395-408. DOI: 10.2217/rme-2018-0023.
61. Petro, C.C., A.S. Prabhu, L. Liu, et al. "An in vivo analysis of Miromesh—a novel porcine liver prosthetic created by perfusion decellularization". *Journal of Surgical Research* 2016, 201 (1), 29-37. DOI: 10.1016/j.jss.2015.10.009.
62. Kamarajah, S.K., S.J. Chapman, J. Glasbey, et al. "Systematic review of the stage of innovation of biological mesh for complex or contaminated abdominal wall closure". *BJS Open* 2018, 2 (6), 371-380. DOI: 10.1002/bjs5.78.
63. Adelman, D.M. and K.G. Cornwell. "Bioprosthetic Versus Synthetic Mesh". *Plastic and Reconstructive Surgery - Global Open* 2018, 6 (5). DOI: 10.1097/gox.0000000000001713.
64. Gurrado, A., I.F. Franco, G. Lissidini, et al. "Impact of pericardium bovine patch (Tutomesh®) on incisional hernia treatment in contaminated or potentially contaminated

fields: retrospective comparative study". *Hernia* 2014, 19 (2), 259-266. DOI: 10.1007/s10029-014-1228-6.

65. Giordano, P., R.D. Pullan, B. Ystgaard, et al. "The use of an acellular porcine dermal collagen implant in the repair of complex abdominal wall defects: a European multicentre retrospective study". *Techniques in Coloproctology* 2015, 19 (7), 411-417. DOI: 10.1007/s10151-015-1307-4.
66. Sullivan, E.K., D.A. Kamstock, A.S. Turner, et al. "Evaluation of a flexible collagen surgical patch for reinforcement of a fascial defect: Experimental study in a sheep model". *Journal of Biomedical Materials Research Part B: Applied Biomaterials* 2008, 87B (1), 88-94. DOI: 10.1002/jbm.b.31073.
67. Zouhair, S., E. Dal Sasso, S.R. Tuladhar, et al. "A Comprehensive Comparison of Bovine and Porcine Decellularized Pericardia: New Insights for Surgical Applications". *Biomolecules* 2020, 10 (3). DOI: 10.3390/biom10030371.
68. Petter-Puchner, A.H., R.H. Fortelny, K. Silic, et al. "Biologic hernia implants in experimental intraperitoneal onlay mesh plasty repair: the impact of proprietary collagen processing methods and fibrin sealant application on tissue integration". *Surgical Endoscopy* 2011, 25 (10), 3245-3252. DOI: 10.1007/s00464-011-1700-7.
69. Ludwicka, K., M. Kolodziejczyk, E. Gendaszewska-Darmach, et al. "Stable composite of bacterial nanocellulose and perforated polypropylene mesh for biomedical applications". *Journal of Biomedical Materials Research Part B: Applied Biomaterials* 2018, 107 (4), 978-987. DOI: 10.1002/jbm.b.34191.
70. García-Moreno, F., P. Pérez-López, S. Sotomayor, et al. "Comparing the host tissue response and peritoneal behavior of composite meshes used for ventral hernia repair". *Journal of Surgical Research* 2015, 193 (1), 470-482. DOI: 10.1016/j.jss.2014.07.049.
71. Sutton, N., M.H. MacDonald, J. Lombard, et al. "Preclinical evaluation of the effect of the combined use of the Ethicon Securestrap<sup>®</sup> Open Absorbable Strap Fixation Device and Ethicon Physiomesh™ Open Flexible Composite Mesh Device on surgeon stress during ventral hernia repair". *Medical Devices: Evidence and Research* 2017, Volume 11, 1-9. DOI: 10.2147/mder.S146761.
72. "International guidelines for groin hernia management". *Hernia* 2018, 22 (1), 1-165. DOI: 10.1007/s10029-017-1668-x.
73. Kumar, A. and J. FitzGerald. "Biologic versus Synthetic Mesh Reinforcement: What are the Pros and Cons?". *Clinics in Colon and Rectal Surgery* 2014, 27 (04), 140-148. DOI: 10.1055/s-0034-1394155.
74. Sawyer, M.A.J. "New Ovine Polymer-Reinforced Bioscaffold in Hiatal Hernia Repair". *JSLS : Journal of the Society of Laparoendoscopic Surgeons* 2018, 22 (4). DOI: 10.4293/jsls.2018.00057.
75. Ferzoco, S.J. "Early experience outcome of a reinforced Bioscaffold in inguinal hernia repair: A case series". *International Journal of Surgery Open* 2018, 12, 9-11. DOI: 10.1016/j.ijso.2018.06.001.
76. Li, S., H. Xiao, L. Yang, et al. "Electrospun P(LLA-CL) Nanoscale Fibrinogen Patch vs Porcine Small Intestine Submucosa Graft Repair of Inguinal Hernia in Adults: A Randomized, Single-Blind, Controlled, Multicenter, Noninferiority Trial". *Journal of the American College of Surgeons* 2019, 229 (6), 541-551.e1. DOI: 10.1016/j.jamcollsurg.2019.08.1446.
77. Scott, J.R., C.R. Deeken, R.G. Martindale, et al. "Evaluation of a fully absorbable poly-4-hydroxybutyrate/absorbable barrier composite mesh in a porcine model of ventral hernia

repair". *Surgical Endoscopy* 2016, 30 (9), 3691-3701. DOI: 10.1007/s00464-016-5057-9.

78. Gruber-Blum, S., A.H. Petter-Puchner, J. Brand, et al. "Comparison of three separate antiadhesive barriers for intraperitoneal onlay mesh hernia repair in an experimental model". *British Journal of Surgery* 2011, 98 (3), 442-449. DOI: 10.1002/bjs.7334.
79. K, J., K. U, P. A, et al. "Elasticity of the anterior abdominal wall and impact for reparation of incisional hernias using mesh implants". *Hernia* 2001, 5 (3), 113-118. DOI: 10.1007/s100290100019.
80. VanEpps, J.S. and J.G. Younger. "Implantable Device-Related Infection". *Shock* 2016, 46 (6), 597-608. DOI: 10.1097/shk.0000000000000692.
81. Ashbaugh, A.G., X. Jiang, J. Zheng, et al. "Polymeric nanofiber coating with tunable combinatorial antibiotic delivery prevents biofilm-associated infection in vivo". *Proceedings of the National Academy of Sciences* 2016, 113 (45). DOI: 10.1073/pnas.1613722113.
82. Jahanmard, F., M. Croes, M. Castilho, et al. "Bactericidal coating to prevent early and delayed implant-related infections". *Journal of Controlled Release* 2020, 326, 38-52. DOI: 10.1016/j.jconrel.2020.06.014.
83. Rebelo, R., J. Padrão, M.M. Fernandes, et al. "Aging Effect on Functionalized Silver-Based Nanocoating Braided Coronary Stents". *Coatings* 2020, 10 (12). DOI: 10.3390/coatings10121234.
84. Ahmed, I., A.J. Boulton, S. Rizvi, et al. "The use of triclosan-coated sutures to prevent surgical site infections: a systematic review and meta-analysis of the literature". *BMJ Open* 2019, 9 (9). DOI: 10.1136/bmjopen-2019-029727.
85. Sanbhal, N., Y. Mao, G. Sun, et al. "Surface modification of polypropylene mesh devices with cyclodextrin via cold plasma for hernia repair: Characterization and antibacterial properties". *Applied Surface Science* 2018, 439, 749-759. DOI: 10.1016/j.apsusc.2017.12.192.
86. Rangwani, S.M., C.T. Kraft, S.J. Schneeberger, et al. "Strategies for Mesh Fixation in Abdominal Wall Reconstruction: Concepts and Techniques". *Plastic & Reconstructive Surgery* 2020, 147 (2), 484-491. DOI: 10.1097/prs.0000000000007584.
87. Hochleitner, G., T. Jüngst, T.D. Brown, et al. "Additive manufacturing of scaffolds with sub-micron filaments via melt electrospinning writing". *Biofabrication* 2015, 7 (3). DOI: 10.1088/1758-5090/7/3/035002.
88. Erwin, E., E. Etriwati, and A. Akhyar. "Clinical observation, imaging, and histopathology of 3D polypropylene mesh for abdominal hernia in rabbits". *The Indian Journal of Animal Sciences* 2023, 93 (8). DOI: 10.56093/ijans.v93i8.125846.
89. Cunha, M.N.B.d., R. Rynkevic, M.E.T.d. Silva, et al. "Melt Electrospinning Writing of Mesh Implants for Pelvic Organ Prolapse Repair". *3D Printing and Additive Manufacturing* 2022, 9 (5), 389-398. DOI: 10.1089/3dp.2021.0010.
90. Sterk, S., M.E.T. Silva, A.A. Fernandes, et al. "Development of new surgical mesh geometries with different mechanical properties using the design freedom of 3D printing". *Journal of Applied Polymer Science* 2023, 140 (46). DOI: 10.1002/app.54687.
91. Hu, Q., Y. Zhang, Y. Song, et al. "3D printing/electrospinning of a bilayered composite patch with antibacterial and antiadhesive properties for repairing abdominal wall defects". *Journal of Materials Chemistry B* 2024, 12 (39), 10054-10067. DOI: 10.1039/d4tb01543f.
92. Klemm, D., E.D. Cranston, D. Fischer, et al. "Nanocellulose as a natural source for groundbreaking applications in materials science: Today's state". *Materials Today* 2018, 21 (7), 720-748. DOI: 10.1016/j.mattod.2018.02.001.

93. Bacakova, L., J. Pajorova, M. Bacakova, et al. "Versatile Application of Nanocellulose: From Industry to Skin Tissue Engineering and Wound Healing". *Nanomaterials* 2019, 9 (2). DOI: 10.3390/nano9020164.
94. Padrão, J. and A. Zille, *Surface Chemistry of Nanocellulose and Its Composites*, in *Nanocellulose and its composites for water treatment applications*, D. Kumar, Editor. 2021, CRC Press. p. 230.
95. Thevenot, P., W. Hu, and L. Tang. " Surface chemistry influences implant biocompatibility". *Current Topics in Medicinal Chemistry* 2008, 4 (4), 270-280. DOI: 10.2174/156802608783790901.
96. de Amorim, J.D.P., K.C. de Souza, C.R. Duarte, et al. "Plant and bacterial nanocellulose: production, properties and applications in medicine, food, cosmetics, electronics and engineering. A review". *Environmental Chemistry Letters* 2020, 18 (3), 851-869. DOI: 10.1007/s10311-020-00989-9.
97. Cacicedo, M.L., M.C. Castro, I. Servetas, et al. "Progress in bacterial cellulose matrices for biotechnological applications". *Bioresource Technology* 2016, 213, 172-180. DOI: 10.1016/j.biortech.2016.02.071.
98. Klemm, D., F. Kramer, S. Moritz, et al. "Nanocelluloses: A New Family of Nature-Based Materials". *Angewandte Chemie International Edition* 2011, 50 (24), 5438-5466. DOI: 10.1002/anie.201001273.
99. Bodea, I.M., F.I. Beteg, C.R. Pop, et al. "Optimization of Moist and Oven-Dried Bacterial Cellulose Production for Functional Properties". *Polymers* 2021, 13 (13). DOI: 10.3390/polym13132088.
100. Zhang, C.J., L. Wang, J.C. Zhao, et al. "Effect of Drying Methods on Structure and Mechanical Properties of Bacterial Cellulose Films". *Advanced Materials Research* 2011, 239-242, 2667-2670. DOI: 10.4028/www.scientific.net/AMR.239-242.2667.
101. Illa, M.P., C.S. Sharma, and M. Khandelwal. "Tuning the physiochemical properties of bacterial cellulose: effect of drying conditions". *Journal of Materials Science* 2019, 54 (18), 12024-12035. DOI: 10.1007/s10853-019-03737-9.
102. Anton-Sales, I., S. Roig-Sanchez, K. Traeger, et al. "In vivo soft tissue reinforcement with bacterial nanocellulose". *Biomaterials Science* 2021, 9 (8), 3040-3050, 10.1039/D1BM00025J. DOI: 10.1039/d1bm00025j.
103. Muangman, P., S. Opasanon, S. Suwanchot, et al. "Efficiency of microbial cellulose dressing in partial-thickness burn wounds". *The Journal of the American College of Certified Wound Specialists* 2011, 3 (1), 16-19. DOI: https://doi.org/10.1016/j.jcws.2011.04.001.
104. Zmejkoski, D.Z., Z.M. Marković, N.M. Zdravković, et al. "Bactericidal and antioxidant bacterial cellulose hydrogels doped with chitosan as potential urinary tract infection biomedical agent". *RSC Advances* 2021, 11 (15), 8559-8568, 10.1039/D0RA10782D. DOI: 10.1039/d0ra10782d.
105. Stanisławska, A., H. Staroszczyk, and M. Szkodo. "The effect of dehydration/rehydration of bacterial nanocellulose on its tensile strength and physicochemical properties". *Carbohydrate Polymers* 2020, 236. DOI: 10.1016/j.carbpol.2020.116023.
106. Chen, S.-Q., P. Lopez-Sanchez, D. Wang, et al. "Mechanical properties of bacterial cellulose synthesised by diverse strains of the genus Komagataeibacter". *Food Hydrocolloids* 2018, 81, 87-95. DOI: 10.1016/j.foodhyd.2018.02.031.
107. Potivara, K. and M. Phisalaphong. "Development and Characterization of Bacterial Cellulose Reinforced with Natural Rubber". *Materials* 2019, 12 (14). DOI: 10.3390/ma12142323.

108. Cazón, P., G. Velázquez, and M. Vázquez. "Characterization of bacterial cellulose films combined with chitosan and polyvinyl alcohol: Evaluation of mechanical and barrier properties". *Carbohydrate Polymers* 2019, 216, 72-85. DOI: 10.1016/j.carbpol.2019.03.093.
109. Liu, K. and J.M. Catchmark. "Enhanced mechanical properties of bacterial cellulose nanocomposites produced by co-culturing Gluconacetobacter hansenii and Escherichia coli under static conditions". *Carbohydrate Polymers* 2019, 219, 12-20. DOI: 10.1016/j.carbpol.2019.04.071.
110. Samyn, P., A. Meftahi, S.A. Geravand, et al. "Opportunities for bacterial nanocellulose in biomedical applications: Review on biosynthesis, modification and challenges". *International Journal of Biological Macromolecules* 2023, 231. DOI: 10.1016/j.ijbiomac.2023.123316.
111. Barja, F. "Bacterial nanocellulose production and biomedical applications". *The Journal of Biomedical Research* 2021, 35 (4). DOI: 10.7555/jbr.35.20210036.
112. Mishra, S., P.K. Singh, R. Pattnaik, et al. "Biochemistry, Synthesis, and Applications of Bacterial Cellulose: A Review". *Frontiers in Bioengineering and Biotechnology* 2022, 10. DOI: 10.3389/fbioe.2022.780409.
113. Randhawa, A., S.D. Dutta, K. Ganguly, et al. "A Review of Properties of Nanocellulose, Its Synthesis, and Potential in Biomedical Applications". *Applied Sciences* 2022, 12 (14). DOI: 10.3390/app12147090.
114. Sandhu, S., A. Arpa, X. Chen, et al. "Engineering Bacterial Cellulose for Diverse Biomedical Applications". *Recent Progress in Materials* 2019, 1 (4), 1-1. DOI: 10.21926/rpm.1904006.
115. Rai, R. and P. Dhar. "Biomedical engineering aspects of nanocellulose: a review". *Nanotechnology* 2022, 33 (36). DOI: 10.1088/1361-6528/ac6fef.
116. Navya, P.V., V. Gayathri, D. Samanta, et al. "Bacterial cellulose: A promising biopolymer with interesting properties and applications". *International Journal of Biological Macromolecules* 2022, 220, 435-461. DOI: 10.1016/j.ijbiomac.2022.08.056.
117. Liu, W., H. Du, M. Zhang, et al. "Bacterial Cellulose-Based Composite Scaffolds for Biomedical Applications: A Review". *ACS Sustainable Chemistry & Engineering* 2020, 8 (20), 7536-7562. DOI: 10.1021/acssuschemeng.0c00125.
118. Sharma, C. and N.K. Bhardwaj. "Bacterial nanocellulose: Present status, biomedical applications and future perspectives". *Materials Science and Engineering: C* 2019, 104. DOI: 10.1016/j.msec.2019.109963.
119. Raghavendran, V., E. Asare, and I. Roy, *Bacterial cellulose: Biosynthesis, production, and applications*. 2020. p. 89-138.
120. Jozala, A.F., L.C. de Lencastre-Novaes, A.M. Lopes, et al. "Bacterial nanocellulose production and application: a 10-year overview". *Applied Microbiology and Biotechnology* 2016, 100 (5), 2063-2072. DOI: 10.1007/s00253-015-7243-4.
121. Skočaj, M. "Bacterial nanocellulose in papermaking". *Cellulose* 2019, 26 (11), 6477-6488. DOI: 10.1007/s10570-019-02566-y.
122. Singhsa, P., R. Narain, and H. Manuspiya. "Physical structure variations of bacterial cellulose produced by different Komagataeibacter xylinus strains and carbon sources in static and agitated conditions". *Cellulose* 2018, 25 (3), 1571-1581. DOI: 10.1007/s10570-018-1699-1.
123. El-Naggar, N.E.-A., A.B.A. Mohammed, and S.E. El-Malkey. "Bacterial nanocellulose production using Cantaloupe juice, statistical optimization and characterization". *Scientific Reports* 2023, 13 (1). DOI: 10.1038/s41598-022-26642-9.

124. Zhong, C. "Industrial-Scale Production and Applications of Bacterial Cellulose". *Frontiers in Bioengineering and Biotechnology* 2020, 8. DOI: 10.3389/fbioe.2020.605374.
125. El-Gendi, H., T.H. Taha, J.B. Ray, et al. "Recent advances in bacterial cellulose: a low-cost effective production media, optimization strategies and applications". *Cellulose* 2022, 29 (14), 7495-7533. DOI: 10.1007/s10570-022-04697-1.
126. Padrão, J. and A. Zille, *Surface chemistry of nanocellulose and its composites*, in *Nanocellulose and its composites for water treatment applications*, D. Kumar, Editor. 2021, CRC Press: Boca Raton. p. 35 - 50.
127. Zhang, P., L. Chen, Q. Zhang, et al. "Using in situ nanocellulose-coating technology based on dynamic bacterial cultures for upgrading conventional biomedical materials and reinforcing nanocellulose hydrogels". *Biotechnology Progress* 2016, 32 (4), 1077-1084. DOI: 10.1002/btpr.2280.
128. Ferro, M., A. Mannu, W. Panzeri, et al. "An Integrated Approach to Optimizing Cellulose Mercerization". *Polymers* 2020, 12 (7). DOI: 10.3390/polym12071559.
129. Dubey, S., R.K. Sharma, P. Agarwal, et al. "From rotten grapes to industrial exploitation: Komagataeibacter europaeus SGP37, a micro-factory for macroscale production of bacterial nanocellulose". *International Journal of Biological Macromolecules* 2017, 96, 52-60. DOI: 10.1016/j.ijbiomac.2016.12.016.
130. Marín, P., S.M. Martirani-Von Abercron, L. Urbina, et al. "Bacterial nanocellulose production from naphthalene". *Microbial Biotechnology* 2019, 12 (4), 662-676. DOI: 10.1111/1751-7915.13399.
131. Dima, S.-O., D.-M. Panaitescu, C. Orban, et al. "Bacterial Nanocellulose from Side-Streams of Kombucha Beverages Production: Preparation and Physical-Chemical Properties". *Polymers* 2017, 9 (8). DOI: 10.3390/polym9080374.
132. Pacheco, G., C.V. de Mello, B.G. Chiari-Andréo, et al. "Bacterial cellulose skin masks—Properties and sensory tests". *Journal of Cosmetic Dermatology* 2017, 17 (5), 840-847. DOI: 10.1111/jocd.12441.
133. Ashrafi, Z., L. Lucia, and W. Krause. "Bioengineering tunable porosity in bacterial nanocellulose matrices". *Soft Matter* 2019, 15 (45), 9359-9367. DOI: 10.1039/c9sm01895f.
134. Lee, S., A. Abraham, A.C.S. Lim, et al. "Characterisation of bacterial nanocellulose and nanostructured carbon produced from crude glycerol by Komagataeibacter sucrofermentans". *Bioresource Technology* 2021, 342. DOI: 10.1016/j.biortech.2021.125918.
135. Sämfors, S., K. Karlsson, J. Sundberg, et al. "Biofabrication of bacterial nanocellulose scaffolds with complex vascular structure". *Biofabrication* 2019, 11 (4). DOI: 10.1088/1758-5090/ab2b4f.
136. Soeiro, V.S., L.L. Tundisi, V.A. Amaral, et al. "Bacterial nanocellulose and fibroin: natural products to produce a structure membranes". *Matéria (Rio de Janeiro)* 2021, 26 (4). DOI: 10.1590/s1517-707620210004.1386.
137. Noremylia, M.B., M.Z. Hassan, and Z. Ismail. "Recent advancement in isolation, processing, characterization and applications of emerging nanocellulose: A review". *International Journal of Biological Macromolecules* 2022, 206, 954-976. DOI: 10.1016/j.ijbiomac.2022.03.064.
138. Tortorella, S., V. Vetri Buratti, M. Maturi, et al. " Surface-Modified Nanocellulose for Application in Biomedical Engineering and Nanomedicine: A Review ". *International Journal of Nanomedicine* 2020, Volume 15, 9909-9937. DOI: 10.2147/ijn.S266103.

139. P. Saastamoinen, P., M.-L. Mattinen, U. Hippi, et al. "Laccase aided modification of nanofibrillated cellulose with dodecyl gallate". *BioResources* 2012, 7 (4), 5749-5770.
140. Wang, Y., X. Wang, Y. Xie, et al. "Functional nanomaterials through esterification of cellulose: a review of chemistry and application". *Cellulose* 2018, 25 (7), 3703-3731. DOI: 10.1007/s10570-018-1830-3.
141. Bangar, S.P., M.M. Harussani, R.A. Ilyas, et al. "Surface modifications of cellulose nanocrystals: Processes, properties, and applications". *Food Hydrocolloids* 2022, 130. DOI: 10.1016/j.foodhyd.2022.107689.
142. Liu, Y., X. Lv, J. Bao, et al. "Characterization of silane treated and untreated natural cellulosic fibre from corn stalk waste as potential reinforcement in polymer composites". *Carbohydrate Polymers* 2019, 218, 179-187. DOI: 10.1016/j.carbpol.2019.04.088.
143. Ghasemlou, M., F. Daver, E.P. Ivanova, et al. "Surface modifications of nanocellulose: From synthesis to high-performance nanocomposites". *Progress in Polymer Science* 2021, 119. DOI: 10.1016/j.progpolymsci.2021.101418.
144. Sanchez-Salvador, J., A. Balea, M. Monte, et al. "Study of The Reaction Mechanism to Produce Nanocellulose-Graft-Chitosan Polymer". *Nanomaterials* 2018, 8 (11). DOI: 10.3390/nano8110883.
145. Rana, A.K., E. Frollini, and V.K. Thakur. "Cellulose nanocrystals: Pretreatments, preparation strategies, and surface functionalization". *International Journal of Biological Macromolecules* 2021, 182, 1554-1581. DOI: 10.1016/j.ijbiomac.2021.05.119.
146. Lunardi, V.B., F.E. Soetaredjo, J.N. Putro, et al. "Nanocelluloses: Sources, Pretreatment, Isolations, Modification, and Its Application as the Drug Carriers". *Polymers* 2021, 13 (13). DOI: 10.3390/polym13132052.
147. Qiao, A., M. Cui, R. Huang, et al. "Advances in nanocellulose-based materials as adsorbents of heavy metals and dyes". *Carbohydrate Polymers* 2021, 272. DOI: 10.1016/j.carbpol.2021.118471.
148. Padrão, J., S. Ribeiro, S. Lanceros-Méndez, et al. "Effect of bacterial nanocellulose binding on the bactericidal activity of bovine lactoferrin". *Heliyon* 2020, 6 (7). DOI: 10.1016/j.heliyon.2020.e04372.
149. Almeida, R.O., T.C. Maloney, and J.A.F. Gamelas. "Production of functionalized nanocelluloses from different sources using deep eutectic solvents and their applications". *Industrial Crops and Products* 2023, 199. DOI: 10.1016/j.indcrop.2023.116583.
150. Iqbal, D., Y. Zhao, R. Zhao, et al. "A Review on Nanocellulose and Superhydrophobic Features for Advanced Water Treatment". *Polymers* 2022, 14 (12). DOI: 10.3390/polym14122343.
151. Barsbay, M. and O. Güven. "Surface modification of cellulose via conventional and controlled radiation-induced grafting". *Radiation Physics and Chemistry* 2019, 160, 1-8. DOI: 10.1016/j.radphyschem.2019.03.002.
152. Salimi, S., R. Sotudeh-Gharebagh, R. Zarghami, et al. "Production of Nanocellulose and Its Applications in Drug Delivery: A Critical Review". *ACS Sustainable Chemistry & Engineering* 2019, 7 (19), 15800-15827. DOI: 10.1021/acssuschemeng.9b02744.
153. Oberlintner, A., V. Shvalya, A. Vasudevan, et al. "Hydrophilic to hydrophobic: Ultrafast conversion of cellulose nanofibrils by cold plasma fluorination". *Applied Surface Science* 2022, 581. DOI: 10.1016/j.apsusc.2021.152276.
154. Matouk, Z., B. Torriss, R. Rincón, et al. "Functionalization of cellulose nanocrystal films using Non-Thermal atmospheric –Pressure plasmas". *Applied Surface Science* 2020, 511. DOI: 10.1016/j.apsusc.2020.145566.

155. Matouk, Z., R. Rincón, B. Torriss, et al. "Functionalization of cellulose nanocrystal powder by non-thermal atmospheric-pressure plasmas". *Cellulose* 2021, 28 (10), 6239-6252. DOI: 10.1007/s10570-021-03927-2.
156. Gromovykh, T.I., A.Y. Vasil, N.A. kov, et al. "Creation of composites of bacterial cellulose and silver nanoparticles: evaluation of antimicrobial activity and cytotoxicity". *International Journal of Nanotechnology* 2019, 16 (6/7/8/9/10). DOI: 10.1504/ijnt.2019.106615.
157. Kadiyala, U., N.A. Kotov, and J.S. VanEpps. "Antibacterial Metal Oxide Nanoparticles: Challenges in Interpreting the Literature". *Current Pharmaceutical Design* 2018, 24 (8), 896-903. DOI: 10.2174/1381612824666180219130659.
158. Ribeiro, A.I., A.M. Dias, and A. Zille. "Synergistic Effects Between Metal Nanoparticles and Commercial Antimicrobial Agents: A Review". *ACS Applied Nano Materials* 2022, 5 (3), 3030-3064. DOI: 10.1021/acsanm.1c03891.
159. Baptista, P.V., M.P. McCusker, A. Carvalho, et al. "Nano-Strategies to Fight Multidrug Resistant Bacteria—"A Battle of the Titans"". *Frontiers in Microbiology* 2018, 9. DOI: 10.3389/fmicb.2018.01441.
160. Luo, L., W. Huang, J. Zhang, et al. "Metal-Based Nanoparticles as Antimicrobial Agents: A Review". *ACS Applied Nano Materials* 2024, 7 (3), 2529-2545. DOI: 10.1021/acsanm.3c05615.
161. Sirelkhatim, A., S. Mahmud, A. Seeni, et al. "Review on Zinc Oxide Nanoparticles: Antibacterial Activity and Toxicity Mechanism". *Nano-Micro Letters* 2015, 7 (3), 219-242. DOI: 10.1007/s40820-015-0040-x.
162. Park, H.-J., J.Y. Kim, J. Kim, et al. "Silver-ion-mediated reactive oxygen species generation affecting bactericidal activity". *Water Research* 2009, 43 (4), 1027-1032. DOI: 10.1016/j.watres.2008.12.002.
163. Lushchak, V.I. "Adaptive response to oxidative stress: Bacteria, fungi, plants and animals". *Comparative Biochemistry and Physiology Part C: Toxicology & Pharmacology* 2011, 153 (2), 175-190. DOI: 10.1016/j.cbpc.2010.10.004.
164. Li, J.J., L. Zou, D. Hartono, et al. "Gold Nanoparticles Induce Oxidative Damage in Lung Fibroblasts In Vitro". *Advanced Materials* 2008, 20 (1), 138-142. DOI: 10.1002/adma.200701853.
165. Ivask, A., K. Juganson, O. Bondarenko, et al. "Mechanisms of toxic action of Ag, ZnO and CuO nanoparticles to selected ecotoxicological test organisms and mammalian cells in vitro: A comparative review". *Nanotoxicology* 2013, 8 (sup1), 57-71. DOI: 10.3109/17435390.2013.855831.
166. Riaz Ahmed, K.B., A.M. Nagy, R.P. Brown, et al. "Silver nanoparticles: Significance of physicochemical properties and assay interference on the interpretation of in vitro cytotoxicity studies". *Toxicology in Vitro* 2017, 38, 179-192. DOI: 10.1016/j.tiv.2016.10.012.
167. Badawy, A.M.E., T.P. Luxton, R.G. Silva, et al. "Impact of Environmental Conditions (pH, Ionic Strength, and Electrolyte Type) on the Surface Charge and Aggregation of Silver Nanoparticles Suspensions". *Environmental Science & Technology* 2010, 44 (4), 1260-1266. DOI: 10.1021/es902240k.
168. Ohta, S., E. Kikuchi, A. Ishijima, et al. "Investigating the optimum size of nanoparticles for their delivery into the brain assisted by focused ultrasound-induced blood–brain barrier opening". *Scientific Reports* 2020, 10 (1). DOI: 10.1038/s41598-020-75253-9.
169. Dakal, T.C., A. Kumar, R.S. Majumdar, et al. "Mechanistic Basis of Antimicrobial Actions of Silver Nanoparticles". *Frontiers in Microbiology* 2016, 7. DOI: 10.3389/fmicb.2016.01831.

170. Lok, C.-N., C.-M. Ho, R. Chen, et al. "Silver nanoparticles: partial oxidation and antibacterial activities". *JBIC Journal of Biological Inorganic Chemistry* 2007, 12 (4), 527-534. DOI: 10.1007/s00775-007-0208-z.
171. Suliman Y, A.O., D. Ali, S. Alarifi, et al. "Evaluation of cytotoxic, oxidative stress, proinflammatory and genotoxic effect of silver nanoparticles in human lung epithelial cells". *Environmental Toxicology* 2015, 30 (2), 149-160. DOI: 10.1002/tox.21880.
172. Dizaj, S.M., F. Lotfipour, M. Barzegar-Jalali, et al. "Antimicrobial activity of the metals and metal oxide nanoparticles". *Materials Science and Engineering: C* 2014, 44, 278-284. DOI: 10.1016/j.msec.2014.08.031.
173. Ando, S., T. Hioki, T. Yamada, et al. "Ag2O3 clathrate is a novel and effective antimicrobial agent". *Journal of Materials Science* 2011, 47 (6), 2928-2931. DOI: 10.1007/s10853-011-6125-0.
174. Vergara-Llanos, D., T. Koning, M.F. Pavicic, et al. "Antibacterial and cytotoxic evaluation of copper and zinc oxide nanoparticles as a potential disinfectant material of connections in implant provisional abutments: An in-vitro study". *Archives of Oral Biology* 2021, 122. DOI: 10.1016/j.archoralbio.2020.105031.
175. Nabila, M.I. and K. Kannabiran. "Biosynthesis, characterization and antibacterial activity of copper oxide nanoparticles (CuO NPs) from actinomycetes". *Biocatalysis and Agricultural Biotechnology* 2018, 15, 56-62. DOI: 10.1016/j.bcab.2018.05.011.
176. Singh, P., A. Garg, S. Pandit, et al. "Antimicrobial Effects of Biogenic Nanoparticles". *Nanomaterials* 2018, 8 (12). DOI: 10.3390/nano8121009.
177. Das, B. and S. Patra, *Antimicrobials*, in *Nanostructures for Antimicrobial Therapy*. 2017. p. 1-22.
178. Alzagameem, Klein, Bergs, et al. "Antimicrobial Activity of Lignin and Lignin-Derived Cellulose and Chitosan Composites Against Selected Pathogenic and Spoilage Microorganisms". *Polymers* 2019, 11 (4). DOI: 10.3390/polym11040670.
179. Gu, X., Z. Xu, L. Gu, et al. "Preparation and antibacterial properties of gold nanoparticles: a review". *Environmental Chemistry Letters* 2020, 19 (1), 167-187. DOI: 10.1007/s10311-020-01071-0.
180. Buchman, J.T., N.V. Hudson-Smith, K.M. Landy, et al. "Understanding Nanoparticle Toxicity Mechanisms To Inform Redesign Strategies To Reduce Environmental Impact". *Accounts of Chemical Research* 2019, 52 (6), 1632-1642. DOI: 10.1021/acs.accounts.9b00053.
181. Yan, L., F. Zhao, J. Wang, et al. "A Safe-by-Design Strategy towards Safer Nanomaterials in Nanomedicines". *Advanced Materials* 2019, 31 (45). DOI: 10.1002/adma.201805391.
182. Saifi, M.A., W. Khan, and C. Godugu. "Cytotoxicity of Nanomaterials: Using Nanotoxicology to Address the Safety Concerns of Nanoparticles". *Pharmaceutical Nanotechnology* 2018, 6 (1), 3-16. DOI: 10.2174/2211738505666171023152928.
183. Najahi-Missaoui, W., R.D. Arnold, and B.S. Cummings. "Safe Nanoparticles: Are We There Yet?". *International Journal of Molecular Sciences* 2020, 22 (1). DOI: 10.3390/ijms22010385.
184. Martínez, G., M. Merinero, M. Pérez-Aranda, et al. "Environmental Impact of Nanoparticles' Application as an Emerging Technology: A Review". *Materials* 2020, 14 (1). DOI: 10.3390/ma14010166.
185. Schmutz, M., O. Borges, S. Jesus, et al. "A Methodological Safe-by-Design Approach for the Development of Nanomedicines". *Frontiers in Bioengineering and Biotechnology* 2020, 8. DOI: 10.3389/fbioe.2020.00258.

186. Lin, S., T. Yu, Z. Yu, et al. "Nanomaterials Safer-by-Design: An Environmental Safety Perspective". *Advanced Materials* 2018, 30 (17). DOI: 10.1002/adma.201705691.
187. Długosz, O., K. Szostak, A. Staroń, et al. "Methods for Reducing the Toxicity of Metal and Metal Oxide NPs as Biomedicine". *Materials* 2020, 13 (2). DOI: 10.3390/ma13020279.
188. Ha, M.K., Y.J. Shim, and T.H. Yoon. "Effects of agglomeration on in vitro dosimetry and cellular association of silver nanoparticles". *Environmental Science: Nano* 2018, 5 (2), 446-455. DOI: 10.1039/c7en00965h.
189. Medici, S., M. Peana, A. Pelucelli, et al. "An updated overview on metal nanoparticles toxicity". *Seminars in Cancer Biology* 2021, 76, 17-26. DOI: 10.1016/j.semcancer.2021.06.020.
190. Sun, H., C. Jiang, L. Wu, et al. "Cytotoxicity-Related Bioeffects Induced by Nanoparticles: The Role of Surface Chemistry". *Frontiers in Bioengineering and Biotechnology* 2019, 7. DOI: 10.3389/fbioe.2019.00414.
191. Ribeiro, A.I., A.M. Dias, and A. Zille. "Synergistic Effects Between Metal Nanoparticles and Commercial Antimicrobial Agents: A Review". *ACS Applied Nano Materials* 2022. DOI: 10.1021/acsanm.1c03891.
192. Manuja, A., B. Kumar, R. Kumar, et al. "Metal/metal oxide nanoparticles: Toxicity concerns associated with their physical state and remediation for biomedical applications". *Toxicology Reports* 2021, 8, 1970-1978. DOI: 10.1016/j.toxrep.2021.11.020.
193. Sethi, S., Saruchi, Medha, et al. "Biopolymer starch-gelatin embedded with silver nanoparticle–based hydrogel composites for antibacterial application". *Biomass Conversion and Biorefinery* 2022. DOI: 10.1007/s13399-022-02437-w.
194. Rónavári, A., N. Igaz, D.I. Adamecz, et al. "Green Silver and Gold Nanoparticles: Biological Synthesis Approaches and Potentials for Biomedical Applications". *Molecules* 2021, 26 (4). DOI: 10.3390/molecules26040844.
195. Soltys, L., O. Olkhovyy, T. Tatarchuk, et al. "Green Synthesis of Metal and Metal Oxide Nanoparticles: Principles of Green Chemistry and Raw Materials". *Magnetochemistry* 2021, 7 (11). DOI: 10.3390/magnetochemistry7110145.
196. Hasan, K.M.F., H. Wang, S. Mahmud, et al. "Coloration of aramid fabric via in-situ biosynthesis of silver nanoparticles with enhanced antibacterial effect". *Inorganic Chemistry Communications* 2020, 119. DOI: 10.1016/j.inoche.2020.108115.
197. Gadkari, R.R., S.W. Ali, M. Joshi, et al. "Leveraging antibacterial efficacy of silver loaded chitosan nanoparticles on layer-by-layer self-assembled coated cotton fabric". *International Journal of Biological Macromolecules* 2020, 162, 548-560. DOI: 10.1016/j.ijbiomac.2020.06.137.
198. Mahmud, S., M. Sultana, M. Pervez, et al. "Surface Functionalization of "Rajshahi Silk" Using Green Silver Nanoparticles". *Fibers* 2017, 5 (3). DOI: 10.3390/fib5030035.
199. Mahmud, S., M.N. Pervez, K.M.F. Hasan, et al. "In situ synthesis of green AgNPs on ramie fabric with functional and catalytic properties". *Emerging Materials Research* 2019, 8 (4), 623-633. DOI: 10.1680/jemmr.19.00012.
200. Raza, Z.A. "In Situ Synthesis and Immobilization of Nanosilver on Knitted Cellulose Fabric". *Journal of Natural Fibers* 2017, 15 (2), 183-190. DOI: 10.1080/15440478.2017.1321517.
201. Hedayati, N., M. Montazer, M. Mahmoudirad, et al. "Cotton fabric incorporated with β-cyclodextrin/ketoconazole/Ag NPs generating outstanding antifungal and antibacterial performances". *Cellulose* 2021, 28 (12), 8095-8113. DOI: 10.1007/s10570-021-04001-7.

202. Khe, Y., M. Sv, S. AA, et al. "Antibacterial effect of cotton fabric treated with silver nanoparticles of different sizes and shapes". *International Journal of Nanomaterials, Nanotechnology and Nanomedicine* 2019, 5 (2), 016-023. DOI: 10.17352/2455-3492.000031.
203. Prasher, P., M. Sharma, M. Mehta, et al. "Current-status and applications of polysaccharides in drug delivery systems". *Colloid and Interface Science Communications* 2021, 42. DOI: 10.1016/j.colcom.2021.100418.
204. Reyes, D.C., Z. Ma, and J.J. Romero. "The Antimicrobial Properties of Technical Lignins and Their Derivatives—A Review". *Polymers* 2024, 16 (15). DOI: 10.3390/polym16152181.
205. Gullón, P., B. Gullón, G. Astray, et al. "Valorization of by-products from olive oil industry and added-value applications for innovative functional foods". *Food Research International* 2020, 137. DOI: 10.1016/j.foodres.2020.109683.
206. Balderrama-González, A.-S., H.-A. Piñón-Castillo, C.-A. Ramírez-Valdespino, et al. "Antimicrobial Resistance and Inorganic Nanoparticles". *International Journal of Molecular Sciences* 2021, 22 (23). DOI: 10.3390/ijms222312890.
207. Betzer, O., M. Shilo, R. Opochinsky, et al. "The Effect of Nanoparticle Size on the Ability to Cross the Blood–Brain Barrier: An In Vivo Study". *Nanomedicine* 2017, 12 (13), 1533-1546. DOI: 10.2217/nnm-2017-0022.
208. Wang, L., Q. Hou, W. Zheng, et al. "Fluorescent and Antibacterial Aminobenzeneboronic Acid (ABA)-Modified Gold Nanoclusters for Self-Monitoring Residual Dosage and Smart Wound Care". *ACS Nano* 2021, 15 (11), 17885-17894. DOI: 10.1021/acsnano.1c06139.
209. Roig-Sanchez, S., O. Torrecilla, J. Floriach-Clark, et al. "One-Step Biosynthesis of Soft Magnetic Bacterial Cellulose Spheres with Localized Nanoparticle Functionalization". *ACS Applied Materials & Interfaces* 2021, 13 (46), 55569-55576. DOI: 10.1021/acsami.1c17752.
210. Huang, C., Q. Ye, J. Dong, et al. "Biofabrication of natural Au/bacterial cellulose hydrogel for bone tissue regeneration via in-situ fermentation". *Smart Materials in Medicine* 2023, 4, 1-14. DOI: 10.1016/j.smaim.2022.06.001.
211. Zhou, J.-J., X.-H. Li, P.-Y. He, et al. "Implantable versatile oxidized bacterial cellulose membrane for postoperative HNSCC treatment via photothermal-boosted immunotherapy". *Nano Research* 2022, 16 (1), 951-963. DOI: 10.1007/s12274-022-4811-7.
212. Li, L., G. Li, Y. Wu, et al. "Dual-functional bacterial cellulose modified with phase-transitioned proteins and gold nanorods combining antifouling and photothermal bactericidal properties". *Journal of Materials Science & Technology* 2022, 110, 14-23. DOI: 10.1016/j.jmst.2021.10.011.
213. Berndt, S., F. Wesarg, C. Wiegand, et al. "Antimicrobial porous hybrids consisting of bacterial nanocellulose and silver nanoparticles". *Cellulose* 2013, 20 (2), 771-783. DOI: 10.1007/s10570-013-9870-1.
214. Tsikourkitoudi, V., B. Henriques-Normark, and G.A. Sotiriou. "Inorganic nanoparticle engineering against bacterial infections". *Current Opinion in Chemical Engineering* 2022, 38. DOI: 10.1016/j.coche.2022.100872.
215. Wan, Y., S. Yang, J. Wang, et al. "Scalable synthesis of robust and stretchable composite wound dressings by dispersing silver nanowires in continuous bacterial cellulose". *Composites Part B: Engineering* 2020, 199. DOI: 10.1016/j.compositesb.2020.108259.

216. Chatchawanwirote, L., P. Chuysinuan, T. Thanyacharoen, et al. "Green synthesis of photomediated silver nanoprisms via a light-induced transformation reaction and silver nanoprism-impregnated bacteria cellulose films for use as antibacterial wound dressings". *Journal of Drug Delivery Science and Technology* 2019, 54. DOI: 10.1016/j.jddst.2019.101305.
217. Xie, Y., L. Yue, Y. Zheng, et al. "The antibacterial stability of poly(dopamine) in-situ reduction and chelation nano-Ag based on bacterial cellulose network template". *Applied Surface Science* 2019, 491, 383-394. DOI: 10.1016/j.apsusc.2019.06.096.
218. Gupta, A., S.M. Briffa, S. Swingler, et al. "Synthesis of Silver Nanoparticles Using Curcumin-Cyclodextrins Loaded into Bacterial Cellulose-Based Hydrogels for Wound Dressing Applications". *Biomacromolecules* 2020, 21 (5), 1802-1811. DOI: 10.1021/acs.biomac.9b01724.
219. Zhao, H., L. Zhang, S. Zheng, et al. "Bacteriostatic activity and cytotoxicity of bacterial cellulose-chitosan film loaded with in-situ synthesized silver nanoparticles". *Carbohydrate Polymers* 2022, 281. DOI: 10.1016/j.carbpol.2021.119017.
220. Song, S., Z. Liu, M.A. Abubaker, et al. "Antibacterial polyvinyl alcohol/bacterial cellulose/nano-silver hydrogels that effectively promote wound healing". *Materials Science and Engineering: C* 2021, 126. DOI: 10.1016/j.msec.2021.112171.
221. Fadakar Sarkandi, A., M. Montazer, T. Harifi, et al. "Innovative preparation of bacterial cellulose/silver nanocomposite hydrogels: In situ green synthesis, characterization, and antibacterial properties". *Journal of Applied Polymer Science* 2020, 138 (6). DOI: 10.1002/app.49824.
222. Nicoara, A.I., A.E. Stoica, D.-I. Ene, et al. "In Situ and Ex Situ Designed Hydroxyapatite: Bacterial Cellulose Materials with Biomedical Applications". *Materials* 2020, 13 (21). DOI: 10.3390/ma13214793.
223. Yang, X., J. Huang, C. Chen, et al. "Biomimetic Design of Double-Sided Functionalized Silver Nanoparticle/Bacterial Cellulose/Hydroxyapatite Hydrogel Mesh for Temporary Cranioplasty". *ACS Applied Materials & Interfaces* 2023, 15 (8), 10506-10519. DOI: 10.1021/acsami.2c22771.
224. Li, J., D. Lu, J. Yang, et al. "Three-dimensional flexible SERS substrate based on bacterial cellulose membrane for detection of glutathione in serum". *Cellulose* 2023, 30 (8), 5187-5200. DOI: 10.1007/s10570-023-05160-5.
225. Ferreira, N., A. Marques, H. Águas, et al. "Label-Free Nanosensing Platform for Breast Cancer Exosome Profiling". *ACS Sensors* 2019, 4 (8), 2073-2083. DOI: 10.1021/acssensors.9b00760.
226. He, W., X. Huang, Y. Zheng, et al. "In situ synthesis of bacterial cellulose/copper nanoparticles composite membranes with long-term antibacterial property". *Journal of Biomaterials Science, Polymer Edition* 2018, 29 (17), 2137-2153. DOI: 10.1080/09205063.2018.1528518.
227. Xie, Y.-Y., X.-H. Hu, Y.-W. Zhang, et al. "Development and antibacterial activities of bacterial cellulose/graphene oxide-CuO nanocomposite films". *Carbohydrate Polymers* 2020, 229. DOI: 10.1016/j.carbpol.2019.115456.
228. Saleh, A.K., H. El-Gendi, E.M. El-Fakharany, et al. "Exploitation of cantaloupe peels for bacterial cellulose production and functionalization with green synthesized Copper oxide nanoparticles for diverse biological applications". *Scientific Reports* 2022, 12 (1). DOI: 10.1038/s41598-022-23952-w.

229. Almasi, H., L. Mehryar, and A. Ghadertaj. "Characterization of CuO-bacterial cellulose nanohybrids fabricated by in-situ and ex-situ impregnation methods". *Carbohydrate Polymers* 2019, 222. DOI: 10.1016/j.carbpol.2019.114995.
230. Zhen, N., X. Wang, X. Li, et al. "Protein-based natural antibacterial materials and their applications in food preservation". *Microbial Biotechnology* 2021, 15 (5), 1324-1338. DOI: 10.1111/1751-7915.13918.
231. Crouvisier-Urion, K., P.R. Bodart, P. Winckler, et al. "Biobased Composite Films from Chitosan and Lignin: Antioxidant Activity Related to Structure and Moisture". *ACS Sustainable Chemistry & Engineering* 2016, 4 (12), 6371-6381. DOI: 10.1021/acssuschemeng.6b00956.
232. Figueiredo, P., K. Lintinen, J.T. Hirvonen, et al. "Properties and chemical modifications of lignin: Towards lignin-based nanomaterials for biomedical applications". *Progress in Materials Science* 2018, 93, 233-269. DOI: 10.1016/j.pmatsci.2017.12.001.
233. Lawoko, M. and J.S.M. Samec. "Kraft lignin valorization: Biofuels and thermoset materials in focus". *Current Opinion in Green and Sustainable Chemistry* 2023, 40. DOI: 10.1016/j.cogsc.2022.100738.
234. Melro, E., A. Filipe, D. Sousa, et al. "Dissolution of kraft lignin in alkaline solutions". *International Journal of Biological Macromolecules* 2020, 148, 688-695. DOI: 10.1016/j.ijbiomac.2020.01.153.
235. Melro, E., L. Alves, F.E. Antunes, et al. "A brief overview on lignin dissolution". *Journal of Molecular Liquids* 2018, 265, 578-584. DOI: 10.1016/j.molliq.2018.06.021.
236. Trovagunta, R., T. Zou, M. Österberg, et al. "Design strategies, properties and applications of cellulose nanomaterials-enhanced products with residual, technical or nanoscale lignin—A review". *Carbohydrate Polymers* 2021, 254. DOI: 10.1016/j.carbpol.2020.117480.
237. Huang, Z., Y. Zhang, C. Zhang, et al. "Lignin-Based Composite Film and Its Application for Agricultural Mulching". *Polymers* 2024, 16 (17). DOI: 10.3390/polym16172488.
238. Nan, N., W. Hu, and J. Wang. "Lignin-Based Porous Biomaterials for Medical and Pharmaceutical Applications". *Biomedicines* 2022, 10 (4). DOI: 10.3390/biomedicines10040747.
239. Rojo, E., M.S. Peresin, W.W. Sampson, et al. "Comprehensive elucidation of the effect of residual lignin on the physical, barrier, mechanical and surface properties of nanocellulose films". *Green Chemistry* 2015, 17 (3), 1853-1866. DOI: 10.1039/c4gc02398f.
240. Wang, X., S. Wang, W. Liu, et al. "Facile fabrication of cellulose composite films with excellent UV resistance and antibacterial activity". *Carbohydrate Polymers* 2019, 225. DOI: 10.1016/j.carbpol.2019.115213.
241. Sadeghifar, H., R. Venditti, J. Jur, et al. "Cellulose-Lignin Biodegradable and Flexible UV Protection Film". *ACS Sustainable Chemistry & Engineering* 2016, 5 (1), 625-631. DOI: 10.1021/acssuschemeng.6b02003.
242. Paulo, F. and L. Santos. "Deriving valorization of phenolic compounds from olive oil by-products for food applications through microencapsulation approaches: a comprehensive review". *Critical Reviews in Food Science and Nutrition* 2020, 61 (6), 920-945. DOI: 10.1080/10408398.2020.1748563.
243. Amara, C., A. El Mahdi, P.K. Akman, et al. "Use of cellulose microfibers from olive pomace to reinforce green composites for sustainable packaging applications". *Food Science & Nutrition* 2023, 11 (9), 5102-5113. DOI: 10.1002/fsn3.3469.
244. Barrère, F., T.A. Mahmood, K. de Groot, et al. "Advanced biomaterials for skeletal tissue regeneration: Instructive and smart functions". *Materials Science and Engineering: R: Reports* 2008, 59 (1), 38-71. DOI: https://doi.org/10.1016/j.mser.2007.12.001.

245. Ramakrishna, S., L. Tian, C. Wang, et al., *Safety testing of a new medical device*, in *Medical Devices*, S. Ramakrishna, et al., Editors. 2015, Woodhead Publishing: Sawston. p. 137-153.
246. Montanaro, L., C.R. Arciola, E. Cenni, et al. "Cytotoxicity, blood compatibility and antimicrobial activity of two cyanoacrylate glues for surgical use". *Biomaterials* 2000, 22 (1), 59-66. DOI: https://doi.org/10.1016/S0142-9612(00)00163-0.
247. Bayda, S., M. Adeel, T. Tuccinardi, et al. "The history of nanoscience and nanotechnology: from chemical–physical applications to nanomedicine". *Molecules* 2020, 25 (1), 112.
248. Park, S.-B., E. Lih, K.-S. Park, et al. "Biopolymer-based functional composites for medical applications". *Progress in Polymer Science* 2017, 68, 77-105. DOI: 10.1016/j.progpolymsci.2016.12.003.
249. Torgbo, S. and P. Sukyai. "Biodegradation and thermal stability of bacterial cellulose as biomaterial: The relevance in biomedical applications". *Polymer Degradation and Stability* 2020, 179. DOI: 10.1016/j.polymdegradstab.2020.109232.
250. Pötzinger, Y., D. Kralisch, and D. Fischer. "Bacterial Nanocellulose: The Future of Controlled Drug Delivery?". *Therapeutic Delivery* 2017, 8 (9), 753-761. DOI: 10.4155/tde-2017-0059.
251. Silva-López, M.S. and L.E. Alcántara-Quintana. "The Era of Biomaterials: Smart Implants?". *ACS Applied Bio Materials* 2023, 6 (8), 2982-2994. DOI: 10.1021/acsabm.3c00284.
252. Sharma, A., G.R. Kokil, Y. He, et al. "Inorganic/organic combination: Inorganic particles/polymer composites for tissue engineering applications". *Bioactive Materials* 2023, 24, 535-550. DOI: 10.1016/j.bioactmat.2023.01.003.
253. de Oliveira Barud, H.G., R.R. da Silva, M.A.C. Borges, et al. "Bacterial Nanocellulose in Dentistry: Perspectives and Challenges". *Molecules* 2020, 26 (1). DOI: 10.3390/molecules26010049.
254. Hussain, Z., W. Sajjad, T. Khan, et al. "Production of bacterial cellulose from industrial wastes: a review". *Cellulose* 2019, 26 (5), 2895-2911. DOI: 10.1007/s10570-019-02307-1.
255. Pang, M., Y. Huang, F. Meng, et al. "Application of bacterial cellulose in skin and bone tissue engineering". *European Polymer Journal* 2020, 122. DOI: 10.1016/j.eurpolymj.2019.109365.
256. Campbell, S., N. Preciado Rivera, S. Said, et al. "Injectable On-Demand Pulsatile Drug Delivery Hydrogels Using Alternating Magnetic Field-Triggered Polymer Glass Transitions". *ACS Applied Materials & Interfaces* 2023, 15 (42), 48892-48902. DOI: 10.1021/acsami.3c09299.
257. Gonçalves, C., Y. Lalatonne, L. Melro, et al. "New dextrin nanomagnetogels as contrast agents for magnetic resonance imaging". *Journal of Materials Chemistry B* 2013, 1 (42). DOI: 10.1039/c3tb21063d.
258. Indoliya, A. and R. Poddar. "Hyperthermic Treatment by Superparamagnetic Iron Oxide Nanoparticles for Targeted Tumor Therapy: An In-Vivo Approach Guided by Swept-Source Optical Coherence Tomography". *Journal of Medical and Biological Engineering* 2022, 43 (1), 32-41. DOI: 10.1007/s40846-022-00769-6.
259. Wagner, K.R., J.T. Kaiser, S.F. DeFroda, et al. "Rehabilitation, Restrictions, and Return to Sport After Cartilage Procedures". *Arthroscopy, Sports Medicine, and Rehabilitation* 2022, 4 (1), e115-e124. DOI: 10.1016/j.asmr.2021.09.029.
260. Gorgieva, S. "Bacterial Cellulose as a Versatile Platform for Research and Development of Biomedical Materials". *Processes* 2020, 8 (5). DOI: 10.3390/pr8050624.

261. BİNgÜL, N.D., Y.E. ÖZ, A. ŞEndemİR, et al. "Microbial biopolymers in articular cartilage tissue engineering". *Journal of Polymer Research* 2022, 29 (8). DOI: 10.1007/s10965-022-03178-0.
262. Revin, V.V., E.V. Liyaskina, M.V. Parchaykina, et al. "Bacterial Cellulose-Based Polymer Nanocomposites: A Review". *Polymers* 2022, 14 (21). DOI: 10.3390/polym14214670.
263. Horbert, V., J. Boettcher, P. Foehr, et al. "Laser perforation and cell seeding improve bacterial nanocellulose as a potential cartilage implant in the in vitro cartilage punch model". *Cellulose* 2019, 26 (1), 647-664. DOI: 10.1007/s10570-019-02286-3.
264. Ong, X.-R., A.X. Chen, N. Li, et al. "Nanocellulose: Recent Advances Toward Biomedical Applications". *Small Science* 2022, 3 (2). DOI: 10.1002/smsc.202200076.
265. Sun, L., C. Chen, X. Gong, et al. "Preparation and characterization of methacrylated gelatin/bacterial cellulose composite hydrogels for cartilage tissue engineering". *Regenerative Biomaterials* 2020, 7 (2), 195-202. DOI: 10.1093/rb/rbz050.
266. Li, G., A.G. Nandgaonkar, Y. Habibi, et al. "An environmentally benign approach to achieving vectorial alignment and high microporosity in bacterial cellulose/chitosan scaffolds". *RSC Advances* 2017, 7 (23), 13678-13688. DOI: 10.1039/c6ra26049g.
267. Roman, M., A.P. Haring, and T.J. Bertucio. "The growing merits and dwindling limitations of bacterial cellulose-based tissue engineering scaffolds". *Current Opinion in Chemical Engineering* 2019, 24, 98-106. DOI: 10.1016/j.coche.2019.03.006.
268. Grigull, N.P., J.I. Redeker, B. Schmitt, et al. "Chondrogenic Potential of Pellet Culture Compared to High-Density Culture on a Bacterial Cellulose Hydrogel". *International Journal of Molecular Sciences* 2020, 21 (8). DOI: 10.3390/ijms21082785.
269. Phatchayawat, P.P., A. Khamkeaw, S. Yodmuang, et al. "3D bacterial cellulose-chitosan-alginate-gelatin hydrogel scaffold for cartilage tissue engineering". *Biochemical Engineering Journal* 2022, 184. DOI: 10.1016/j.bej.2022.108476.
270. Zeng, J., L. Jia, D. Wang, et al. "Bacterial nanocellulose-reinforced gelatin methacryloyl hydrogel enhances biomechanical property and glycosaminoglycan content of 3D-bioprinted cartilage". *International Journal of Bioprinting* 2022, 9 (1). DOI: 10.18063/ijb.v9i1.631.
271. Dou, C., Z. Li, J. Gong, et al. "Bio-based poly (γ-glutamic acid) hydrogels reinforced with bacterial cellulose nanofibers exhibiting superior mechanical properties and cytocompatibility". *International Journal of Biological Macromolecules* 2021, 170, 354-365. DOI: 10.1016/j.ijbiomac.2020.12.148.
272. Wang, K., Q. Ma, Y.-M. Zhang, et al. "Preparation of bacterial cellulose/silk fibroin double-network hydrogel with high mechanical strength and biocompatibility for artificial cartilage". *Cellulose* 2019, 27 (4), 1845-1852. DOI: 10.1007/s10570-019-02869-0.
273. Bao, L., J. Tang, F.F. Hong, et al. "Physicochemical Properties and In Vitro Biocompatibility of Three Bacterial Nanocellulose Conduits for Blood Vessel Applications". *Carbohydrate Polymers* 2020, 239. DOI: 10.1016/j.carbpol.2020.116246.
274. Bao, L., F.F. Hong, G. Li, et al. "Implantation of air-dried bacterial nanocellulose conduits in a small-caliber vascular prosthesis rabbit model". *Materials Science and Engineering: C* 2021, 122. DOI: 10.1016/j.msec.2021.111922.
275. Hu, G., L. Bao, G. Li, et al. "Vascular cells responses to controlled surface structure and properties of bacterial nanocellulose artificial blood vessel after mercerization". *Carbohydrate Polymers* 2023, 306. DOI: 10.1016/j.carbpol.2023.120572.
276. R, R., E. Philip, D. Thomas, et al. "Bacterial nanocellulose: engineering, production, and applications". *Bioengineered* 2021, 12 (2), 11463-11483. DOI: 10.1080/21655979.2021.2009753.

277. Tang, J., L. Bao, X. Li, et al. "Potential of PVA-doped bacterial nano-cellulose tubular composites for artificial blood vessels". *Journal of Materials Chemistry B* 2015, 3 (43), 8537-8547. DOI: 10.1039/c5tb01144b.
278. Wacker, M., J. Riedel, H. Walles, et al. "Comparative Evaluation on Impacts of Fibronectin, Heparin–Chitosan, and Albumin Coating of Bacterial Nanocellulose Small-Diameter Vascular Grafts on Endothelialization In Vitro". *Nanomaterials* 2021, 11 (8). DOI: 10.3390/nano11081952.
279. Bao, L., F.F. Hong, G. Li, et al. "Improved Performance of Bacterial Nanocellulose Conduits by the Introduction of Silk Fibroin Nanoparticles and Heparin for Small-Caliber Vascular Graft Applications". *Biomacromolecules* 2020, 22 (2), 353-364. DOI: 10.1021/acs.biomac.0c01211.
280. Bao, L., C. Li, M. Tang, et al. "Potential of a Composite Conduit with Bacterial Nanocellulose and Fish Gelatin for Application as Small-Diameter Artificial Blood Vessel". *Polymers* 2022, 14 (20). DOI: 10.3390/polym14204367.
281. Piasecka-Zelga, J., P. Zelga, K. Gronkowska, et al. "Toxicological and Sensitization Studies of Novel Vascular Prostheses Made of Bacterial Nanocellulose Modified with Chitosan (MBC) for Application as the Tissue-Engineered Blood Vessels". *Regenerative Engineering and Translational Medicine* 2021, 7 (2), 218-233. DOI: 10.1007/s40883-021-00209-y.
282. Liu, L., X. Ji, L. Mao, et al. "Hierarchical-structured bacterial cellulose/potato starch tubes as potential small-diameter vascular grafts". *Carbohydrate Polymers* 2022, 281. DOI: 10.1016/j.carbpol.2021.119034.
283. Tandon, R., R. Singh, N. Gupta, et al. "Corneal transplantation in the modern era". *Indian Journal of Medical Research* 2019, 150 (1). DOI: 10.4103/ijmr.IJMR_141_19.
284. Shirzaei Sani, E., A. Kheirkhah, D. Rana, et al. "Sutureless repair of corneal injuries using naturally derived bioadhesive hydrogels". *Science Advances* 2019, 5 (3). DOI: 10.1126/sciadv.aav1281.
285. Luo, Y., G. Li, L. Chen, et al. "Preparation and Evaluation of Bacterial Nanocellulose/Hyaluronic Acid Composite Artificial Cornea for Application of Corneal Transplantation". *Biomacromolecules* 2022, 24 (1), 201-212. DOI: 10.1021/acs.biomac.2c01052.
286. Jia, Y., W. Zhu, M. Zheng, et al. "Bacterial cellulose/hyaluronic acid composite hydrogels with improved viscoelastic properties and good thermodynamic stability". *Plastics, Rubber and Composites* 2018, 47 (4), 165-175. DOI: 10.1080/14658011.2018.1447340.
287. Han, Y., C. Li, Q. Cai, et al. "Studies on bacterial cellulose/poly(vinyl alcohol) hydrogel composites as tissue-engineered corneal stroma". *Biomedical Materials* 2020, 15 (3). DOI: 10.1088/1748-605X/ab56ca.
288. Ajdary, R., R. Abidnejad, J. Lehtonen, et al. "Bacterial nanocellulose enables auxetic supporting implants". *Carbohydrate Polymers* 2022, 284. DOI: 10.1016/j.carbpol.2022.119198.
289. Piasecka-Zelga, J., P. Zelga, J. Szulc, et al. "An in vivo biocompatibility study of surgical meshes made from bacterial cellulose modified with chitosan". *International Journal of Biological Macromolecules* 2018, 116, 1119-1127. DOI: 10.1016/j.ijbiomac.2018.05.123.
290. Khan, S., M. Ul-Islam, M.W. Ullah, et al. "Fabrication strategies and biomedical applications of three-dimensional bacterial cellulose-based scaffolds: A review". *International Journal of Biological Macromolecules* 2022, 209, 9-30. DOI: 10.1016/j.ijbiomac.2022.03.191.

291. Lv, X., C. Feng, Y. Liu, et al. "A smart bilayered scaffold supporting keratinocytes and muscle cells in micro/nano-scale for urethral reconstruction". *Theranostics* 2018, 8 (11), 3153-3163. DOI: 10.7150/thno.22080.
292. Binnetoglu, A., B. Demir, D. Akakin, et al. "Bacterial cellulose tubes as a nerve conduit for repairing complete facial nerve transection in a rat model". *European Archives of Oto-Rhino-Laryngology* 2019, 277 (1), 277-283. DOI: 10.1007/s00405-019-05637-9.
293. Wu, Z., S. Xie, Y. Kang, et al. "Biocompatibility evaluation of a 3D-bioprinted alginate-GelMA-bacteria nanocellulose (BNC) scaffold laden with oriented-growth RSC96 cells". *Materials Science and Engineering: C* 2021, 129. DOI: 10.1016/j.msec.2021.112393.
294. Wei, Z., F.F. Hong, Z. Cao, et al. "In Situ Fabrication of Nerve Growth Factor Encapsulated Chitosan Nanoparticles in Oxidized Bacterial Nanocellulose for Rat Sciatic Nerve Regeneration". *Biomacromolecules* 2021, 22 (12), 4988-4999. DOI: 10.1021/acs.biomac.1c00947.
295. Liu, G., M. Ma, H. Meng, et al. "In-situ self-assembly of bacterial cellulose/poly(3,4-ethylenedioxythiophene)-sulfonated nanofibers for peripheral nerve repair". *Carbohydrate Polymers* 2022, 281. DOI: 10.1016/j.carbpol.2021.119044.
296. Ludwicka, K., M. Kolodziejczyk, E. Gendaszewska-Darmach, et al. "Stable composite of bacterial nanocellulose and perforated polypropylene mesh for biomedical applications". *Journal of Biomedical Materials Research Part B: Applied Biomaterials* 2019, 107 (4), 978-987. DOI: https://doi.org/10.1002/jbm.b.34191.
297. Krystel-Whittemore, M., K.N. Dileepan, and J.G. Wood. "Mast cell: a multi-functional master cell". *Frontiers in Immunology* 2016, 6, Review. DOI: 10.3389/fimmu.2015.00620.
298. Zharikov, A.N., V.G. Lubyansky, E.K. Gladysheva, et al. "Early morphological changes in tissues when replacing abdominal wall defects by bacterial nanocellulose in experimental trials". *Journal of Materials Science: Materials in Medicine* 2018, 29 (7), 95. DOI: 10.1007/s10856-018-6111-z.
299. Guo, Z., F. Zhang, H. Wu, et al. "Preparation of antiadhesion polypropylene mesh using bacterial cellulose combined with chitosan hydrogel application in rat abdominal incisional hernia". *International Journal of Abdominal Wall and Hernia Surgery* 2023, 6 (4), 227-235. DOI: 10.4103/ijawhs.ijawhs_40_23.
300. Cui, T., F. Yu, Q. Zhang, et al. "Double-layered bacterial cellulose mesh for hernia repair". *Colloid and Interface Science Communications* 2021, 44. DOI: 10.1016/j.colcom.2021.100496.
301. Hestrin, S. and M. Schramm. "Synthesis of cellulose by Acetobacter xylinum. 2. Preparation of freeze-dried cells capable of polymerizing glucose to cellulose*". *Biochemical Journal* 1954, 58 (2), 345-352. DOI: 10.1042/bj0580345.
302. Gouveia, S., C. Fernández-Costas, M.A. Sanromán, et al. "Polymerisation of Kraft lignin from black liquors by laccase from Myceliophthora thermophila: Effect of operational conditions and black liquor origin". *Bioresource Technology* 2013, 131, 288-294. DOI: 10.1016/j.biortech.2012.12.155.
303. Magalhães, C., A. Isabel Ribeiro, R. Rodrigues, et al. "DBD plasma-treated polyester fabric coated with doped PEDOT:PSS for thermoregulation". *Applied Surface Science* 2025, 686. DOI: 10.1016/j.apsusc.2024.162152.
304. Lee, R.A., C. Bédard, V. Berberi, et al. "UV–Vis as quantification tool for solubilized lignin following a single-shot steam process". *Bioresource Technology* 2013, 144, 658-663. DOI: 10.1016/j.biortech.2013.06.045.

305. Costa, P. and J.M. Sousa Lobo. "Evaluation of Mathematical Models Describing Drug Release from Estradiol Transdermal Systems". *Drug Development and Industrial Pharmacy* 2003, 29 (1), 89-97. DOI: 10.1081/ddc-120016687.
306. Zhang, Y., M. Huo, J. Zhou, et al. "DDSolver: An Add-In Program for Modeling and Comparison of Drug Dissolution Profiles". *The AAPS Journal* 2010, 12 (3), 263-271. DOI: 10.1208/s12248-010-9185-1.
307. Deshmukh, A.R., P.K. Dikshit, and B.S. Kim. "Green in situ immobilization of gold and silver nanoparticles on bacterial nanocellulose film using Punica granatum peels extract and their application as reusable catalysts". *International Journal of Biological Macromolecules* 2022, 205, 169-177. DOI: 10.1016/j.ijbiomac.2022.02.064.
308. Dhar, P., K. Sugimura, M. Yoshioka, et al. "Synthesis-property-performance relationships of multifunctional bacterial cellulose composites fermented in situ alkali lignin medium". *Carbohydrate Polymers* 2021, 252. DOI: 10.1016/j.carbpol.2020.117114.
309. Fouilloux, J., S. Abbad Andaloussi, V. Langlois, et al. "Chemical Modification of Commercial Fabrics by Photoinduced Grafting Tannic Acid to Produce Antioxidant and Antibacterial Textiles". *Sustainability* 2024, 16 (11). DOI: 10.3390/su16114352.
310. Guo, L., M. Li, Q. Xu, et al. "Bio-based films with high antioxidant and improved water-resistant properties from cellulose nanofibres and lignin nanoparticles". *International Journal of Biological Macromolecules* 2023, 227, 365-372. DOI: 10.1016/j.ijbiomac.2022.12.128.
311. Guo, L., Y. Xu, Q. Xu, et al. "Nanocellulose-lignin films incorporating AgNPs for potential wound dressing: green synthesis, antioxidant ability, antibacterial capability and biocompatibility". *Cellulose* 2024, 31 (12), 7569-7585. DOI: 10.1007/s10570-024-06040-2.
312. Bisht, G., S. Srivastava, R. Kulshreshtha, et al. "Applications of red pigments from psychrophilic Rhodonellum psychrophilum GL8 in health, food and antimicrobial finishes on textiles". *Process Biochemistry* 2020, 94, 15-29. DOI: 10.1016/j.procbio.2020.03.021.
313. Lee, C. "Targeted hyperalkalization with NaOH-loaded starch implants enhances doxorubicin efficacy in tumor treatment". *Asian Journal of Pharmaceutical Sciences* 2023, 18 (5). DOI: 10.1016/j.ajps.2023.100853.
314. Chanioti, S., M. Katsouli, and C. Tzia. "Novel Processes for the Extraction of Phenolic Compounds from Olive Pomace and Their Protection by Encapsulation". *Molecules* 2021, 26 (6). DOI: 10.3390/molecules26061781.
315. Ma, Q., L. Wang, H. Zhai, et al. "Lignin dissolution model in formic acid–acetic acid–water systems based on lignin chemical structure". *International Journal of Biological Macromolecules* 2021, 182, 51-58. DOI: 10.1016/j.ijbiomac.2021.03.179.
316. Su, S., R. Kopitzky, S. Tolga, et al. "Polylactide (PLA) and Its Blends with Poly(butylene succinate) (PBS): A Brief Review". *Polymers* 2019, 11 (7). DOI: 10.3390/polym11071193.
317. Jeremic, S., L. Djokic, V. Ajdačić, et al. "Production of bacterial nanocellulose (BNC) and its application as a solid support in transition metal catalysed cross-coupling reactions". *International Journal of Biological Macromolecules* 2019, 129, 351-360. DOI: 10.1016/j.ijbiomac.2019.01.154.
318. Cielecka, I., M. Ryngajłło, W. Maniukiewicz, et al. "Highly Stretchable Bacterial Cellulose Produced by Komagataeibacter hansenii SI1". *Polymers* 2021, 13 (24). DOI: 10.3390/polym13244455.

319. Bimmer, M., M. Reimer, A. Klingl, et al. "Analysis of cellulose synthesis in a high-producing acetic acid bacterium Komagataeibacter hansenii". *Applied Microbiology and Biotechnology* 2023, 107 (9), 2947-2967. DOI: 10.1007/s00253-023-12461-z.
320. Souza, L., R. Antônio, D. Hotza, et al. "Lignin-incorporated bacterial nanocellulose for proton exchange membranes in microbial fuel cells". *Materials Chemistry and Physics* 2023, 293. DOI: 10.1016/j.matchemphys.2022.126963.
321. Fredricks, J.L., M. Parker, P. Grandgeorge, et al. "The effects of temperature, pressure, and time on lignin incorporation in bacterial cellulose materials". *MRS Communications* 2022, 12 (3), 394-402. DOI: 10.1557/s43579-022-00191-8.
322. Choi, S.M., K.M. Rao, S.M. Zo, et al. "Bacterial Cellulose and Its Applications". *Polymers* 2022, 14 (6). DOI: 10.3390/polym14061080.
323. Gromovykh, T.I., M.A. Pigaleva, M.O. Gallyamov, et al. "Structural organization of bacterial cellulose: The origin of anisotropy and layered structures". *Carbohydrate Polymers* 2020, 237. DOI: 10.1016/j.carbpol.2020.116140.
324. Li, D., X. Tian, Z. Wang, et al. "Multifunctional adsorbent based on metal-organic framework modified bacterial cellulose/chitosan composite aerogel for high efficient removal of heavy metal ion and organic pollutant". *Chemical Engineering Journal* 2020, 383. DOI: 10.1016/j.cej.2019.123127.
325. Zhang, H., X. Xu, C. Chen, et al. "In situ controllable fabrication of porous bacterial cellulose". *Materials Letters* 2019, 249, 104-107. DOI: 10.1016/j.matlet.2019.04.026.
326. Núñez, D., R. Cáceres, W. Ide, et al. "An ecofriendly nanocomposite of bacterial cellulose and hydroxyapatite efficiently removes lead from water". *International Journal of Biological Macromolecules* 2020, 165, 2711-2720. DOI: 10.1016/j.ijbiomac.2020.10.055.
327. Adepu, S. and M. Khandelwal. "Ex-situ modification of bacterial cellulose for immediate and sustained drug release with insights into release mechanism". *Carbohydrate Polymers* 2020, 249. DOI: 10.1016/j.carbpol.2020.116816.
328. Hu, J., L. Wang, M. Xiao, et al. "Insights into bacterial cellulose for adsorption and sustained-release mechanism of flavors". *Food Chemistry: X* 2025, 25. DOI: 10.1016/j.fochx.2024.102110.
329. Lowell, S., J.E. Shields, M.A. Thomas, et al., *Characterization of Porous Solids and Powders: Surface Area, Pore Size and Density*. Particle Technology Series. 2004.
330. Rashid, T., C.F. Kait, and T. Murugesan. "A "Fourier Transformed Infrared" Compound Study of Lignin Recovered from a Formic Acid Process". *Procedia Engineering* 2016, 148, 1312-1319. DOI: 10.1016/j.proeng.2016.06.547.
331. Ribeiro, T.B., A.L. Oliveira, C. Costa, et al. "Total and Sustainable Valorisation of Olive Pomace Using a Fractionation Approach". *Applied Sciences* 2020, 10 (19). DOI: 10.3390/app10196785.
332. Mun, J.-S., J.A. Pe, and S.-P. Mun. "Chemical Characterization of Kraft Lignin Prepared from Mixed Hardwoods". *Molecules* 2021, 26 (16). DOI: 10.3390/molecules26164861.
333. Nunes, M.A., J.D. Palmeira, D. Melo, et al. "Chemical Composition and Antimicrobial Activity of a New Olive Pomace Functional Ingredient". *Pharmaceuticals* 2021, 14 (9). DOI: 10.3390/ph14090913.
334. Crugeira, P.J.L., H. Khelifa, L.M.d.S. Barreira, et al. "Bacterial cellulose biosynthesis in the presence of raw moist olive pomace: A green sustainable approach that enhances biopolymer production and properties". *Biomass and Bioenergy* 2025, 197. DOI: 10.1016/j.biombioe.2025.107789.

335. Zimmermann, K.A., J.M. LeBlanc, K.T. Sheets, et al. "Biomimetic design of a bacterial cellulose/hydroxyapatite nanocomposite for bone healing applications". *Materials Science and Engineering: C* 2011, 31 (1), 43-49. DOI: 10.1016/j.msec.2009.10.007.
336. Sabry, N.W., I. Naeem, S.A. Hassanien, et al. "Alkali-treatment of Lupine peels for valorizing adsorption of organic cationic pollutants from wastewater: Kinetics, isotherm, thermodynamic, regeneration, and mechanism". *Next Materials* 2025, 8. DOI: 10.1016/j.nxmate.2025.100568.
337. Wang, Y., H. Guo, X. Li, et al. "Peracetic acid (PAA)-based pretreatment effectively improves medium-chain fatty acids (MCFAs) production from sewage sludge". *Environmental Science and Ecotechnology* 2024, 20. DOI: 10.1016/j.ese.2023.100355.
338. Chiang, Y.-C., C.-C. Lee, and H.-C. Lee. "Characterization of microstructure and surface properties of heat-treated PAN-and rayon-based activated carbon fibers". *Journal of Porous Materials* 2006, 14 (2), 227-237. DOI: 10.1007/s10934-006-9028-8.
339. Krishna, D.N.G. and J. Philip. "Review on surface-characterization applications of X-ray photoelectron spectroscopy (XPS): Recent developments and challenges". *Applied Surface Science Advances* 2022, 12. DOI: 10.1016/j.apsadv.2022.100332.
340. Zhang, A.A., Z.X. Wang, Z.B. Fang, et al. "Long-Range π–π Stacking Brings High Electron Delocalization for Enhanced Photocatalytic Activity in Hydrogen-Bonded Organic Framework". *Angewandte Chemie International Edition* 2024, 63 (46). DOI: 10.1002/anie.202412777.
341. Gengenbach, T.R., G.H. Major, M.R. Linford, et al. "Practical guides for x-ray photoelectron spectroscopy (XPS): Interpreting the carbon 1s spectrum". *Journal of Vacuum Science & Technology A: Vacuum, Surfaces, and Films* 2021, 39 (1). DOI: 10.1116/6.0000682.
342. Sivaranjini, B., R. Mangaiyarkarasi, V. Ganesh, et al. "Vertical Alignment of Liquid Crystals Over a Functionalized Flexible Substrate". *Scientific Reports* 2018, 8 (1). DOI: 10.1038/s41598-018-27039-3.
343. Lin, C.-f., O. Karlsson, O. Myronycheva, et al. "Phosphorylated and carbamylated Kraft lignin for improving fire- and biological-resistance of Scots pine wood". *International Journal of Biological Macromolecules* 2024, 276. DOI: 10.1016/j.ijbiomac.2024.133734.
344. Mohamad, S., L.C. Abdullah, S.S. Jamari, et al. "Influence of drying method on the crystal structure and thermal property of oil palm frond juice-based bacterial cellulose". *Journal of Materials Science* 2022, 57 (2), 1462-1473. DOI: 10.1007/s10853-021-06685-5.
345. Sánchez-Ávila, N., A. Cardarelli, M. Carmona-Cabello, et al. "Kinetic and thermodynamic behavior of co-pyrolysis of olive pomace and thermoplastic waste via thermogravimetric analysis". *Renewable Energy* 2024, 230. DOI: 10.1016/j.renene.2024.120880.
346. Parit, M., H. Du, X. Zhang, et al. "Flexible, Transparent, UV-Protecting, Water-Resistant Nanocomposite Films Based on Polyvinyl Alcohol and Kraft Lignin-Grafted Cellulose Nanofibers". *ACS Applied Polymer Materials* 2022, 4 (5), 3587-3597. DOI: 10.1021/acsapm.2c00157.
347. Ojeda, J.J., M.E. Romero-González, R.T. Bachmann, et al. "Characterization of the Cell Surface and Cell Wall Chemistry of Drinking Water Bacteria by Combining XPS, FTIR Spectroscopy, Modeling, and Potentiometric Titrations". *Langmuir* 2008, 24 (8), 4032-4040. DOI: 10.1021/la702284b.
348. Jacobs, T.W., J.T. Dillon, D.J. Cohen, et al. "Different Methods to Modify the Hydrophilicity of Titanium Implants with Biomimetic Surface Topography to Induce Variable Responses in Bone Marrow Stromal Cells". *Biomimetics* 2024, 9 (4). DOI: 10.3390/biomimetics9040227.

349. Cazón, P., G. Puertas, and M. Vázquez. "Characterization of multilayer bacterial cellulose-chitosan films loaded with grape bagasse antioxidant extract: Insights into spectral and water properties, microstructure, and antioxidant activity". *International Journal of Biological Macromolecules* 2024, 268. DOI: 10.1016/j.ijbiomac.2024.131774.
350. Ruwoldt, J., F.H. Blindheim, and G. Chinga-Carrasco. "Functional surfaces, films, and coatings with lignin – a critical review". *RSC Advances* 2023, 13 (18), 12529-12553. DOI: 10.1039/d2ra08179b.
351. Roche, S., G. D'Ippolito, L.A. Gomez, et al. "Comparative analysis of protein expression of three stem cell populations: Models of cytokine delivery system in vivo". *International Journal of Pharmaceutics* 2013, 440 (1), 72-82. DOI: 10.1016/j.ijpharm.2011.12.041.
352. Costa, L., A.F. Carvalho, A.J.S. Fernandes, et al. "Bacterial nanocellulose as a simple and tailorable platform for controlled drug release". *International Journal of Pharmaceutics* 2024, 663. DOI: 10.1016/j.ijpharm.2024.124560.
353. Sugiarto, S., Y. Leow, C.L. Tan, et al. "How far is Lignin from being a biomedical material?". *Bioactive Materials* 2022, 8, 71-94. DOI: 10.1016/j.bioactmat.2021.06.023.
354. Domínguez-Robles, J., Á. Cárcamo-Martínez, S.A. Stewart, et al. "Lignin for pharmaceutical and biomedical applications – Could this become a reality?". *Sustainable Chemistry and Pharmacy* 2020, 18. DOI: 10.1016/j.scp.2020.100320.
355. Vieira, B., J. Padrão, C. Alves, et al. "Enhancing Functionalization of Health Care Textiles with Gold Nanoparticle-Loaded Hydroxyapatite Composites". *Nanomaterials* 2023, 13 (11). DOI: 10.3390/nano13111752.
356. Jiji, S., S. Udhayakumar, K. Maharajan, et al. "Bacterial cellulose matrix with in situ impregnation of silver nanoparticles via catecholic redox chemistry for third degree burn wound healing". *Carbohydrate Polymers* 2020, 245. DOI: 10.1016/j.carbpol.2020.116573.
357. Yang, W., E. Fortunati, F. Dominici, et al. "Effect of cellulose and lignin on disintegration, antimicrobial and antioxidant properties of PLA active films". *International Journal of Biological Macromolecules* 2016, 89, 360-368. DOI: 10.1016/j.ijbiomac.2016.04.068.
358. Lammi, S., E. Gastaldi, F. Gaubiac, et al. "How olive pomace can be valorized as fillers to tune the biodegradation of PHBV based composites". *Polymer Degradation and Stability* 2019, 166, 325-333. DOI: 10.1016/j.polymdegradstab.2019.06.010.
359. Ghanbari Shendi, E., D. Sivri Ozay, M.T. Ozkaya, et al. "Changes occurring in chemical composition and oxidative stability of virgin olive oil during storage". *Ocl* 2018, 25 (6). DOI: 10.1051/ocl/2018052.
360. Mulinacci, N., F. Ieri, G. Ignesti, et al. "The freezing process helps to preserve the quality of extra virgin olive oil over time: A case study up to 18months". *Food Research International* 2013, 54 (2), 2008-2015. DOI: 10.1016/j.foodres.2013.03.052.
361. Cunliffe, A.J., P.D. Askew, I. Stephan, et al. "How Do We Determine the Efficacy of an Antibacterial Surface? A Review of Standardised Antibacterial Material Testing Methods". *Antibiotics* 2021, 10 (9). DOI: 10.3390/antibiotics10091069.
362. Madureira, J., I. Gonçalves, J. Cardoso, et al. "Effects of Electron Beam Radiation on the Phenolic Composition and Bioactive Properties of Olive Pomace Extracts". *Antioxidants* 2024, 13 (5). DOI: 10.3390/antiox13050558.
363. Yang, J., C. Liu, H. Sun, et al. "The progress in titanium alloys used as biomedical implants: From the view of reactive oxygen species". *Frontiers in Bioengineering and Biotechnology* 2022, 10. DOI: 10.3389/fbioe.2022.1092916.
364. Lourençon, T.V., G.G. de Lima, C.S.P. Ribeiro, et al. "Antioxidant, antibacterial and antitumoural activities of kraft lignin from hardwood fractionated by acid precipitation".

*International Journal of Biological Macromolecules* 2021, 166, 1535-1542. DOI: 10.1016/j.ijbiomac.2020.11.033.

365. Črešnar, K.P., A. Zamboulis, D.N. Bikiaris, et al. "Kraft Lignin/Tannin as a Potential Accelerator of Antioxidant and Antibacterial Properties in an Active Thermoplastic Polyester-Based Multifunctional Material". *Polymers* 2022, 14 (8). DOI: 10.3390/polym14081532.
366. Quero, J., L.F. Ballesteros, P. Ferreira-Santos, et al. "Unveiling the Antioxidant Therapeutic Functionality of Sustainable Olive Pomace Active Ingredients". *Antioxidants* 2022, 11 (5). DOI: 10.3390/antiox11050828.
367. Cabañas-Romero, L.V., C. Valls, S.V. Valenzuela, et al. "Bacterial Cellulose–Chitosan Paper with Antimicrobial and Antioxidant Activities". *Biomacromolecules* 2020, 21 (4), 1568-1577. DOI: 10.1021/acs.biomac.0c00127.
368. Buruaga-Ramiro, C., S.V. Valenzuela, C. Valls, et al. "Development of an antimicrobial bioactive paper made from bacterial cellulose". *International Journal of Biological Macromolecules* 2020, 158, 587-594. DOI: 10.1016/j.ijbiomac.2020.04.234.
369. Gómez-Cruz, I., M. del Mar Contreras, I. Romero, et al. "A biorefinery approach to obtain antioxidants, lignin and sugars from exhausted olive pomace". *Journal of Industrial and Engineering Chemistry* 2021, 96, 356-363. DOI: 10.1016/j.jiec.2021.01.042.
370. Zhao, L., D. Jiang, Y. Cai, et al. "Tuning the size of gold nanoparticles in the citrate reduction by chloride ions". *Nanoscale* 2012, 4 (16). DOI: 10.1039/c2nr30957b.
371. Wan, Y., Z. Guo, X. Jiang, et al. "Quasi-spherical silver nanoparticles: Aqueous synthesis and size control by the seed-mediated Lee–Meisel method". *Journal of Colloid and Interface Science* 2013, 394, 263-268. DOI: 10.1016/j.jcis.2012.12.037.
372. Mehravani, B., A.I. Ribeiro, U. Cvelbar, et al. "In Situ Synthesis of Copper Nanoparticles on Dielectric Barrier Discharge Plasma-Treated Polyester Fabrics at Different Reaction pHs". *ACS Applied Polymer Materials* 2022, 4 (5), 3908-3918. DOI: 10.1021/acsapm.2c00375.
373. Dar, M.A., R. Xie, J. Liu, et al. "Current Paradigms and Future Challenges in Harnessing Nanocellulose for Advanced Applications in Tissue Engineering: A Critical State-of-the-Art Review for Biomedicine". *International Journal of Molecular Sciences* 2025, 26 (4). DOI: 10.3390/ijms26041449.
374. *Nano-Inspired Biosensors for Protein Assay with Clinical Applications*. 2019.
375. Coe, J., C. Kupitz, S. Basu, et al., *Crystallization of Photosystem II for Time-Resolved Structural Studies Using an X-ray Free Electron Laser*, in *Membrane Proteins—Engineering, Purification and Crystallization*. 2015. p. 459-482.
376. Bluhm, H., *X-ray photoelectron spectroscopy (XPS) for in situ characterization of thin film growth*, in *In Situ Characterization of Thin Film Growth*. 2011. p. 75-98.
377. Welker, R.W., *Size Analysis and Identification of Particles*, in *Developments in Surface Contamination and Cleaning*. 2012. p. 179-213.
378. Hang, Y., A. Wang, and N. Wu. "Plasmonic silver and gold nanoparticles: shape- and structure-modulated plasmonic functionality for point-of-caring sensing, bio-imaging and medical therapy". *Chemical Society Reviews* 2024, 53 (6), 2932-2971. DOI: 10.1039/d3cs00793f.
379. Pashkov, D.M., A.A. Guda, M.V. Kirichkov, et al. "Quantitative Analysis of the UV–Vis Spectra for Gold Nanoparticles Powered by Supervised Machine Learning". *The Journal of Physical Chemistry C* 2021, 125 (16), 8656-8666. DOI: 10.1021/acs.jpcc.0c10680.

380. Sikder, M., J.R. Lead, G.T. Chandler, et al. "A rapid approach for measuring silver nanoparticle concentration and dissolution in seawater by UV–Vis". *Science of The Total Environment* 2018, 618, 597-607. DOI: 10.1016/j.scitotenv.2017.04.055.
381. Tsilo, P.H., A.K. Basson, Z.G. Ntombela, et al. "Biosynthesis and Characterization of Copper Nanoparticles Using a Bioflocculant Produced by a Yeast Pichia kudriavzevii Isolated from Kombucha Tea SCOBY". *Applied Nano* 2023, 4 (3), 226-239. DOI: 10.3390/applnano4030013.
382. Stetefeld, J., S.A. McKenna, and T.R. Patel. "Dynamic light scattering: a practical guide and applications in biomedical sciences". *Biophysical Reviews* 2016, 8 (4), 409-427. DOI: 10.1007/s12551-016-0218-6.
383. Zhang, C., Z. Jin, B. Zeng, et al. "Characterizing the Brownian Diffusion of Nanocolloids and Molecular Solutions: Diffusion-Ordered NMR Spectroscopy vs Dynamic Light Scattering". *The Journal of Physical Chemistry B* 2020, 124 (22), 4631-4650. DOI: 10.1021/acs.jpcb.0c02177.
384. Katepetch, C., R. Rujiravanit, and H. Tamura. "Formation of nanocrystalline ZnO particles into bacterial cellulose pellicle by ultrasonic-assisted in situ synthesis". *Cellulose* 2013, 20 (3), 1275-1292. DOI: 10.1007/s10570-013-9892-8.
385. Chung, J., H. Yin, R. Wang, et al. "Applying heteroatom co-doped carbon nanotube for manifesting high performance in the electrochemical reduction of aqueous nitrogen oxide by gold nanoparticles". *Nano Research* 2023, 17 (3), 1151-1164. DOI: 10.1007/s12274-023-5943-0.
386. Satulu, V., B. Mitu, V. Ion, et al. "Combining Fluorinated Polymers with Ag Nanoparticles as a Route to Enhance Optical Properties of Composite Materials". *Polymers* 2020, 12 (8). DOI: 10.3390/polym12081640.
387. Ouyang, L., V. Noël, A. Courty, et al. "Copper Nanoparticles with a Tunable Size: Implications for Plasmonic Catalysis". *ACS Applied Nano Materials* 2022, 5 (2), 2839-2847. DOI: 10.1021/acsanm.2c00016.
388. Krkobabić, A., M. Radetić, A. Zille, et al. "Plant-Assisted Synthesis of Ag-Based Nanoparticles on Cotton: Antimicrobial and Cytotoxicity Studies". *Molecules* 2024, 29 (7). DOI: 10.3390/molecules29071447.
389. Palacios-Hinestroza, H., C. Molina-Ramírez, M.C. López-Jaramillo, et al. "Standardizing the Production and Processing of Bacterial Nanocellulose to Produce Microparticles via a Spray-Dried Method with the Potential to Be Used in the Food Industry". *Polymers* 2025, 17 (16). DOI: 10.3390/polym17162193.
390. Gama, M., P. Gatenholm, and D. Klemm, *Bacterial NanoCellulose*. 2016.
391. Mira-Cuenca, C., T. Meslier, S. Roig-Sanchez, et al. "Patterning Bacterial Cellulose Films with Iron Oxide Nanoparticles and Magnetic Resonance Imaging Monitoring". *ACS Applied Polymer Materials* 2021, 3 (10), 4959-4965. DOI: 10.1021/acsapm.1c00723.
392. Cazón, P., M. Vázquez, and G. Velazquez. "Composite Films with UV-Barrier Properties of Bacterial Cellulose with Glycerol and Poly(vinyl alcohol): Puncture Properties, Solubility, and Swelling Degree". *Biomacromolecules* 2019, 20 (8), 3115-3125. DOI: 10.1021/acs.biomac.9b00704.
393. Nikolova, M.P. and M.S. Chavali. "Metal Oxide Nanoparticles as Biomedical Materials". *Biomimetics* 2020, 5 (2). DOI: 10.3390/biomimetics5020027.
394. Helmlinger, J., C. Sengstock, C. Groß-Heitfeld, et al. "Silver nanoparticles with different size and shape: equal cytotoxicity, but different antibacterial effects". *RSC Advances* 2016, 6 (22), 18490-18501. DOI: 10.1039/c5ra27836h.

395. Lelong, I.H. and G. Rebel. "ph drift of "physiological buffers" and culture media used for cell incubation during in vitro studies". *Journal of Pharmacological and Toxicological Methods* 1998, 39 (4), 203-210. DOI: 10.1016/s1056-8719(98)00019-7.
396. Costa, L., A.F. Carvalho, A.J.S. Fernandes, et al. "On the microstructural anisotropy and mechanical properties of bacterial nanocellulose obtained by static culture". *International Journal of Biological Macromolecules* 2025, 330. DOI: 10.1016/j.ijbiomac.2025.148114.
397. Wang, Y.-Y., X.-Q. Zhao, D.-M. Li, et al. "Review on the strategies for enhancing mechanical properties of bacterial cellulose". *Journal of Materials Science* 2023, 58 (39), 15265-15293. DOI: 10.1007/s10853-023-08803-x.
398. Lee, K.-Y., J.J. Blaker, and A. Bismarck. "Surface functionalisation of bacterial cellulose as the route to produce green polylactide nanocomposites with improved properties". *Composites Science and Technology* 2009, 69 (15-16), 2724-2733. DOI: 10.1016/j.compscitech.2009.08.016.
399. Wang, B., D. Yang, H.-r. Zhang, et al. "Preparation of Esterified Bacterial Cellulose for Improved Mechanical Properties and the Microstructure of Isotactic Polypropylene/Bacterial Cellulose Composites". *Polymers* 2016, 8 (4). DOI: 10.3390/polym8040129.